DI Adrian Ruckhofer, BSc

Investigation of topological and 2D material surfaces using helium atom scattering

DOCTORAL THESIS

to achieve the university degree of

Doktor der technischen Wissenschaften

submitted to

Graz University of Technology

Supervisor:
Em. Univ.-Prof. Dipl.-Phys. Dr.rer.nat Wolfgang E. Ernst
Institute of Experimental Physics

Co-advisor:
Priv.-Doz. Dipl.-Ing. Dr.techn. Anton Tamtögl
Institute of Experimental Physics

Graz, July 2021

AFFIDAVIT

I declare that I have authored this thesis independently, that I have not used other than the declared sources/resources, and that I have explicitly indicated all material which has been quoted either literally or by content from the sources used. The text document uploaded to TUGRAZonline is identical to the present doctoral thesis.

Date

Signature

Contents

Abstract VII

Kurzfassung IX

Research output XI

List of figures XV

List of tables XVII

Abbreviations XIX

1 Introduction 1

2 Theoretical background 5
2.1 Helium atom scattering . . . 5
2.2 Elastic scattering: Surface structure and electronic corrugation . . . 6
2.3 Scattering calculations and atom-surface interaction potential . . . 7
2.4 Inelastic scattering: Surface phonon dispersion . . . 10
2.5 Debye-Waller factor and electron phonon coupling . . . 11
2.5.1 Debye-Waller attenuation . . . 12
2.5.2 Electron phonon coupling . . . 13
2.6 Semimetals and topological insulators . . . 14
2.7 Vicinal surfaces . . . 16
2.8 Two-dimensional materials . . . 16

3 Experimental setup 19

4 Results 23
4.1 Outline . . . 23
4.2 Helium-Surface Interaction and Electronic Corrugation of Bi_2Se_3(111) . . . 23
4.3 Atom-Surface van der Waals Potentials of Topological Insulators and Semimetals from Scattering Measurements . . . 45
4.4 Terahertz Surface Modes & Electron-Phonon Coupling on Bi_2Se_3(111) . . . 69
4.5 Inelastic Helium Atom Scattering from Sb_2Te_3(111): Phonon Dispersion, Focusing Effects and Surfing . . . 89
4.6 Strong-Coupling Charge Density Wave in a One-Dimensional Topological Metal . . . 101

4.7 Origin of the Electron-Phonon Interaction of Topological Semimetal Surfaces Measured with HAS 115
4.8 In Situ Analysis of Intermediate Structures in 2D Materials Growth: h-BN on Ru(0001) . 125

5 Summary and conclusion **145**

Bibliography **147**

Danksagung **173**

Abstract

The study of surface structure and dynamics using helium atom scattering has enabled fundamental insights into various fields of science. The main focus of previous works was the investigation of insulator and metal surfaces. Within this thesis, new results for the material classes of topological insulators, semimetals and two-dimensional materials are presented. The strictly surface sensitive, non-destructive method of helium atom scattering allows for the investigation of surface specific phenomena. Various experimental results demonstrate the relevance of this scattering technique to obtain fundamental insights about the structure and dynamics of these materials.

Elastic scattering experiments on the topological insulators Bi_2Se_3 and Sb_2Te_3 are analysed with respect to the diffraction peak intensities to obtain the surface electronic corrugation. Selective adsorption resonance features in the angular scattering distributions give insight into the interaction between the helium atom and the surface and are further used to determine the interaction potential. Quantum mechanical scattering calculations are then employed based on a close-coupling algorithm to obtain the diffraction intensities and refine the potential parameters.

In the case of the vicinal surface Bi(114) helium scattering is able to show the transition to a dimerization-like reconstruction at low temperatures. Such a phase transition is closely related to charge density waves - periodic modulations of the electron density which are an ubiquitous phenomenon in crystalline metals.

Energy dispersive time-of-flight measurements are employed to determine the phonon energies of the first few atomic layers of the investigated topological insulators. Inelastic helium atom scattering is particularly suitable for the determination of acoustic surface phonons with an energy below 15 meV. From a multitude of experimental data the complete surface phonon dispersion is constructed and compared with theoretical *ab initio* calculations. The comparison shows good agreement, with the exception of several vibrational states below the Rayleigh mode which are attributed to collective charge density oscillations. The existence of such charge density waves at the surface of the investigated topological insulators and semimetals has previously not been reported experimentally.

In addition, the Debye-Waller attenuation of the specular reflection is used to determine the surface Debye temperature of the investigated materials. From this data a new approach for the determination of the electron-phonon coupling constant λ for two-dimensional conducting materials is employed. λ is an important parameter describing energy dissipation in electronic transport and the suitability in future electronic applications.

Finally helium scattering is used for *in situ* monitoring the growth of adlayers on a metal substrate. In the case of hexagonal boron nitride on top of Ru(0001) the employed technique reveals a precursor phase which allows to shed light on a largely unexplored area with respect to the growth of two-dimensional materials.

Kurzfassung

Die Untersuchung der Oberflächenstruktur und Dynamik mit Helium-Atom-Streuung gibt Einblicke in so unterschiedliche Bereiche wie Oberflächenphysik oder Materialwissenschaften. Der Hauptfokus früherer Arbeiten lag auf der Studie von Metall- und Isolatoroberflächen. Innerhalb dieser Dissertation werden neue Resultate zur Materialklasse der topologischen Isolatoren, zu Halbmetallen und zu zweidimensionalen Materialien präsentiert. Heliumstreuung ist komplett oberflächensensitiv und nicht oberflächenverändernd, was eine Untersuchung von empfindlichen Oberflächenphänomenen ermöglicht. Verschiedene experimentelle Ergebnisse zeigen, dass die Methode einen wichtigen Beitrag zum Verständnis der strukturellen und dynamischen Eigenschaften dieser Materialien leistet.

Elastische Streuexperimente von Bi_2Se_3 und Sb_2Te_3 werden bezüglich der Streuintensitäten analysiert, um Informationen über die elektronische Oberflächen-Korrugation zu erhalten. Aufgrund der attraktiven Wechselwirkung kann das Heliumatom für kurze Zeit an der Oberfläche gebunden werden. Winkelaufgelöste Helium-Streuspektren zeigen kleine Intensitätsvariationen im Hintergrundsignal zwischen den elastischen Streupositionen. Diese sogenannten selektiven Adsorptionssignale geben Einblick in die Interaktion zwischen dem Heliumatom und der Oberfläche. Diese Information wird genützt, um ein Interaktionspotential zu bestimmen, welches dann im Rahmen von theoretischen Berechnungen Anwendung findet. Mit Hilfe von quantenmechanischen Streusimulationen basierend auf der Close-Coupling Methode werden die Streuintensitäten berechnet und die Potentialparameter weiter optimiert.

Helium-Streumessungen der gestuften Oberfläche Bi(114) zeigen den Übergang zu einer dimer-ähnlichen Rekonsturktion bei niedriger Temperatur. Diese Phasenübergänge stehen in enger Beziehung zu periodischen Modulationen der Elektronendichte, die eine universelle Eigenschaft von kristallienen Metallen darstellen.

Energieaufgelöste Flugzeitmessungen werden angewendet, um Phononenenergien der obersten atomaren Schichten der topologischen Isolatoren zu bestimmen. Inelastische Streumessungen eignen sich besonders, um akustische Phononen mit einer Energie unter 15 meV zu detektieren. Aus den gesamten experimentellen Daten wird die Oberflächenphononen-Dispersion konstruiert und mit *ab initio* Simulationen verglichen, welche eine gute Übereinstimmung zeigen. Unter dem Rayleigh-Mode werden jedoch auch Schwingungszustände festgestellt, die als kollektive Schwingungen von Ladungsverteilungen erklärt werden können. Diese Ladungsverteilungen auf den Oberflächen von topologischen Isolatoren und Halbmetallen wurden noch nie zuvor experiementell nachgewiesen.

Messungen der spekulären Streuintensität in Abhängigkeit der Probentemperatur untersuchen die Schwingungsdynamiken und erlauben es, die Oberflächen-Debye-Temperatur der untersuchten Materialien zu ermitteln. Im Rahmen dieser Auswertung wird eine neue Methode für die Ermittlung der Elektron-Phonon-Kopplungskonstante λ für zweidimensionale leitende Materialien angewendet. λ ist ein wichtiger Parameter für die Beschreibung von Energieverlust in Elektronentransport und gibt einen

Ausblick auf zukünftige elektronische Anwendungen von topologischen Isolatoren.

Schließlich ermöglicht Helium-Streuung, das Wachstum von dünnen Schichten auf metallischen Oberflächen zu verfolgen. Für hexagonales Bohrnitrid auf Ru(0001) wird in diesem Zusammenhang gezeigt, dass dem Wachstum eine zusätzliche Struktur vorangeht. Diese Erkenntnisse eröffnen neue Einblicke in die kontrollierte Synthese von zweidimensionalen Materialien.

Research output

The following publications are subject to the current PhD thesis. Full texts are found in chapter 4, including detailed descriptions of the respective author contributions and supplementary informations. All helium atom scattering experiments were performed and analysed by the author of this thesis.

Peer-reviewed publications:

1. A. Ruckhofer, A. Tamtögl, M. Pusterhofer, M. Bremholm, and W. E. Ernst
   Helium-Surface Interaction and Electronic Corrugation of $Bi_2Se_3(111)$
   The Journal of Physical Chemistry C **123**, 17829–17841, 2019

2. A. Tamtögl, A. Ruckhofer, D. Campi, W. Allison, and W. E. Ernst
   Atom-Surface van der Waals Potentials of Topological Insulators and Semimetals from Scattering Measurements
   Physical Chemistry Chemical Physics **23**, 7637-7652, 2021

3. A. Ruckhofer, D. Campi, M. Bremholm, P. Hofmann, G. Benedek, M. Bernasconi, W. E. Ernst, and A. Tamtögl
   Terahertz Surface Modes & Electron-Phonon Coupling on $Bi_2Se_3(111)$
   Physical Review Research **2**, 023186, 2020

4. P. Hofmann, M. M. Ugeda, A. Tamtögl, A. Ruckhofer, W. E. Ernst, G. Benedek, A. J. Martínez-Galera, A. Stróżecka, J. M. Gómez-Rodríguez, E. Rienks, M. F. Jensen, J. I. Pascual, and J. W. Wells
   Strong-Coupling Charge Density Wave in a One-Dimensional Topological Metal
   The Journal of Physical Review B **99**, 035438, 2019

5. G. Benedek, S. Miret-Artés, J. R. Manson, A. Ruckhofer, W. E. Ernst, and A. Tamtögl
   Origin of the Electron-Phonon Interaction of Topological Semimetal Surfaces Measured with Helium Atom Scattering
   The Journal of Physical Chemistry Letters **11**, 1927–1933, 2020

6. A. Ruckhofer, S. Halbritter, H.E. Lund, A.J. Holt, M. Bianchi, M. Bremholm, G. Benedek, P. Hofmann, W. E. Ernst, and A. Tamtögl
   Inelastic Helium Atom Scattering from $Sb_2Te_3(111)$: Phonon Dispersion, Focusing Effects and Surfing
   Physical Chemistry Chemical Physics **23**, 7806-7813, 2021

In preparation:

1. A. Ruckhofer*, M. Sacchi, A. Payne, A.P. Jardine, W. E. Ernst, N. Avidor and A. Tamtögl
   In Situ Analysis of Intermediate Structures in 2D Materials Growth: h-BN on Ru(0001).
   submitted to *Small*

The following publications are not subject to this thesis, but contain contributions by the author that were achieved during the time of his PhD.

Peer-reviewed publications:

1. G. Benedek, J. R. Manson, S. Miret-Artés, A. Ruckhofer, W. E. Ernst, A. Tamtögl and J. P. Toennies
   Measuring the Electron–Phonon Interaction in Two-Dimensional Superconductors with He-Atom Scattering
   Condensed Matter **5**, 79, 2020

List of figures

2.1 Schematic of a simple helium scattering setup and basic representation of the various scattering processes on the surface . . . 6
2.2 Illustration of the diffraction geometry using the typical scattering vectors and of the characteristic interference pattern upon elastic scattering . . . 7
2.3 He-surface interaction potentials: The laterally averaged Morse potential and corrugated Morse potential are shown in dependence of z . . . 8
2.4 Basic representation of the inelastic scattering process and illustration of the detection of subsurface phonon states . . . 11
2.5 Schematic of the Debye-Waller attenuation on the surface . . . 11
2.6 Basic crystal structure and surface electronic band structure of topological insulators . . . 15
2.7 Schematic top and side-view of h-BN on a Ru(0001) substrate . . . 17

3.1 Basic representation of the apparatus used for all measurements . . . 20

4.1 Scattered He intensities for $Bi_2Se_3(111)$ versus parallel momentum transfer . . . 28
4.2 Contour plot of the scattered He intensities versus parallel momentum transfer . . . 29
4.3 Comparison of measured intensities with CC-calculations . . . 31
4.4 Normalised intensity of the specular peak in dependence of the incident wavevector k_i . . . 34
4.5 Reliability factors of varying potential well depth D and stiffness κ . . . 35
4.6 Drift scan calculations for various values of D . . . 40
4.7 Drift scan calculations for various values of κ . . . 41
4.8 Drift scan calculations for various values of ξ_{pp} . . . 42
4.9 Determination of the step heights from the oscillations present in the drift scan . . . 43
4.10 Illustration of the helium-surface scattering process . . . 47
4.11 Calculated He-surface interaction potential above a Bi(111) surface . . . 48
4.12 Side view of the Bi(111), Sb(111) and binary topological insulator structures . . . 51
4.13 Schematic illustration of a selective adsorption resonance process in the free-atom approximation . . . 53
4.14 Illustration of the resonance condition in the free atom approximation and specular intensity for scattering of He from Bi(111) at 150 K . . . 54
4.15 Contour plot of the scattered He intensity in dependence of momentum transfer and incident energy along the $\overline{\Gamma K}$ azimuth . . . 55
4.16 Scattered intensity versus parallel momentum transfer along the $\overline{\Gamma M}$ azimuth of $Sb_2Te_3(111)$ 56
4.17 Normalised scattered intensity of the diffraction peaks versus incident wavevector k_i with CC-calculations . . . 58

4.18 Comparison of the laterally averaged potentials $V_{\mathbf{0}}(z)$ for the binary TIs 60
4.19 Contour plot of the scattered He intensities in dependence of the momentum transfer and incident energy along the $\overline{\Gamma\mathrm{M}}$ azimuth 65
4.20 Single slices of temperature dependent measurements as obtained in a FT-HAS scan . . . 66
4.21 Surface phonon dispersion of $Sb_2Te_3(111)$ according to theory and Bose factors plotted versus reduced inverse temperature 67
4.22 Crystal structure and electronic dispersion of Bi_2Se_3 71
4.23 HAS diffraction scans and Debye-Waller attenuation for $Bi_2Se_3(111)$ 73
4.24 TOF measurements along $\overline{\Gamma\mathrm{M}}$ with their respective scancurves 76
4.25 Comparison of the measured phonon dispersion relation with DFPT calculations 77
4.26 Polarisation of the calculated phonon dispersion of Bi_2Se_3 from DFPT 78
4.27 Inelastic bound-state resonance conditions along the $\overline{\Gamma\mathrm{M}}$ direction 79
4.28 Inelastic bound-state resonance conditions with and without SOC 82
4.29 Surface phonon dispersion at a Q-vector corresponding to $2\mathrm{k}_F$ 83
4.30 Shear horizontal polarisation of the calculated phonon dispersion 84
4.31 HAS diffraction scans for $Bi_2Se_3(111)$ 85
4.32 Comparison of different TOF spectra in the $\overline{\Gamma\mathrm{M}}$ direction 86
4.33 TOF spectrum with corresponding scan curve 87
4.34 LEED-pattern, Auger spectrum, crystal structure and helium scattering distribution along the $\overline{\Gamma\mathrm{M}}$ azimuth for Sb_2Te_3 91
4.35 Photoemission intensity at the Fermi level and along $\overline{\mathrm{K}\Gamma\mathrm{M}}$ 93
4.36 Experimental surface phonon dispersion of $Sb_2Te_3(111)$ from helium atom scattering in comparison with DFPT calculations 94
4.37 TOF-spectrum with corresponding resonance conditions for the $(0\bar{1})$ **G**-vector and scancurve 96
4.38 Diagrams illustrating various HAS focusing effects as a function of parallel momentum (wavevector) Q 97
4.39 Compilation of several TOF spectra measured along the $\overline{\Gamma\mathrm{M}}$ azimuth at various incident energies E_i and angles ϑ_i 99
4.40 Electronic states in one dimension at half-filling and of Bi(114) 103
4.41 STM images of Bi(114) showing the dimer formation 104
4.42 LEED patterns collected above and below the temperature of the phase transition 105
4.43 Scattered He intensities versus parallel momentum transfer along $\overline{\Gamma} - \overline{\mathrm{X}}$ 106
4.44 Photoemission intensity in the low-temperature phase, close to and below the CDW transition 108
4.45 Comparison of several TOF spectra for the cooled sample and at room temperature . . . 109
4.46 LEED data sets for several temperatures with the LEED intensity integrated along k_y . . 111
4.47 Additional photoemission spectra in the low-temperature phase 112
4.48 Time-of-flight scans at the position of the CDW superlattice peak with corresponding peak areas 113
4.50 HAS angular distributions for several different temperatures showing the appearance of the CDW feature 120
4.51 ARPES data and DW exponent slopes of three Bi chalcogenides 121
4.52 Schematic illustrating the epitaxial growth of h-BN by chemical vapour deposition 126
4.53 Angular diffraction scans for Ru(0001) and h-BN as well as additional superstructures . . 128
4.54 *In situ* monitoring of the integrated peak intensities of the $\mathrm{BN_I}$ structure and h-BN . . . 129
4.55 DFT calculations of the most favourable configurations on the Ru(0001) surface 131

4.56 Peak areas of the characteristic diffraction peaks representing the different structures versus borazine exposure . . . 133
4.57 Schematic growth diagram of the different BN structures observed on a Ru surface 134
4.58 Diffraction scans of the h-BN peak position . . . 135
4.59 DFT results (top and sideview) for various configurations . . . 138
4.60 Schematic of the possible route from the partially dehydrogenated precursor structure to h-BN . . . 139
4.61 Comparison of the diffraction scans of the clean Ru(0001) surface, graphene on Ru and h-BN on Ru . . . 140
4.62 2-dimensional scan of the (3×4) structure . . . 141
4.63 Thermal expansion for the Ru surface and bulk h-BN as well as monolayer h-BN 143

List of tables

4.1 Bound state values for the He–Bi_2Se_3(111) interaction potential 30
4.2 Comparison of the potential parameters for the binary topological insulators as well as the single-elemental semimetals 59
4.3 Bound state values of the He–Sb_2Te_3(111) interaction potential with the corresponding internal linewidths $\Delta\epsilon_n$, lifetimes τ_n and travel distances L_n 61
4.4 Internal linewidths $\Delta\epsilon_n$, corresponding lifetimes τ_n and travel distances L_n of the He-Sb_2Te_3(111) at room temperature 63
4.5 Slopes of the RW along the $\overline{\Gamma M}$ and $\overline{\Gamma K}$ direction based on a linear fit and the corresponding group velocities v_{RW} of the RW 95
4.6 Input data for the calculation from the HAS DW exponent, and results for the e-ph coupling constant $\lambda_{HAS}^{(2D)}$ 122
4.7 DFT results for the adsorption structures of borazine on Ru(0001) with a 60° rotation . . 130
4.8 DFT results for the adsorption structures of borazine on Ru(0001) with a 0° rotation . . . 139
4.9 DFT results for different configurations/structures with their respective energies 140

Abbreviations

2D	two-dimensional
2DEG	two-dimensional electron gas
AES	Auger electron spectroscopy
ARPES	angle resolved photoemission spectroscopy
CC	close-coupling
CDW	charge density wave
CMP	corrugated Morse potential
CVD	chemical vapor deposition
DFT	density functional theory
DFPT	density functional perturbation theory
DOS	density of states
DW	Debye-Waller
e-ph	electron-phonon
FWHM	full width at half maximum
HAS	helium atom scattering
h-BN	hexagonal boron nitride
KA	Kohn-anomaly
KF	kinematical focusing
LEED	low energy electron diffraction
QL	quintuple layer
RW	Rayleigh wave
SAR	selective adsorption resonance
SOC	spin-orbit coupling
STM	scanning tunneling micorscopy
TI	topological insulator
TOF	time-of-flight
UHV	ultra-high vacuum
vdW	van der Waals

Chapter 1

Introduction

The field of surface science is defined as the investigation of physical interactions and reactions at interfaces between various phases. Surface science is divided into numerous research areas which include material growth, friction, nanostructures, surface-tension, self-assembly, adsorption, catalysis and many others. Important questions include: How does the atomic structure of the surface look like compared to the bulk? How do the electronic and vibrational properties change when a surface is created? How are the surface properties altered when an atom or molecule is adsorbed on the surface?

First motivations in studying surfaces go back to the understanding of heterogeneous catalysis. In the early 19^{th} century the phenomenon that solids could accelerate chemical reactions without modifying the solid itself was discovered. More than a century later, a strong interest in semiconductor technology and microelectronics emerged, which introduced more and more challenging research questions. The field is nowadays much wider known under the terminus "nanotechnology". With the need to build ever smaller structures, interactions at interfaces and their properties became more important, since with smaller structures the relative importance of the surface itself increases. Therefore, the quality of experimental analysis of surface specific measurements is facing more and more challenges with respect to resolution.

Another important task is the manufacturing of these nano-structures with high precision and to have flat interfaces within them. Related to the increased importance of surfaces is that the electronic properties are governed by quantum-confinement effects in which the surface defines the boundary conditions. In some cases of a nano-object, it might even happen that surface-localised electronic states dominate the electronic properties of the whole system. Moreover, surfaces provide an opportunity to study two-dimensional electronic structures such as a 2D-electron gas. The new emerging material class of topological insulators exhibits peculiar effects at the surface, which are investigated in this work. In addition to the electronic properties, another important surface characteristic are the vibrational states. Due to the change in coordination number at the surface, the phonon energies change significantly at the interface between the solid and the gas phase.

All of the mentioned properties are nowadays studied with a wide range of powerful surface science techniques such as scanning-tunnelling microscopy, angle-resolved photoemission spectroscopy, atomic-force microscopy as well as scattering techniques. Among those, helium atom scattering is particularly applied in this thesis. Helium atom scattering is often seen as a niche method but still acts as a reference tool for the investigation of surface specific properties. Other scattering particles, such as neutrons generally have a lower probability to interact with matter, which results in large penetration depths.

This makes it exceedingly hard to obtain surface specific properties, which on the other hand is possible when using helium atoms. In addition, helium atom scattering is the only experimental method which allows to resolve phonon modes in the low meV region.

The contents presented in this work provide insight in the interaction of helium atoms with topological insulator and semimetal surfaces as well as with a two-dimensional material. The features recorded in helium scattering experiments originate from the interaction of the inert particles with the electron density above the surface. The inelastic scattering process allows for the determination of vibrational surface modes and kinematic effects. In addition, the helium-surface interaction potentials of these materials are determined together with the electronic corrugation at the surface. The peculiar effect of charge density waves is studied at the surface of the semimetal Bi(114). Moreover, results about energy losses via electron-phonon coupling for various surfaces are presented in experiment and theoretical analysis. This characteristic property is particularly important for possible future applications in spintronic devices.

Why perform helium atom experiments?

Compared to many other well established techniques, helium atom scattering is a surface sensitive and at the same time non-destructive method. Due to its relatively difficult experimental setup and complex analysis in reciprocal space only a few experimental setups exist.

The study of surfaces using helium atom scattering has so far been widely applied to various surfaces including insulators (LiF(001) [1, 2]), metals (Bi(111) [3–5], Sb(111) [6, 7], Cu(111) [8, 9], ...), thin films [10, 11], transition metal dichalcogenides (TaS_2 [12, 13], $TaSe_2$ [14, 15]) and many more. The manifold of results yielded a multitude of new insights in surface science as well as some complementary results to other techniques [16].

If ^{3}He-atoms are used as the scattering particles, the helium-3 spin-echo technique provides a generic ultra high energy resolution scattering tool for studying dynamics at surfaces [17–19]. This unique method can be applied to several classes of surface dynamic measurements and is particularly appropriate for measuring adsorbate dynamics at surfaces, as it provides surface correlation measurements in the picosecond to nanosecond time range on nanoscale distances. Recent results showed the significant coupling between the diffusion and the orientation of organic molecules [20] as well as the effect of inter-adsorbate forces [21]. Since the helium-3 spin-echo technique is not part of this work please refer to mentioned publications [22, 23].

The focus of this thesis is the class of topological insulators (Bi_2Se_3(111) [24, 25] and Sb_2Te_3(111) [26, 27]) and a vicinal semimetal (Bi(114) [28]) as well as the two-dimensional material hexagonal boron nitride. In the following chapter, the various applications of helium atom scattering are discussed in detail and compared to other surface science techniques.

Helium atom scattering can act as a missing link between bulk studies and other surface investigation methods, as it provides several advantages, which are shortly summarized in the following:

1. In comparison to other measurement techniques which penetrate the investigated material, helium atom scattering is strictly surface sensitive. This allows to readily verify important structural properties such as the surface lattice constant and give insights on the surface electronic corrugation already during first initial measurements.

2. More specific experimental results determine the surface Debye-temperature and the electron-phonon coupling constant λ, which acts as a reference for future applications of the investigated materials. The profound knowledge of these properties has great relevance both from a fundamental point of view as well as for various applications such as two-dimensional superconductivity in nanotechnology.

3. The interaction between the impinging helium atoms in the low energy region of a few meV serves as a benchmark for state-of-the-art van der Waals corrected density functional theory approaches. The extremely small adsorption energies of He atoms on surfaces can be used to test the suitability of studies like the Post-Hartree-Fock method.

4. The high sensitivity to periodic charge modulations above the surface allows for the investigation of charge density waves, which had not been reported for certain materials beforehand. In the particular case of Bi_2Se_3 the method revealed periodic charge density distributions on the surface with oscillating behaviour in the Terahertz regime [25].

5. In the case of Bi(114), the surface scattering approach permits to precisely monitor phase transitions in low dimensional materials and complement findings from scanning tunnelling microscopy and angle-resolved photoemission spectroscopy [28].

6. The low incident energy of the impinging helium atom allows for an investigation of the surface vibrational states in particular in the low energy region. From energy dispersive measurements the surface phonon dispersion along the high symmetry directions can be constructed and can thereby be directly compared to theoretical *ab initio* calculations [27].

7. Helium scattering can give insight in the growth of nanostructures on top of metal substrates. As a reciprocal space technique it provides real-time evidence of the long-range order of the investigated system. Helium scattering is particularly sensitive to adsorbates and allows to follow structural changes directly and *in situ*. In addition, due to the inert nature of the scattered atoms, the scattering is not affected by issues like beam-damage as observed in X-ray and electron spectroscopy and has therefore no impact on the growth mechanism itself.

Chapter 2

Theoretical background

In the following chapter, the scientific background of the thesis is presented. At first, a basic introduction into helium atom scattering is given, followed by a summary of the most important measurements and their analysis. Finally, semimetal and topological insulator surfaces, which are investigated in this thesis, are introduced.

2.1 Helium atom scattering

In this thesis all experimental measurements were performed on periodic crystal surfaces using helium atom scattering (HAS). Various experiments were carried out on the HAS apparatus at the Institute of Experimental Physics in Graz, which is described in Chapter 3.

In Fig. 2.1a a basic representation of a HAS setup is shown, which includes the beam generation through a microscopic nozzle, the sample surface and the helium detector. For inelastic measurements a chopper disc is placed in the continuous beam to perform energy-resolved measurements. The basic scattering geometry is given by the incident and final angle ϑ_i and ϑ_f, respectively.
HAS is a strictly surface sensitive probing method, due to the inert nature of the ^{4}He-atom. The impinging atoms with an energy of 8–25 meV are scattered directly from the electron density above the surface (Fig. 2.1b). If the helium atom is scattered off a periodic surface various processes such as elastic/inelastic scattering and selective adsorption/trapping can occur. Due to the low kinetic energies involved in the scattering process, HAS is a completely non-destructive probing technique. Therefore, HAS is a very gentle method when investigating TIs which are susceptible to changes in the electronic bands when illuminated with intensive ultraviolet light [30].

In Fig. 2.1b an atom of mass m arrives at the surface with a characteristic incident wavevector $\mathbf{k}_i$. The kinetic energy of the particle is then given by $E_i = \frac{\hbar^2}{2m}\mathbf{k}_i^2$. In the low energy range, the helium atoms are scattered by the electron gas, several Angströms away from the surface. The interaction is described by the potential $V(\mathbf{r})$ with the position $\mathbf{r}$ usually given in dependence of the coordinates in the surface plane $\mathbf{R}$ and the distance z normal to the surface, $\mathbf{r} = (\mathbf{R}, z)$.

In an elastic event no energy is exchanged with the surface, whereas during inelastic scattering the energy and hence the wavelength of the particle is altered. If certain scattering parameters are met the helium atom can undergo a transition into a bound state of the surface potential. The atom-surface interaction potential (Fig. 2.3b) [31, 32] exhibits a corrugated short-range repulsive wall in addition to

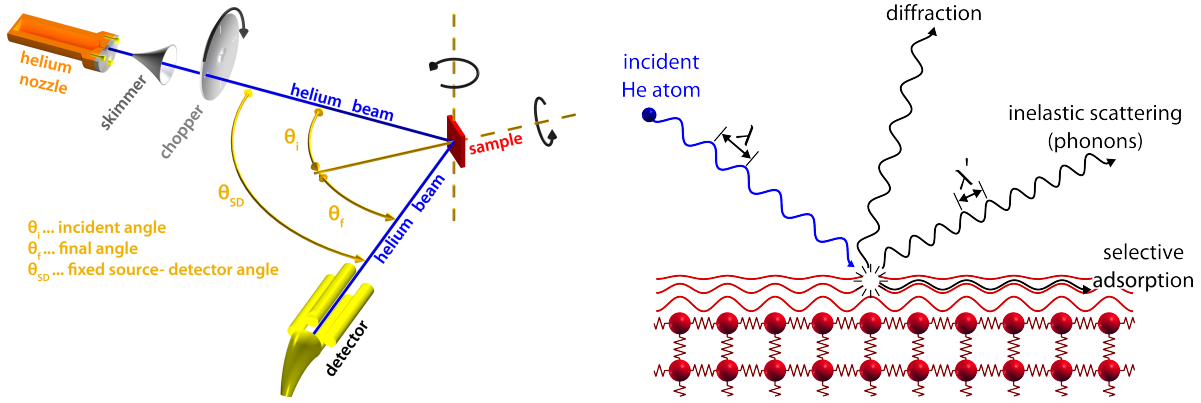

(a) Basic representation of the scattering geometry. After the helium beam is generated through an expansion through a nozzle it is scattered off the sample surface in a fixed source-detector angle. The diffracted beam is detected in a quadrupole mass-spectrometer. Energy dependent measurements are performed by adding a chopper into the beam to measure the time-of-flight.

(b) Different scattering processes for a monochromatic He beam on a periodic surface. Elastic scattering, where no energy is exchanged between the He atom and the surface, gives rise to a diffraction pattern. During inelastic scattering the wavelength changes, while a phonon is created or annihilated. Lastly the He atom can be temporarily trapped on the surface in a selective adsorption process.

Figure 2.1: Schematic of a simple helium scattering setup (a) and basic representation of the various scattering processes on the surface (b) [29].

a less corrugated attractive well. The position of selective adsorption resonances in the experiment give insight about the bound state energy values and the potential shape.

Many details about the fundamentals and applications of HAS are described in a recent book by Benedek and Toennies [16].

2.2 Elastic scattering: Surface structure and electronic corrugation

When a monochromatic atom beam is elastically scattered off a periodic surface a characteristic diffraction pattern is created, which is comparable to other scattering methods such as X-ray and electron diffraction. Due to the wave particle duality and the de-Broglie relation a wavelength can be attributed to the helium atoms, which is in the range of a few Å. Hence, if a helium beam is scattered off a periodic surface of similar length scale a diffraction pattern is formed, consisting of a specular reflection and several diffraction peaks (Fig. 2.2b).

A typical HAS setup with the characteristic scattering vectors is given in Fig. 2.2a. The incident wavevector $\mathbf{k}_i$ is defined by the polar incident angle ϑ_i and the respective component parallel to the surface is $\mathbf{K}_i$. For a setup with a fixed source-detector angle ($\vartheta_i + \vartheta_f = \vartheta_{SD}$) as shown in Fig. 2.1a, the parallel momentum transfer is given as

$$|\Delta\mathbf{K}| = |\mathbf{K}_f - \mathbf{K}_i| = |\mathbf{k}_i| \left[\sin(\vartheta_{SD} - \vartheta_i) - \sin\vartheta_i\right]. \tag{2.1}$$

According to Bragg's law the parallel momentum transfer $\mathbf{K}$ has to be equal to a surface reciprocal lattice vector $\mathbf{G}$ to get constructive interference and therefore yield a diffraction peak. Typically the diffraction pattern along a high symmetry direction of a crystal surface, as seen in Fig. 2.2b, is plotted versus ϑ_i. The distance between the individual diffraction peaks then provides information about the lattice constant a of the surface.

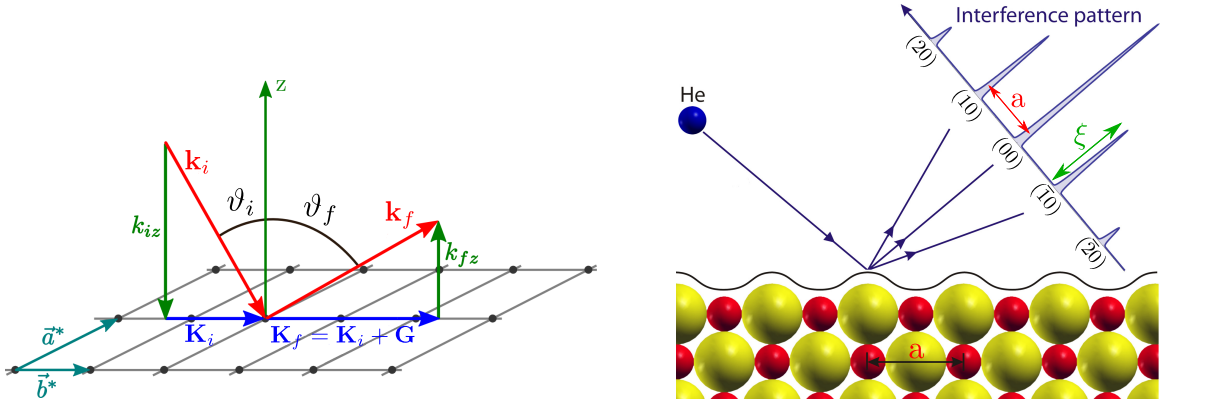

(a) Schematic of the characteristic scattering wavevectors $\mathbf{k}_i$ and $\mathbf{k}_f$, where the subscripts i, f denote the incident and final states. The incident angle ϑ_i is defined with respect to the surface normal z. The vector components parallel to the surface are given in capital letters ($\mathbf{K}_i$, $\mathbf{K}_f$) and during a scattering process a reciprocal lattice vector $\mathbf{G}$ can be added to the final momentum.

(b) Diffraction of a monochromatic helium beam gives rise to a periodic interference pattern for various $\mathbf{G}$-vectors in dependence of the incident angle ϑ_i. In addition to the specular reflection first and second order diffraction peaks are observed. The lattice constant a is defined by the distance between the peaks, whereas the peak height gives information about the corrugation ξ.

Figure 2.2: Illustration of the diffraction geometry using the typical scattering vectors (a) and of the characteristic interference pattern upon elastic scattering (b), adapted from [29].

In addition the individual peak heights in a diffraction scan give insight in the electronic corrugation ξ of the investigated surface. The corrugation describes the shape of the charge distribution on the surface, which greatly influences the scattering of the inert helium atoms. The surface charge density $\xi(\mathbf{R})$ can be expressed as a function of the lateral position $\mathbf{R}$ in the surface plane and is modulated periodically.

The experimental diffraction peak heights can be calculated theoretically by using a first estimate of the corrugation height ξ. A systemic comparison between the calculated and experimental values then allows for the determination of an optimised value of ξ. For this approach we used quantum-mechanical scattering calculations based on the close-coupling algorithm as described in the next Section 2.3.

2.3 Scattering calculations and atom-surface interaction potential

As described in the previous sections helium atoms are scattered from the electronic corrugation of the surface. Many earlier works tried to theoretically study the interaction and simulate the diffraction intensities [6, 31, 33]. For an accurate description of the He-surface interaction the time-dependent Schrödinger equation needs to be solved using a suitable interaction potential. Due to the scaling with increasing number of involved atoms (many-body interaction) it is difficult to consider a realistic potential. An approximation would be the hard-wall potential which is applicable if the distance of the classical turning point in the potential with respect to $z = 0$ is comparable to the He diameter. In addition, the computational costs of solving the scattering process can be simplified using the Eikonal approximation [34].

In this work we will only consider the elastic close-coupling (CC) method which is more exact than the hard-wall approximation and still computationally manageable. We follow here the derivation by Miret-Artés from Ref. [35]. In this approach the time-independent Schrödinger equation is considered

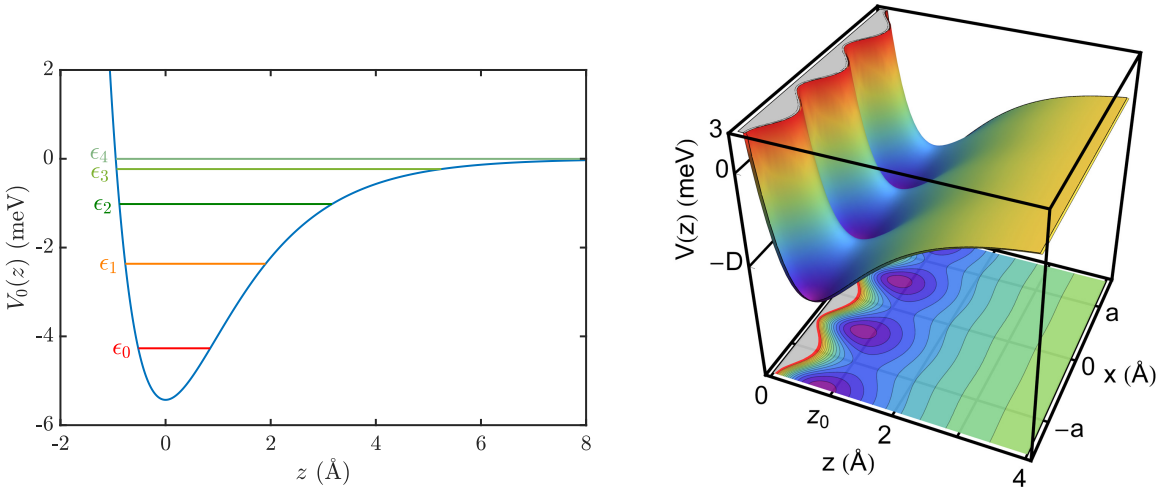

(a) Laterally averaged Morse potential for He-Sb_2Te_3(111) with the five bound states ϵ_{0-4} (coloured horizontal lines). The bound state spacing become narrower near the threshold ($\epsilon = 0$).

(b) Illustration of the corrugated Morse potential $V(z)$ along the surface in dependence of the distance from the surface z. D denotes the well depth of the laterally averaged potential.

Figure 2.3: He-surface interaction potentials: The laterally averaged Morse potential (a) and corrugated Morse potential (b) are shown in dependence of z [29].

for a potential $V(\mathbf{r})$ as

$$\left[-\frac{\hbar^2}{2m}\nabla^2 + V(\mathbf{r}) - \frac{\hbar^2\mathbf{k}_i^2}{2m}\right]\Psi(\mathbf{r}) \;=\; 0, \tag{2.2}$$

with m being the mass of the scattered atom and $\mathbf{k}_i$ the incident wavevector. Considering the periodicity of the surface lattice, both the surface potential $V(\mathbf{r})$ and the wave function $\Psi(\mathbf{r})$ can be written as a Fourier series:

$$\begin{aligned} V(\mathbf{r}) &= \sum_{\mathbf{G}} V_{\mathbf{G}}(z)\, \exp(\mathbb{i}\mathbf{G}\cdot\mathbf{R}) \\ \Psi(\mathbf{r}) &= \sum_{\mathbf{G}} \Psi_{\mathbf{G}}(z)\, \exp(\mathbb{i}(\mathbf{G}+\mathbf{K})_i\cdot\mathbf{R})\,. \end{aligned} \tag{2.3}$$

$\mathbf{G}$ depicts the reciprocal lattice vector and $\mathbf{K}_i$ is the projection of the incoming wavevector onto the surface plane (see Fig. 2.2a).

Substituting both Fourier expansions into Eq. (2.2) yields the CC equations:

$$\left[\frac{\mathrm{d}^2}{\mathrm{d}z^2} + \mathbf{k}_{\mathbf{G},z}^2 - V_0(z)\right]\Psi_{\mathbf{G}}(z) = \sum_{\mathbf{G}'\neq\mathbf{G}} V_{\mathbf{G}-\mathbf{G}'}(z)\Psi_{\mathbf{G}'}(z) \tag{2.4}$$

for the z-direction, where $\mathbf{k}_{\mathbf{G},z}^2$ is the z-component of the particles kinetic energy after the interaction with a lattice vector $\mathbf{G}$ and V_0 the laterally averaged interaction potential. $V_{\mathbf{G}}$ denotes the Fourier component of the interaction potential with respect to $\mathbf{G}$.

If $\mathbf{k}_{\mathbf{G},z}^2 > 0$ the involved scattering channel is defined as "open", which describes a process where the He atom is directly scattered off the surface. However, if $\mathbf{k}_{\mathbf{G},z}^2 < 0$ the atom gets trapped on the surface for a short time period in a so-called "closed" channel. In this process of selective adsorption resonance (SAR), the atom is trapped in a bound state of the interaction potential, before leaving the surface again. The potential $V(\mathbf{r})$ is defined by the Pauli-repulsion and through attractive dispersion forces. An analytical potential which is often used to describe these characteristics is the laterally averaged Morse potential as shown in Fig. 2.3a. Depending on the depth and stiffness, the potential accommodates a

certain number of bound state energies ϵ_n.

Various potential shapes were investigated previously, with the corrugated Morse potential (CMP) showing the best agreement with respect to the experiment [31]. For this potential shape a corrugation is introduced to the surface, i.e. the Morse potential is periodically varied in z, as depicted in Fig. 2.3b. In this work we will mainly concentrate on the CMP with the potential parameters D for the well depth and χ for the stiffness:

$$V(\mathbf{R}, z) = D\left[\frac{1}{\nu_{0,0}} e^{-2\kappa[z-\xi(\mathbf{R})]} - 2e^{-\kappa z}\right] . \tag{2.5}$$

Here $\xi(\mathbf{R})$ is again the corrugation function with $\nu_{0,0}$ being the surface average over the term $e^{-2\kappa\xi(\mathbf{R})}$.

For a hexagonal system the corrugation function $\xi(\mathbf{R})$ in the surface plane is chosen as a two-parameter Fourier ansatz:

$$\begin{aligned}\xi(\mathbf{R}) = \xi(x,y) = \xi_0 \Bigg\{ &\cos\left[\frac{2\pi}{a}\left(x - \frac{y}{\sqrt{3}}\right)\right] + \cos\left[\frac{2\pi}{a}\left(x + \frac{y}{\sqrt{3}}\right)\right] \\ &+ \cos\left[\frac{2\pi}{a}\frac{2y}{\sqrt{3}}\right]\Bigg\} + h.o.\end{aligned} \tag{2.6}$$

where x and y depict the coordinates in the surface plane and ξ_0 determines the corrugation amplitude.

SAR features in the experiment allow for the determination of the bound state values. If the incident energy and the kinetic energy of the atom moving parallel to the surface matches a binding energy ϵ_n, conservation of energy gives:

$$E_i = \frac{\hbar^2 \mathbf{k}_i^2}{2m} = \frac{\hbar^2(\mathbf{K}_i + \mathbf{G})^2}{2m} + \epsilon_n(\mathbf{K}_i, \mathbf{G}) . \tag{2.7}$$

Here the bound state energy is defined as a function of the momentum $\mathbf{K}_i$ parallel to the surface and the interacting G-vector $\mathbf{G}$. If the bound state values are therefore known from the SARs of an experiment the potential can be determined.

Inserting Eq. (2.5) into Eq. (2.4) then yields a set of coupled equations, with the coupling terms $V_{\mathbf{G}-\mathbf{G}'}$ which can be written in matrix-form. This matrix equation is then solved for using the Numerov and Fox-Goodwin algorithms [36]. From the extracted scattering matrix the individual scattering channels are extracted and further compared to experimental values. The simulations are performed for all open channels and a specified number of closed channels which significantly influences the computational time.

The comparison between scattering calculations and the experiment are performed using the peak areas of the experimental diffraction peaks. This minimizes the experimental uncertainty due to the broadening of the elastic peaks caused by the energy spread of the helium beam as well as by the apparatus and defects on the surface.

In other words, the corrugation $\xi(\mathbf{R})$ describes the fraction of the incident beam which scatters into a diffractive channel and therefore defines the respective diffraction peak intensity. The corrugation is iteratively optimized by looking at several angular scans in various high symmetry directions and over various incident energies. The goal is to minimize the deviation R:

$$R = \frac{1}{N}\sqrt{\sum_G \left(I_G^{\mathrm{exp}} - I_G^{\mathrm{sim}}\right)^2} , \tag{2.8}$$

with N being the number of compared diffraction peaks and I_G^{exp} and I_G^{sim} the experimental and calculated diffraction intensities, respectively.

In addition, it should also be mentioned that earlier works considered inelastic scattering calculations

to account for inelastic effects during a scattering event [37]. This formalism starts with the time-dependent Schrödinger equation and includes the displacement of the near-surface atoms from their respective equilibrium positions using a harmonic oscillator model. For a more accurate description of the important phonon states the surface phonon dispersion has to be know, which is explained in the following Section 2.4.

2.4 Inelastic scattering: Surface phonon dispersion

Similar to the electronic properties of a material, the vibrational states of surface atoms are altered significantly due to the change in coordination number. These special modes which are localized on the surface are called surface phonons [16]. HAS is particularly suitable for investigating the surface phonons modes due to the low incident energy in combination with relatively high momenta. The low atomic mass of the helium atoms allows for the determination of acoustic phonons in the low meV regime, while the inert nature is especially suitable for only detecting vibrational states in the first few atomic layers.

In an inelastic scattering event, one has to distinguish between the creation and annihilation of surface phonons depending on whether energy is lost or gained by the He atom, respectively. In Fig. 2.4a a schematic for both processes is shown in which the final momentum $\mathbf{k}_f$ changes in dependence of the inelastic event. The change in energy and momentum can be measured by using the time-of-flight (TOF) technique which determines the involved phonon energies. For a particular incident angle ϑ_i and parallel momentum transfer ΔK the so-called scancurve links the phonon energy E_{ph} to a certain wavevector Q in reciprocal space [38]:

$$k_i \sin\vartheta_i + Q = \sin\vartheta_f \sqrt{2m(E_i + E_{ph})/\hbar}\ , \tag{2.9}$$

with k_i being the norm of the incident wavevector and m the He atom mass.

During an inelastic HAS measurement the TOF data is converted to an energy scale, which then shows features on either side of the diffuse elastic peak $\Delta E = 0$. By convention, negative energies account for an energy loss of the helium atom and therefore for a creation process, while positive energies describe an annihilation process, respectively.
By varying the scattering conditions the entire surface phonon dispersion relation can be determined. All phonons with a parallel momentum $|\Delta K| + G$, with G being a reciprocal lattice vector in the scattering plane, need to be folded back into the first Brillouin zone (*umklapp* processes).

Since helium atoms only interact with the electronic cloud of the surface the detection of phonons is only possible through the electron-phonon (e-ph) coupling. Therefore, energy-resolved measurements of metal, semimetal or semiconductor surfaces provide information about the e-ph interaction, as shown in Fig. 2.4b. Hence, phonon modes which exhibit a stronger e-ph interaction will show up with higher intensity in HAS measurements. Earlier works showed that this behaviour opens the possibility to measure subsurface phonon modes [4, 39].

A more detailed description of the e-ph coupling of metal and semimetal surfaces is given in the following Section 2.5.

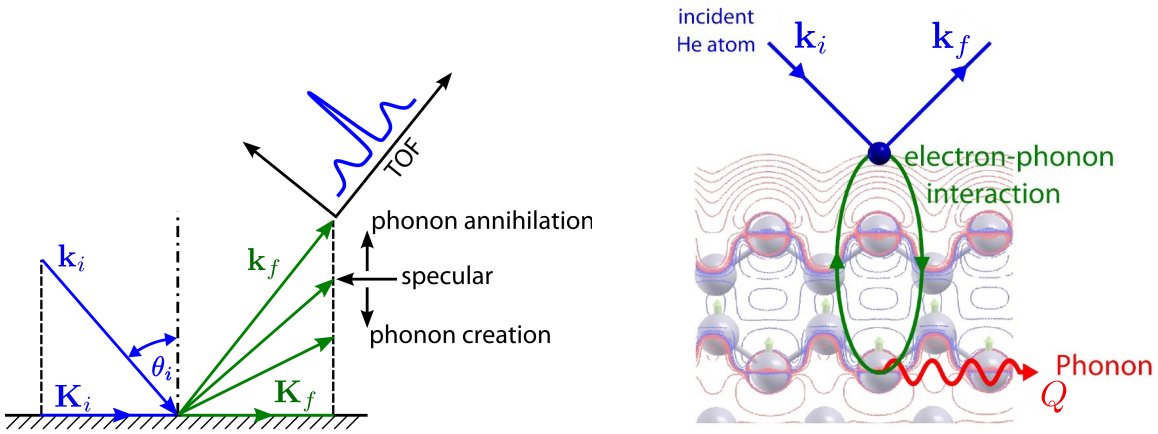

(a) Schematic of the inelastic scattering process in which a phonon is either created or annihilated. According to the conservation laws the helium atom either looses or gains energy and momentum, yielding a change in $\mathbf{k}_f$. The additional change in energy can be measured in the time-of-flight spectrum.

(b) Helium atoms are sensitive to phonons only through the electron-phonon interaction in the first few atomic layers. Depending on the mode-specific electron-phonon coupling, phonons with wavevector Q can be detected in subsurface layers.

Figure 2.4: Basic representation of the inelastic scattering process (a) and illustration of the detection of subsurface phonon states (b) [29].

2.5 Debye-Waller factor and electron phonon coupling

When scattering atoms from a surface at finite temperatures, thermal vibrations give rise to an increase of inelastic scattering events and therefore an attenuation of the elastic signal [34]. In addition to zero-point motion, higher surface temperature T_S lead to a bigger occupation of vibrational states and higher amplitudes of the surface oscillators.

In the schematic of Fig. 2.5 the incident helium atom with wavelength λ_i scatters of a surface and the total scattered intensity separates into elastic and inelastic channels. At temperatures $T_S > 0\,\mathrm{K}$ the probability for inelastic scattering increases and the wavelength of the particle changes to λ_f. The increase in the inelastic signal leads to a decrease in the elastic intensity and thus to a decay of the specular reflection with increasing sample temperature.

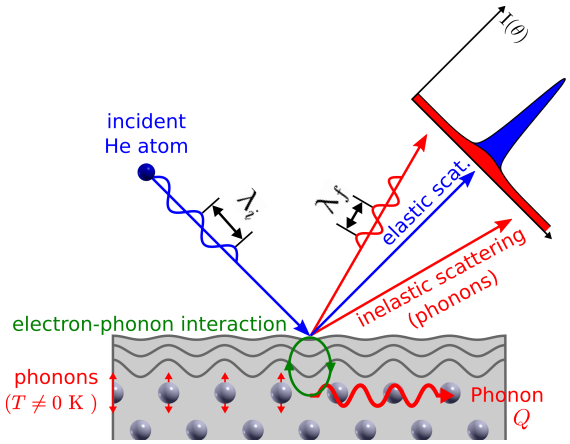

Figure 2.5: Schematic of the Debye-Waller attenuation on the surface. The inelastic background increases with surface temperature, yielding less intensity in the elastic scattering channel. From this attenuation in dependence of the surface temperature the electron-phonon interaction can be calculated [29].

Since impinging helium atoms are only sensitive to the electronic corrugation, (sub-)surface phonons are detected through the electron-phonon (e-ph) coupling. The characterizing parameter of this e-ph coupling strength is the mass-enhancement factor λ which can be determined from surface temperature dependent measurements, as discussed later in Section 2.5.2.

2.5.1 Debye-Waller attenuation

The attenuation of the elastically scattered signal $I(T_S)$ in dependence of the surface temperature T_S is described by the so-called Debye-Waller (DW) factor. It is given with respect to I_0, the intensity at rest ($T_S = 0$) as

$$I(T_S) \;=\; I_0 \cdot \mathrm{e}^{-2W(T_S)}. \tag{2.10}$$

In the two-body collision model, where the incident beam directly interacts with the target atom, the exponent $W(T_S)$ is defined as

$$2W(T_S) \;=\; \left\langle (\mathbf{u} \cdot \Delta\mathbf{k})^2 \right\rangle_{T_S}, \tag{2.11}$$

with $\mathbf{u}$ being the displacement vector of a lattice atom out of its thermal equilibrium position and $\Delta\mathbf{k} = (\mathbf{k}_f - \mathbf{k}_i)$ the total change in momentum of the scattering vector during a scattering event. The angle brackets $\langle \dots \rangle_{T_S}$ indicate that the thermal average is taken [40]. In the case of a specular reflection, the momentum transfer parallel to the surface equals zero (see Fig. 2.2a) which reduces Eq. (2.11) to:

$$2W(T_S) \;=\; \left\langle u_z^2 \right\rangle \cdot (\Delta k_z)^2, \tag{2.12}$$

with $\left\langle u_z^2 \right\rangle$ describing the average squared atomic displacement perpendicular to the surface. If the vibrations are treated like a harmonic oscillator, $\left\langle u_z^2 \right\rangle$ can then be described by

$$\left\langle u_z^2 \right\rangle \;=\; \frac{3k_\mathrm{B}T}{M\omega^2}, \tag{2.13}$$

with M being the effective mass of the oscillating surface atoms.

In the Debye model, the vibrational frequency ω is substituted by the so-called Debye frequency ω_D given by the Debye temperature Θ_D by $\omega_D \;=\; \frac{k_\mathrm{B}\Theta_D}{\hbar}$. When all equations are combined the DW factor becomes

$$2W(T_S) \;=\; \frac{3\hbar^2 T_S}{M k_\mathrm{B} \Theta_D^2} (\Delta k_z)^2. \tag{2.14}$$

Hence, if the natural logarithm of the specular intensity $\ln[I(T_S)/I_0]$ is plotted versus the surface temperature T_S the DW exponent can be obtained experimentally. In this simple Debye model the surface Debye temperature Θ_D can also be determined and compared to bulk values from X-ray or neutron scattering.

For a more accurate description of the thermal attenuation, the attractive and repulsive part of the atom-surface interaction potential need to be taken into account. Since the attractive part of the surface potential leads to an acceleration of the incoming helium atom this effect needs to be considered in the Beeby-correction. In this model the attraction is accounted for by adding the energy of the well depth D to the incident beam energy. The new perpendicular momentum transfer then reads

$$\Delta k_z \to k_i \left[\sqrt{\cos^2(\vartheta_f) + \frac{D}{E_i}} + \sqrt{\cos^2(\vartheta_i) + \frac{D}{E_i}} \right]. \tag{2.15}$$

In Eq. (2.14) Δk_z is now replaced with the Beeby-correction (Eq. (2.15)). In the special case of the specular reflection $\vartheta_i = \vartheta_f$ holds, which leads to the expression:

$$W(T_S) \;=\; \frac{12m\left[E_i \cos^2(\vartheta_i) + D\right]}{2M k_\mathrm{B} \Theta_D^2} T_S, \tag{2.16}$$

where m is the mass of the impinging (helium) particle.

One downside of this description is that the mass of the oscillating surface atoms M is not a priori

known. In most cases M is chosen as the mass of the atoms in the first crystal layer, since these ion cores will give the most contribution to the attenuation. This assumption is based on other scattering techniques and does not necessarily hold for helium atoms which are scattered by the electron density at the surface. The e-ph coupling links the surface Debye temperature Θ_D to these charge density oscillations rather than the ion cores, as discussed in the next section. HAS allows for an accurate determination of Θ_D, whereas other techniques need to consider an effective surface Debye temperature Θ_D^* and a surface effective atom mass M^*, which include the contributions arising from the e-ph interaction.

2.5.2 Electron phonon coupling

In recent years energy dissipation via e-ph coupling in materials was a widely studied topic, due to its relevance for future applications in semiconductor physics or spintronics. The e-ph coupling changes the dispersion and lifetime of the electronic states in a material and is defined as the mass-enhancement λ [41, 42]. From solid state physics it is well known that the electronic dispersion close to the Fermi energy E_F is renormalized and therefore flattened out. The resulting increase in the effective electron mass is described by $m_e^* = m_0(1+\lambda)$, where m_e^* and m_0 are the effective masses with and without e–ph interaction, respectively [42].

In a simple picture, the e–ph coupling changes the dispersion and limits the lifetime of excited electrons (or holes) of the electronic states in a material. Two complementary methods which are both necessary to get a complete picture of the e-ph coupling at a surface are angle resolved photoemission spectroscopy (ARPES) and HAS [43]. ARPES measurements are mainly used to investigate the electronic dispersion close to the Fermi surface. In contrary, HAS measures the renormalisation of the surface phonon dispersion due to e-ph interactions. Therefore, the thermal attenuation of the elastically scattered helium atoms is used from a DW measurement, as described above in Section 2.5.1.

To determine the mass-enhancement factor λ using ARPES, the temperature dependence of the total linewidth is monitored. The total linewidth consists of contributions from electron-electron and defect scattering as well as the e-ph component which is approximated to be the only temperature dependence [41]. One downside of this method is the larger contribution from bulk states compared to methods using HAS. In addition, the thermal attenuation monitored with HAS allows for easier experimental conditions and can therefore allow for a more practical and more accurate determination of λ for various material classes, as discussed below.

E-ph coupling from HAS for metal surfaces

As shown in Fig. 2.5 the decreasing elastic intensity with increasing surface temperature can be linked to the e-ph interaction. The dependence of the DW exponent on the surface temperature allows for the determination of the mass-enhancement factor λ for conducting surfaces, which has been investigated in several earlier studies [32, 44–48] as well as this work [25, 26].

As described in Section 2.5.1 the impinging helium atoms, with an energy of a few meV, are exclusively scattered by the surface electron density. A phonon can only be created or annihilated via the e-ph interaction in which the modulation of the surface free-electron gas is induced by vibrational states in the first few atomic layers. Due to conventions in quantum mechanics it is more appropriate to write the DW factor in dependence of the scattering vectors, i.e. $W(\mathbf{k}_i, \mathbf{k}_f, T_S)$. Manson *et al.* related the DW factor to λ according to [46]:

$$W(\mathbf{k}_i, \mathbf{k}_f, T_S) \;\cong\; 4\,\mathcal{N}(E_F)\frac{m}{m_e^*}\frac{E_{iz}}{\phi}\;\lambda\;k_B T_S\;. \tag{2.17}$$

In Eq. (2.17) λ is given for a helium atom with mass m which scatters with an initial wavevector $\mathbf{k}_i$ into a final state with wavevector $\mathbf{k}_f$. With $\mathcal{N}(E_F)$ being the density of electronic states at the Fermi level, ϕ the work function, m_e^* the effective electron mass, E_{iz} the normal component of the incident energy and k_B the Boltzmann constant. For a more accurate description the incident energy needs to be corrected with the Beeby correction $k_{iz}^2 \longrightarrow k_{iz}^2 + 2mD/\hbar^2$ (Eq. (2.15)).

When Eq. (2.10) and Eq. (2.17) are combined, the e-ph coupling constant can be related to the temperature dependence of the HAS specular intensity $I(T_S)$. Using the slope $\ln(I_0/I)/T_S$ from the DW measurement then gives

$$\lambda_{HAS} \;\cong\; \frac{1}{4\mathcal{N}(E_F)} \frac{m_e^*}{m} \frac{\phi}{k_B E_{iz}} \frac{\ln(I_0/I)}{T_S} \;. \tag{2.18}$$

Eq. (2.18) yields a value of the e-ph constant which provides the correct average over all contributing phonon modes. Benedek *et al.* investigated the dependence of λ with respect to different phonon energies and modes $\omega_{\mathbf{Q},\nu}\{\mathbf{Q},\nu\}$ [45]. This description allows to determine a mode-specific coupling constant $\lambda_{\mathbf{Q},\nu}$, however here we only consider the mode averaged λ. Eq. (2.18) was applied for various metals and semimetals to determine λ_{HAS} and shows good agreement with values from other techniques [46].

This approach for the determination of λ at metal surfaces can also be adapted to the material classes of semiconductors, topological insulators and transition metal dichalcogenides, as described below.

E-ph coupling from HAS for semiconductors and topological insulators

The material class of topological insulators (TIs) exhibits metallic surface states with semiconducting properties in the bulk, for which the above described method can be adapted. When considering semiconductors, the surface charge density in the first atomic layers is linked to the Thomas-Fermi screening length λ_{TF}. Adapting Eq. (2.18) with respect to the special electronic properties of TIs yields [26]:

$$\lambda = \frac{\pi}{2n_s}\alpha\,, \quad \alpha \equiv \frac{\phi}{A_c\, k_{iz}^2} \frac{\partial \ln I(T_S)}{k_B\, \partial T_S}\,, \tag{2.19}$$

where n_s is the number of conducting layers contributing to phonon induced modulations of the electronic density, ϕ the work function, A_c the surface unit cell area, k_{iz} the normal component of the incident wavevector and $I(T_S)$ the specular HAS intensity. n_s is given in terms of the Thomas-Fermi screening length λ_{TF} with $n_s = 2\lambda_{TF}/c_0$, where c_0 is the quintuple layer thickness and the factor 2 accounts for two metallic sheets per quintuple layer. Similar to Eq. (2.15) the incident wavevector k_{iz} needs to be adapted with the Beeby correction to account for the attractive and repulsive part of the surface potential.

Strictly speaking, Eq. (2.19) is only valid for two-dimensional cases, i.e. a 2DEG which is present on most common TIs. As shown later in this theses (Section 4.6), the expression for λ can also be extended to various dimensions [48].

2.6 Semimetals and topological insulators

In recent years several new aspects and novel characteristics for semimetals such as Bi and Sb were investigated with state of the art experimental and theoretical methods [28, 49]. It was discovered that surfaces, which are already well characterized with respect to their bulk properties, may still show unexplored new interesting physical and chemical features at the surface. Especially in semimetals and topological insulators the surface exhibits novel electronic states such as topological surface states. The fundamental properties of these materials are described below.

All investigated materials are either characterised as semimetals or semiconductors with respect to their

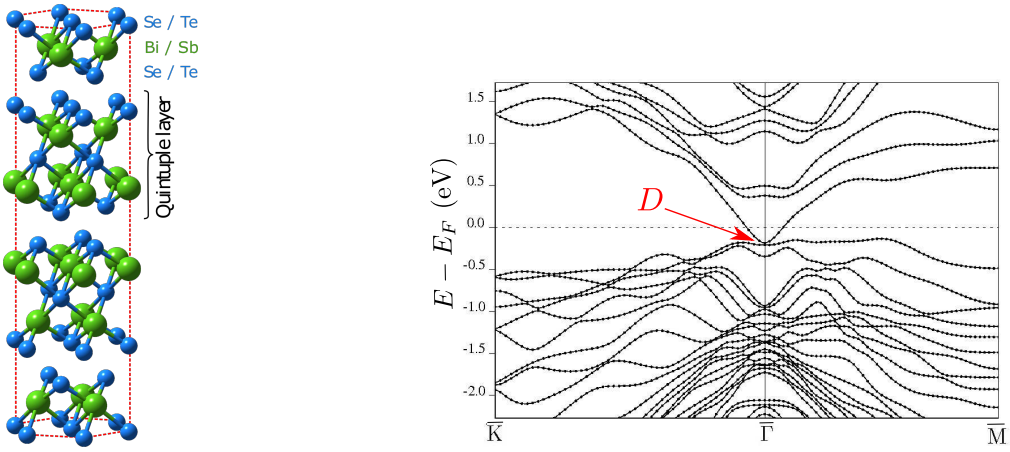

(a) Crystal structure of a typical topological insulator based on the conventional hexagonal unit cell which consists of three quintuple layers separated by weak van der Waals bonds.

(b) Surface electronic band structure of $Bi_2Se_3(111)$ with spin-orbit coupling included in the DFT calculation. D marks the position of the Dirac point below the Fermi energy.

Figure 2.6: Basic crystal structure and surface electronic band structure of topological insulators.

bulk electronic structure. Semimetals are defined by a small overlap of the top of the valence band and the bottom of the conduction band, therefore yielding no band gap. In contrary semiconductors exhibit a small band gap of a few eV between both bands. Compared to pure metallic materials semimetals show a smaller density of states at the Fermi level and have electrons as well as holes as their charge carriers [50]. Therefore semimetals also show electrical conductivity at zero temperature, while semiconductors have zero conductivity at this temperature. Because of electron phonon interaction the conductivity decreases with increasing temperatures in pure metals. However, in semimetals and semiconductors the temperature dependence has a more peculiar behaviour and is influenced by both charge carrier types.

In recent years the emerging field of topological insulators (TIs) brought many new aspects to the field of condensed matter and electronic materials. Three-dimensional TIs exhibit an insulating gap in the bulk and conducting states on the surface [51, 52]. Materials such as the TI Bi_2Se_3 had already been well known for their thermoelectric properties with a large Seebeck coefficient [53–57] and have therefore been used in thermoelectric refrigeration for a long time. Recent works focused more on the peculiar electronic states at the surface. The topological surface states are characterised by an odd number of relativistic Dirac fermions and are protected by time-reversal symmetry. The carriers are locked to their spin-momentum, hence the direction in which the carriers are travelling is defined by the orientation of the spin. The linear relationship between energy and momentum is known as Dirac cone. In Fig. 2.6b the electronic band structure of the TI $Bi_2Se_3(111)$ is plotted with the characteristic Dirac point D below the Fermi energy E_F. Due to the large spin-orbit splitting the topological surface state exhibits no spin degeneracy [51, 58].

The crystal structure of the prominent three-dimensional TIs Bi_2Se_3 and Sb_2Te_3 are shown in Fig. 2.6a. The layered hexagonal structure consists of three quintuple layers (QLs), which are separated by weak van der Waals bonds.

The material class of TIs opens up new possibilities for using the spin degree of freedom in emerging applications for information processing technologies. Future spintronic devices may be used for spin filtering, spin control, memory devices and to store magnetic properties. In addition, surface dominated electronic transport in TIs plays an important rule in quantum sensing by inducing electronic changes with the adsorption of molecules [59–61]. The adsorption of various atoms and molecules also allows for

a tuning of the electronic properties and can therefore change the conduction type (n- or p-type doping). Finally, TIs could further be used in flexible electronics [62] and non-linear optics.

2.7 Vicinal surfaces

Defects on solid surfaces have a great impact on surface chemical properties due to their low dimensionality, which play an important role in catalysis. It is well known that there is a major gap in understanding the chemical reactions on an ideal flat surface and of an actual catalyst. For example detailed knowledge of the processes happening during surface oxidation plays an important role in the understanding of corrosion [63]. Therefore, it is important to characterise the chemical and physical properties of various types of defects such as steps. Stepped surfaces like Bi(114) may even present a quasi-one-dimensional system.

Periodically stepped (vicinal) surfaces are ideal model systems for isolating one type of defect, namely a step edge, which becomes particularly accessible by studying diffraction techniques [64, 65]. Early works using inelastic helium atom scattering investigated stepped surfaces to determine step-localized phonon modes [66]. In addition, the study of the intensities of elastically scattered helium atoms allows for the determination of the corrugation of stepped surfaces [65, 67].

In many cases vicinal surfaces undergo a reconstruction, as described later in this thesis for Bi(114), in order to minimize the energy of the system [28, 68]. Surface reconstructions can be also be induced by dosing gas molecules on stepped surface [63].

2.8 Two-dimensional materials

Recently, intensive research focused on two-dimensional (2D) materials, including graphene, hexagonal boron nitride (h-BN) and transition metal dichalcogenides which received a great deal of research interest [69]. After single-layer graphene was successfully isolated for the first time in 2004 [70] myriads of experimental and theoretical investigations followed. The extraordinary features such as gapless, linear band structure, ultrahigh carrier mobility, high mechanical strength, and high thermal conductivity received massive interest in potential applications. Therefore, graphene paved the way to the world of so-called 2D materials which consist of layered atomic thin sheets with strong in-plane covalent bonding and weak interactions between layers, usually of van der Waals type [69].

After more than ten years of development, 2D materials have become one of the most important topics in materials research: Dozens of new materials have been synthesized experimentally and even more predicted theoretically [71]. Fabrication of 2D materials is usually based on epitaxial growth. For a controlled synthesis, often chemical vapour deposition (CVD) in an ultra-high vacuum environment is employed. The enormous variety of different combinations of substrates and adlayers led to the findings of many new phenomena and physical properties [72–74]. The unique electrical, optical and thermal properties in 2D materials are associated with their strictly defined low dimensionalities, providing a wide range of building blocks for future electronic applications [73].

The 2D material h-BN, also called ”white graphene”, has gained significant research interest in the last decade. In this particular 2D structure boron and nitrogen atoms are alternately arranged in a honeycomb lattice (see Fig. 2.7). Due to the large bandgap of 5.97 eV, h-BN acts as a unique insulator and thus may be used as an ideal dielectric in heterostructures [69]. The very good thermal conductivity makes h-BN a prime candidate as a thermal heat spreader in 2D nanoelectronics [75, 76].
Controlled synthesis of high-quality 2D h-BN layers is very demanding since the physical and chemical

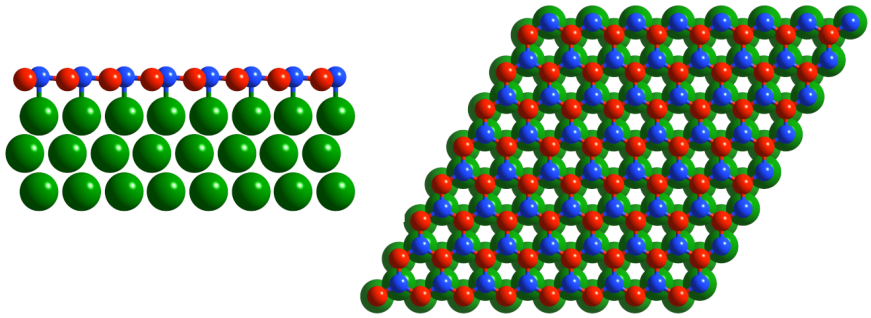

Figure 2.7: Schematic top and side-view of h-BN on a Ru(0001) substrate (green spheres), where the boron (nitrogen) atoms are depicted in red (blue), respectively. Depending on the atoms the interatomic distances change leading to a buckled structure.

properties of the adlayer depend on the used synthesis method. Besides exfoliation, in most cases h-BN is synthesized by CVD where a gas-phase precursor is deposited on a solid substrate, diffuses, dehydrogenates or fragments and eventually attaches to a growing 2D cluster. This method offers relatively large grain sizes, however the CVD systems are often complex, making it difficult for a controlled synthesis of the adlayer. As later shown in this theses, the mechanisms behind the controlled growth of h-BN on metal systems are still not fully understood. Slightly different starting conditions can give rise to different structures and the system may therefore be an ideal playground to end up with different nano-structures.

Chapter 3

Experimental setup

The experiments within this thesis were all (with one exception) conducted on the apparatus H.A.N.S (Helium Atom Nondestructive Scattering) at the Institute of Experimental Physics, TU Graz. The work on the growth of hexagonal boron nitride (Section 4.8) was conducted on the ^{3}He-Spin-echo apparatus at the University of Cambridge, UK. For an accurate description of this setup please refer to Refs. [17–19, 77, 78]. However, the principles of elastic scattering for both setups are the same as described in Chapter 2.

The whole apparatus at the TU Graz is depicted in a schematic in Fig. 3.1. After the setup was characterized and improved [79], first measurements were done on the Bi(111) [3, 5, 29, 44, 80] and Sb(111) surfaces [4, 6, 31, 79]. The complete setup consists of three main components: the source chamber, the scattering/main chamber and the detector arm. The apparatus was already accurately described in the PhD thesis of Anton Tamtögl [29].

Source Arm

The source arm (see Fig. 3.1), which consists of two chambers generates the nearly monoenergetic atomic beam by using a supersonic expansion. The ^{4}He gas is expanded (50 bar $\rightarrow \approx 1 \times 10^{-6}$ mbar) through a nozzle with a diameter of $d = 10\,\mu$m. The final particle velocity of the beam is given by

$$v_{\parallel} = \sqrt{\frac{5k_{\mathrm{B}}T_0}{m_{He}}}, \tag{3.1}$$

with k_{B} being the Boltzmann's constant, T_0 the nozzle temperature (T_0 between 47 to 300 K) and m_{He} the atomic mass of helium.

The central part of the beam is then selected by a skimmer before it enters the second chamber in which the chopper disc is located, which represents the central part for performing TOF measurements. For these experiments a pseudo-random chopper disc was used to yield better signal to noise ratios [79].

Main Chamber

In the main chamber the investigated sample is mounted on a seven-axis manipulator, which allows for an accurate adjustment of the desired scattering position. To avoid contamination of the sample over time the main chamber is constantly kept at ultra-high vacuum (UHV) conditions ($p \leq 2 \times 10^{-10}$ mbar). The

sample can be heated electrically using a button heater and cooled via a thermal connection to a liquid nitrogen reservoir. The apparatus is designed for in-plane scattering measurements, in which the surface normal and the wavevectors of the incident and the scattered beam are in the same plane. The angle between source arm and detector arm is fixed, having a solid-angle value of $\vartheta_{SD} = 91.5°$. In addition the main chamber is equipped with a quadrupole mass spectrometer, a low energy electron diffraction (LEED) system and an Auger electron spectrometer (AES). The LEED is used to orient the crystal in the desired high symmetry orientation while the AES allows for an initial surface characterization with respect to contaminants.

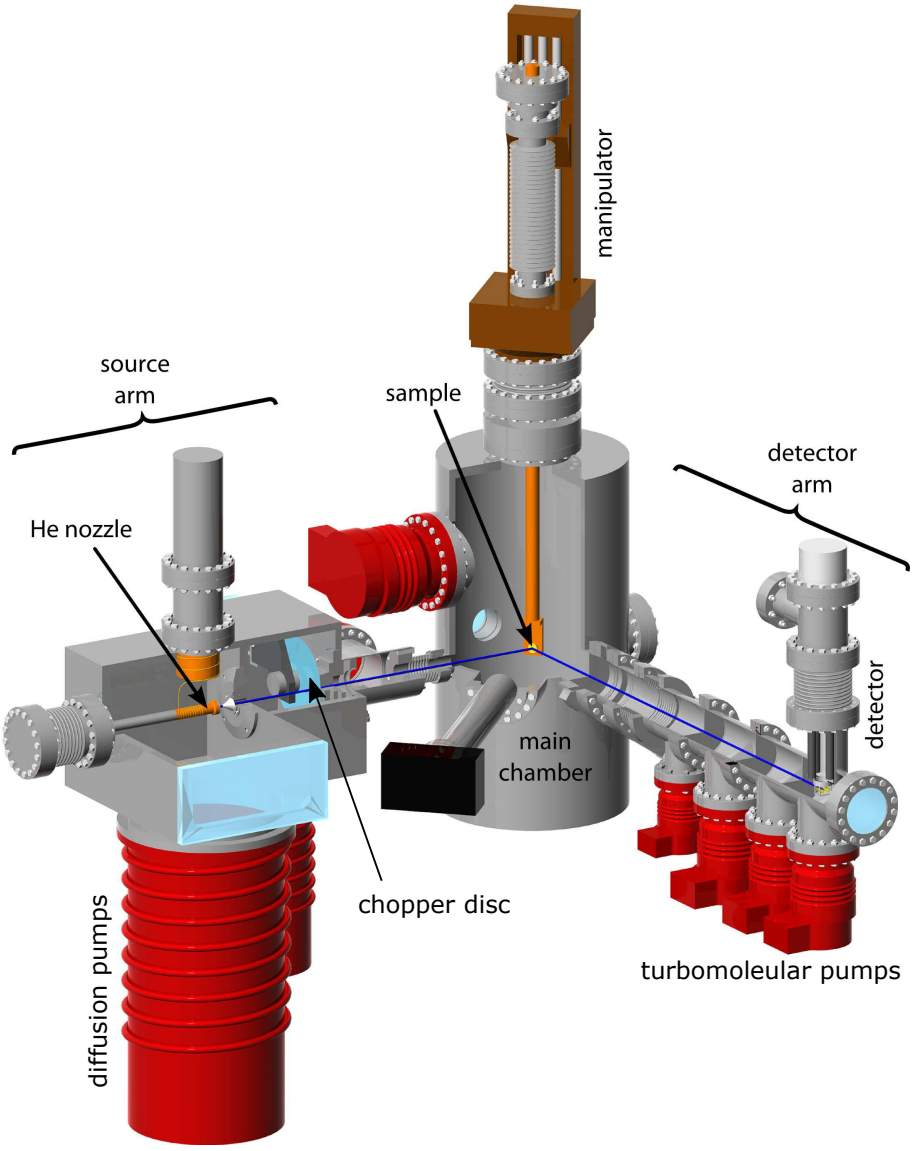

Figure 3.1: Basic CAD representation of the HAS apparatus used during the work for this thesis. Adapted from A. Tamtögl [29]

Detector Arm

If the helium atoms are scattered off the samples surface in the direction of the detector arm they pass through smaller chambers with several pumping stages. At the end of the arm the atoms are detected

using a quadrupole mass spectrometer. The neutral helium atoms are ionized using a cross beam ion source and are deflected by 90° to reach the detector, which contains a secondary electron multiplier. For the TOF measurements, the quadrupole mass spectrometer is equipped with a multi-channel analyser system. Due to different velocities after an inelastic scattering event, the helium atoms are spread spatially and arrive at the detector at different times which can be distinguished by unfolding the signal according to the chopper sequence [79].

Sample preparation

Depending on the crystal samples used in this thesis various surface preparations were used. For the Bi(114) surface (Section 4.6) multiple cycles of Ar^+-sputtering with consecutive annealing were used. In between the cycles the surface cleanliness was investigated using the LEED system. The sharpness and intensity of the LEED diffraction spots were used as an indication for the amount of remaining adsorbates and impurities on the surface.

For the material class of TIs the exfoliation method was applied for the preparation of a clean surface. In these materials the individual quintuple layers (QLs) are held together by weak vdW-forces, which allows for an easy removal of the first few QLs. In the recently introduced load-lock chamber [81] a scotch tape is applied to the sample surface under ambient conditions followed by an evacuation of the chamber. Attached to this chamber is a vacuum suitcase containing a gripping mechanism which can then be used to grab the sample holder and therefore peel off the applied scotch tape. This *in situ* method under UHV conditions is essential for a clean crystal surface and to avoid contamination of the surface. Using the gripping mechanism the sample is then transferred into the main chamber, where it is placed in the manipulator. After the gripping mechanism left the main chamber the valve is closed and the sample can be characterized using LEED, AES and HAS.

Chapter 4

Results

4.1 Outline

This chapter presents the results obtained during the work of this thesis in sections which are arranged according to their thematic results. Sections 4.2, 4.3, 4.4, 4.5, 4.6 and 4.7 consist of already peer-reviewed and published publications while section 4.8 contains results which are currently under peer-review.

4.2 Helium-Surface Interaction and Electronic Corrugation of $Bi_2Se_3(111)$

This section consists of the following published publication:

Helium-Surface Interaction and Electronic Corrugation of $Bi_2Se_3(111)$

A. Ruckhofer*, A. Tamtögl, M. Pusterhofer, M. Bremholm, and W. E. Ernst

The Journal of Physical Chemistry C **123**, 17829–17841, 2019

https://doi.org/10.1021/acs.jpcc.9b03450

* corresponding author

contributions	
funding	W.E. Ernst, A. Tamtögl
experimental design	A. Tamtögl, A. Ruckhofer
sample synthesis	M. Bremholm
data acquisition	A. Ruckhofer, M. Pusterhofer
CC simulations	A. Ruckhofer, M. Pusterhofer
data analysis & interpretation	A. Ruckhofer, A. Tamtögl
publication writing	A. Ruckhofer, A. Tamtögl
discussion and editing	A. Ruckhofer, A. Tamtögl, W.E. Ernst

Abstract

We present a study of the atom-surface interaction potential for the He–Bi_2Se_3(111) system. Using selective adsorption resonances, we are able to obtain the complete experimental band structure of atoms in the corrugated surface potential of the topological insulator Bi_2Se_3. He atom scattering spectra show several selective-adsorption resonance features which are analysed, starting with the free-atom approximation and a laterally averaged atom-surface interaction potential. Based on quantum mechanical calculations of the He-surface scattering intensities and resonance processes we are then considering the three-dimensional atom-surface interaction potential which is further refined in order to reproduce the experimental data.

Following this analysis, the He–Bi_2Se_3(111) interaction potential is best represented by a corrugated Morse potential with a well depth $D = (6.54 \pm 0.05)$ meV, a stiffness $\kappa = (0.58 \pm 0.02)$ Å^{-1} and a surface electronic corrugation of (5.8 ± 0.2)% of the lattice constant. The experimental data may also be used as a challenging benchmark system to analyse the suitability of several van der Waals approaches: The He–Bi_2Se_3(111) interaction captures the fundamentals of weak adsorption systems where the binding is governed by long-range electronic correlations.

Introduction

The material class of topological insulators (TIs) has lately received broad attention [52, 58, 82–85], due to their protected metallic surface states and the insulating bulk electronic structure [86, 87]. An archetypal TI and one of the most studied examples is the here presented Bi_2Se_3 [88, 89]. Topological surfaces show modifications of their electronic structure upon adsorption of atoms and molecules [59, 60, 90, 91]. However, the interaction of TI surfaces with their environment, i.e. atom-surface interaction potentials are barely investigated by experiment despite the fact that topology can have implications far beyond electronic transport properties and topological materials provide a perfect platform for studying phenomena such as heterogeneous catalysis or sensing applications [61, 92].

Understanding the atom-surface interaction on topological insulators is interesting from a fundamental point of view and may help to obtain a deeper understanding of the interaction with gases and molecules in the physisorption regime [93, 94]. E.g. as shown recently the long-range part of the potential can be responsible for band bending effects upon adsorption [95].

Here we present a study of the atom-surface interaction potential for the He–Bi_2Se_3(111) system. The shape of the interaction potential between the surface and atoms can be extracted from atom-surface scattering experiments and we follow this approach using helium atom scattering from the surface of Bi_2Se_3(111). Helium atom scattering (HAS) is strictly surface sensitive and allows the investigation of surface structure and dynamics of conducting as well as insulating materials [34]. The technique permits measurements of the atom-surface interaction potential to a very high accuracy via selective adsorption resonances (SARs) [22, 96]. Studying SARs provides access to the bound state energies ϵ_n which are supported by the atom-surface interaction potential and more importantly, to the atom-surface interaction potential itself. Previous experimental studies of SARs have mainly been performed on salts with the NaCl structure [22, 34, 96–100] while only recently semimetals and semiconductors have been studied using this approach [5, 6, 101].

In addition to experimental measurements of SARs, *ab initio* approaches have been employed in order to determine a numerical atom-surface interaction potential [102–104]. On the one hand, the extremely small adsorption energies of He atoms on surfaces (in the few meV region) and the de-localised nature and mobility of electrons on conducting surfaces makes such systems particularly challenging, even for

state-of-the-art van der Waals (vdW) corrected density functional theory (DFT) approaches [104]. On the other hand, since measurements of the atom-surface potential give insight into the atom-surface interaction dynamics within the vdW regime, experimental results can be used to test the ability of dispersion corrected DFT approaches to simulate nonlocal interactions [102, 105, 106].

The atom-surface interaction potential is also a necessary ingredient for quantum-mechanical calculations of elastic scattering intensities [37, 107, 108] allowing for a comparison with experimentally observed He diffraction peak intensities. In this context, the influence of vdW forces in atom-surface scattering calculations of noble gases has recently been studied [107, 109] and the experimental diffraction intensities may even be used as a benchmark to test the performance of different vdW corrected DFT approaches [110].

However, the comparison with diffraction intensities merely considers a small number of diffraction channels which are accessible in the experiment and thus a comparison of quantum mechanical scattering calculations with SARs provides an even more rigorous test in terms of the sought atom-surface interaction potential. Following this approach we use experimental SARs together with quantum mechanical He-surface scattering calculations in order to determine an accurate three-dimensional atom-surface interaction potential. Herein experimental data from complex surfaces such as TIs may be especially valuable, in particular since it was shown only recently that for an accurate theoretical description of the layered structure of TIs the inclusion of vdW corrections is essential [111].

Experimental Details

The experimental data in this work was obtained at the HAS apparatus in Graz which is able to generate a nearly monochromatic beam of ^{4}He. The scattering geometry is defined by a fixed source-sample-detector angle with 91.5° (for a description in greater detail see [3]). In brief, the He beam is generated via a supersonic expansion from a base pressure of 50 bar to 10^{-6} mbar through a cooled nozzle of 10 µm. The central part is selected with a skimmer (310 µm orifice) creating a He beam with an energy spread of $\Delta E/E \approx 2\%$. By varying the nozzle temperature the beam energy can be tuned between 9 and 20 meV. The beam then hits the sample in the main chamber under ultra-high-vacuum (UHV) conditions ($p \leq 2 \times 10^{-10}$ mbar) and is further detected using a quadrupole mass analyser. For varying the incident angle ϑ_i in the fixed source-sample-detector geometry the sample can be rotated.

For a detailed description of the sample growth procedure see Bianchi *et al.* [112]. After *in situ* cleavage of the sample in a load-lock chamber [113] the cleanness and purity of the sample can be further studied using low energy electron diffraction (LEED) and Auger electron spectroscopy (AES). The rhombohedral crystal structure Bi_2Se_3 is built of quintuple layers (QL) which are bound to each other through weak van der Waals forces [112]. The unit cell consists of 3 QLs and shows Se termination upon cleavage. The surface along the (111) cleavage plane has a lattice constant of $a = 4.14$ Å at room temperature [114]. The sample was fixed on a sample holder using thermally conductive epoxy.

The intensity of the specular reflection throughout the measurements typically reached values with a signal-to-noise ratio of 10^3 above the diffuse elastic background (Fig. 4.3) while the full width at half maximum (FWHM) was typically about 0.015 Å^{-1}. Hence the angular broadening of the specular peak is mainly limited by the angular broadening of the apparatus giving rise to an estimate (lower limit) for the quality of the crystal [47] with domain sizes larger than 1000 Å.

The sample temperature was varied between cryogenic temperatures (113 K, via a thermal connection to a liquid nitrogen reservoir) and room temperature (300 K). For a first characterisation the scattered specular intensity was measured in dependence of the sample temperature in order to determine the

surface Debye temperature ($\Theta_D = 122\,\mathrm{K}$ [26, 81]). All scattering calculations presented in this work have been corrected by the according Debye-Waller attenuation based on the experimentally determined Debye temperature.

After the first characterisation of the crystal, various elastic diffraction scans at 113 K and room temperature were collected in both high symmetry directions and at different incident energies. Furthermore, measurements of the specular reflection in dependence of the beam energy (measured at 113 K) allow to obtain further details of the SARs and the atom-surface interaction potential (section "Refinement of the interaction potential").

Results and Discussion

After an introduction to the atom-surface interaction potential and the kinematic analysis we begin our analysis of the SAR features following the free-atom model. Based on the approximate surface-averaged potential we are then determining the corrugation amplitude of the potential from diffraction measurements in order to acquire a three-dimensional potential. Finally we are going to compare the experimental SARs with quantum mechanical scattering calculations to further refine the three-dimensional atom-surface interaction potential.

The atom-surface interaction potential

As stated by Bragg's law, if an atom is scattered by a periodic surface, the change of the wavevector component parallel to the surface, $\mathbf{K}$, must be equal to a surface reciprocal lattice vector, $\mathbf{G}$.
Here we present mainly measurements where the polar (incident) angle ϑ_i is varied around the corresponding axis while the scattered beam intensity is detected. For elastic scattering, the momentum transfer parallel to the surface, $\Delta\mathbf{K}$, is then given by

$$|\Delta\mathbf{K}| = |\mathbf{K}_f - \mathbf{K}_i| = |\mathbf{k}_i|\left(\sin\vartheta_f - \sin\vartheta_i\right) , \tag{4.1}$$

where $\mathbf{k}_i$ is the incident wavevector and ϑ_i and ϑ_f are the incident and final angles with respect to the surface normal, respectively.

Selective adsorption phenomena which may appear upon scattering of atoms from a periodic surface, occur due to the attractive part of the atom-surface interaction potential. For an elastic process, the kinematically-allowed $\mathbf{G}$-vectors are those for which the wavevector component perpendicular to the surface $k_{f,z}^2$ is positive. If an incident He atom hits the surface it can undergo a transition into a bound state on the surface with $-|\epsilon_n|$. The process happens while the He atom is diffracted into a channel which is kinematically disallowed ($k_{f,z}^2 < 0$). Such SARs can only happen if the difference between the energy of the incident atom and the kinetic energy of the atom moving parallel to the surface matches the binding energy ϵ_n of the adsorbed atom [97]:

$$E_i = \frac{\hbar^2\mathbf{k}_i^2}{2m} = \frac{\hbar^2(\mathbf{K}_i + \mathbf{G})^2}{2m} + \epsilon_n(\mathbf{K}_i, \mathbf{G}) , \tag{4.2}$$

where m is the He mass. From Eq. (4.2) it is clear that studying SARs provides access to the bound state energies $\epsilon_n(\mathbf{K}_i, \mathbf{G})$ and more importantly to the atom-surface interaction potential.

In this work we have analysed SARs upon scattering of He from Bi_2Se_3 using a corrugated Morse potential (CMP). In spite of the deviation of the CMP from the expected z^{-3} asymptotic behaviour, it has been shown that the overall shape of the CMP represents the measured bound states well enough. A

comparative study of various potentials with different asymptotic behaviour has shown similar outcome when subsequently used in close-coupling calculations [31, 37]. Likewise the validity of this potential for TI surfaces [115] and other layered materials such as transition metal dichalcogenides [116] has been proven. In addition the CMP greatly simplifies the treatment of several steps within the close-coupling (CC) algorithm, allowing for an analytical solution in those cases, which leads to a reduced computational cost.

The three-dimensional CMP, written in dependence of the lateral position $\mathbf{R}$ on the surface and the distance z with respect to the surface is [117]:

$$V(\mathbf{R}, z) = D\left[\frac{1}{\nu_{0,0}} e^{-2\kappa[z-\xi(\mathbf{R})]} - 2e^{-\kappa z}\right] \tag{4.3}$$

with the stiffness parameter κ, D the depth of the potential well and the surface average $\nu_{0,0}$ of the exponent of the corrugation function. The electronic surface corrugation is described by $\xi(\mathbf{R})$ where $\mathbf{R}$ describes a periodically modulated surface corresponding to a constant total electron density.

For $\xi(\mathbf{R})$ a two-parameter Fourier ansatz was used which is described by a summation of cosine terms. The Fourier series expansion is based on the sixfold symmetry of the topmost layer of the surface (see Eq. (4.14) in the Appendices), which is the only relevant layer when considering the energies of the impinging He atoms used in this study [6, 37]. The corrugation magnitude is then typically given in terms of the peak-to-peak value ξ_{pp} of $\xi(\mathbf{R})$.

The laterally averaged surface potential V_0 (i.e. without corrugation) of Eq. (4.3) is given via:

$$V_0(z) = D\left[e^{-2\kappa z} - 2e^{-\kappa z}\right] \tag{4.4}$$

The bound states can be described analytically by:

$$\epsilon_n = -D + \hbar\omega\left(n + \tfrac{1}{2}\right)\left(1 - \frac{n + \frac{1}{2}}{2\gamma}\right) \tag{4.5}$$

where n depicts a positive integer, $\omega = \kappa\sqrt{\frac{2D}{m}}$ is the Debye-frequency and $\gamma = \frac{2D}{\hbar\omega}$ with m the mass of the impinging He atom.

In order to determine the three-dimensional potential we start firstly with the laterally averaged atom-surface interaction potential, trying to identify SARs in various diffraction scans. After determining a laterally averaged atom-surface interaction potential based on the SAR positions and the free atom model we determine the corrugation amplitude ξ_0 of the potential by comparison of the diffraction intensities based on close-coupled calculations with the experimentally determined diffraction intensities. We are then further refining the potential using close-coupled calculations of the resonance positions, optimising the agreement with the experimental measurements of SARs. The whole procedure is described in more detail below.

Determination of SARs in the elastic scans

In a first step of determining the atom-surface interaction potential the laterally averaged atom-surface interaction potential is used to identify the SARs in various elastic scans. When performing a diffraction scan according to Eq. (4.1), the kinematic condition Eq. (4.2) can be fulfilled for specific values of ϑ_i. Two typical diffraction scans for the high symmetry direction $\overline{\Gamma\mathrm{M}}$ are shown in Fig. 4.1. The x-axis has been transformed to parallel momentum transfer using Eq. (4.1). In addition to the diffraction peaks, smaller features caused by SARs can be seen.

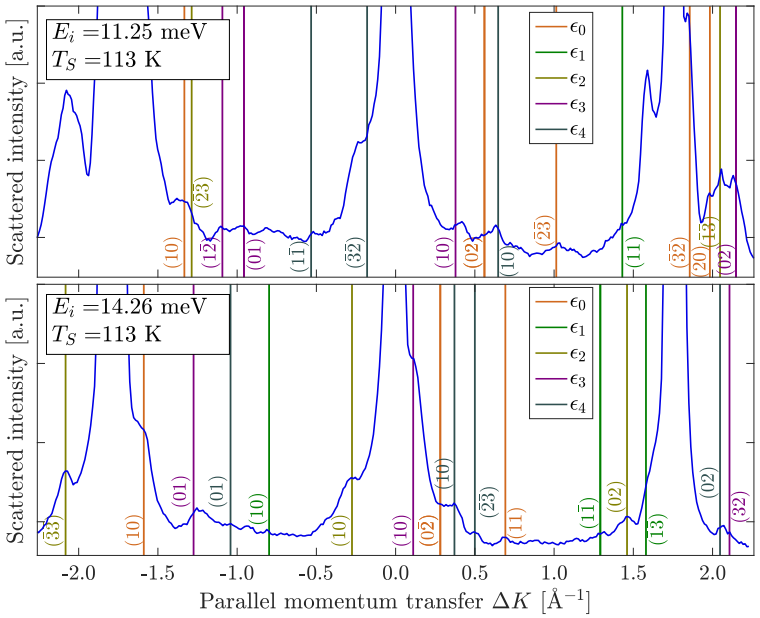

Figure 4.1: Scattered He intensities for $Bi_2Se_3(111)$ versus parallel momentum transfer $\Delta\mathbf{K}$ along the $\overline{\Gamma M}$ azimuth with a sample temperature of 113 K. The incident beam energy E_i is 11.25 and 14.26 meV in the top and bottom panels, respectively. The intensity scale has been expanded and in addition to the diffraction peaks which are cut off due to their high intensity, small peaks and dips corresponding to selective adsorption processes can be seen. The vertical lines in various colours illustrate the kinematic conditions for five bound-state energies ϵ_0-ϵ_4 according to Eq. (4.6). Each line is labelled with the Miller indices of the associated $\mathbf{G}$ vector for the particular resonance condition.

At first we will restrict the kinematic condition given in Eq. (4.2) to the free atom approximation which assumes that the surface potential is adequately described by the laterally averaged interaction potential Eq. (4.4). Strictly speaking it holds only in the case where the surface corrugation approaches zero, which is not possible in reality, since corrugation is necessary to provide the $\mathbf{G}$-vector for the resonance processes. We will then use and refine the full three-dimensional atom-surface interaction potential at a later point within the formalism of close-coupled calculations.

Nevertheless the free atom approximation is useful for a first identification of SARs, as it treats the binding energies $\epsilon_n(\mathbf{K}_i, \mathbf{G})$ in Eq. (4.2) as constants and therefore independent of $\mathbf{K}_i$ and $\mathbf{G}$. The introduction of a corrugation may give rise to changes of the resonance positions which tend to become more important with increasing surface electronic corrugation. Since the peak-to-peak corrugation of similar materials is in the region of 5–9 % of the lattice constant [37, 47] one needs to keep in mind that considerable shifts of the resonance positions may occur.

Using the free atom model as a starting point, the position of the SARs Eq. (4.2) can be rewritten in terms of the incident angle ϑ_i and the incident wave vector k_i. The latter is given by the beam energy which is determined by the nozzle temperature. The scattering vector $\mathbf{G}$ can be separated into two parts $\mathbf{G} = (G_\parallel, G_\perp)$ parallel and normal to the incidence plane:

$$k_i^2 = \left(k_i \sin\vartheta_i + G_\parallel\right)^2 + G_\perp^2 - \tfrac{2m}{\hbar^2}|\epsilon_n|\,. \tag{4.6}$$

The peaks or dips at a particular incident angle ϑ_i in the scans can be associated with a certain bound state energy ϵ_n and scattering channel using Eq. (4.6). The position of several SARs is indicated with vertical lines (based on solving Eq. (4.6) for ϑ_i) in Fig. 4.1 and labelled according to their diffraction channel $\mathbf{G}$ while the different colours correspond to different bound states ϵ_n. For better visibility of the

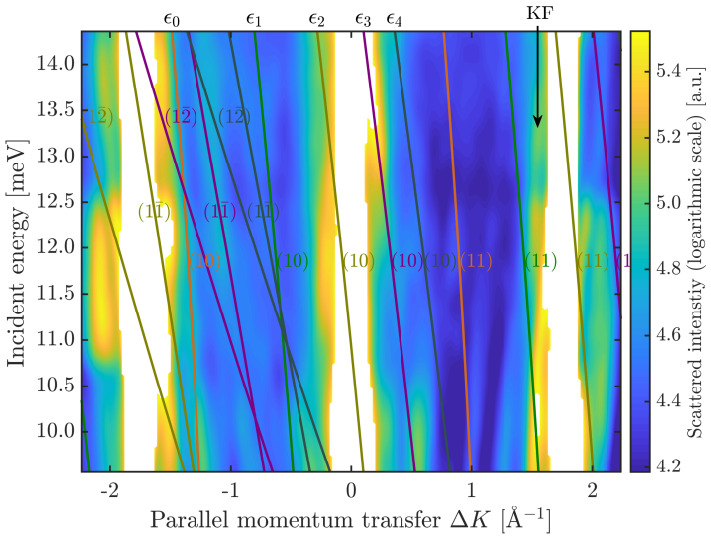

Figure 4.2: Contour plot of the scattered He intensities (logarithmic scale) versus parallel momentum transfer and incident energy of the He atom along the $\overline{\Gamma M}$ azimuth and at a sample temperature of 113 K. The superimposed solid lines correspond to the resonance conditions calculated with the free atom approximation. Each line is labelled with the Miller indices of the associated **G**-vector for the resonance condition. The labels $\epsilon_0 - \epsilon_4$ at the top-abscissa denote the series of eigenvalues associated with the (10) **G**-vector. Scattered intensities (mainly the diffraction peaks) exceeding a certain value have been cut off in order to increase the visibility of the resonance effects. The black arrow labelled with KF indicates a region of increased intensity which is likely to correspond to kinematical focusing (KF) rather than a resonance effect.

SARs the sample was cooled down to 113 K to minimise the inelastic background as well as the linewidth of the resonances. The scan in the upper panel was measured with an incident beam energy of 11.25 meV and the lower panel at 14.26 meV respectively. The vertical lines are according to the first 5 bound state energies ϵ_0-ϵ_4 of the later determined laterally averaged interaction potential defined by their colour while the numbers next to the lines denote the corresponding reciprocal lattice vectors.

It becomes immediately evident that the assignment of resonances in a single diffraction scan such as Fig. 4.1 is quite ambiguous since numerous combinations of ϵ_n and **G** can be thought of in order to fulfill Eq. (4.6). For a better assignment of the bound states and **G**-vectors a collection of numerous scans was put together as shown in the contour plot of Fig. 4.2. To monitor the drift of the resonances versus the incident beam energy many diffraction scans with various E_i were performed. Putting this collection of measurements together allows to identify the bound state resonances much easier. In particular the curvature of a certain resonance feature allows to determine the corresponding **G**-vector which greatly simplifies the search for the associated bound state ϵ_n which fulfills Eq. (4.6).

A total of 27 ϑ-scans at incident energies ranging from 9.5 meV up to 14.5 meV was collected in order to construct the contour plot. The x-axis in Fig. 4.2 corresponds to the parallel momentum-transfer and the z-axis to the scattered intensity. The y-axis is formed by plotting the scans with various incident energies, i.e. a cut at y =constant would result in a graph such as Fig. 4.1. The plot was constructed by connecting the individual scans on a two-dimensional grid using a linear interpolation while the intensity (z-axis) is plotted on a logarithmic scale. Scattered intensities (mainly the diffraction peaks) that exceed a certain value have been cut off in order to increase the visibility of the resonance effects. The superimposed solid lines correspond to identified bound states according to the free atom approximation Eq. (4.2) with the colour coding and associated **G** vectors labelled in the same way as in Fig. 4.1. A number of lines of

Table 4.1: Experimentally determined bound state values for the laterally averaged He–Bi_2Se_3(111) interaction potential. The corresponding internal linewidths $\Delta\epsilon_n$ of the bound states (based on the experimental width of the resonances) and their lifetimes τ_n are also given.

bound state	ϵ_n [meV]	$\Delta\epsilon_n$ [meV]	τ_n [ps]
ϵ_0	5.6	0.39	1.7
ϵ_1	3.8	0.33	2.0
ϵ_2	2.3	0.30	2.2
ϵ_3	1.2	0.27	2.4
ϵ_4	0.5	0.13	4.9

high and low intensities, which we identify as selective adsorption resonances features, can be seen to run across the data set.

Following the described approach in analysing the position of these SARs, a set of five distinct eigenvalues of the laterally averaged potential is obtained (Tab. 4.1). The experimentally found bound states are then used to determine the laterally averaged potential Eq. (4.5) by minimising σ_ϵ:

$$\sigma_\epsilon \;=\; \frac{1}{N}\sqrt{\sum_{n=0}^{N-1}\left|\epsilon_n^{\mathrm{exp}} - \epsilon_n^{\mathrm{pot}}\right|^2}, \tag{4.7}$$

with N the number of bound-states included. In doing so a laterally averaged potential with the parameters $D = (6.6 \pm 0.2)\,\mathrm{meV}$ and $\kappa = (0.58 \pm 0.07)\,\mathrm{\AA}^{-1}$ is determined. The obtained potential supports a total of 7 bound states with ϵ_5 and ϵ_6 being quite close to zero i.e. to the threshold condition.

Note that not all lines of high and low intensities can be explained using SARs based on the free atom approximation. We will later see that using a three-dimensional potential will give rise to shifts compared to the free-atom approximation while considering inelastic channels can give rise to changes from maxima to minima and vice versa [118]. There are also some features present which cannot be explained by SARs even when considering a full three-dimensional potential. The features we are referring to show only a weak dependence of ΔK with respect to the incident energy E_i and thus no associated $\mathbf{G}$-vector can be found which would explain such a curvature. One of these features, indicated by the black arrow labelled with KF in Fig. 4.2, is likely to correspond to a kinematical focusing (KF) effect (see Ref. [6]).

Moreover, there appear to be features with increased intensity next to the first order diffraction peaks (see e.g. the top panel in Fig. 4.1). Additional features in diffraction scans due to spin-conserving electronic interpocket transitions have been observed for the semimetal Sb(111) [49] and the observability of similar transitions in the TI Sb_2Te_3 has been suggested by theory [119]. The observation of additional dispersion curves in Bi_2Se_3 [24] in analogy to Sb(111) suggests a similar assignment of the additional peaks in the diffraction spectra. On the other hand the surface electronic structure of both Sb(111) and Sb_2Te_3 exhibit narrow electron pockets while the situation for Bi_2Se_3 is different, with a single Dirac cone close to $\overline{\Gamma}$ that typically evolves into multiple states due to the formation of quantum well states. For the latter case it is still under debate whether both storage in the UHV chamber and exposure to intense ultraviolet light are a necessary ingredient [30, 112]. The distance of the above mentioned features in terms of ΔK with respect to the diffraction peaks would make an electronic transition, induced by the helium atom possible (via scattering from $-k$ to $+k$). However, the question remains whether this would be a spin-conserving transition e.g. between the Rashba spin-split quantum well states or whether e.g. a phonon would be required in the process to allow for a spin-flip. In any case, since we can exclude that these features are related to SARs, their origin is not relevant for a determination of the atom-surface

interaction potential. Hence the assignment and discussion about these features is beyond the scope of this work and will be treated separately [24].

Calculation of the scattering intensities

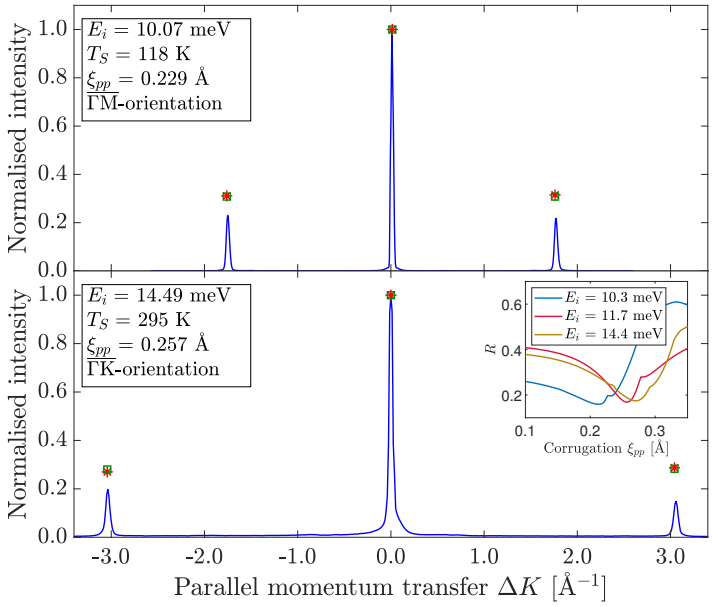

Figure 4.3: Scattered He intensities for $Bi_2Se_3(111)$ versus parallel momentum transfer. In the top (bottom) panel the elastic scan taken along the $\overline{\Gamma M}$ ($\overline{\Gamma K}$) azimuth with a sample temperature of 113 K (room temperature) and an incident energy E_i of 10.07 meV (14.49 meV) is plotted. The green squares show the area of the measured diffraction peaks while the red stars depict the calculated values. The inset shows the R-factor Eq. (4.8) for different values of the corrugation amplitude ξ_{pp} using diffraction data at three different incident energies. The minimum of R shifts to higher values of ξ_{pp} with increasing E_i.

Once a first estimate of the laterally averaged atom-surface interaction potential has been established we are going to consider the three-dimensional CMP Eq. (4.3). A comparison of quantum mechanical calculations of the scattered intensities with the experimentally found ones yields a value for the corrugation ξ_{pp}. The process of elastically scattering a He atom from a surface can be described by the time-independent Schrödinger equation together with the CMP. In the exponential term of the potential Eq. (4.3), the Fourier series expansion (see Eq. (4.14)) is used which yields a set of coupled equations for the outgoing waves. These waves are solved for in the close-coupling algorithm for a finite set of closed channels [5, 33] (see section "Appendix A: The close-coupling formalism" for details about the calculations). The corresponding coupling terms for the CMP can be found in several references [6, 31, 37].

To determine the corrugation of the sample surface the elastic peak intensities are calculated with the close-coupling algorithm and compared with the experimentally measured values of the peak areas [47]. The calculated values of the diffraction peak intensities are corrected with the Debye-Waller attenuation (Θ_D = 122 K [26, 81]) while the measured intensities are determined from the peak area using a fitted Voigt profile [37]. The reason for using the measured peak areas rather than the peak heights is the need to account for the broadening due to the energy spread of the He beam and additional broadening of the diffraction peaks caused by the angular resolution of the apparatus as well as domain size effects of the crystal surface. While the values for D and κ of the potential were held constant the corrugation ξ_{pp} was

varied between 0.01–0.6 Å with a step width of 0.001 Å. The corrugation amplitude ξ_{pp} which describes the best correspondence between measured (I_G^{exp}) and calculated diffraction intensities (I_G^{sim}) is found by minimising a measure of the deviation R,

$$R = \frac{1}{N}\sqrt{\sum_G \left(I_G^{\mathrm{exp}} - I_G^{\mathrm{sim}}\right)^2}, \tag{4.8}$$

with N being the number of experimentally measured diffraction peaks [34].

For the analysis we used a total of 35 elastic scans at various incident energies, trying to minimise Eq. (4.8) i.e. searching for the global minimum of R in dependence of ξ_{pp}. In Fig. 4.3 two of these diffraction scans along the two high-symmetry directions of $Bi_2Se_3(111)$ are shown together with the measured and calculated peak areas (symbols in the figure).

The equipotential surface describing the electronic corrugation $\xi(\mathbf{R})$ corresponds to the classical turning points of the potential, i.e. the locus of all points for which $V(\mathbf{R}, z) = E_i$ holds. Hence one may expect that with increasing beam energy the turning point shifts to distances closer to the ion cores and the scattered He atoms experience a larger corrugation amplitude ξ_{pp}. The corrugation then shows a dependence on the incident energy of the molecular beam, typically following a monotonic increase with E_i [120]. Therefore, the above described optimisation routine was repeated by taking into account several experimental spectra recorded around three specific incident energies E_i as shown in the inset of Fig. 4.3. Indeed when only diffraction scans taken at the lowest incident energy are considered in the analysis explained above, the best fit value of ξ_{pp} decreases. For medium incident energies ($E_i = 10.3\,\mathrm{meV}$) the minimum of R is found with $\xi_{pp} = 0.21\,\text{Å}$ while for higher incident energies ($E_i = 14.4\,\mathrm{meV}$) it increases to $\xi_{pp} = 0.27\,\text{Å}$. Optimising Eq. (4.8) based on all recorded diffraction spectra yields $\xi_{pp} = 0.25\,\text{Å}$ which is thus an average corrugation over the whole range of beam energies considered in this study. We will later see (section "Refinement of the interaction potential") that for the SARs, small changes in terms of ξ_{pp} are much less important compared to changes of the well depth D and the stiffness κ.

As mentioned above the free atom approximation used in the first approach (section "Determination of SARs in the elastic scans") of determining a potential neglects the corrugation of the surface meaning that the coupling term vanishes and the band structure would solely consist of parabolic bands. In considering surfaces with larger corrugations higher-order Fourier components of the surface potential have to be considered. The three-dimensional corrugated surface potential Eq. (4.3) may then give rise to substantial deviations from the free atom parabolic bands. Hence we will use again quantum mechanical calculations to accurately describe the resonance positions and in doing so refine the full three-dimensional potential in the following. We will also rerun the optimisation routine for the electronic corrugation ξ_{pp} which was at first determined using D and κ as obtained from the averaged potential, with the refined three-dimensional potential.

Refinement of the interaction potential

In addition to elastic ϑ-scans the intensity of the specular peak can be measured as a function of the incident wavevector k_i. Such a so-called drift spectrum shows again SARs at places where the kinematic condition Eq. (4.2) is fulfilled. As can be seen in Fig. 4.2 the SAR conditions "move through" the specular condition and cause the intensity to change. However, in contrast to the ϑ-scans where most SARs appear as weak features in between the diffraction peaks, a measurement while staying at the specular reflection allows for the highest signal-to-noise ratio in the experiment. The top panel in Fig. 4.4 shows such a drift scan along the $\overline{\Gamma\mathrm{K}}$ azimuth where a multitude of broad and narrow peaks and dips is visible. Hence such a measurement gives access to the detailed shape of the potential and by comparison with calculations

we will further refine the potential, looking into shifts with respect to the free atom approximation.

At the same time additional effects may complicate the analysis of SARs in a drift scan. Firstly, the incident beam intensity decreases with increasing nozzle temperature T_N since the He flow through the nozzle is proportional to $1/\sqrt{T_N}$. The effect can however be easily accounted for by correcting the scattered He intensity in the measurement with the corresponding factor (as done in the top panel of Fig. 4.4). Secondly, surface imperfections such as terraces and steps can give rise to variations of the scattered intensity: The interference of outgoing waves which are scattered from different terraces can cause periodic oscillation of the detected signal as a function of k_i [6, 34]. From the major peaks and dips of these oscillations the terrace height(s) of the investigated sample can be calculated [6, 34]. These peaks are typically much broader than the peaks and dips caused by SARs and we will attempt to analyse those in the Appendices.

Moreover, the energy distribution of the incident beam will give rise to a broadening of the natural linewidths of SARs, which can be incorporated by numerically convoluting the elastic intensity with the appropriate distribution in incident energy (see the turquoise dash-dotted curve in the bottom panel of Fig. 4.4[1]). Finally, SARs tend to become less pronounced and broader with increasing sample temperature due to a linewidth broadening and the increasing importance of inelastic effects as can be seen when comparing Fig. 4.4 with Fig. 4.9.

We turn now to the refinement of the interaction potential based on the drift scan (top panel of Fig. 4.4) which shows the measured specular intensity as a function of the incident wavevector k_i. The sample was aligned along the $\overline{\Gamma\mathrm{K}}$ azimuth and held at a sample temperature of 113 K while changing the nozzle temperature from 44 to 100 K. The coloured lines display the SAR positions according to the free atom approximation using the optimised surface potential. The numbers next to the lines denote the corresponding reciprocal lattice vectors following the same nomenclature as for Fig. 4.1. In cases where several **G**-vectors lead to the same solution of the kinematic equation, the Miller indices of only one **G**-vector are given. In addition, the vertical dashed lines correspond to the threshold energies of the surface potential. In principle, threshold resonances can also give rise to intensity variations which have been predicted to be experimentally detectable for scattering of atoms from highly corrugated surfaces [33, 121]. On the other hand, threshold resonances have only been observed experimentally for scattering He from a ruled grating upon grazing incidence [122].

The measured drift spectrum can be simulated using calculations based on the elastic close-coupling formalism. The simulated spectra can then be compared to the SAR positions in the experimental data and in doing so the surface potential can be further refined. For these calculations the corrugation values from above were used while the values of D and κ were varied in the neighbourhood of the first estimated values. After the potential parameters D and κ which describe the closest agreement with the measurements have been found, the corrugation ξ_{pp} is further refined by minimising Eq. (4.8). In the bottom panel of Fig. 4.4 the result of the simulation using the close-coupling formalism is plotted which has further been multiplied with the corresponding Debye-Waller factor (see section "Appendix A: The close-coupling formalism" for further details about the calculations).

Note that due to the above described additional effects it is not possible to resemble the actual shape of the whole measured drift spectrum using the elastic close-coupling simulation since at finite temperature the linewidth and the shape of the SARs will be influenced by inelastic channels while at the same time the oscillations caused by terraces are superimposed onto the experimental spectrum. From a theoretical point of view, these effects have been mainly considered in the limit of low corrugated surfaces [35, 123, 124] but it is well known that inelastic events are expected to account for the attenuation of the line shapes

[1] In reality the broadening changes with E_i but the convolution with a single Gaussian presents a simple illustration of the general effect.

as observed in the experiment and can even turn maxima into minima [118, 123]. In the elastic theory of resonant scattering it has been shown that the occurrence of minima, maxima and mixed extrema can be explained and predicted by establishing some general rules. However, in many cases their applicability is limited since these were derived for weak coupling conditions and hard model potentials [35]. Thus we will mainly concentrate our analysis on the position of the SARs in terms of k_i as described below. Despite the complications caused by linewidth broadening and the additional oscillations caused by the terraces, most peaks and dips of the measured data can be identified in the simulated drift scan. The position of the SARs based on the free atom approximation, denoted by the coloured lines, are shifted with respect to the peaks of the quantum mechanical calculations using the full three-dimensional potential. Generally resonances with higher corresponding **G**-vectors tend to show a larger shift compared to those with lower indices (see section "Appendix B: Close-coupled calculations of the drift scan" for a set of simulated curves showing how the SARs change upon variation of D, κ and ξ_{pp}). However, it is hard to assign each peak in the calculation to the corresponding resonance condition of the free atom approximation.

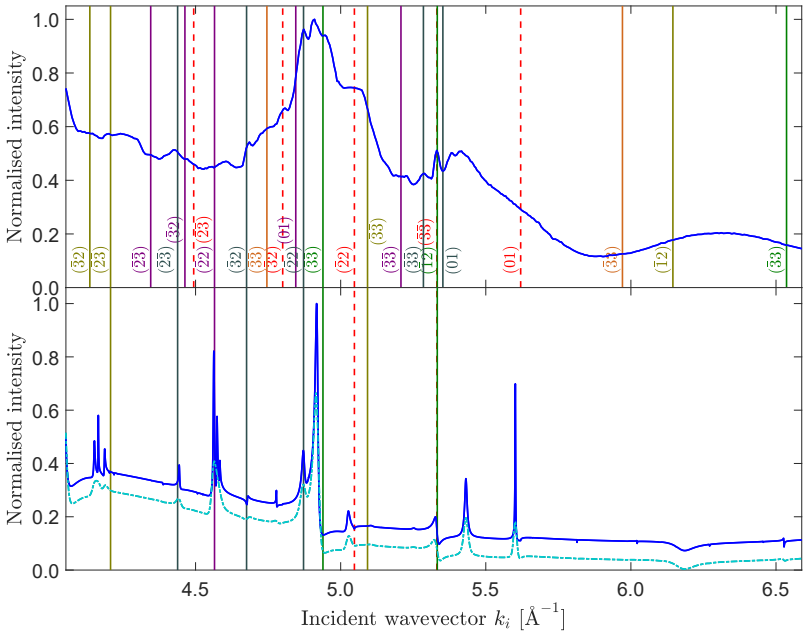

Figure 4.4: Normalised intensity of the specular peak in dependence of the incident wavevector k_i. Top: Measured drift spectrum along $\overline{\Gamma\mathrm{K}}$ with a sample temperature of 113 K and corrected for the He flux through the nozzle. The vertical lines show the predicted positions of the SARs using the free atom approximation. The colours symbolise the different bound state energies (same nomenclature as used in Fig. 4.1), with the dashed lines illustrating the threshold energy. The number next to the lines corresponds to the specific interacting **G**-vector. Bottom: Simulated drift spectrum using elastic close-coupled calculations with the optimised three-dimensional potential after multiplication with the corresponding Debye-Waller factor. A few vertical lines from the top panel have been extended as a guide to the eye. The turquoise dash-dotted curve illustrates the experimental broadening due to a convolution of the energy distribution in the incident beam with the SARs.

Instead of defining a global χ^2 parameter for the goodness of fit that would not distinguish between different aspects, we will concentrate on optimising the position of a number of specific features. Due to the above described broadening effects and superimposed oscillations from the terraces it is impossible to define a simple parameter that adequately describes the overall agreement between experiment and

simulation. An approach that considers a global χ^2 parameter will be highly sensitive to unimportant aspects such as the energy broadening of the incident beam or the described oscillations due to the terraces which modulate the intensities. Hence we concentrate on optimising the position of a number of specific "target" features, which can be identified directly in the experimental measurement and which are then checked qualitatively to give an improvement over the entire data set. Target features should be representative of the entire potential, i.e being associated with different **G**-vectors and bound states. Furthermore, for practical purposes we choose features that can be unambiguously identified, clearly above the background and preferably with no other resonances close enough to cause confusion with a different SAR channel or an intersection with another feature. Finally SARs leading to peaks are generally preferred to those leading to dips [96]. We concentrate on testing the positions k_i of the SARs in the simulated data compared to the peak positions in the experimental spectrum:

$$R_{\mathrm{p}}^2 = \frac{1}{N^2} \sum_{i=1}^{N} \left(\frac{k_i^{\mathrm{sim}} - k_i^{\mathrm{exp}}}{\sigma_i} \right)^2 \tag{4.9}$$

where k_i^{exp} are the experimental data values with uncertainties σ_i ($\sigma_i \approx 0.02\,\text{Å}^{-1}$) and k_i^{sim} are the calculated peak positions. Fig. 4.5 shows the effect on R_{p}^2 if the potential well depth D and stiffness κ are varied around the optimised parameters. The whole set of simulated drift spectra for this purpose can be found in the section "Appendix B: Close-coupled calculations of the drift scan". Note that the effect of varying ξ_{pp} (Fig. 4.8) on the resonance positions is rather small, with the main effect being changes in the shape and amplitude of the resonances. Thus ξ_{pp} is better determined in a comparison with the diffraction peak intensities and we concentrate on a refinement of D and κ based on the position of the SARs in the drift scan. Fig. 4.5 clearly illustrates that the final optimised values of D and κ correspond to a minimum in terms of R_{p}^2.

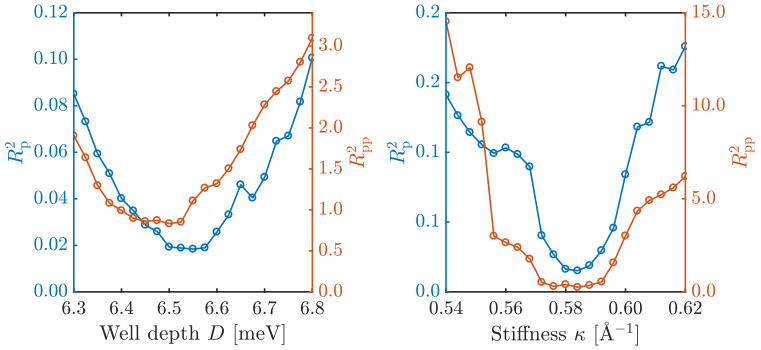

Figure 4.5: The effect of varying the potential well depth D and stiffness κ around the optimised potential parameters. The left panel shows a measure of the agreement between the simulations and the experimental data while D is varied using Eq. (4.9) on the left ordinate and Eq. (4.10) on the right ordinate, respectively. The right panel shows the same reliability factors, varying now κ while D is held constant.

Another possibility for a measure of the agreement between simulation and experiment is to try and adopt an R-factor in analogy to what has been used in LEED in experiments. According to Pendry [125] a good R-factor for comparison with calculated LEED experiments should be sensitive to the peak position. It should not be sensitive to the absolute intensities but take into account the relative intensities of features that are close in energy. Based on those criteria an R factor for SARs can be defined by considering a

measure of the curvature i.e. the second derivative of the intensity I''_{exp} in the drift scan according to:

$$R^2_{\mathrm{pp}} = \frac{1}{\int \left(I''_{\mathrm{exp}}\right)^2 \mathrm{d}k} \int \left(I''_{\mathrm{exp}} - c \cdot I''_{\mathrm{sim}}\right)^2 \mathrm{d}k \tag{4.10}$$

where the scaling constant $c = \int I_{\mathrm{exp}} \mathrm{d}k / \int I_{\mathrm{sim}} \mathrm{d}k$ is used to normalise the experimental and simulated curves with respect to each other [125, 126]. Unfortunately, the number of additional effects in the experimental spectrum makes such an approach quite difficult. We can restrict the approach to certain regions in the calculated and simulated spectra, e.g. considering the region between $k_i = 5.1\,\text{Å}^{-1}$ and $k_i = 5.4\,\text{Å}^{-1}$. We see from Fig. 4.5 that the overall trend is the same compared to using R_{p} as a measure, though the latter seems to be more robust in the present case.

Following this optimisation process, the parameters of the final refined three-dimensional atom-surface interaction potential are found as:

$$D = (6.54 \pm 0.05)\,\text{meV}$$
$$\kappa = (0.58 \pm 0.02)\,\text{Å}^{-1}.$$

Compared to the results from 4.2, the well depth D decreased while the stiffness κ showed only a subtle change. By using this optimisation process we can define a measure for the agreement between the close-coupled calculations and the experiment. With respect to the first approach based on the free-atom approximation the uncertainties of all values are significantly reduced.

In comparison to previously studied systems, the value of the well depth D is between those found for Bi_2Te_3(111) (6.22 meV) [115] and Bi(111) (7.9 meV) [37] while the stiffness κ of the He–Bi_2Se_3(111) potential is significantly smaller than for Bi_2Te_3(111) and for the Bi(111) single crystal though larger compared to Sb(111) [31].

Because Bi_2Se_3 has a smaller vdW gap than Bi_2Te_3 and Sb_2Te_3 [111, 112, 127], a different interaction of the outermost layer in the weak vdW regime might be expected and indeed this is confirmed by the determined potential in terms of the different stiffness κ. Due to the polarisability of both Bi and Se one would expect a "soft" potential with a significant long-range attractive part. On the other hand the determined potential parameters indicate that the potential is actually "stiffer" than the typical potential of a simple flat metallic surface. Detailed simulations will be required to resolve the importance of the above mentioned effects and the presented data may provide a benchmark in order to test challenging vdW approaches in DFT.

Finally, revisiting the calculation of the diffraction peak intensities with the refined potential parameters yields a peak-to-peak corrugation

$$\xi_{pp} = (0.26 \pm 0.01)\,\text{Å},$$

for an incident beam energy $E_i = 11.7\,\text{meV}$. The average over all beam energies considered in this study corresponds to a surface electronic peak-to-peak corrugation of $(5.8 \pm 0.2)\,\%$ of the surface lattice constant. The value is similar to the semimetal Bi(111)(5 %) [37] while being smaller than the reported 9.6 % for Bi_2Te_3 [115].

Since the spin-orbit coupling in Bi_2Se_3 is stronger than in Bi_2Te_3 giving rise to a different electronic structure of the topological surface states [88, 128] this may also cause a different electronic surface corrugation though it is of course difficult to make any connections between the localised electronic bands in terms of k-space and the "global" surface electronic corrugation. At the same time the work functions of Bi_2Se_3 and Bi_2Te_3 are quite similar [47, 129] and hence one might not expect large differences in terms of the surface electronic corrugation. Nevertheless, we can certainly conclude that the surface electronic

corrugation of both Bi_2Se_3 and Bi_2Te_3 is of the same order of magnitude and the charge smoothing due to the Smoluchowski effect is definitely less pronounced for both TIs than compared to the observations of flat metal surfaces [34].

The linewidth and lifetime of SARs

The angular broadening of SARs in experimental measurements is related to the lifetime of the corresponding bound state, i.e. the time that the He atom spends in the bound state before it leaves the surface. The experimentally determined (external) width has to be corrected for resolution aspects of the apparatus in order to determine the internal or natural linewidth of the bound state [33, 130]. The external full width at half maximum (FWHM) was determined by fitting the SAR features in several angular diffraction scans with a Gaussian function. The external width $\Delta\vartheta_{total}$ is corrected for the resolution aspects based on the convolution of two Gaussian distributions, yielding an internal angular width $(\Delta\vartheta_{res})^2 = (\Delta\vartheta_{total})^2 - (\Delta\vartheta_{app})^2$. $\Delta\vartheta_{app}$ accounts for the angular resolution of the apparatus as well as the energy spread in the beam and was obtained from the FWHM of the associated diffraction channel. The natural linewidth $\Delta\epsilon_n$ of the bound state in terms of energy is then given via [130]:

$$\Delta\epsilon_n = \left|\frac{\partial\epsilon}{\partial\vartheta_i}\right| \Delta\vartheta_i \quad \text{with} \quad \left|\frac{\partial\epsilon}{\partial\vartheta_i}\right| = \frac{\hbar^2}{m} k_i \cos\vartheta_i (k_i \sin\vartheta_i + G_{\parallel}) \,, \tag{4.11}$$

where $G_{\parallel}$ is the parallel component of the **G**-vector associated with the resonance. Finally, the lifetime τ of the bound states can be established from the uncertainty principle using $\tau_n = \hbar/\Delta\epsilon_n$ [33].

The natural linewidths and corresponding lifetimes of all bound states are listed in Tab. 4.1. The lifetimes increase with increasing quantum number n of the bound state. The trend is expected since bound states with a higher n are further away from the surface and thus experience less of the surface corrugation, decreasing also the probability of scattering events that would cause the He atom to leave the surface.

In general, various factors will affect and limit the lifetime of a bound state. For elastic scattering the lifetime is limited by the probability of being scattered out of the bound state channel which relates to the form and amplitude of the lateral corrugation in the atom-surface potential. Considering inelastic processes, the natural lifetime will be further reduced by factors such as defect or phonon scattering, with the latter becoming more important with increasing temperature [33, 101].

Due to the required high experimental resolution, information about the linewidth and lifetime of SARs is limited to a very small number of systems [31, 101, 130, 131]. Direct experimental information is only available for the He–LiF(001) system [130] and the He–Sb(111) system [31]. The internal linewidths of He–LiF(001) system are comparable to those found for He–Bi_2Se_3 in Tab. 4.1. Based on elastic scattering events and the similarity of the atom-surface interaction potentials (similar depth though larger corrugation in the case of He–LiF(001)) one would expect similar linewidths in both cases and indeed this is confirmed by the measurements. On the one hand, with increasing surface temperature (room temperature in Ref. [130] compared to 113 K in our study) inelastic events may become more important, on the other hand the higher Debye temperature of LiF compared to Bi_2Se_3 suggests that phonon scattering will again be similar when comparing both studies.

The influence of different atom-surface interaction potentials on the linewidth has also been subject to previous studies. As noted by Tuddenham *et al.* [101] based on close-coupled calculations, a Morse potential with the same corrugation as a corresponding reference potential gives features whose linewidth is similar to those seen in the experiment. Hence we hope that the experimental determination of the linewidths presented in this study will initiate further work in this direction and e.g., in comparison with

inelastic close-coupled calculations, eventually allow to rule out whether elastic or inelastic scattering channels are mainly responsible for the lifetime of bound states.

Summary and Conclusion

In summary, we have determined an atom-surface interaction potential for the He–Bi_2Se_3(111) system by analysing selective adsorption resonances in helium atom scattering spectra. For a first approximation we start with the free-atom approximation and a laterally averaged atom-surface interaction potential which is then further improved and refined based on close-coupled calculations in order to obtain an accurate three-dimensional atom-surface interaction potential. The free atom approximation cannot provide information about the shape of the resonances and by comparison with close-coupled calculations we are able to obtain the complete experimental band structure of atoms in the corrugated surface potential. Following a systematic analysis, the He–Bi_2Se_3(111) potential is best represented by a corrugated Morse potential which exhibits a well depth $D = (6.54 \pm 0.05)\,\mathrm{meV}$ and a stiffness $\kappa = (0.58 \pm 0.02)\,\mathrm{\AA}^{-1}$. The surface electronic corrugation varies slightly depending on the incident beam energy with an average of $(5.8 \pm 0.2)\%$ of the lattice constant.

Inelastic processes and phonon mediated resonances have been proven to play important roles, and a precise atom-surface interaction potential as determined in this study is a necessary ingredient to investigate effects such as the temperature dependence and linewidth of selective adsorption resonances. From the angular width of selective adsorption resonances in the scattering spectra we are able to obtain the natural linewidth of the resonances and an estimate for the lifetime of the bound states. Moreover, since a meV He beam is scattered in the low density region dominated by the tails of Fermi level surface states, studying selective adsorption resonances provides access to the interaction of TI surfaces within the weak adsorption regime. Hence we hope that the present data will encourage future *ab initio* studies to test the ability of vdW corrections on the current system.

As a side-note, in the Appendices we use intensity oscillations due to the interference of the He beam being scattered from different terraces, to analyse the step heights of the cleaved crystal surface. The analysis confirms the existence of steps with a quintuple layer height with an indication that sub-quintuple layer steps may exist as well. Despite the existence of terraces, the angular broadening in the diffraction spectra speaks for the high quality of the cleaved sample with domain sizes larger than 1000 Å.

Acknowledgement

We would like to thank G. Benedek for many helpful discussions. The authors gratefully acknowledge support by the FWF within the projects J3479-N20 and P29641-N36 as well as financial support by the Aarhus University Research Foundation, VILLUM FONDEN via the Centre of Excellence for Dirac Materials (Grant No. 11744) and the SPP1666 of the DFG (Grant No. HO 5150/1-2). M. B. acknowledges financial support from the Center of Materials Crystallography (CMC) and the Danish National Research Foundation (DNRF93).

Appendices

Appendix A: The close-coupling formalism

Considering the periodicity of the surface lattice, both the surface potential $V(\mathbf{r})$ and the wave function $\psi(\mathbf{r})$ can be written as a Fourier series:

$$\begin{aligned} V(\mathbf{r}) &= \sum_{\mathbf{G}} V_{\mathbf{G}}(z)\exp(\mathbb{i}\mathbf{G}\cdot\mathbf{R}) \\ \psi(\mathbf{r}) &= \sum_{\mathbf{G}} \psi_{\mathbf{G}}(z)\exp(\mathbb{i}(\mathbf{G}+\mathbf{K}_i)\cdot\mathbf{R})\,. \end{aligned} \tag{4.12}$$

Inserting the latter into the time-independent Schrödinger equation yields:

$$\left[\frac{d^2}{dz^2} + \mathbf{k}^2_{\mathbf{G},z} - V_0(z)\right]\psi_{\mathbf{G}}(z) = \sum_{\mathbf{G}'\neq\mathbf{G}} V_{\mathbf{G}-\mathbf{G}'}(z)\psi_{\mathbf{G}'}(z) \tag{4.13}$$

for the z-direction, where $\mathbf{k}^2_{\mathbf{G},z}$ is the z-component of the particles kinetic energy after the surface interaction and V_0 the laterally averaged interaction potential.

Eq. (4.13) is a set of coupled equations with $V_{\mathbf{G}-\mathbf{G}'}$ being the coupling terms, which can be written in a matrix-form, since the close-coupling method treats each $\psi_{\mathbf{G}}$ as a scattering channel. Finally, the matrix equation is solved by using a Numerov algorithm [6, 33].

The two-parameter Fourier ansatz used for the corrugation function $\xi(\mathbf{R})$ is:

$$\begin{aligned} \xi(x,y) = \xi_0 \Bigg\{ &\cos\left[\frac{2\pi}{a}\left(x - \frac{y}{\sqrt{3}}\right)\right] + \cos\left[\frac{2\pi}{a}\left(x + \frac{y}{\sqrt{3}}\right)\right] \\ &+ \cos\left[\frac{2\pi}{a}\frac{2y}{\sqrt{3}}\right]\Bigg\} + h.o. \end{aligned} \tag{4.14}$$

where x and y depict the coordinates and ξ_0 determines the corrugation amplitude. The value of the corrugation is determined by the peak-to-peak corrugation ξ_{pp} of Eq. (4.14).

For all close-coupled calculations presented in this work all open channels were considered in the simulations. The number of closed channels was adjusted until the error was determined to be $< 10^{-4}$. In the drift simulations a value of less than 100 closed channels was sufficient while for the calculation of the diffraction intensities a minimum of 150 channels was required for the result to converge. For the drift spectrum calculated in Fig. 4.3, 100 closed channels were used and the integration boundaries in terms of z were set to [-9, 20] Å with an energy resolution of dE = 0.001 meV.

As mentioned in the main part of the manuscript, the value of the corrugation ξ_{pp} exhibits a feeble dependence on the incident energy E_i. Therefore the best fit value of ξ_{pp} was determined for several sets of diffraction spectra with each set taken at a different incident energy. In a first approximation we assume that the corrugation increases linearly within the considered energy region, according to:

$$\xi_{pp}[\text{Å}] = 0.013 \cdot E_i[\text{meV}] + 0.092\,, \tag{4.15}$$

which is further used for the CC-calculations of the drift spectra in the section "Appendix B: Close-coupled calculations of the drift scan".

Appendix B: Close-coupled calculations of the drift scan

Fig. 4.6-Fig. 4.8 show the complete sets of close-coupled calculations used for comparison with the experimental drift scan. Fig. 4.6 and Fig. 4.7 have been used in the section "Refinement of the interaction potential" for the refinement of the potential and the calculation of the reliability factors. For these simulations, the corrugation magnitude was varied according to the incident energy, following Eq. (4.15).

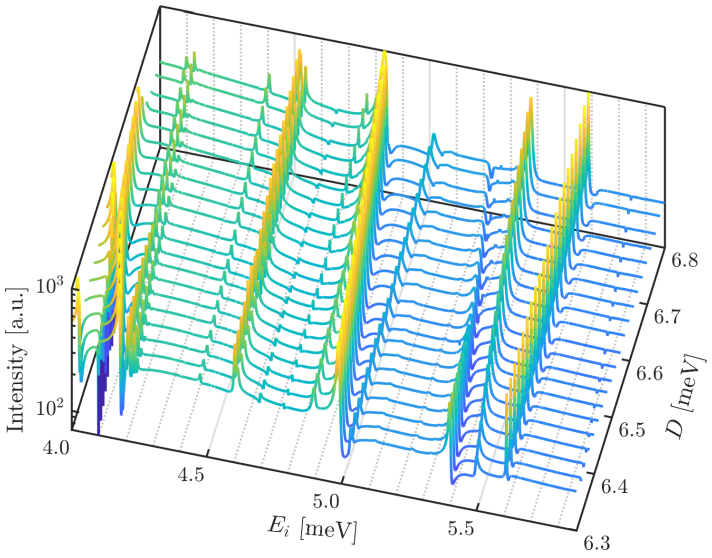

Figure 4.6: Simulation of the drift scan using elastic close-coupled calculations for various values of D with $\kappa = 0.58\,\text{Å}^{-1}$ and ξ_{pp} according to Eq. (4.15).

In Fig. 4.6 the well depth D is varied within a range of 6.3 to 6.8 meV which clearly shows different shifts of the individual features in the drift spectrum depending on D. With increasing well depth the peaks wander towards lower incident energies E_i. In addition it becomes clear that certain features shift at various "speeds" upon varying the well depth. For instance the position of the sharp feature at $E_i \approx 5.6$ meV barely changes along the calculated range of D. Therefore this feature might be caused by a threshold condition. In general peaks originating from lower index **G**-vectors show a slower shift, as already mentioned in the main part of the manuscript.

In the next step the well depth was held constant while the stiffness κ was varied in a range from 0.54 to 0.62 Å^{-1}. The peaks in Fig. 4.7 tend to shift to higher incident energies with increasing stiffness. The most prominent feature changes its position rapidly from 4.7 to 5.1 meV over the whole calculated range of κ.

Finally, the corrugation ξ_{pp} was varied from 0.14 to 0.32 Å. From Fig. 4.8 it becomes clear that the influence of the corrugation within the considered range of ξ_{pp} is much more subtle in terms of the position of the peaks. However, ξ_{pp} significantly changes the shape and intensity of the individual features. For example, the peak at $E_i \approx 4.9$ meV changes its shape from a minimum to a pronounced maximum when increasing ξ_{pp}. In addition some features might not even be visible at lower values of the corrugation, changing to sharp maxima at higher values of ξ_{pp}.

Appendix C: Detailed analysis of the in-phase/anti-phase conditions due to steps

If the specular intensity is dominated by interference of waves scattered from different terraces, the drift spectrum can also be used to determine the terrace height(s) of the investigated sample surface [6, 34, 132].

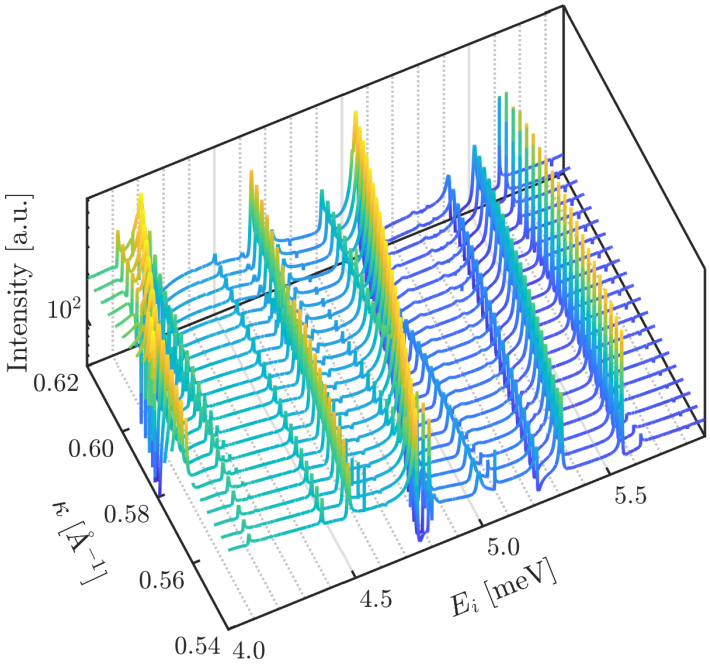

Figure 4.7: Simulation of the drift scan using elastic close-coupled calculations for various values of κ with $D = 6.54\,\text{meV}$ and ξ_{pp} according to Eq. (4.15).

When changing the incident wavevector k_i, the specular intensity shows oscillations due to constructive (in-phase) and destructive (antiphase) interference of the outgoing waves. The phase difference φ upon scattering from two terraces separated by a step height h is given by [6, 132]

$$\varphi = 2hk_i \cos\vartheta_i = 2hk_{iz} = h\Delta k_z \tag{4.16}$$

where Δk_z is the momentum transfer perpendicular to the surface. In Fig. 4.9 the specular intensity is plotted as a function of the incident wavevector k_i for both high symmetry directions $\overline{\Gamma M}$ and $\overline{\Gamma K}$ with the sample held at room temperature. The measured intensity has again been corrected for the decreasing He flux with increasing nozzle temperature T_N [6]. The variation of the intensity can then be described by a simple model which overlaps the plane waves that are reflected of the different terraces from the sample. The intensity as a function of Δk_z is described as:

$$I(\Delta k_z) = I_0 \mathrm{e}^{-2W} \left| 1 + \sum_{j=0}^{N} a_j e^{-\mathrm{i}h_j \Delta k_z} \right|^2 \tag{4.17}$$

for N different step heights h_j with a probability a_j. I_0 is the intensity of an ideal surface without any steps and the exponential prefactor accounts for the Debye-Waller attenuation with W being the Debye-Waller factor [6, 132]. The latter considers that the Debye-Waller factor changes with increasing perpendicular incident momentum k_{iz} [6] during a drift scan.

The individual QLs in Bi_2Se_3 as well as other layered TIs are bound to each other through weak vdW forces which gives easy access to the (111) surface by cleavage [112, 115]. Hence steps which occur upon cleaving are expected to correspond to the QL distance along the c-axis of the conventional hexagonal unit cell (9.6 Å at room temperature [114]). Indeed the main oscillation in Fig. 4.9 suggests a step height of 9.9 Å (red dash-dotted curve according to Fig. 4.9) in good agreement with the separation between the Se termination layers of a QL [133]. The small deviation from the theoretical QL distance may be due

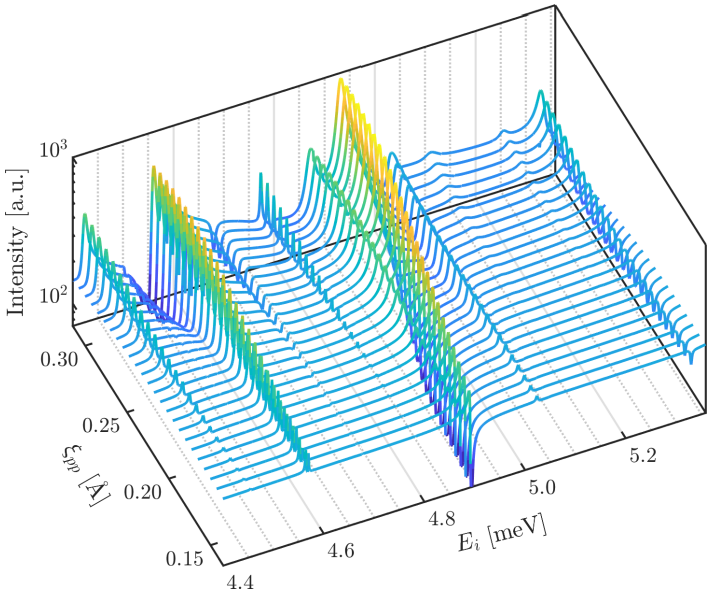

Figure 4.8: Simulation of the drift scan using elastic close-coupled calculations for various values of ξ_{pp} with $D = 6.54\,\text{meV}$ and $\kappa = 0.58\,\text{Å}^{-1}$.

to electron spill-out, i.e. the fact that the electronic step height observed in HAS does not necessarily correspond to the crystallographic one as measured e.g. with LEED [134]. On the other hand it appears from Fig. 4.9 that an additional oscillation, giving rise to a further modulation of the intensities from the QL steps and according to a smaller step height, is present as well. Sub-QL steps have previously been observed during thin film growth of TIs [135, 136] while different terminations have also been found for cleaved single-crystals depending on the sample treatment [137, 138]. Inclusion of a second step-height ($h_2 = 3.6\,\text{Å}$, dashed curves in Fig. 4.9) seems to improve the agreement with the experimental data which suggests that terraces with the internal Se layer exist in some cases [138]. Here, considering a different number of steps along the $\overline{\Gamma\text{K}}$ and $\overline{\Gamma\text{M}}$ gives a better agreement with the experimental data, which would imply that the orientation of the terraces is not completely random and depends on the crystal orientation. The fact that Bi_2Se_3 has a smaller vdW gap than Bi_2Te_3 and Sb_2Te_3 might explain the existence of sub-QL steps of the cleaved samples.

Note however, that the number of parameters in Eq. (4.17) and the overlapping with SARs makes an exact determination of the step height difficult. While some of the peaks appear in the $\overline{\Gamma\text{K}}$ as well as in the $\overline{\Gamma\text{M}}$ direction, the peak at around $k_i = 4.9\,\text{Å}^{-1}$ can only be found in the $\overline{\Gamma\text{K}}$ direction. It should also be considered that SARs with lower interacting **G**-vector "move" slower across the specular peak which may lead to peaks that look like oscillations caused by the steps. From the above analysis it is clear that oscillations due the QL spacing are present while there is also a hint towards sub-QL steps. At the same time we would like to stress that during such a drift scan HAS is particularly sensitive to single defects and hence the appearance of sub-QL steps is likely to be negligible. In fact as mentioned in the section "Experimental Details" the small width of the specular and the diffraction peaks in the elastic scans suggests a very high quality of the cleaved crystals.

Finally, as already mentioned above, the measurements at room temperature (Fig. 4.4) show quite nicely upon comparison with the low temperature measurements (Fig. 4.9), that the resonance effects are more pronounced for the latter. At higher temperatures the natural linewidth of the SARs increases which makes it harder to distinguish them from noise. At lower temperature mainly elastic scattering channels need to be considered, while at elevated temperatures the inelastic channels become important

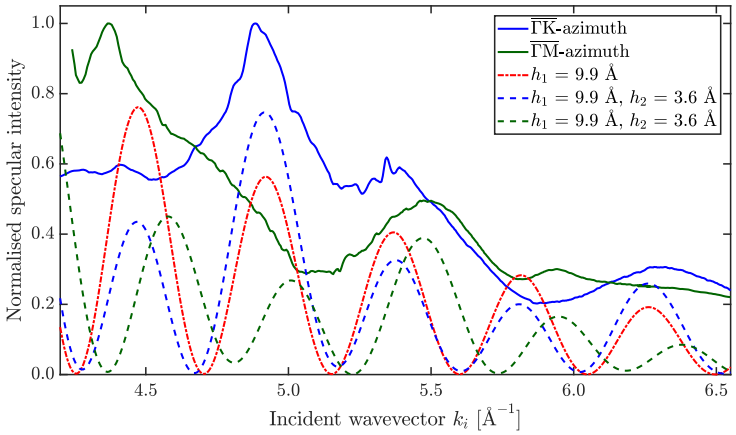

Figure 4.9: Determination of the step heights from the oscillations present in the drift scan. The solid lines show the measured specular intensity as a function of the incident wavevector k_i measured at room temperature with the crystal aligned along the $\overline{\Gamma M}$ and $\overline{\Gamma K}$ azimuth, respectively. The red dash-dotted line shows intensity oscillations (Eq. (4.17)) which are expected in the presence of terraces separated by steps with a quintuple layer height. The dashed lines show oscillations for quintuple and sub-quintuple layer steps, with a different number of sub-quintuple layer steps for $\overline{\Gamma M}$ and $\overline{\Gamma K}$.

as well, making an inclusion of these channels in the quantum-mechanical calculations necessary.

4.3 Atom-Surface van der Waals Potentials of Topological Insulators and Semimetals from Scattering Measurements

This section consists of the following published publication:

Atom-Surface van der Waals Potentials of Topological Insulators and Semimetals from Scattering Measurements

A. Tamtögl*, A. Ruckhofer, D. Campi, W. Allison, and W. E. Ernst

Physical Chemistry Chemical Physics **23**, 7637-7652, 2021
https://doi.org/10.1039/D0CP05388K

* corresponding author

	contributions
funding	W.E. Ernst, A. Tamtögl
experimental design	A. Tamtögl, A. Ruckhofer
data acquisition	A. Ruckhofer, A. Tamtögl
data analysis	A. Ruckhofer, A. Tamtögl
DFT simulations	D. Campi
interpretation	A. Ruckhofer, A. Tamtögl, W. Allison
publication writing	A. Tamtögl, A. Ruckhofer
discussion and editing	all authors

Abstract

The phenomenology of resonant scattering has been known since the earliest experiments upon scattering of atomic beams from surfaces and is a means of obtaining experimental information about the fundamentals of weak adsorption systems in the van der Waals regime. We provide an overview of the experimental approach based on new experimental data for the He–Sb_2Te_3(111) system, followed by a comparative overview and perspective of recent results for topological semimetal and insulator surfaces. Moreover, we shortly discuss the perspectives of calculating helium-surface interaction potentials from *ab initio* calculations.

Our perspective demonstrates that atom-surface scattering provides direct experimental information about the atom-surface interaction in the weak physisorption regime and can also be used to determine the lifetime and mean free path of the trapped atom. We further discuss the effects of elastic and inelastic scattering on the linewidth and lifetime of the trapped He atom with an outlook on future developments and applications.

Introduction

Since the earliest scattering experiments of atomic beams from surfaces, the phenomenology of resonant scattering and its connection to molecular adsorption at a surface has been known [139, 140]. Understanding the scattering of atoms and molecules from surfaces forms a central point of many aspects in physical chemistry, including chemical reaction at surfaces and providing the link for an atomistic understanding of heterogeneous catalysis [141–143]. Scattering experiments provide access to the atom-surface interaction potential which is the necessary prerequisite for any quantitative description and theoretical treatment of molecular adsorption [144] or surface reaction processes. Scattering approaches to chemisorption [145, 146] and the coordinates relevant to the reaction potential [141–143] rely on such treatment.

While atomic force microscopy has been used to obtain information about the forces between a single molecule and the surface [147, 148], direct experimental information for the weak physisorption regime of the atom-surface interaction potential (in the region of several meV) is only available through atom-surface scattering [18, 22, 97]. Diffraction of atomic and molecular beams is based on their wave nature with momentum and wavelength being inversely proportional via the de Broglie relation. He atoms with a wavelength of 1.4 Å exhibit an incident energy of only 10 meV [34]. As slow neutral particles, they are non-destructive with a classical turning being at about 2–3 Å above the surface. Their low energy allows to observe effects of the attractive part of the atom-surface potential onto the atomic beam in a similar energy region.

Here we present an overview of the experimental approach in obtaining atom-surface interaction potentials from He atom scattering (HAS) experiments based on the study of selective adsorption resonances (SARs), in which the helium atom briefly gets trapped on the surface. SARs in HAS provide very high accuracy information for the determination of the atom-surface interaction potential [22, 96] and we present new experimental data for the He–Sb_2Te_3(111) system and compare it with previous results for binary topological insulators and semimetals. We illustrate the principle in the context of classical HAS and Fourier-transform (FT)-HAS studies. The presented systems have certain aspects in common, with the bulk being non-metallic, while the surfaces exhibit metallic surface states and the corrugation in the repulsive part of the potential being of comparable magnitude ($\approx$ 0.2–0.6 Å) [24, 31]. Moreover, while significant theoretical effort has been devoted to understanding the lifetime of these effects [33, 131] experimental information is quite limited and we present temperature-dependent experimental data.

The atom-surface interaction potential

Fig. 4.10 shows a schematic diagram of the atom-surface scattering processes with elastic scattering and trapping. An atom of mass m arrives at the surface with an incident wavevector $\mathbf{k}_i$ and kinetic energy $E_i = \frac{\hbar^2}{2m}\mathbf{k}_i^2$ and is scattered by the electron cloud at the surface, where the atom interacts with all atoms of the semi-infinite crystal via a total potential $V(\mathbf{r})$. The momentary position of the atom $\mathbf{r} = (\mathbf{R}, z)$ is expressed in terms of coordinates in the surface plane (capital letters) and normal to it along the z-axis (likewise for the wavevector $\mathbf{k} = (\mathbf{K}, k_z)$, as illustrated in Fig. 4.10).

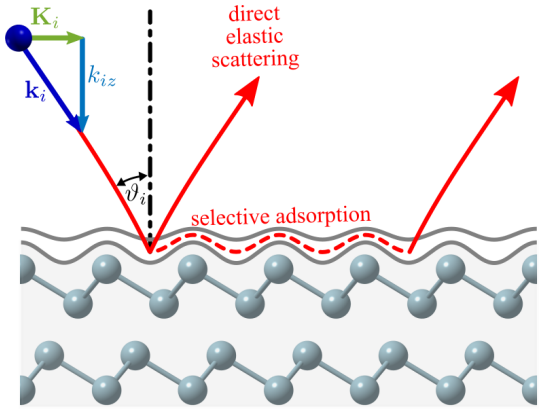

Figure 4.10: Illustration of the helium-surface scattering process. The incoming He atom can scatter (or diffract) elastically, scatter inelastically (not shown) or enter selective adsorption where it is transiently trapped in one of the energy levels of the potential well.

A precise model of He-surface scattering is rather complicated, due to the extended nature of the interaction with the surface [18, 106]. Scattering calculations require a realistic He-surface potential and a suitable calculation scheme, for which both empirical and theoretical approaches have been used to establish interaction potentials [18, 33]. The LiF(001) surface was the first surface on which He diffraction was observed and to date most of the best existing theoretical potentials for He–LiF(001), as well as for other systems, are based on summed pair potentials [18].

Conventionally the potential $V(\mathbf{r})$ is divided into a corrugated short-range repulsive wall and a less corrugated attractive well (typically 5–50 meV) for rare gas atoms. The former arises from the Pauli repulsion of the electrons of the probe atom with the electrons of the surface; the latter is due to dispersion forces resulting from the electrostatic polarisation of the atom induced by the surface charge distribution.

The equipotential surface at which the potential $V(\mathbf{R}, z)$ equals the He atom incident energy for the vertical component of motion $E_{iz} = \frac{\hbar^2}{2m}k_{iz}^2$ is given by

$$V(\mathbf{R}, z) = E_{iz} \ , \tag{4.18}$$

where the resulting surface $z = z(\mathbf{R}, E_{iz})$ defines the closest approach of the atom to the surface, i.e., the locus of the classical turning point for the given surface potential and vertical incident energy [16].

Classical reflection corresponds to the incident He atom reaching the turning point i.e. the repulsive part of the interaction potential while reflection coming from the long-range attractive part is referred to as quantum threshold reflection [122, 149]. The effect of the attractive part of the potential onto the incident He atom can be seen as an analogy to refraction for classical scattering from an isolated target. Since only the z-component is important, refraction can also be made visible in the case of fast Ne atoms, if angles close to grazing incidence are used [150].

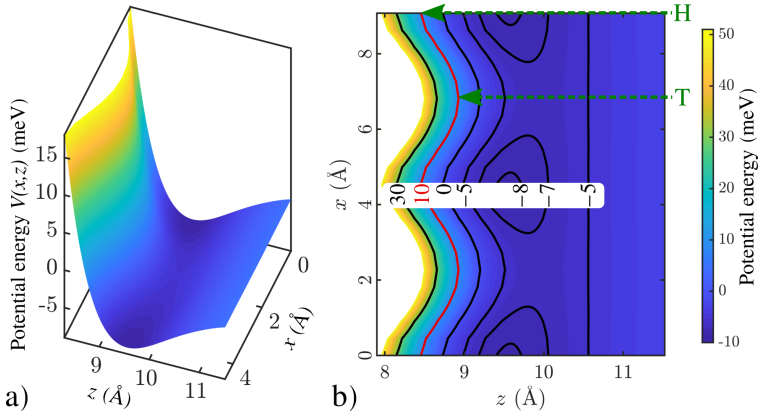

Figure 4.11: Calculated He-surface interaction potential above a Bi(111) surface. a) shows a surface plot of $V(x, z)$ while b) shows a contour plot with several equipotential lines. The potential follows the periodicity of the surface along x and has the general z-dependence shown. As illustrated in b), the classical turning point (e.g. for an energy of 10 meV as shown by the red line) depends on the lateral position x, occurring at different distances z from the surface for top (T) and hollow (H) sites, respectively.

Fig. 4.11 shows a calculated He-surface interaction potential for Bi(111) (see computational details in the Appendices). Fig. 4.11a) shows a surface plot, with the potential energy as a function of lateral distance x and distance z with respect to the surface, where the potential rises steeply already at several Ångstroms away from the top-most layer. In Fig. 4.11b) a contour plot with equipotential lines is shown, illustrating that the turning point depends (e.g. for an energy of 10 meV as shown by the red line) on the lateral position x. Since the potential follows the two-dimensional periodicity of the surface layer, it is possible to express the static potential in terms of a Fourier series representation [16], which in turn is useful for scattering calculations.

For scattering calculations, a range of accurate and approximate techniques have been established [33, 34, 151–154] and within the exact quantum mechanical methods the close-coupling (CC) method is nowadays mainly used for scattering calculations [24, 37, 115]. For the calculation of diffraction intensities alone, sometimes simple approximations for the interaction potential can be used and the simplest one is the hard corrugated surface. In the case of graphene (graphite) where the potential is steep and deep the graphene layer on the substrate may be considered to act like a hard wall. The latter is also confirmed in inelastic HAS measurements for metal-supported graphene, where only phonons from the substrate are seen via the electron spill out through the electron-phonon coupling [108]. Roughly speaking, if the distance of the classical turning point in the potential with respect to $z = 0$ is comparable to the He diameter then approximate results may be obtained with the hard corrugated wall. This is confirmed by the calculation of diffraction intensities for graphene on SiC(0001) which are fairly well reproduced using a hard-corrugated-wall model [155].

On the other hand, in the case of metallic surfaces (see Fig. 4.11) the latter should be avoided because the potential is typically both shallow and has a long range component and scattering calculations require a more realistic He-surface interaction potential. Before we come to experimental approaches based on atom-surface scattering experiments in the section "Experimental approaches based on gas-surface scattering", we will discuss *ab initio* approaches for such a potential in the section "Helium-surface interaction from *ab initio* calculations" and the characteristics of a few potential shapes in the section "The characteristics of different potentials".

Helium-surface interaction from *ab initio* calculations

Besides the use of semi-empirical potentials, which are fitted to experimental data, it is possible to generate numerical atom-surface interaction potentials from first-principle calculations. However, a precise description of the He-surface interaction still represents a considerable challenge due to the difficulties in accurately and simultaneously describing the short range repulsive part and the long range van der Waals (vdW) interactions. Various methods, with different degrees of complexity have been used over the years.

Very sophisticated protocols combining Moller-Plesset perturbation theory (MP2) with high order corrections computed from coupled-cluster CCSDT(Q) have been proven to provide a good agreement with He scattering experiments for the MgO(100) surface [103, 107]. Other works used time-dependent density functional response theory to compute the long range dispersion contributions [156] obtaining a good description of the interaction of He and Ar on Au(111) [157]. Accurate interaction energies with noble gases have also been obtained using a self-consistent exact-exchange random phase approximation (EXX/RPA) formalism [158, 159]. All these methods however, are computationally expensive and often require a careful material-dependant tailoring.

Density functional theory (DFT), on the other hand, is computationally cheap and readily applicable. As such, various flavours of DFT have been used to calculate the He adsorption energies or the HAS diffraction spectra of a broad variety of systems with mixed results [106, 160–166]. It is known that standard approximations for the exchange-correlation functional in DFT, like the local-density approximation (LDA) and the generalised-gradient approximation (GGA), neglect long-range dispersion effects since they include only local contributions to the electron correlation.

Different methods have been developed to overcome this problem from the addition of semi-empirical or *ab initio* based long-range corrective terms [167–171] to truly non-local functionals [172–174]. Such an approach has also been used for the numerical Bi(111) potential shown in Fig. 4.11, with the full computational details being given in the Appendices. In addition, new theoretical approaches include the implementation of neural networks for molecule-surface scattering [175] as well as vdW corrected semilocal density functionals to determine molecule-surface interactions on transition-metal surfaces [166].

It is generally recognised that vdW corrected functionals consistently improve the adsorption energies of molecules and noble gases both on insulating and metallic surfaces [176, 177] and can lead to a good agreement with scattering experiments [109]. On the other hand, a recent comparison between experimentally measured and theoretically predicted diffraction probabilities, shows how these functionals can give rise to large overestimations of the corrugation, i.e. despite providing good results for absorption energies the long-distance corrugation of the potential energy surface further away from the surface is overestimated [110]. These results highlight the importance of atom-surface scattering experiments as a benchmark for any *ab initio* treatment of the long range interaction and their contribution in the improvement of those.

The characteristics of different potentials

Upon scattering from a solid with a closed-shell system such as ionic crystals the static potential $V(\mathbf{R}, z)$ can be reduced to a sum of two-body interatomic potentials. However, for semiconducting and metal surfaces the interaction of the He atom with the surface is to a large extent mediated by the conduction electrons and exhibits a many-body character [16]. For example, the 9-3 potential results from pair-wise summation of the Lennard-Jones potential and describes the correct long-range behaviour but does not reproduce the correct repulsive behaviour and it has been shown that it cannot reproduce the measured SARs in the case of semimetal surfaces [31].

Instead a combination of two exponential forms for both the repulsive and attractive part, known as the Morse potential, is frequently used due to its algebraic simplicity. The three-dimensional corrugated Morse potential (CMP) as a function of the lateral position $\mathbf{R}$ on the surface and the distance z is given by [117]

$$V(\mathbf{R}, z) = D\left[\frac{1}{\upsilon_{\mathbf{0}}}\mathrm{e}^{-2\kappa[z-\xi(\mathbf{R})]} - 2\mathrm{e}^{-\kappa z}\right], \tag{4.19}$$

with the potential parameters κ for the stiffness and D for the well depth. $\xi(\mathbf{R})$ describes the periodically modulated surface and $\upsilon_{\mathbf{0}}$ is the surface average over $\mathrm{e}^{2\kappa\xi(\mathbf{R})}$. In the limit of classical reflection, $\xi(\mathbf{R})$ corresponds to the turning point defined in Eq. (4.18).

Quantum mechanical arguments suggest an exponential form for the short range Pauli repulsion which is correctly described by the Morse potential. On the other hand, Eq. (4.19) does not have the z^{-3} long range dependence which is expected by theory [16]. Here, the hybrid Morse potential can be used as an improvement of the Morse potential since it exhibits the expected asymptotic long rang behaviour [31].

An appropriate potential which considers exponential repulsion and the attractive part according to a power law is the Tang-Toennies potential [178], however, it follows from a summation over pair-potentials which can only be considered accurate for ionic crystals as described above. While the short range repulsion exerted by all surface atoms on the He atom can be considered to be only slightly larger than the two-body repulsion, the joint long range attraction of the surface largely exceeds the summation of pair potentials [16].

For the study of SARs the above mentioned potentials are often simplified to the first order Fourier coefficient leading to the lateral surface averaged potential. For surfaces which resemble a hard corrugated wall the latter provides approximate results, however, in terms of Eq. (4.19) it can be seen that such an approximation is only valid for $\kappa z << 1$, and in order to describe the complete experimental band structure of the He atom in the corrugated surface potential (section "The three-dimensional potential and quantum-mechanical scattering calculations") higher order Fourier components need to be included which are easily obtained for the CMP.

Since the three-dimensional CMP does not treat correctly the long range attraction, it is not so appropriate for quantum mechanical calculations of inelastic HAS resonances and focusing effects. Instead optical potentials have been used previously to study the effect of inelasticity on resonance scattering, e.g. on graphite(0001) [179] and for the $\mathrm{Si}(111)-(1\times1)\mathrm{H}$ surface [101]. However, in SAR studies of the latter system it was noted that a significant corrugation exists in the region of the attractive well which cannot be reproduced by such a potential. The effect is subtle as it does not manifest itself strongly in the diffraction intensities and instead causes a broadening of the resonance features [101].

Despite some limitations in using the pure exponential form for the atom-surface potential Eq. (4.19), many useful results can be obtained for conducting surfaces [16] and earlier studies have shown that this potential shape reproduces the measured bound states of semimetal and topological insulator surfaces [24, 31, 37, 115]. In particular, the CMP greatly simplifies the treatment of several steps within the CC algorithm, allowing for an analytical solution in those cases, which leads to reduced computational costs. The obtained coupling terms are then only valid for the three-dimensional CMP. Hence in order to avoid inconsistencies in the CC calculations and to provide a simple comparison with the atom-surface interaction obtain for similar systems we will restrict the following discussion to the CMP.

Considering also the challenges theorists are facing in describing the vdW interaction correctly, CC calculations in combination with the three-dimensional CMP are clearly a sensitive tool for determining the atom-surface interaction potential, at least in the case of conducting surfaces. Although some functionals have been proven to yield good results for diffraction from alkali metal surfaces [180, 181], Ne diffraction [109] and physisorption energies in He/metal systems [110], the performance for HAS from

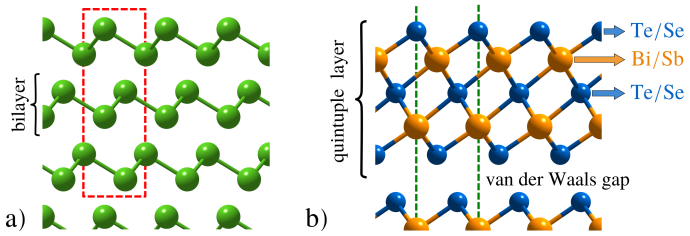

Figure 4.12: Side view of the structures. a) The semimetal surfaces Bi(111) and Sb(111) both exhibit a typical bilayer structure with the hexagonal unit cell as red dashed line. b) The binary topological insulators are composed of quintuple layers with the terminating layer being either Te or Se. The hexagonal unit cell is illustrated by the green dashed lines (which continues to the top and the bottom).

conducting surfaces is still under debate [182]. As noted by del Cueto *et al.* [182], up to now none of the available vdW functionals have been proven to yield good He diffraction probabilities, most probably due to the in section "Helium-surface interaction from *ab initio* calculations" described overestimation of the long-distance corrugation which is probed by the He atom [182].

Topological semimetals and insulators

One of the most fascinating aspects when studying surfaces is that their physical and chemical properties can be radically different from those of the corresponding bulk material. The semimetals Bi and Sb are striking examples for these differences with the surfaces being much better metals than the bulk due to the existence of electronic surface states [28, 49, 183]. There are even more peculiar surface dominated effects when it comes to topological insulators: The material class of topological insulators (TIs) has recently attracted high interest [52, 82–85, 184], due to their unique electronic structure which exhibits protected conducting surface as well as insulating bulk states [86, 87]. Most previous studies investigated the prominent binary TIs Bi_2Te_3 and Bi_2Se_3 [89, 184], while Sb_2Te_3 is discussed in fewer works [88].

Most classic semimetallic elements belong to group 15 of the periodic table, including Sb and Bi. The side view of the typical structures of these semimetals is shown in Fig. 4.12a), while Fig. 4.12b) shows the structure of the binary TIs. The semimetals Bi and Sb show a typical bilayer structure, with intralayer bonding being mostly covalent, whereas the layers are held together by weaker interactions predominantly of vdW character. The binary TIs such as Sb_2Te_3 are composed of layered hexagonal structures (Fig. 4.12b)) where quintuple layers (QLs) are weakly bound to each other through weak vdW forces which allow for an easy cleaving of the samples. Consequently, crystal samples of binary TIs are cleaved *in situ* using a load-lock system [113] directly before putting those into the scattering chamber, while the semimetals Bi and Sb are usually prepared by several Ar^+-sputtering and annealing cycles. In the case of binary TIs, recent research has also shown the importance of an accurate theoretical description of their layered structure, where the inclusion of vdW corrections is essential for surface dynamics as well as diffusion [111, 185].

Hence experimental access to the vdW interaction on these surfaces is not only interesting from a fundamental point of view. For example, vertical stacking of different layered materials held together by vdW interactions is emerging as a new scientific approach to achieve desired properties by design. Recent studies have shown that the vdW interactions affect electronic and phonon properties of such structures with consequences for transport and optical applications [115, 186]. In addition, an accurate description of the atom-surface interaction helps to understand the adsorption of atoms and molecules in the physisorption regime [93–95] including modifications of the surface electronic structure via adsorption [26, 59, 90, 91] and effects relevant for heterogeneous catalysis or sensing applications [61, 92].

Experimental approaches based on gas-surface scattering

Experimental studies of the atom-surface interaction potential based on the mechanism of SARs, provide very high accuracy information for the determination of the atom-surface interaction potential [22, 96]. Earlier studies of SARs mainly investigated salts with the NaCl structure [22, 34, 96–100], semiconductors [101] and more recently layered materials such as TIs [24, 115, 116]. In order to determine an accurate three-dimensional atom-surface interaction potential the analysis of SARs has to be combined with quantum mechanical scattering calculations [37, 107, 108] as outlined below.

The process of a SAR involves trapping of an impinging He atom on the surface until it scatters with a **G**-vector or a phonon to leave it again [22, 96]. A simple semi-classical view of the process is illustrated in Fig. 4.10: Scattering at the resonance condition corresponds to a double scattering event where one part of the incident wave is scattered directly into an open channel, while a fraction undergoes diffractive scattering into an evanescent, resonant state that propagates parallel to the surface. After a short time, a second process scatters the wave into an open channel with subsequent interference between the two scattered components leading to modulations in the outgoing intensity, which can be observed in an experiment.

An SAR process occurs when the outgoing wavevector component perpendicular to the surface $k_{f,z}^2$ becomes negative which is a kinematically disallowed state. This appears when the difference between the incident energy and the kinetic energy of the atom moving parallel to the surface matches the binding energy ϵ_n of an adsorbed atom [97]:

$$E_i = \frac{\hbar^2}{2m}\mathbf{k}_i^2 = \frac{\hbar^2}{2m}\big(\mathbf{K}_i + \mathbf{G}\big)^2 + \epsilon_n\big(\mathbf{K}_i, \mathbf{G}\big)\,, \tag{4.20}$$

as illustrated in Fig. 4.13. The bound state ϵ_n is here defined as a function of the parallel momentum $\mathbf{K}_i$ and the interacting G-vector **G**. Hence studying the SAR processes on the surface leads to the bound state energies which in succession allows to determine the atom-surface interaction potential.

This semi-classical picture provides insights into the origin of the experimental intensity variations, however, the process can only be fully understood from a quantum standpoint [33]. The two key properties in resonant scattering processes are the kinematic condition giving rise to a particular resonance, and the lineshape of the resonance. The former provides information on the energy of the resonant state and thus in the weak corrugation limit, the z-dependence of the laterally averaged potential $V_{\mathbf{0}}(z)$ as described in the section "The laterally averaged potential from diffraction scans". The lineshape, on the other hand, provides information about the corrugation (see sections "Surface electronic corrugation and "The three-dimensional potential and quantum-mechanical scattering calculations)" which taken together offers one of the most precise experiments considering physisorption potentials [144]. In the free atom approximation, once the He atom has entered a bound state, it can move freely parallel to the surface as illustrated in Fig. 4.13. It corresponds to a simplification of Eq. (4.20), neglecting the corrugation of the potential: ϵ_n is then the n^{th} bound state of the laterally averaged potential, $V_{\mathbf{0}}(z)$ (ϵ_n in Eq. (4.20) becomes independent of $\mathbf{K}_i$ and **G**). Such an approximation is useful in order to obtain a first "idea" of the potential parameters from the experimental data (see section "The laterally averaged potential from diffraction scans") which can then subsequently be refined using a three-dimensional model potential that is matched to the experimental results.

As further noted by Jardine *et al.* [18], for weakly corrugated surfaces, the He wavefunctions in the resonant state can be approximated as

$$\Psi_{(\mathbf{K}+\mathbf{G}),n}\left(\mathbf{R}, z\right) \approx \phi_n\left(z\right) \exp\left[\mathbb{i}\left(\mathbf{K}+\mathbf{G}\right)\cdot\mathbf{R}\right], \tag{4.21}$$

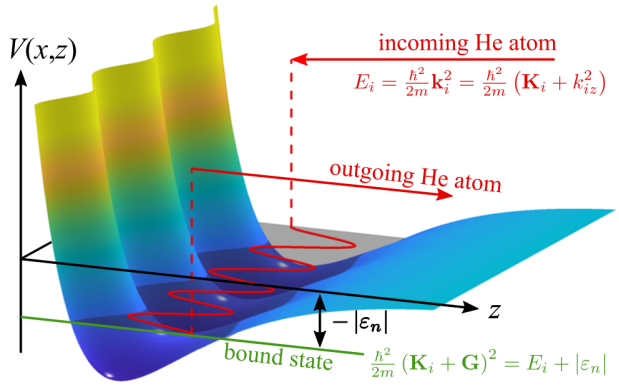

Figure 4.13: Schematic illustration of a selective adsorption resonance process in the free-atom approximation, with the kinematic conditions for entering a bound state with energy ϵ_n.

with $\phi_n(z)$ being an eigenfunction of $V_{\mathbf{0}}(z)$ and the $\mathbf{R}$-dependence becomes that of a plane wave (see Fig. 4.13) [97].

The time spent in the resonant state depends on the lateral corrugation of the potential since the "strength" of diffractive scattering is determined by the corrugation, thus making resonant scattering a useful experimental probe of the three-dimensional atom-surface potential. Resonances involving the ground state are most sensitive to the potential near the minimum, since that position corresponds to the largest weight of $\phi_0(z)$. On the other hand, higher lying states extend further into the vacuum region and are a useful probe of the exact potential shape at larger distances z [18].

For accurate studies of corrugated systems, large amounts of high resolution, high quality data are required. According to the kinematic condition Eq. (4.20), one can either vary E_i or the parallel momentum transfer $\mathbf{K}_i$. In a conventional HAS experiment [34], there are three variables: the incident energy, E_i, together with the polar and azimuthal scattering angles, ϑ_i and φ_i. Here, the scattering angles correspond to changes of $\mathbf{K}_i$ as determined by the scattering geometry.

Often the energy and azimuthal angle are fixed while the polar angle ϑ_i is varied followed by a simplified analysis based on approximations, such as Eq. (4.21). However, in particular potentials with a large corrugation, derived on the assumption of the free-atom approximation, are inaccurate and the bound-state energies are known to be systematically misplaced. The full picture is analogous to a two-dimensional (2D) band structure of nearly-free particles due to the periodic corrugation of the potential, i.e., in the laterally averaged potential, each bound state gives rise to a 2D sub-band of the overall band structure (see Fig. 4.14b)) [18, 97, 187, 188]. Hence for an accurate determination of the three-dimensional atom-surface interaction potential, several of the above described experimental variables should be varied, thus providing a larger data set while at the same time solving the elastic scattering problem exactly by using computational methods such as the CC algorithm.

By using Fourier-transform (FT) HAS, a wide range of incident energies can be studied at once, producing large datasets over a wide range of kinematic conditions (see Fig. 4.14a)). In FT-HAS, the spread of energies in the incident beam is intentionally broadened as far as possible (illustrated by the red gradient in Fig. 4.14a)), and the spin-echo principle is then used to analyse the energy distribution of the scattered beam, thus providing energy dependent reflectivity information [18, 115] as plotted in Fig. 4.14b) for Bi(111): A large number of resonant features can be seen as bright and dark stripes, dispersing across the plot. The advantage of FT-HAS with respect to conventional HAS is, that the energy resolution is unaffected by the spread in the incident beam, and the data taking time depends on the required spectral resolution, rather than the spectral range [18]. The superimposed red lines in Fig. 4.14b) according to

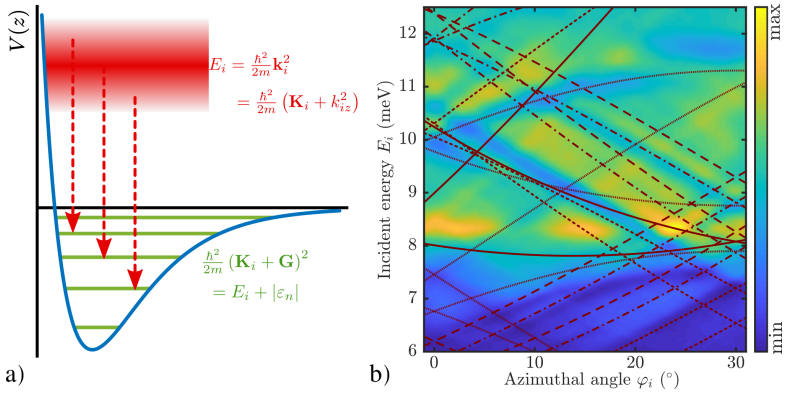

Figure 4.14: a) Illustration of the resonance condition in the free atom approximation, when using an incident beam with a broad energy distribution. b) Specular intensity for scattering of He from Bi(111) at 150 K, obtained from a FT-HAS measurement. The scattered intensity is plotted as a colour map versus incident energy, E_i, and azimuthal angle, φ_i, showing a large number of resonant features which disperse across the plot. The superimposed lines show the kinematic conditions in the free atom approximation.

the kinematic conditions in the free-atom approximation, illustrate that there are significant offsets and shifts with respect to the maxima/minima in the experimental data which can only be reproduced when considering the full three-dimensional potential.

The laterally averaged potential from diffraction scans

As described above, in order to obtain the laterally averaged potential $V_\mathbf{0}(z)$, which in turn can be used as a first starting point for the determination of the three-dimensional potential, often only one experimental variable is varied. Such an experiment is e.g. an elastic scan where the sample is rotated around the polar (incident) angle ϑ_i. The parallel momentum transfer to the surface $\Delta K = |\Delta\mathbf{K}|$, is then given by

$$\Delta K = |\mathbf{K}_f - \mathbf{K}_i| = |\mathbf{k}_i| \left[\sin(\vartheta_{SD} - \vartheta_i) - \sin\vartheta_i\right] , \tag{4.22}$$

where the final scattering angle $\vartheta_f = \vartheta_{SD} - \vartheta_i$ is determined by the fixed source-detector angle ϑ_{SD}. In such an experiment, SARs will typically become visible as smaller features in-between the diffraction peaks and the position of the SAR features in the scans are related to the bound state energies.

Following the free-atom approximation we can directly obtain the bound state energies of the laterally averaged potential which assumes a surface without corrugation, $V_\mathbf{0}(z) = D\left[e^{-2\kappa z} - 2e^{-\kappa z}\right]$. The kinematic condition Eq. (4.20) at certain values of the parallel momentum transfer ΔK needs to be fulfilled, but in the free-atom approximation, the binding energies $\epsilon_n(\mathbf{K}_i, \mathbf{G})$ are considered constant and therefore independent of $\mathbf{K}_i$ and $\mathbf{G}$. Eq. (4.20) can then be expressed in terms of the incident angle ϑ_i and the incident wave vector k_i:

$$\tfrac{2m}{\hbar^2}|\epsilon_n| = (k_i \sin\vartheta_i + G_\parallel)^2 + G_\perp^2 - k_i^2 . \tag{4.23}$$

Here $\mathbf{G}$ has been split into its parallel and normal component $(G_\parallel, G_\perp)$ with respect to the incidence plane.

Such an approximation is useful in order to obtain a first idea about the potential parameters. However, the assignment of SARs to a certain bound state energy ϵ_n is not always unambiguous due to the manifold of various $\mathbf{G}$-vectors and the known systematic displacement in the free-atom approximation. A more robust approach considers the different curvatures associated with a certain $\mathbf{G}$-vector, either using the

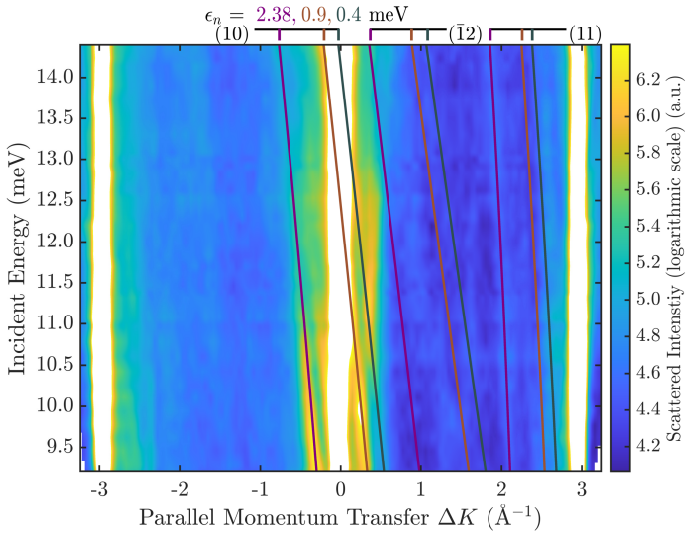

Figure 4.15: Contour plot of the scattered He intensity in dependence of momentum transfer and incident energy along the $\overline{\Gamma\mathrm{K}}$ azimuth, for the Sb_2Te_3(111) sample at 113 K. The solid lines are the positions of the SAR features according to the free atom model with the different colours denoting the bound state energies $\epsilon_{1,2,3}$. The Miller indices of the interacting **G**-vectors are given in brackets.

FT-HAS technique [115] or considering consecutive elastic angular scans in terms of their incident energy [24].

By combining many elastic scans along the same azimuthal direction with various incident energies E_i, the scattered intensity as a function of two variables (ϑ_i, E_i) can be obtained. Hence a similar data set as in a FT-HAS experiment is obtained, although it will be resolution limited to some extent by the apparatus. Such a two-dimensional intensity plot is shown in Fig. 4.15 for the $\overline{\Gamma\mathrm{K}}$ azimuth of Sb_2Te_3(111). The x-axis has been converted from incident angle to parallel momentum transfer according to Eq. (4.22) and the y-axis corresponds to the incident energy E_i while the colour map represents the scattered intensity. The high intensity of the specular and first order diffraction peaks has been omitted for better visibility of the SAR features in the surface plot.

In order to decrease the linewidth and thus the separation of the SAR features, the sample is typically cooled down (e.g. to 113 K in Fig. 4.15) for these angular scans. The peak position at a certain k_i can now be used to identify the corresponding diffraction channel **G** and bound state energy ϵ_n in the free atom-approximation. The coloured lines represent the kinematic conditions Eq. (4.23) for various ϵ_n, with the number in brackets denoting the interacting **G**-vector. For simplicity only the three most prominent interacting **G**-vectors, which show stronger intensities, are drawn. Analogous to an FT-HAS scan such as in Fig. 4.14(b), different **G**-vectors will give rise to different curvatures, versus incident energy, in these kind of plots, thus allowing for a better assignment of the involved **G**-vectors and bound states.

Following such an initial analysis for the He-Sb_2Te_3(111) system, three prominent lines can be attributed to three different bound state energies with the **G**-vector (10) with 2.38, 0.9 and 0.4 meV. The same measurement as in Fig. 4.15 was performed along the $\overline{\Gamma\mathrm{M}}$ azimuthal direction (see Appendices) from which, in addition to confirming the bound state energies along $\overline{\Gamma\mathrm{K}}$ an additional bound state at 4.28 meV can be identified.

Finally, the four obtained bound-state energies were fitted to the laterally averaged Morse potential using a least squares method [24]. The fit yields a potential with the parameters $D = (5.5 \pm 0.2)$ meV for the well depth and $\kappa = (0.76 \pm 0.05)$ Å^{-1} for the stiffness.

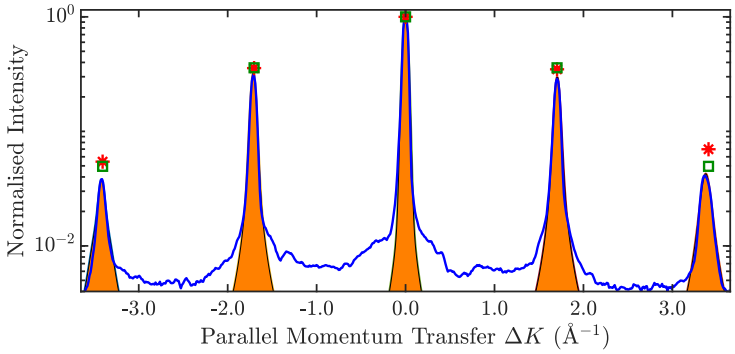

Figure 4.16: The blue line shows the scattered intensity versus the parallel momentum transfer along the $\overline{\Gamma M}$ azimuth of Sb_2Te_3(111). The orange areas show the fitted measured intensities based on a Voigt-profile, resulting in a value displayed as red stars. The green squares correspond to the calculated values based on elastic quantum-mechanical scattering calculations.

Surface electronic corrugation

After the determination of the laterally averaged atom-surface interaction potential $V_{\mathbf{0}}$, the surface electronic corrugation ξ_{pp}, as it appears in the corrugated potential needs to be considered. In principle, the corrugation determines the fraction of the incident beam which is scattered into diffractive channels and thus the diffraction intensities. Thus, following quantum mechanical scattering calculations the intensities in the angular diffraction scans can be determined [47] and compared with the experimental intensities.

Calculations of the scattered intensities can be performed using the elastic CC approach in which the time-independent Schrödinger equation is solved. Inserting the Fourier series of the surface potential and the wave function in this equation gives a set of coupled equations for the outgoing waves. These waves are numerically solved for in the CC-algorithm for a finite set of closed channels [5, 33]. The method of solving the set of coupled equations has been discussed widely in previous publications [5, 6, 31, 33, 37] and the Fourier ansatz with the corrugation function and the corresponding coupling terms can be found in Refs. [6, 31, 37] The elastic CC-calculations further need to be corrected for the Debye-Waller attenuation, using a previously determined Debye-Waller factor [44] / surface Debye temperature Θ_D (see Appendices).

As a starting point, the potential parameters from the kinematic analysis and an estimated value of the corrugation are used for the elastic CC-calculations. By comparing a data set of several angular scans over the high symmetry directions and at various sample temperatures the value of the corrugation is iteratively improved. The optimisation is usually performed by minimising a measure of the deviation R:

$$R = \frac{1}{N}\sqrt{\sum_G \left(I_G^{\mathrm{exp}} - I_G^{\mathrm{sim}}\right)^2}\,, \tag{4.24}$$

with I_G^{exp} and I_G^{sim} being the measured and calculated diffraction intensities and N the number of experimentally measured diffraction peaks [34].

In Fig. 4.16 an exemplary comparison is depicted for a scan along the $\overline{\Gamma K}$ direction of Sb_2Te_3 with an incident energy of 15.4 meV. The peak areas of the diffraction channels are fitted using Voigt profiles and shown as orange shaded regions, while the obtained values of the peak areas are indicated by the red stars. The calculated scattering intensities are plotted as green rectangles, showing good agreement with the experimentally determined values. Following this optimisation, the best fit value for the peak to peak corrugation of Sb_2Te_3 in percentage of the lattice constant is found to be $\xi_{pp} = 5.5\,\%$.

The three-dimensional potential and quantum-mechanical scattering calculations

Although we have considered the surface electronic corrugation in the section "Surface electronic corrugation" based on a comparison of diffraction intensities with quantum-mechanical scattering calculations, the potential parameters D and κ are still those based on the initial analysis following the free-atom approximation. In order to obtain a realistic, three-dimensional atom-surface interaction potential, further refinement of the potential based on the inclusion of larger experimental data sets and a comparison with quantum-mechanical scattering calculations is required as outlined in the following.

While an analysis based on the free-atom approximation may be appropriate for "flat" metal surfaces, i.e. with a negligible electronic corrugation [189], surface corrugation is a necessary ingredient for SAR processes to occur. In fact, considering the semi-classical picture, the strength of diffractive scattering both into and out of a resonant state is determined by the corrugation and the "quality" of experimental SAR data will depend on the magnitude of the corrugation.

With increasing corrugation, resonances become stronger since more of the incident wave scatters into the resonant state. On the other hand, a larger corrugation will give rise to a greater deviation from the free-atom model making an analysis solely based on Eq. (4.23) and Eq. (4.21) much more difficult. The analysis of SARs is also affected by the dimensionality of the corrugation function since one-dimensional problems, such as e.g. stepped surfaces [33, 131], have a simple band structure, while for systems which exhibit a two-dimensional corrugation there are many more open channels making it more difficult to find "isolated" SAR features. The strong deviation from the simple free-atom like dispersion and the broadening and overlap of SAR features for systems with a large two-dimensional corrugation makes the analysis much more challenging [190].

In order to identify systematic shifts/misplacements due to the corrugation and dispersion in the picture of the three-dimensional interaction potential (see Fig. 4.14b)), quantum mechanical scattering calculations considering the full-dimensional potential need to be used for a comparison. However, reproducing an angular scan, where ϑ_i is varied is rather difficult to implement in a CC-calculation. Instead it is much easier to follow the variation of the scattered intensity for a specific scattering channel in the CC calculation which is then compared to an experiment where e.g. E_i is varied while ϑ_i remains fixed in a conventional HAS experiment. The latter corresponds to a single slice at fixed φ_i of a FT-HAS experiment.

The so-called "drift scan" in a conventional HAS experiment is easily realised by changing $E_i = \frac{\hbar^2}{2m}k_i^2$ via the nozzle temperature while measuring the scattered intensity. Usually, this is done by monitoring the intensity of the specular channel, since the specular reflection provides the highest signal-to-noise ratio. Various dips and peaks in the drift scans give access to the detailed shape of the potential and can further be compared with the mentioned scattering calculations. The left-most and the central panel in Fig. 4.17 show such a measurement (blue line) taken at 113 K for Sb_2Te_3, with several features that can be attributed to SAR processes. The dash-dotted light green line shows the CC calculation while the dark green curves were convoluted with a Gaussian function to account for an apparative broadening of the natural linewidths [24]. By adjusting the parameters of the initial potential and comparing the position of the features (in terms of k_i) from the scattering calculations with the experimental data it allows for a refinement of the potential parameters.

A more detailed description of the analysis of such drift scan spectra, including the adaptation of a corresponding R-factor and additional experimental effects such as nozzle flow corrections and surface terraces can be found in Ref. [24]. The scattered intensity of the $(\bar{1}1)$ diffraction peak at a momentum transfer of $\Delta K = -3\,\text{Å}^{-1}$ as shown in the right-most panel of Fig. 4.17 can also be analysed in the same

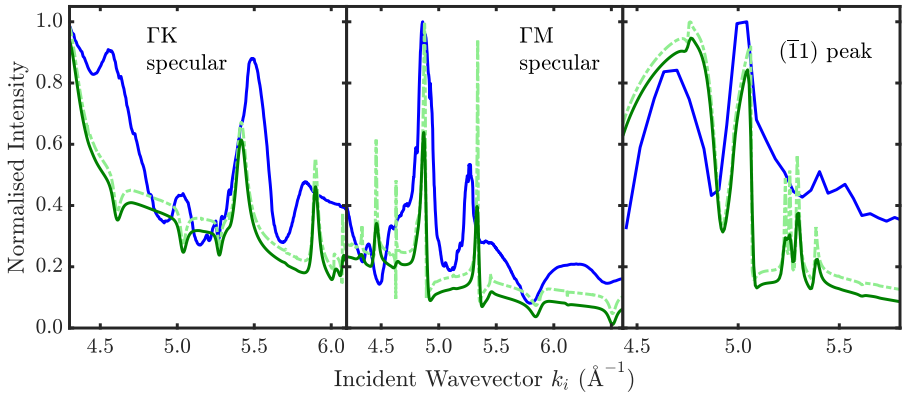

Figure 4.17: Normalised scattered intensity of the diffraction peaks versus incident wavevector k_i. The blue curve shows the measured data at 113 K with the solid green curve corresponding to the elastic CC-calculations corrected by the Debye-Waller factor according to the optimised three-dimensional potential. The dash-dotted curve has been convoluted with a Gaussian to account for the experimental/beam broadening. The so-called drift scans are plotted (from left to right) for the $\overline{\Gamma K}$ specular, the $\overline{\Gamma M}$ specular and the $(\bar{1}1)$ diffraction peak, respectively.

manner. However, the fact that the position of the diffraction peak will shift with ϑ_i complicates such a measurement - hence the number of experimental points is much smaller compared to measurements at specular position. Nonetheless, several SAR features are again very well reproduced with the elastic CC-calculations using the same potential.

The final potential parameters following this kind of analysis and iterative optimisation can be found in Tab. 4.2. Therefore, once the potential parameters D and κ have been optimised, the corrugation ξ_{pp} is further improved by following the procedure of comparing the diffraction intensities as discussed in the section "Surface electronic corrugation".

Finally, it should be noted that inelastic effects cannot be reproduced within the scheme of elastic CC-calculations, meaning that in addition to apparative broadening effects it is not possible to resemble the actual shape of the whole measured drift spectrum based on elastic calculations. One can clearly see that, e.g. for the measurement along the $\overline{\Gamma K}$ azimuth, the peaks at 4.6 and 5.0 Å^{-1} occur as dips in the calculation which can possibly by explained by inelastic events that turn maxima into minima and vice versa [118, 123]. We can however obtain an estimate of the influence of inelastic events based on a comparison of how the broadening of SAR features changes when changing the sample temperature (see section "Elastic and inelastic contributions")

Linewidth and lifetime of SARs

As outlined in the section "The three-dimensional potential and quantum-mechanical scattering calculations", corrugation is a necessary ingredient for SARs to occur and as the corrugation increases the resonances become stronger, as more of the incident wave scatters into the resonant state. However, at the same time resonances will become simultaneously broader since the resonance lifetime decreases through stronger scattering out of the resonant state [18].

Consequently, the broadening of SAR features in experimental measurements is related to the lifetime of the He atom in that particular bound state. The usual approach is to determine the external linewidth from e.g. an angular scan which has to be corrected with respect to resolution aspects of the apparatus, in order to obtain the actual internal/natural linewidth [33, 130].

However, in the few experimental studies available up to now, there is some ambiguity about how to

obtain the corresponding lifetime from the measured linewidth which shall be clarified at this point. The lifetime follows from the uncertainty principle which is based on the standard deviations and therefore one should use the half-width at half-maximum (HWHM): Following the uncertainty principle, the relation in terms of lifetime is a consequence of the Fourier theorem i.e. in classical wave mechanics the uncertainty of the frequency times the uncertainty in time is $\geq \frac{1}{2}$. Based on the derivation of response functions within the theory of time-dependent perturbations [16], a SAR exhibits a Lorentzian lineshape which decays according to $\exp(-t/\tau)$, where τ is the lifetime. From the corresponding HWHM Γ of the Lorentzian it follows $\Gamma = \hbar/\tau$ and hence the experimental broadening can be used to determine the lifetime τ.

On the other hand, upon using the angular broadening of SARs in diffraction scans, those tend to be fitted with Gaussian functions since it makes a subtraction of the experimental broadening (being the sum of two Gaussians) to obtain the internal linewidth easier and the uncertainty in doing that is usually negligible. Following this approach, the SAR features in several diffraction scans are fitted with a Gaussian function which is then corrected for the effects of the angular resolution of the apparatus as well as the energy spread in the beam (see Ref. [24] for further details). The HWHM $\Delta\epsilon_n$ of the Gaussian then yields the natural linewidth which is related to the lifetime τ of the bound state via $\tau_n = \hbar/\Delta\epsilon_n$ [16, 33].

Moreover, using the lifetime, the distance that the He atom travels parallel to the surface can be estimated. Based on the parallel momentum $K_{||} = k_i \sin\vartheta_i + G_{||}$, where $G_{||}$ is the parallel component of the interacting G-vector, the velocity of the He atom parallel to the surface can be determined which together with the corresponding lifetime τ_n yields the travel distance L_n.

A comparison for semimetals and TIs

In the following, we provide a comparison of the He-surface interaction potential of binary TIs as well as of single-elemental Bi(111) and Sb(111) [5, 6, 24, 115]. The determined potential parameters for the well depth D, stiffness κ and surface electronic corrugation ξ_{pp} are summarised in Tab. 4.2. All quantities have been determined based on HAS experiments, assuming a corrugated Morse potential following the approach presented in this perspective.

Table 4.2: Comparison of the potential parameters well depth D, stiffness κ and surface electronic corrugation ξ_{pp} in % of the lattice constant for the binary topological insulators as well as the single-elemental semimetals which are part of the compounds forming binary TIs.

crystal	D (meV)	κ (Å^{-1})	ξ_{pp} (%)	Ref.
Bi_2Se_3(111)	6.54	0.58	5.8	[24]
Bi_2Te_3(111)	6.22	0.92	9.6	[115]
Sb_2Te_3(111)	5.43	0.73	6.6	[2]
Bi(111)	7.9	0.88	8.1	[37]
Sb(111)	4.28	0.39	13.7	[31]

Single elemental Sb(111) exhibits the most shallow potential well depth with $D = 4.28\,\text{meV}$ and the smallest stiffness $\kappa = 0.39\,\text{Å}^{-1}$, while at the same time, the value for the corrugation is the largest, with $\xi_{pp} = 13.7\,\%$ of the surface lattice constant. In comparison, single elemental Bi(111) exhibits the deepest potential well depth, possibly due to a larger polarisability of Bi compared to the other elements, giving rise to stronger vdW interactions and thus a deeper potential well. The latter also seems to transfer to the well depth of the binary TIs containing the element as described below.

[2] current study

In Fig. 4.18 the laterally averaged Morse potentials for all three binary TIs are plotted, based on the parameters from Tab. 4.2. The different well depths can be clearly seen in the potential energy values at zero distance from the surface. Bi_2Se_3 exhibits the deepest well depth among these binary TIs ($D = 6.54\,\text{meV}$), but at the same time the smallest stiffness $\kappa = 0.58\,\text{Å}^{-1}$. Taken together it means that the laterally averaged potential of Bi_2Se_3 contains the largest number of bound states with a total of seven states with ϵ_5 and ϵ_6 being quite close to zero i.e. to the threshold condition. The well depth of Sb_2Te_3 is the most shallow one within the group of binary TIs and as the only binary TI without Bi in the compound this may be due to the influence of the heavier Bi atoms in the other two compounds (Bi_2Se_3 and Bi_2Te_3) with respect to the attractive part of the potential - i.e. the large polarisability of Bi as mentioned above.

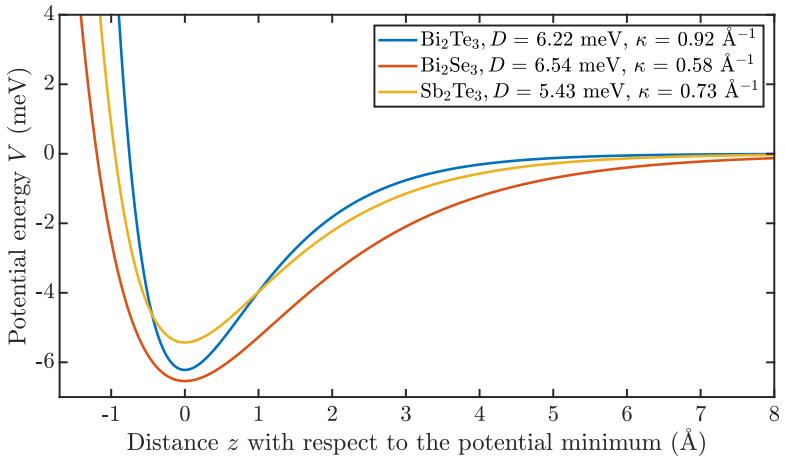

Figure 4.18: Comparison of the laterally averaged potentials $V_{\mathbf{0}}(z)$ for the binary TIs based on the determined corrugated Morse potentials in Tab. 4.2.

While some properties of the single-elemental group 15 semimetals (Bi, Sb) seem to transfer to the binary compounds, the uppermost layer of these binary TIs is either Se or Te (see Fig. 4.12b)). Since the Se atoms are "smaller" compared to Te, the He atoms may get closer to the surface and might therefore experience stronger effects from the heavier Bi elements in the second atomic layer. The latter would make the Bi_2Se_3 interaction potential deeper compared to the Bi_2Te_3 potential with the terminating Te layer as is indeed the case according to Tab. 4.2.

These simple trends in terms of the atom-surface interaction well depth and stiffness seem to work upon comparison of the group 15 semimetals and the compounds forming the binary TIs, however, other data suggests that they cannot easily be extended to other groups across the periodic table. For example, for the layered material 2H-MoS_2(0001), a He-surface potentital with a well depth $D = 13.6\,\text{meV}$ and stiffness $\kappa = 1.15\,\text{Å}^{-1}$ had recently been reported [116].

The linewidth and lifetime of resonances

While several theoretical efforts have been devoted to studies of the lifetime of SAR effects [33, 131, 191–193] and we will compare our findings with a few of those, experimental studies about the lifetimes of SARs are particularly scarce, with the exception of the He–LiF(001) system [130], a stepped copper surface [194] and a few preceding studies of semimetal and TI surfaces [24, 31].

The natural linewidths, corresponding lifetimes and travel distances for all four bound states of the He-Sb_2Te_3(111) potential are listed in Tab. 4.3. As expected, the lower the bound state (higher binding

Table 4.3: Bound state values of the laterally averaged He–Sb_2Te_3(111) interaction potential. The determined internal linewidths $\Delta\epsilon_n$ of the corresponding bound states (based on the experimental width of the resonances) and their lifetimes τ_n are also given. From the lifetime the distance L_n travelled in the bound state can be calculated. All data was collected at 113 K and the overall accuracy is estimated to be about ±15%.

bound state	ϵ_n (meV)	$\Delta\epsilon_n$ (meV)	τ_n (ps)	L_n (Å)
ϵ_0	4.27	0.29	3.1	13
ϵ_1	2.37	0.165	4.5	34
ϵ_2	1.02	0.11	6.2	44
ϵ_3	0.23	0.055	12.2	86

energies) the broader the natural linewidth $\Delta\epsilon_n$ yielding a shorter corresponding lifetime [18]. As follows from Eq. (4.21), for bound states lying just below the threshold, the majority of the weight in $\phi_n(z)$ lies well away from the repulsive wall. Hence higher lying bound states couple weakly to the repulsive lateral corrugation: The He atom will remain longer in that particular state since the probability of scattering "out" of the bound state is smaller and the SAR exhibits a long lifetime and a narrow width in energy. In contrast, the lower lying bound states are broader, reflecting greater coupling to the repulsive corrugation.

In comparison with other binary TIs, the internal linewidths for Bi_2Se_3 are very similar to the here reported values for Sb_2Te_3. The bound state $\epsilon_2 = 2.3$ meV for Bi_2Se_3 exhibits a lifetime of $\tau_2 = 4.4$ ps [3] and thus exhibits a very similar lifetime as the bound state ϵ_1 in the case of Sb_2Te_3 (Tab. 4.3), which occurs at a similar binding energy. The same holds for Bi_2Te_3, where upon analysis of the angular scan for ^{3}He scattering [115], a lifetime of about 15 ps for $\epsilon_2 \approx 0.3$ meV is obtained.

The distances L_n, travelled parallel to the surface are also reported in Tab. 4.3 for Sb_2Te_3. Naturally, longer lifetimes in Tab. 4.3 correspond to longer distances travelled parallel to the surface with the longest lifetime in the case of Sb_2Te_3 (12.2 ps) corresponding to a travel length of 86 Å. The travel distances of bound states with similar energies among the binary TIs are again quite similar, e.g. ϵ_1 for Sb_2Te_3 in Tab. 4.3 is in good agreement with the 36 Å for ϵ_2 in the case of Bi_2Se_3. In fact the travel distances are also close to previous works of different systems. E.g. for LiF(001) $L_1 = 17$ Å is found[4] for the $\epsilon_1 = 2.46$ meV bound state at room temperature, whereupon we obtain $L_1 = 25$ Å for ϵ_1 when measured at room temperature (Tab. 4.4).

In addition to elastic and defect scattering, inelastic processes involving phonon scattering will further limit the lifetime, which becomes more important at elevated temperatures [101] and will be further discussed below. The natural linewidth of a resonance will usually be given by the sum of elastic and inelastic processes, so that for the corresponding lifetime $\tau^{-1} = \tau_{el}^{-1} + \tau_{inel}^{-1}$ holds.

The longest travel distance $L_3 = 86$ Å for Sb_2Te_3 implies that the crystal surface can be regarded as being perfect over this range. To put this in context, the angular broadening of the specular peak gives rise to an estimate (lower limit) for the quality of the crystal. For Sb_2Te_3 the domain sizes are larger than 500 Å while for Bi_2Se_3 and Bi_2Te_3 values of ≈ 1000 Å were found [24, 47]. Hence considering the travel distances it follows that inelastic effects must have a large influence on scattering out of the bound states, even for the cooled samples.

Even though SARs are certainly not the method of choice for the determination of crystal qualities we will in the following attempt to compare our findings with other methods such as scanning probe

[3] Note that here we use the HWHM from [24] where originally the values were obtained for the full width at half maximum
[4] Note that Ref. [130] used the relation $\tau_n = \hbar/\Delta\epsilon_n$ with the Plank constant $\hbar$. Therefore, the travel lengths L_n need to be recalculated using $\hbar$.

microscopy measurements. In general there seems to be a consensus that the cleavage of single crystals as well as the growth of thin films gives rise to terraces which are separated by one QL steps ($\approx 1\,\mathrm{nm}$ high) [195, 196], though sub-QL steps have also been reported in some cases [197]. The step height can also be determined from HAS measurements upon intensity oscillations with varying beam energy and comparable results have been obtained for Bi_2Se_3 single crystals [24]. The overall size of individual terraces is generally reported to range between 100 nm to 1 µm [195]. These can be readily compared with the domain sizes from the angular broadening of the HAS specular peak and are in good agreement with the above mentioned sizes.

In addition, there is experimental evidence coming from scanning tunneling microscopy that the surfaces of Sb_2Te_3 [198] and Bi_2Te_3 [199] but also similar materials such as $PdTe_2$ [200] and $PtTe_2$ [201] contain a substantial number of point defects with a characteristic clover shape, separated not more than 10 nm. While we do not expect that single point defects would have an influence on the mentioned width of the specular peak, these could possibly scatter the He atom out of the bound state and thus reduce the travel length. On the other hand, in Landau level spectroscopy of Sb_2Te_3 films grown by molecular beam epitaxy, a mean free path of about 80 nm is found in accordance with comparable terrace sizes [198] which is again in very good agreement with the longest travel length of 86 Å reported for the highest bound state of the cooled Sb_2Te_3 sample. Hence while the travel length may be reduced due to inelastic scattering at single point defects, the contribution of inelastic phonon scattering channels to the lifetime is best discussed upon considering temperature dependent measurements as done in the following.

Elastic and inelastic contributions

The comparison in terms of the travel distances between several binary TIs shows that for similar materials but different potentials the travel distances are quite similar. Together with the much larger estimated domain sizes it follows that inelastic effects must in general play an important role. In fact it has already been noted quite early for SARs when scattering from graphite, that an appreciable amount must come from inelastic processes [202]. Moreover, calculations of the corrugation in the example of Bi(111), where the inelastic CC gives a smaller corrugation with 6.3% of the lattice constant [37] compared to the value from the elastic CC in Tab. 4.2 already imply the importance of inelastic phonon scattering and these should also be included in future studies.

While elastic and defect scattering should be independent of the temperature, higher surface temperatures will give rise to an increase of inelastic (phonon) scattering events which will in turn significantly decrease the lifetimes. Tab. 4.4 shows the lifetimes for Sb_2Te_3, obtained at room temperature. In addition the temperature dependence of the linewidths of the ^{3}He–Bi_2Te_3(111) and the ^{3}He–Bi(111) system are shown in the Appendices, illustrating clearly an increased broadening with increasing temperature.

Comparing the lifetimes for Sb_2Te_3 at $T = 113\,\mathrm{K}$ (Tab. 4.3) and $T = 296\,\mathrm{K}$ (Tab. 4.4) shows that the lifetimes are by a factor of about 1.5 larger at low temperature. Assuming a linear increase with temperature, the effect is largest for the lowest bound state yielding $\Delta\tau/\Delta T \approx 0.02\,\mathrm{ps\,K^{-1}}$, although the changes relative to the lifetime at room temperature ($\alpha_\tau = \frac{1}{\tau}\frac{\Delta\tau}{\Delta T}$), as shown in the last column of Tab. 4.4 are comparable within the uncertainties.

The increase of phonon scattering with temperature can be compared to an earlier work of the stepped Cu(115) surface by Armand *et al.* [194] and temperature dependent changes of the resonance peak width reported therein. Following the analysis for Sb_2Te_3, we obtain a value of $\approx 1 \times 10^{-4}\,\mathrm{rad\,K^{-1}}$ for the FWHM of the ϵ_1 bound state and the $(\bar{1}0)$ vector which is larger than for the bound states of the Cu(115) system with $(1\text{–}2) \times 10^{-5}\,\mathrm{rad\,K^{-1}}$. Note however, that the interaction potential of Cu(115) is possibly closer to a 1D case as described above and for a stepped surface one expects a much shorter

Table 4.4: The internal linewidths $\Delta\epsilon_n$ and the corresponding lifetimes τ_n and travel distances L_n of the He-Sb_2Te_3(111) interaction potential, analogous to Tab. 4.3 but now for measurements at room temperature. Comparing the lifetimes obtained at $T = 296\,\mathrm{K}$ with the measurements at $T = 113\,\mathrm{K}$ (Tab. 4.3) provides an estimate of the temperature dependence $\alpha_\tau = \frac{1}{\tau}\frac{\Delta\tau}{\Delta T}$.

bound state	$\Delta\epsilon_n$ (meV)	τ_n (ps)	L_n (Å)	α_τ (10^{-3} K^{-1})
ϵ_0	0.32	2.3	19	2.0
ϵ_1	0.19	3.4	25	1.7
ϵ_2	0.14	4.8	35	1.7
ϵ_3	0.08	8.2	58	2.8

lifetime compared to flat surfaces based on elastic scattering channels alone [131]. At the same time, the temperature dependence of the natural linewidths of molecular hydrogen adsorbed on Cu(001) shows a similarly strong temperature dependence [192] compared to Sb_2Te_3(111). Thus we conclude that at least for the here presented binary TIs, surface imperfections only have a small influence on the linewidth of SARs and a large contribution comes from inelastic phonon scattering effects.

Actual quantitative statements of how the linewidths should change with temperature have not been addressed in any detail up to now. Some previous attempts to include phonon scattering effects in the description of SARs are based on a Debye-Waller theory. As shown for SARs on graphite, including a Debye-Waller factor may account for phonon scattering processes to some extend [118], but at specific incident energies the method becomes inadequate for the description of inelastic effects on the experimental resonance lineshapes [203, 204]. Moreover, the He–C(0001) potential is both steep and deep [97] and thus closer to the situation of a hard wall potential in comparison to the here presented potentials.

In reality the temperature dependent population of the phonon states changes with the Einstein-Bose distribution, and hence phonon states are less populated at lower temperatures which therefore minimises the scattering probability. On the other, due to the heavy elements present in the here presented semimetals and TIs, the acoustic phonon modes will already be completely occupied even for the low temperature measurements (see Appendices). In this context it is also interesting to note that the temperature dependence in Tab. 4.4 is comparable for all binding energies, in contrast to the trend for the (absolute) linewidth, where higher lying bound states exhibit a weaker coupling and thus a longer lifetime. It suggests that the relative importance of phonon scattering contributions is larger for the higher lying bound states.

Conclusions

Studying the position, shape and width of selective adsorption resonances provides a powerful route for an experimental determination of the attractive part of the helium-surface potential, and hence an exceptionally sensitive test of any corresponding theory with one of the most precise sources of information about physisorption potentials. While recent experimental approaches for the study of van der Waals interactions based on atomic force microscopy measurements via pulling a single molecule [148] and Xe-functionalised tips [205] have achieved broad attention, resonance effects in atom-surface scattering, as an approach to study the vdW interaction at the surfaces have not been appreciated up to date.

Within this perspective we have presented the experimental approach in observing effects of the attractive atom-surface interaction potential in gas-surface scattering experiments. While the great majority of recent experiments have concentrated on measuring resonance positions in order to determine an effec-

tive, laterally averaged potential our approach shows that experimental data can be used together with quantum mechanical scattering calculations to obtain an exact three-dimensional atom-surface potential. We have further shown that for the surfaces of semimetals and binary topological insulators a few general trends in terms of the atom-surface interaction well depth and stiffness exist.

A short view on recent *ab intio* approaches for the calculation of He-surface interaction potentials shows that it remains still difficult to accurately and simultaneously describe both the short range repulsive and the long range vdW part. It highlights the importance of atom-surface scattering experiments as a benchmark for *ab initio* treatments, in particular in terms of improving treatments of the long range interaction part.

Finally, we provide also experimental data about a number of so far much less studied features, namely the lifetime of SARs. Despite some general guidelines about the occurrence of maxima and minima in SARs [206] the linewidth and lifetime of SARs remain an elusive subject. E.g if inelastic effects are considered in calculations, those are often based on the assumption of a flat surface [207]. Recent works have shown that the interaction of a particle with a vibrating corrugated surface can be described theoretically [208, 209] and the linewidths of SARs can also be studied within the formalism of inelastic close-coupled calculations. Such an additional analysis could show whether elastic or inelastic phonon scattering channels are mainly responsible for the lifetime of bound states. It would further allow to establish whether indeed the lifetimes of SARs on topological insulator surfaces are mainly limited due to inelastic effects as found in our experimental study.

With this perspective, we hope that the herein presented experimental approach and data will stimulate further research with respect to quantum studies of the trapping of light particles on surfaces.

Acknowledgment

We would like to thank G. Benedek for many helpful discussions. Our earlier works on the subject benefited in particular from the works and discussions with P. Kraus and S. Miret-Artés. The authors are grateful for financial support by the FWF (Austrian Science Fund) within the project P29641-N36 and NAWI Graz. A. T. acknowledges also financial support within the FWF project J3479-N20. We would like to thank Henriette E. Lund and Martin Bremholm for the synthesis of the samples, Marco Bianchi for his advice and help in terms of the sample preparation, and Philip Hofmann as well as the aforementioned colleagues for many helpful discussions and additional characterisations of the samples.

Appendices

Appendix A: Computational details

The interaction potential between He and the Bi(111) surface has been calculated by means of density functional theory (DFT) using the QUANTUM-ESPRESSO suite of codes [210]. A scalar relativistic norm-conserving pseudopotential with five valence electrons and the Perdew-Burke-Ernzerhof [211] approximation for the exchange-correlation energy functional was used. To better describe the long range interactive part of the potential the calculation has also been performed with the addition of a grimme-d2 semiempirical correction [168] and with non-local vdw-df functional [172]. The electron wave functions were expanded in plane waves up to an energy cutoff of 35 Ry. A Gaussian smearing of 0.01 Ry was introduced in the occupation of states to deal with the semimetallic nature of Bi. We used a $(8 \times 8 \times 1)$ Monkhorst-Pack mesh [212] to sample the Surface Brillouin Zone (SBZ). The Bi(111) surface has been

modelled by a slab including 2 bilayers. The slabs have been separated by a 30 Å vacuum gap to ensure that spurious interactions between the periodic replicas of the slabs are avoided.

Appendix B: Experimental details

The experimental data for Sb_2Te_3 was obtained at the helium atom scattering (HAS) apparatus in Graz which uses a supersonic expansion of ^{4}He gas to generate a nearly monochromatic beam in the energy range of 9–20 meV. The apparatus consists of a fixed source-sample-detector setup with an angle of 91.5°. After the central part of the beam was selected with a 310 µm skimmer the He atoms hit the surface in an ultra-high-vacuum chamber and are reflected to the detector consisting of a quadrupole mass analyser. By rotating the sample, the incident angle ϑ_i and furthermore the parallel momentum transfer is changed. A more detailed description of the experimental setup can be found elsewhere [3].

The Sb_2Te_3 single crystal was grown at the Center of Material Crystallography at Aarhus University by slow-cooling from the melt in sealed quartz tubes. Powder X-ray diffraction at room temperature confirmed the phase purity and a Rietveld refinement was performed to extract the unit cell parameters ($a = 4.254$ Å at room temperature [114] along the (111) cleavage plane). A small piece was selected from the whole ingot which showed a nice clean cleavage plane. The crystal was attached onto the sample holder with thermally conductive epoxy and then cleaved *in situ* in a load-lock chamber [113] directly before putting it into the scattering chamber.

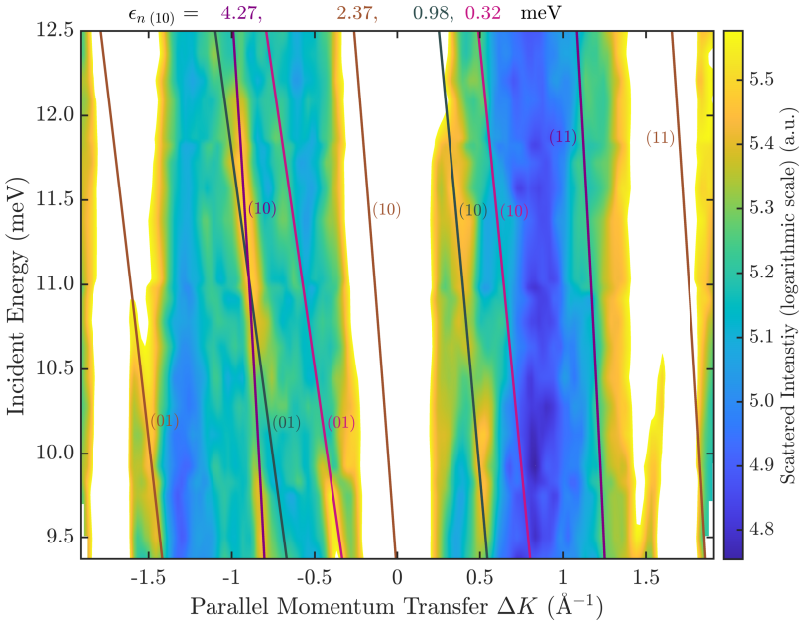

Figure 4.19: Contour plot of the scattered He intensities in dependence of the momentum transfer and incident energy along the $\overline{\Gamma M}$ azimuth with the Sb_2Te_3 sample being held at 113 K. The solid lines are the selective adsorption positions according to the free atom model with the colours denoting the bound state energies. The values on top of the plot denote the series of bound state values associated with the (10) **G**-vector

An initial alignment of the sample along the high symmetry direction was done based on the low energy electron diffraction (LEED) picture. The cleanness of the sample was verified with Auger electron spectroscopy (AES) as well as by monitoring the specular reflectivity in HAS. The sample can be cooled via a connection to a liquid nitrogen reservoir which allows for measurements to be taken at cryogenic

temperatures of 113 K and at room temperature. In a first measurement the thermal attenuation of the specular intensity was measured to determine the surface Debye temperature Θ_D. All elastic quantum mechanical scattering calculations of this work were corrected according to the experimentally determined value of $\Theta_D = (141 \pm 3)$ K.

Moreover, Fourier-transform (FT) HAS, was used for the collection of a number of additional data-sets as shortly outlined in the main part of the manuscript. In FT-HAS, the spread of energies in the incident beam is intentionally broadened as far as possible, and the spin-echo principle is then used to analyse the energy distribution of the scattered beam [18]. The method thus provides energy dependent reflectivity information and further information of how to convert the raw data can be found in Ref. [115].

Appendix C: Additional temperature dependent data

Examination of the temperature dependence of selective adsorption resonances (SARs) provides general rules for how inelastic scattering and SARs will effect each other depending on the relative contributions of elastic coupling and inelastic scattering to the width of the resonances. In the following we show additional experimental data which provide information about the influence of inelastic events on the linewidth of SARs. As mentioned in the main text, in addition to elastic and defect scattering, inelastic

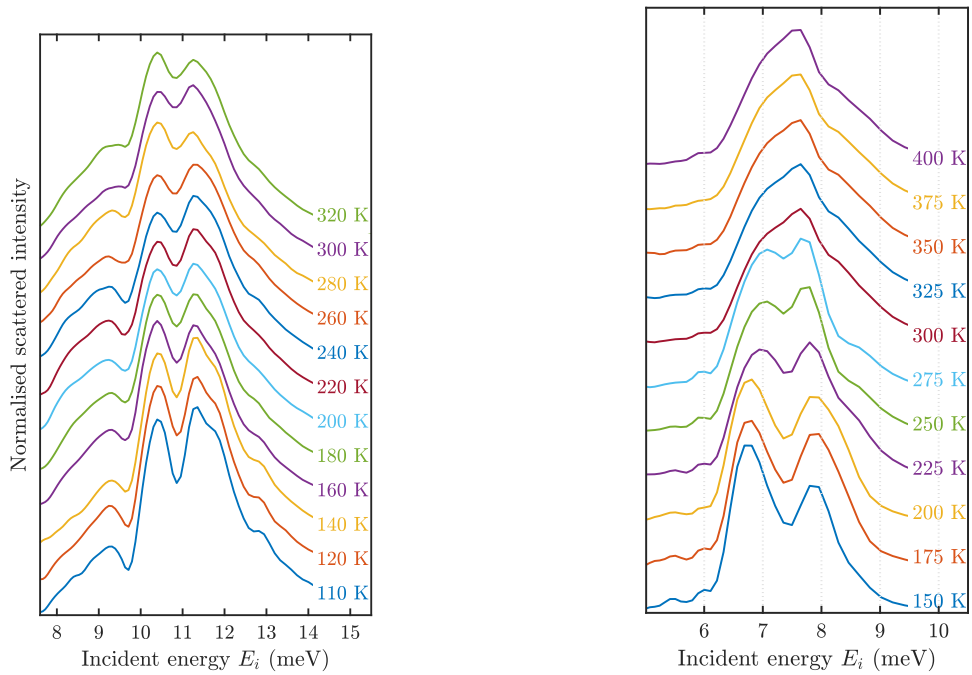

(a) $Bi_2Te_3(111)$ measurements along $\overline{\Gamma M}$ with a broad beam centred around $E_i = 12$ meV

(b) Bi(111) measurements along $\overline{\Gamma M}$ with a broad beam centred around $E_i = 8$ meV.

Figure 4.20: Single slices of temperature dependent measurements as obtained in a FT-HAS scan. Measurements at individual temperatures have been offset vertically, for better visibility.

processes involving phonon scattering further limits the lifetime. The latter becomes more important at elevated temperatures thus increasing the linewidth of SARs at higher surface temperatures. As reported in Tab. 4.4 in the main text, the internal linewidths $\Delta\epsilon_n$ of the bound state values of the He–$Sb_2Te_3(111)$ interaction potential for the sample at room temperature ($T = 296$ K) can be obtained by following the same procedure as outlined in the section "The linewidth and lifetime of resonances" of the main text. The internal linewidths $\Delta\epsilon_n$ are acquired from the half width at half maximum (HWHM) of the

corresponding SAR peaks in the diffraction scans (taken at room temperature for the latter case), after correction with respect to resolution aspects of the apparatus.

In addition, in Fig. 4.20 the temperature dependence of Fourier-transform (FT)-HAS scans for $Bi_2Te_3(111)$ and Bi(111) are plotted, with the sample aligned along the $\overline{\Gamma\mathrm{M}}$ azimuth in both cases. These FT-HAS scans are not limited in terms of the resolution of the apparatus, however, due to the internal broadening and overlap of several SAR features, the internal linewidth for an individual SAR features is not readily obtained. Nevertheless, the changes with increasing temperature imply that for $Bi_2Te_3(111)$ and Bi(111) a large contribution to the linewidth broadening comes from inelastic effects in line with the findings for Sb_2Te_3.

While Fig. 4.20b shows measurements with a broad incident beam centred around $E_i = 8\,\mathrm{meV}$, Fig. 4.20a shows measurements with the incident beam centred around $E_i = 12\,\mathrm{meV}$. For both cases, small individual peaks and dips in the data due to SARs are clearly discernible at low temperature but become increasingly broader at higher temperatures. In the case of Bi(111) in Fig. 4.20b, two strong peaks can be seen which have basically merged into one broad peak once reaching 400 K, thus reflecting mainly the intensity distribution of the incident beam at this sample temperature.

Appendix D: Inelastic effects and phonon occupation

Considering the actual surface phonon dispersion of $Sb_2Te_3(111)$ (Fig. 4.21a), calculated with density functional perturbation theory by Campi *et al.* [119], the intense acoustic phonon modes will already be occupied considering the thermal energy that corresponds to a surface temperature of 115 K, while at room temperature essentially all phonon modes should be occupied.

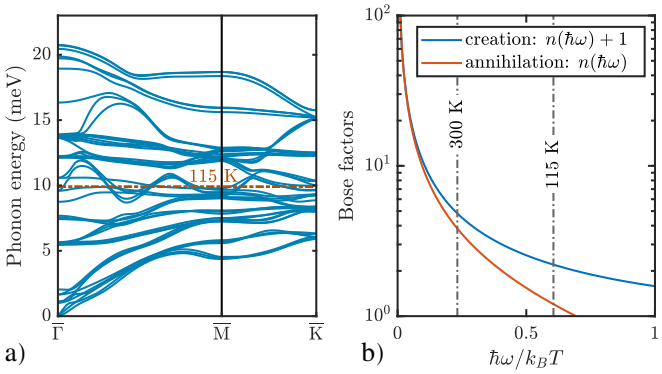

Figure 4.21: a) Surface phonon dispersion of $Sb_2Te_3(111)$ according to Campi *et al.* [119]. The intense acoustic phonon modes will already be occupied at a thermal energy of 115 K. b) Bose factors plotted versus the reduced inverse temperature $\hbar\omega/k_BT$, providing the probability for phonon creation and annihilation. The vertical dash-dotted lines illustrate the temperature change for a 6 meV phonon event.

On the other hand, the probability that either a phonon annihilation or creation event occurs upon scattering is given by the Bose-factors $n(\hbar\omega)$ and $n(\hbar\omega)+1$, respectively [16]. These follow from the occupation number for a given phonon energy $\hbar\omega$ as determined by the Bose-statistics [16]:

$$n\left(\hbar\omega\right) = \frac{1}{\exp\left[\hbar\omega/\left(k_BT\right)\right] - 1}\,. \tag{4.25}$$

In Fig. 4.21b) the Bose-factors are plotted versus the reduced inverse temperature $\hbar\omega/k_BT$. The Bose factors provide the probability for phonon creation and annihilation as a function of the surface temperature. For $T \ll \hbar\omega/k_B$ hardly any annihilation events are expected. As the typically intense surface

acoustic modes in $Sb_2Te_3(111)$ tend to reach energies of 5–6 meV at the Brillouin zone boundary, the vertical dash-dotted lines have been added to illustrate the temperature change for a 6 meV phonon event.

4.4 Terahertz Surface Modes & Electron-Phonon Coupling on $Bi_2Se_3(111)$

This section consists of the following published publication:

Terahertz Surface Modes & Electron-Phonon Coupling on $Bi_2Se_3(111)$

A. Ruckhofer*, D. Campi, M. Bremholm, P. Hofmann, G. Benedek, M. Bernasconi, W. E. Ernst, and A. Tamtögl

Physical Review Research **2**, 023186, 2020
https://doi.org/10.1103/PhysRevResearch.2.023186

* corresponding author

contributions	
funding	W.E. Ernst, A. Tamtögl, P. Hofmann
experimental design	A. Tamtögl, A. Ruckhofer
sample synthesis	M. Bremholm
data acquisition	A. Ruckhofer, A. Tamtögl
DFPT simulations	D. Campi, M. Bernasconi
data analysis	A. Ruckhofer, A. Tamtögl
interpretation	A. Ruckhofer, A. Tamtögl, G. Benedek
publication writing	A. Ruckhofer, A. Tamtögl, G. Benedek
discussion and editing	all authors

Abstract

We present a combined experimental and theoretical study of the surface vibrational modes of the topological insulator Bi_2Se_3 with particular emphasis on the low-energy region below 10 meV that has been difficult to resolve experimentally. By applying inelastic helium atom scattering (HAS), the entire phonon dispersion was determined and compared with density functional perturbation theory (DFPT) calculations. The intensity of the phonon modes is dominated by a strong Rayleigh mode, in contrast to previous experimental works. Moreover, also at variance with recent reports, no Kohn anomaly is observed. These observations are in excellent agreement with DFPT calculations. Besides these results, the experimental data reveal—via bound-state resonance enhancement—two additional dispersion curves in the gap below the Rayleigh mode. They are possibly associated with an excitation of a surface electron density superstructure that we observe in HAS diffraction patterns. The electron-phonon coupling parameter $\lambda = 0.23$ derived from our temperature dependent Debye-Waller measurements compares well with values determined by angular resolved photoemission or Landau level spectroscopy. Our work opens up a new perspective for THz measurements on two-dimensional (2D) materials as well as the investigation of subtle details (band bending, the presence of a 2D electron gas) with respect to the electron-phonon coupling.

Introduction

Bi_2Se_3 (Fig. 4.22) is categorised as a three-dimensional topological insulator (TI), a new state of quantum matter with a bulk gap and spin-orbit split surface states forming a Dirac cone across the gap [51, 52]. The interaction of electrons with surface phonons in Bi_2Se_3 has been studied intensively due to its important role in transport properties and possible constraints for potential applications in a variety of nanotechnologies [213–219]. Bismuth selenide as well as telluride alloys are classical thermoelectric materials [53, 55] with a large Seebeck coefficient and, as such, they have been used in thermoelectric refrigeration for a long time [220]. However, to fully understand the thermoelectric properties of Bi_2Se_3 thin films and nanoscale devices [221, 222], information on the surface phonon dispersion curves and the electron-phonon (e-ph) interaction is crucial [221, 223, 224].

So far experimental information about the surface phonon dispersion curves of $Bi_2Se_3(111)$ was limited to previous helium atom scattering (HAS) studies by Zhu *et al.* [217, 225], in the low energy part of the phonon spectrum. These studies suggested the presence of a deep Kohn anomaly (KA) in the 7.5 meV optical phonon branch (S2) coupled to the electronic (spin-forbidden) transition across the Dirac cone [225]. However, existing first-principle calculations of $Bi_2Se_3(111)$ phonon dispersion curves, do not show any evidence of KAs in the S2 branch [226].

A convenient parameter to characterise the e-ph coupling strength is the mass-enhancement λ [41] and in recent years it was demonstrated that HAS from conducting surfaces can directly measure the mode-selected e-ph coupling constants $\lambda_{\mathbf{Q},j}$ [4, 229], besides the surface phonon dispersion curves [16]. Moreover the temperature-dependence of the HAS Debye-Waller factor was shown to provide the global e-ph coupling constant λ at the surface of thin metal films [16, 32] and topological insulators [26, 47]. Yet the large λ as estimated based on the KA [217] is at odds with theoretical findings that indicate that the major contribution to λ comes from the higher optical phonon branches [226], especially when the Fermi level crosses the surface quantum-well states above the conduction band minimum (see Fig. 4.22(c)). The situation is actually met in recent high-resolution ^{3}He-spin scattering studies on $Bi_2Te_3(111)$, where the weak signature of a KA is detected in the surface longitudinal acoustic resonance [111], also not found in adiabatic *ab initio* calculations of the phonon branches.

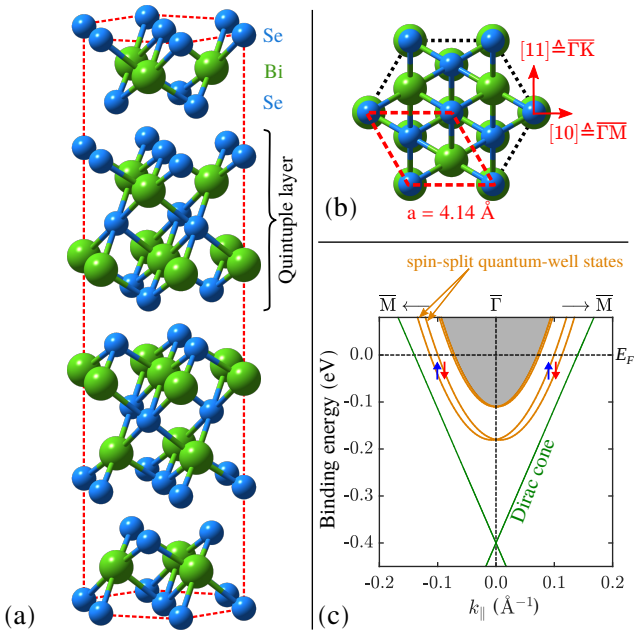

Figure 4.22: (a) Crystal structure of Bi_2Se_3 based on the conventional hexagonal unit cell. The unit cell consists of three quintuple layers of which each one is terminated by a Se layer. (b) Top view of the (111) surface with the red rhombus illustrating the hexagonal surface unit cell with lattice constant a. The two high-symmetry scanning directions are indicated by the red arrows. (c) Illustration of the electronic dispersion around the $\overline{\Gamma}$-point (see Refs. [227, 228]). Despite the Dirac cone, quantum-well states as illustrated by the orange lines exist on the surface as well. The quantum-well states are split due to Rashba coupling, thus making the previously degenerate spin states (illustrated by the red and blue arrows) separate into an inner and outer branch, each having a spin texture with opposite chirality.

In order to elucidate these conflicting results, we have undertaken a HAS study of the surface phonon dispersion curves and the e-ph interaction of $Bi_2Se_3(111)$. Supersonic neutral He atom beams with incident energies in the range ≤ 20 meV have been used to probe low-energy surface excitations with the best available resolution, while being an inert completely nondestructive probe [16, 34]. The technique allows to measure most of the surface phonon branches in the acoustic and optical regions. Low-energy He atoms impinging on a conducting surface are exclusively scattered by the surface charge density [4, 6] and inelastic scattering from surface phonons only occurs via the phonon-induced charge density oscillations, i.e., via the e-ph interaction. It is in this way that inelastic HAS provides a first-hand information on the e-ph interaction, with the neutral He atoms acting as a sort of local mechanical probe on the electron density.

Energy and momentum, inelastically exchanged by He atoms with the surface can, however, be retained by the electron system in the form of low-energy collective excitations. In principle, the HAS signal from this kind of excitations is expected to be quite small. Nevertheless, an increased e-ph interaction due to surface quantum-well states [230] in combination with an enhancement from HAS bound-state resonances [231], suggests to assign two branches of low-energy modes in the gap well below the Rayleigh waves (RW) to some sort of collective electronic excitations. Actually anomalous acoustic plasmons have been recently reported in $Bi_2Se_3(111)$ by Jia *et al.* [232], from high-resolution electron energy-loss spectroscopy, although these modes turn out to be superimposed in the first Brillouin zone onto the RW branch.

Plasmons in a two-dimensional electron gas (2DEG) with a $\sqrt{Q}$ dispersion in dependence of a parallel wavevector Q (2D plasmons) have been predicted long ago by Frank Stern [233, 234]. Later it was shown

that the coupling of 2DEG plasmons arising from two different quantum-well minibands, as found in semiconductor surface accumulation layers, yield a surface plasmon pair: a 2D plasmon and an acoustic surface plasmon (ASP) with a linear dispersion above the upper edge of the single-particle excitation spectrum [235, 236]. Similarly the coupling of a 2DEG at a metal surface coupled to the underlying 3D electron gas yields an ASP in addition to the ordinary surface plasmon [230, 237–239]. As discussed below, the assignment of the two additional low-energy branches as collective polaron excitation recently suggested by Shvonski *et al.* [235], although plausible in semimetals with a large dielectric constant, definitely requires further ad-hoc studies, possibly with even higher resolution as available, e.g., with ^{3}He spin-echo spectroscopy [111, 185].

Experimental and computational details

Experimental Details

The reported measurements were performed on a HAS apparatus which generates a nearly monochromatic beam ($\Delta E/E \approx 2\%$) of ^{4}He that is scattered off the sample surface in a fixed 91.5° source-sample-detector geometry. The beam is produced in a supersonic expansion of He through a 10 µm nozzle followed by sampling the core of the supersonic expansion via a 310 µm skimmer. For a detailed description of the apparatus please refer to [3].

Energy dispersive measurements for inelastic scattering can be performed using time-of-flight (TOF) measurements with a pseudo-random chopper disc. After deconvolution with the pseudo random chopper sequence, the TOF signal is further transformed to an energy transfer scale which allows to determine inelastic (phonon) scattering events [3]. The scattering spectra were mainly taken with the crystal at room temperature, while a few spectra were taken with the sample cooled down to 115 K. The incident He beam energy was varied between 10 and 18 meV.

The crystal structure of Bi_2Se_3 is rhombohedral, formed of quintuple layers (QLs) which are bound to each other through weak van der Waals forces [240]. The hexagonal unit cell of the Bi_2Se_3 crystal, shown in Fig. 4.22, consists of 3 QLs. Each QL is terminated by Se atoms, giving rise to the (111) cleavage plane that exhibits a hexagonal structure ($a = 4.14$ Å at room temperature [114], see Fig. 4.22(b)). The Bi_2Se_3 crystal was attached onto a sample holder using thermally conductive epoxy. The sample holder was then inserted into the transfer chamber using a load-lock system and cleaved *in situ* [113]. The sample can be heated using a button heater on the backside of the crystal or cooled down to 115 K via a thermal connection to a liquid nitrogen reservoir. The sample temperature was measured using a chromel-alumel thermocouple.

Computational Details

The surface dynamical properties of Bi_2Se_3 were studied using density functional perturbation theory DFPT calculations [241] within the Quantum-ESPRESSO package [210]. Norm-conserving pseudopotentials and the Perdew-Burke-Ernzerhof (PBE) approximation [211] for the exchange and correlation functional were used as implemented in the Quantum-ESPRESSO package. The surface phonon dispersion was calculated using a slab consisting of 3 QLs separated from its periodic replica by 20 Å of vacuum, without the inclusion of spin-orbit corrections (SOC) (see also "Appendix A: Additional calculations and the effect of SOC" for calculations with SOC). For an accurate calculation of the surface lattice vibrations, in principle both SOC and van der Waals (vdW) corrections are necessary, both due to the presence of heavy elements in the compound and the latter to fully account for the weak bonds between the individ-

ual quintuple layers. However, as thoroughly discussed for $Bi_2Te_3(111)$ [111], it appears that for layered crystals with heavy elements SOC alone gives a general softening of the phonon spectrum, compensated by the inclusion of vdW correction, so that satisfactory results are obtained at a minor computational cost without both SOC and vdW corrections and with a better agreement with experiment [4, 242]. Also for Bi_2Se_3 better agreement with the experiment is achieved with no SOC and no vdW corrections (see section "Time-of-flight measurements and phonon dispersion curves"), likely due to a compensation of errors between the underbinding often characterising PBE functionals and SOC contributions and the overbinding due to vdW forces [111]. More precisely, the effect of SOC was found however to be weak for the low energy surface vibrational modes of typical TIs such as Bi_2Te_3 and Sb_2Te_3 [111, 119] while on the other hand it was shown that vdW corrections become important for an exact description of the low energy optical modes of Bi_2Te_3 [111].

Results and discussion

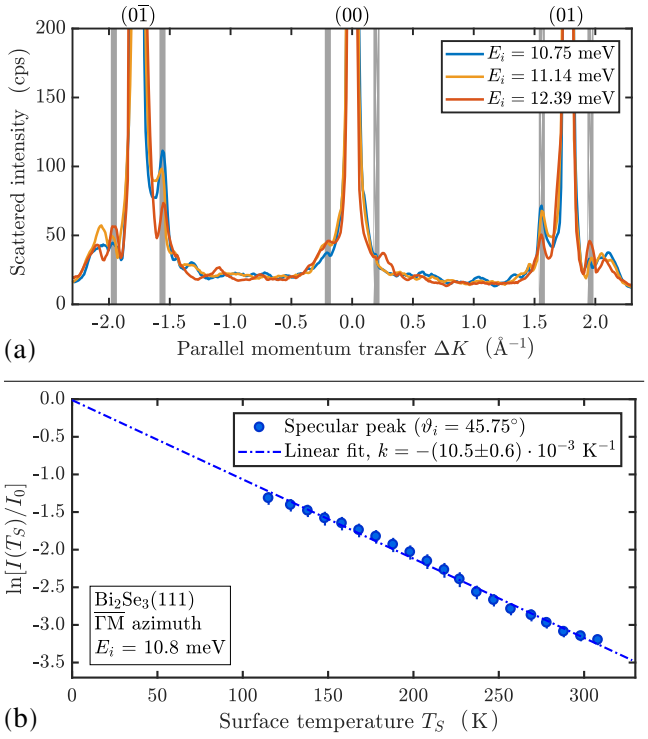

Figure 4.23: (a) HAS diffraction scans for $Bi_2Se_3(111)$ measured at various incident energies with the sample at 113 K, aligned along the $\overline{\Gamma M}$ azimuth. The smaller features between the specular and the two diffraction peaks are due to bound-state resonances and kinematical focusing [24]. The vertical shaded regions next to the diffraction peaks illustrate additional features which appear to be independent of E_i, at a distance of about 0.2 Å^{-1} form the specular and first order diffraction peaks. (b) The temperature dependence of the Debye-Waller exponent of $Bi_2Se_3(111)$ for the specular peak with the sample aligned along $\overline{\Gamma M}$.

Fig. 4.23(a) shows several diffraction scans along the $\overline{\Gamma M}$ azimuth plotted versus momentum transfer $\Delta K = |\Delta \mathbf{K}|$ parallel to the surface, while in Fig. 4.23(b) the temperature dependence of the specular peak intensity is plotted, which can be used to extract the e-ph coupling constant λ (section "Electron-phonon coupling"). The diffraction scans in Fig. 4.23(a) have been measured at three different incident energies E_i, at a sample temperature of 113 K. The intensity scale has been scaled to show additional

features with smaller intensity. Besides some features assigned to bound-state resonances and kinematic focusing, which are easily recognised due to the strong dependence of their position on the incident energy [6], there are features that occur at fixed values of ΔK, independently of E_i with a distance of about $0.2\,\text{Å}^{-1}$ from the specular and first order diffraction peaks, as indicated by the vertical shaded regions (further diffraction scans, including also the $\overline{\Gamma\text{K}}$ azimuth can be found in "Appendix B: Additional diffraction scans").

We recently observed with HAS a multivalley charge density wave (CDW) in Sb(111) originating from the $\overline{\text{M}}$-point electron pockets giving rise to additional peaks in the diffraction pattern [49]. In Bi_2Se_3(111), however, no carrier pockets exist besides the Dirac cone and the quantum-well minibands occurring around the zone center (see Fig. 4.22(c)). The latter provide nesting wavevectors of about $0.2\,\text{Å}^{-1}$ between states of equal spin, which correspond fairly well to the parallel momentum transfers of the satellites observed aside the $(0, \pm 1)$ peaks in HAS diffraction spectra (and likely also aside the specular peak, despite the coincidence with bound-state resonances) (Fig. 4.23(a)). Charge density structures typically show a strong temperature dependent behaviour and vanish when the temperature approaches T_c. In the present work we performed full angular scans at 113 K and room temperature (see Fig. 4.31 in "Appendix B: Additional diffraction scans"). In comparison, the satellite peaks become smaller at room temperature but are still discernible above the inelastic background. While we do not have a full temperature-dependent measurement at hand which would allow a determination of e.g. the critical exponent, it appears from the comparison that any transition temperature would be above room temperature, as we did not go to much higher temperatures due to the low melting point of the material and the risk of degrading the sample at those temperatures.

It should be noted, however, that the observation of satellite peaks whose position is independent of the HAS incident energy is by itself indicative of a long-period superstructure of the electron density, possibly incommensurate or weakly commensurate with the surface atomic lattice. Charge density oscillations as low as 10^{-6} atomic units, presently accessible to HAS, can in principle sustain very low-energy collective phase and amplitude excitations in the meV spectral range [49], and suggest an assignment of the present low-energy branches (section "Low-energy branches").

Time-of-flight measurements and phonon dispersion curves

The phonon energies were determined by performing TOF measurements over a wide range of incident angles between the first-order diffraction peaks and at various beam energies. The phonon dispersion was then obtained by calculating the parallel momentum transfer ΔK for each extracted phonon energy from the conservation laws of energy and parallel momentum providing the so-called scan curve for planar scattering (see Eq. (4.29) in "Appendix C: From TOF measurements to the phonon dispersion and additional TOF data" and Refs. [4, 243]).

In Fig. 4.24(a) an example of a TOF spectrum after conversion to the energy transfer scale is shown. The measurement was taken in the high symmetry direction $\overline{\Gamma\text{M}}$ with an incident beam energy $E_i = 17.97\,\text{meV}$ and at an incident angle of $\vartheta_i = 34.25°$. The TOF spectrum consists of several peaks which are located on the creation ($\Delta E < 0$) as well as the annihilation ($\Delta E > 0$) side. The peak at zero energy transfer corresponds to elastically scattered helium atoms [34, 111]. The scan curve, shown in the two centre panels of Fig. 4.24 for phonon annihilation (blue) and creation (red) events, associates each phonon event with a specific momentum transfer ΔK. The scan curve has been backfolded into the irreducible part of the Brillouin zone and is plotted on top of the calculated dispersion. The different symbols on the scan curves, marking the main inelastic features, have been associated to phonons of different character and polarisation.

The large peaks in the TOF spectra marked with the red circles in Fig. 4.24, correspond to the Rayleigh wave (RW) as seen in the DFPT calculations. Note that in the present TOF spectra the RW exhibits typically the largest intensity of all inelastic events (cfr. the intensities in Fig. 4.24(a)). There is a fair correspondence between the present HAS data and those previously reported by Zhu *et al.* [225]. Curiously Zhu *et al.* stated that the RW is not observed, whereas it appears in their plot, though with only a few data points, in reasonable agreement with the present one in the $\overline{\Gamma K}$ direction; it also occurs in the $\overline{\Gamma M}$ direction, once it is recognised that there is an avoided crossing, so that the RW at $\overline{M}$ is not the lowest mode. There is however an important difference with respect to Zhu *et al.* [225]: Present HAS data do not show any evidence of a KA in the ≈ 8 meV branch for wavevectors around $0.2\,\text{Å}^{-1}$ (see also Fig. 4.33 in "Appendix C: From TOF measurements to the phonon dispersion and additional TOF data") and associated with the nesting at the Fermi level across the Dirac cone (or more likely across the parabolic dispersion of surface quantum-well states [227, 228]).
Fig. 4.25 shows the entire experimental surface phonon dispersion (symbols) superimposed onto the DFPT calculations (grey lines). The different symbols have been associated to phonons of different character and polarisation based on the proximity to particular modes of the DFPT calculations. In total, we are able to distinguish at least 8 different branches.

The polarisation analysis of the calculated surface phonon modes can be found in Fig. 4.26 where the intensity of each polarisation projected onto the corresponding layer is given by the colour code. The left column shows the longitudinal polarisations for the first (L1), second (L2), and third (L3) layer. The right column shows the shear vertical polarisation for the first three layers (SV1-SV3), while the shear horizontal polarisation can be found in Fig. 4.30 of "Appendix A: Additional calculations and the effect of SOC". The theoretical dispersion curves are seen to agree quite well with the HAS data and also with the experimental Raman-active modes at $\overline{\Gamma}$ (green triangles in Fig. 4.26 according to [244]).
A closer comparison of the experimental data points in Fig. 4.25 with Fig. 4.26 shows that mainly phonon events with the largest amplitude in the two topmost layers of the sample are observed in the experiment. In particular in the low energy region (< 10 meV), most contributions come from phonons with the largest amplitude in the second layer (L2, SV2), which is a Bi layer and therefore about 2.5 times heavier than the first Se layer. The most prominent mode in the TOF spectra, the RW, corresponds predominantly to L and SV polarisations, due to its elliptical polarisation, with a particularly strong SV2 component at the Brillouin zone boundary.

Note that the calculation does not reproduce the KA reported by Zhu *et al.* [225] (see "Appendix A: Additional calculations and the effect of SOC" for calculations with SOC), in agreement with other recent *ab initio* calculations including SOC by Heid *et al.* [226] as well as with the experimental and theoretical studies of Bi_2Te_3(111) [111]. Heid *et al.* [226] suggested that the KA observed by Zhu *et al.* [217, 225] may be connected to a strong e-ph interaction in the doped bulk material rather than to a surface state. According to their calculations, the largest contribution to the e-ph coupling comes from an in-plane polar-type branch in the optical region between 10 and 18 meV [226].

In fact, the strong dispersion of the optical phonon modes (Fig. 4.26), also found in Bi and Sb tellurides [111, 119] may already be regarded as a manifestation of a significant e-ph interaction. In addition, Sobota *et al.* [245] reported a strong coupling of the A_{1g}^1 mode at a phonon energy of 8.48 meV which manifests itself in time-dependent renormalisations of the Dirac cone in angle-resolved photoemission spectroscopy (ARPES) measurements. The excellent quality of the DFPT calculations is further confirmed upon comparison with the experimentally observed softening of the A_{1g}^1 phonon mode at the surface, as reported by Sobota *et al.* [245] and as shown by the blue triangle in Fig. 4.26: The softening becomes apparent for the two lower branches of the DFPT calculations for 3 QLs.

We note that in the region around 15 meV the number of experimental data points is small and any

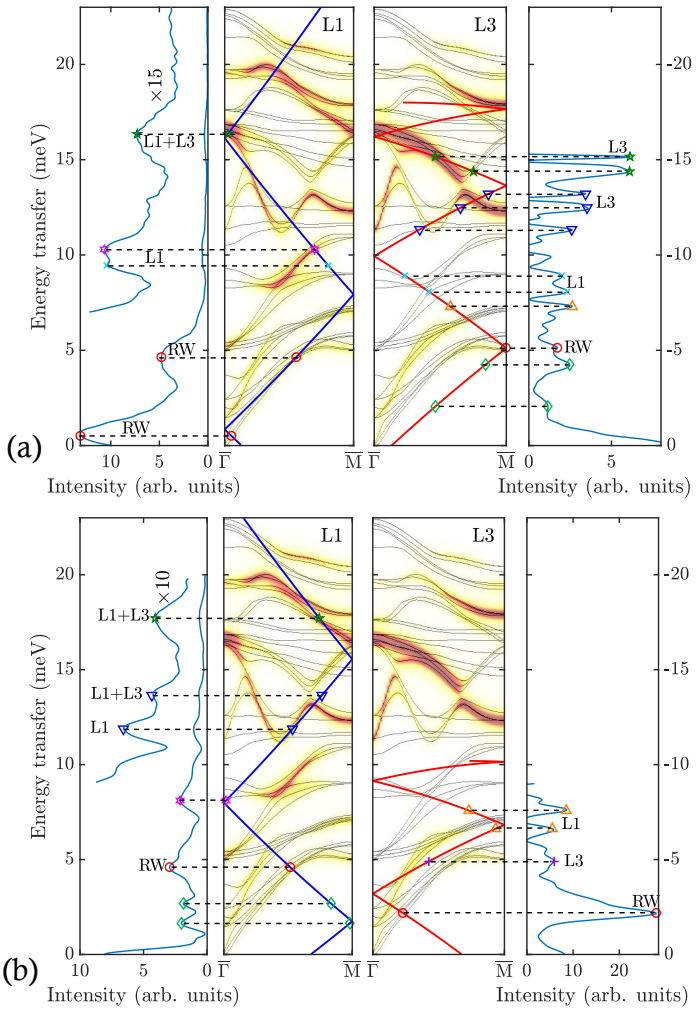

Figure 4.24: Plot of two typical TOF measurements with the sample along $\overline{\Gamma M}$ and at room temperature. In (a) the incident energy is $E_i = 17.97\,\text{meV}$ with $\vartheta_i = 34.25°$ while in (b) $E_i = 10.19\,\text{meV}$ and $\vartheta_i = 40.25°$. The left and right-most panel show the TOF spectrum after conversion to energy transfer. The blue (phonon annihilation, $\Delta E > 0$) and red (phonon creation, $\Delta E < 0$) lines in the centre panels show the scan curves superimposed onto the calculated dispersion using DFPT (The colour code giving the intensity of the longitudinal L1 and L3 modes projected onto the first and third surface layer, respectively, is that of Fig. 4.26). The symbols denote peaks in the TOF spectrum which have been assigned to phonon events (RW = Rayleigh wave). The two distinct low-energy peaks (green diamonds) observed on the creation (panel (a)) and annihilation (panel (b)) sides in the phonon gap below the RW are tentatively assigned to low-energy collective surface electronic excitations, associated with the long-period surface superstructure and revealed through HAS bound-state resonance enhancement.

mode assignment is probably accompanied by a large uncertainty, due to the strong dispersion and the avoided crossings of the calculated curves. Nevertheless it appears from the DFPT calculations that the optical phonon branch starting at about 16.5 meV at the $\overline{\Gamma}$-point softens to about 11 meV along $\overline{\Gamma M}$, in particular when considering the strong longitudinal character of this mode on the first atomic layer as shown in the top-left panel of Fig. 4.26. Such a softening could be caused by a screening of the quantum well electrons in analogy to the electron screening manifest as phonon softening of the optical phonon mode at 8.48 meV in the work of Sobota *et al.* [245], although in the latter case coupling appears mainly

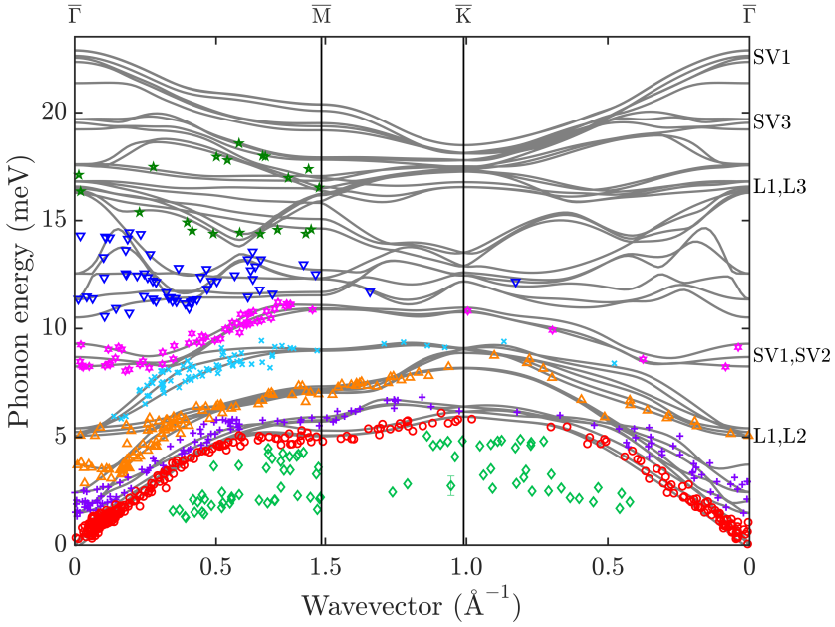

Figure 4.25: Comparison of the measured phonon dispersion relation with DFPT calculations for three quintuple layers. The solid grey lines represent the DFPT calculation while different symbols for the experimentally determined points correspond to different phonon modes. The assignment of the symbols is based on the proximity to particular modes.

to the electrons of the Dirac cone rather than the quantum well states. It is also in accordance with our findings about the e-ph coupling (section "Electron-phonon coupling") which appears to be larger in the presence of a 2DEG upon comparison with systems that exhibit exclusively the Dirac topological states [26].

We turn now to the acoustic energy region and in particular the group velocity of the RW. In the long wavelength limit (close to $\overline{\Gamma}$) the dispersion relation of the RW is linear. Its slope provides the RW group velocity in the two symmetry directions $\overline{\Gamma M}$ and $\overline{\Gamma K}$:

$$\overline{\Gamma M} : v_{RW}(112) = (1.63 \pm 0.07)\ \text{km/s}$$
$$\overline{\Gamma K} : v_{RW}(110) = (1.80 \pm 0.15)\ \text{km/s}\ .$$

In order to appreciate the degree of localisation of the RW in the two symmetry directions, these values are to be compared with the corresponding speeds of sound. The present DFPT values (compared with values in parentheses derived from the available elastic constants [246]) are:

$$\overline{\Gamma M}: \quad v_{T,SV} = 1.757\ (1.91)\ \text{km/s} \quad v_{T,SH} = 2.290\ (2.24)\ \text{km/s}$$
$$\overline{\Gamma K}: \quad v_{T,SV} = 3.227\ (2.93)\ \text{km/s} \quad v_{T,SH} = 1.416\ (1.22)\ \text{km/s}\ .$$

It appears that the RW has a velocity in the $\overline{\Gamma M}$ direction smaller than both transverse bulk values and is therefore a localised surface wave, whereas in the $\overline{\Gamma K}$ direction it has a velocity larger than that of the SH transverse sound, and is therefore a pseudo-surface wave [247, 248]. Actually in the absence of mirror symmetry for the sagittal plane in this direction, the RW is a resonance. The fact may have suggested (see Zhu *et al.* [217, 225]) that in $Bi_2Se_3(111)$ the RW is suppressed but the present comparison with the DFPT calculation confirms that the RW is actually observed in both directions, though as a resonance

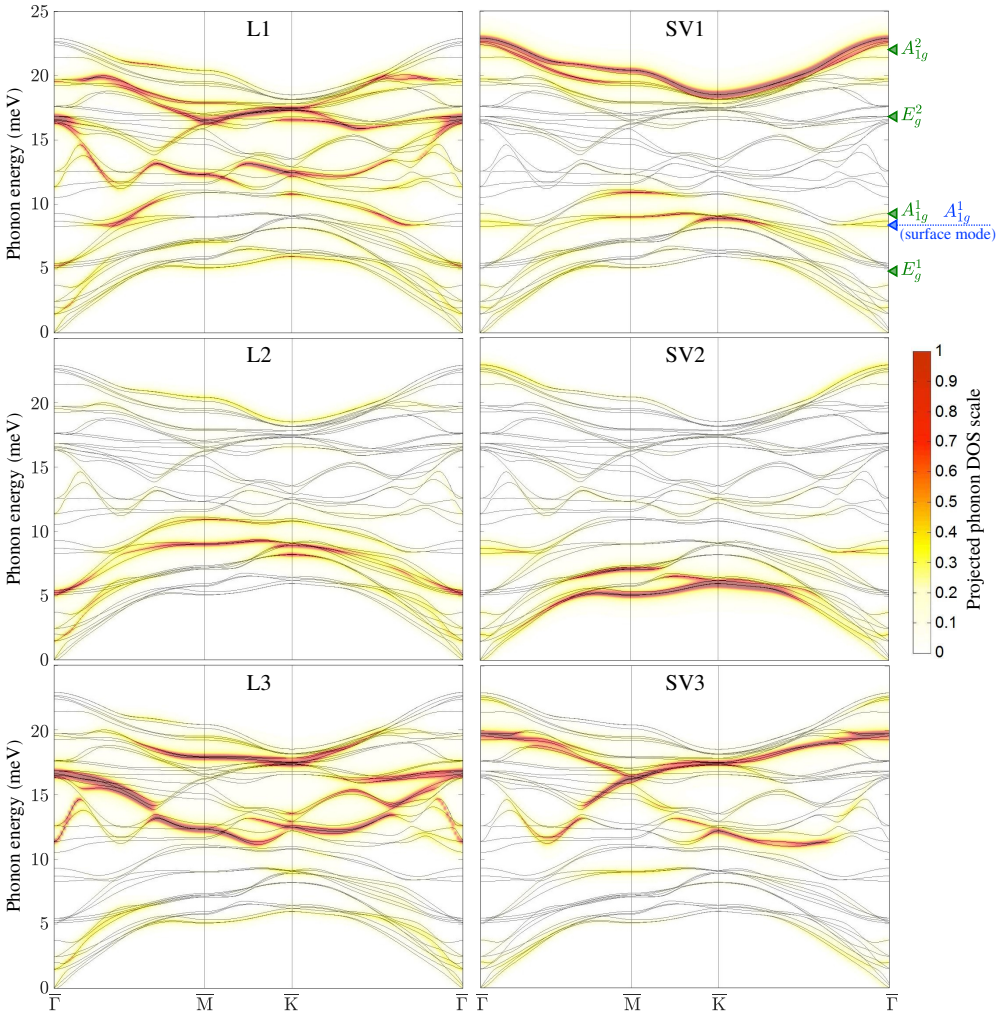

Figure 4.26: Polarisation of the calculated phonon dispersion of Bi_2Se_3 from DFPT. The left column shows longitudinal polarisation for the topmost three atomic layers (L1-L3). The right column shows shear vertical polarisation (SV1-SV3). The colour code bar on the right-hand side gives the intensity of the mode projected onto the corresponding layer. The green triangles at the top-right ordinate indicate the experimental energies of bulk Raman active modes according to Ref. [244], while the blue triangle shows the surface phonon softening according to Ref. [245].

along $\overline{\Gamma K}$. Values for the bulk longitudinal ($v_L = 2.9$ km/s) and transverse ($v_T = 1.7$ km/s) group velocities of Bi_2Se_3 have also been reported in the framework of the isotropic elastic continuum theory [218, 249]. In this approximation the corresponding RW velocity, obtained by solving the cubic Rayleigh equation [250], would be $v_{RW} = 1.56$ km/s in any direction.

Low-energy branches

The measured HAS-TOF spectra displayed in Fig. 4.24 show also distinct peaks yielding two branches of elementary excitations with an energy below the RW branch (green diamonds in Fig. 4.25). On the basis of present DFPT surface phonon dispersion curves, they cannot be attributed to any possible phonon branch of the ideal surface. HAS from conducting surfaces exclusively occurs through the interaction (mostly Pauli repulsion) with the surface electron density, and therefore also electronic excitations in the THz range can be observed by HAS, with a 0.5 meV resolution and sensitivity to charge density

oscillations in the 10^{-6} atomic units range.

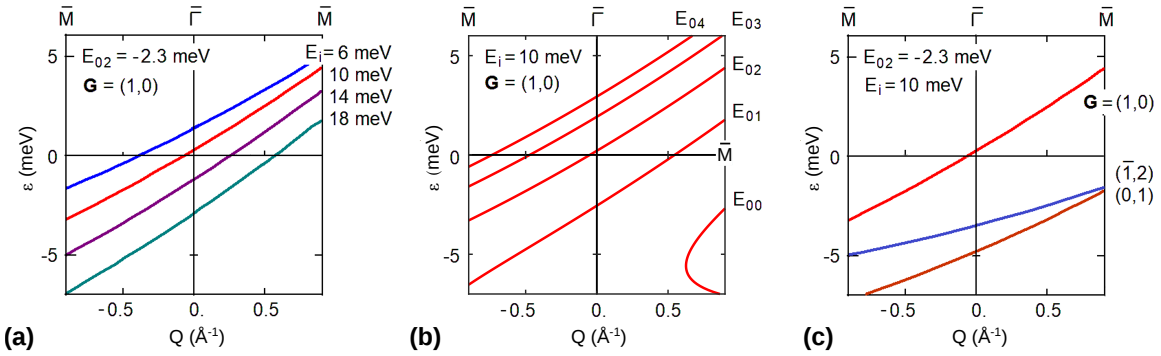

Figure 4.27: Inelastic bound-state resonance conditions along the $\overline{\Gamma M}$ direction in the first Brillouin zone: (a) for $\mathbf{G} = (1,0) \equiv (1.76,0)$ Å^{-1}, the bound state $n = 2$ and different incident energies; (b) for a given $E_i = 10$ meV, $\mathbf{G} = (1,0)$ and the different bound states $n = 0, 1 \ldots 4$; (c) for $E_i = 10$ meV, the bound state $n = 2$ and three different $\mathbf{G}$ vectors $(1,0), (\bar{1},2) \equiv (0, 3.05)$ Å^{-1}, $(0,1) \equiv (0.88, 1, 53)$ Å^{-1}. Here, the integer indices refer to the hexagonal reciprocal lattice base, while the components in Å^{-1} units are those of $\mathbf{G} = (G_\parallel, G_\perp)$. Other $\mathbf{G}$-values yield inelastic resonances in the low-energy range $|\varepsilon| < 5$ meV only for wavevectors Q outside the first BZ. Suitable combinations of E_i, E_{0n}, and of the $\mathbf{G}$-vector permit to scan the phonon gap region below the RW branch, which can be used to tune the conditions for localised excitations, to detect those via a resonance enhancement.

Actually the observed low-energy branches are reminiscent of those recently observed with HAS in Sb(111), which have been attributed to elementary excitations (phasons/amplitons) of a multi-valley CDW [49]. The concomitant presence of a commensurate component associated with the $\overline{\text{M}}$-point electron pockets at the Fermi level, and an incommensurate one due to the hole pockets along the $\overline{\Gamma M}$ direction, allows for collective excitations with a comparatively small gap at $Q = 0$. On the other hand no low-energy phason/ampliton modes have been detected with HAS for the perfectly commensurate multivalley CDW reported in the quasi-1D surface Bi(114) [28], discommensuration being a requisite for depinning and a vanishing/small gap at $\overline{\Gamma}$. $Bi_2Se_3(111)$ has no pocket states at the Fermi level, besides the rings around $\overline{\Gamma}$ of the surface topological Dirac and the quantum-well states [227, 228]. The satellites near the HAS diffraction peaks (see Fig. 4.23(a)) suggest some long-period charge-density structures and possibly low-energy collective excitations. In order to detect the associated, seemingly small inelastic features in the TOF spectra, we rely on the bound-state resonance enhancement method (Ref. [231] and Chap. 10 of Ref. [16]), applicable to highly corrugated surfaces and successfully used to detect with HAS high-energy optical surface modes in ionic crystals [16, 251]. The complete set of He-surface bound states has been measured previously [24].

Bound-state inelastic resonances occur in the HAS-TOF spectrum, with a possibly large enhancement of the inelastic intensities, at the locus of intersections of the scan curve Eq. (4.26) [4] with the inelastic bound-state resonance condition Eq. (4.27) (see Chap. 30 of Ref. [16]). For elementary excitations with an energy $\Delta E = \varepsilon$ and wavevector $\Delta K = Q$ the equations become:

$$k_i \sin\vartheta_i + Q = \sin\vartheta_f \sqrt{2m(E_i + \varepsilon)/\hbar} \tag{4.26}$$

$$E_i + \varepsilon = -|E_{0n}| + \frac{\hbar^2}{2m}\left[(k_i \sin\vartheta_i + Q + G_\parallel)^2 + G_\perp^2\right]. \tag{4.27}$$

At the mentioned intersection of Eq. (4.26) and Eq. (4.27), an elementary excitation with (ε, Q) assists the selective adsorption of the atom of mass m, incident energy E_i, wavevector k_i and angle ϑ_i into a

bound state of energy $-|E_{0n}|$, via the exchange of a surface reciprocal lattice vector $\mathbf{G} = (G_\parallel, G_\perp)$. On returning the **G**-vector to the surface lattice, the atom is selectively desorbed from the bound state into the final angle ϑ_f. In Eq. (4.27) the vector **G** has been conveniently expressed via its components parallel and orthogonal to the scattering plane, respectively. In $Bi_2Se_3(111)$ the measured He-surface bound-state energies [24] are $E_{0n} = -5.6, -3.8, -2.3, -1.2, -0.5$ meV for $n = 0$, 1, 2, 3, 4, respectively. For a fixed scattering geometry $\vartheta_i + \vartheta_f = \vartheta_{SD}$ (here $\vartheta_{SD} = 91.5°$), Eq. (4.26) and Eq. (4.27) provide, via the elimination of $\vartheta_i = \vartheta_{SD} - \vartheta_f$, the locus of intersections $\varepsilon = \varepsilon_{E_i,n;\mathbf{G}}(Q)$ for any incident energy E_i, bound state n and reciprocal surface vector **G**.

The three panels of Fig. 4.27 show some plots of $\varepsilon = \varepsilon_{E_i,n;\mathbf{G}}(Q)$ in the $\overline{\Gamma M}$ direction for: (a) different values of the incident energy E_i at a given bound state ($n = 2$) and $\mathbf{G} = (1, 0)$; (b) different bound state energies at a given incident energy $E_i = 10$ meV; (c) several different **G**-vectors at a given incident energy $E_i = 10$ meV and for the bound state $n = 2$. The functions $\varepsilon = \varepsilon_{E_i,n;\mathbf{G}}(Q)$ cross the phonon gap below the RW in the first BZ. In practice the phonon gap can be fully scanned by the resonance curves $\varepsilon = \varepsilon_{E_i,n;\mathbf{G}}(Q)$ upon varying the incident energy, so as to detect, via resonance enhancement, weak elementary excitations.

Since the low-energy data points appear to align along two dispersion curves, independently of the incident energy, as well as of n and **G**, rather than being spread over the entire gap, they cannot be attributed to a resonance-enhanced many-phonon background. Furthermore, frustrated translational modes of adsorbates like CO would show no dispersion and would appear at higher vibrational energies [252]. More likely these points indicate two branches of low-energy excitations associated with the surface charge-density superstructure observed in the diffraction spectra, as anticipated above.

In this respect it is worth mentioning a recent work by Shvonski *et al.* [235] where it is argued that a strong e-ph interaction affecting the surface 2DEG of a 3D topological crystal allows for collective polaron excitations (plasmon-polarons). Their dispersion is predicted to be that of an acoustic plasmon running below the single-particle excitation spectrum as an effect of the polaron-polaron attractive interaction. The theoretical analysis by Shvonski *et al.* [235] is actually interpreting the recent observation with high-resolution electron energy loss spectroscopy (HREELS) by Jia *et al.* [232] of an anomalous acoustic plasmon (AAP) mode from the topologically protected states of $Bi_2Se_3(111)$, with energy between 0 and 6.5 meV (and its continuation in the second zone up to ≈ 10 meV). The present HAS data do not permit to identify this AAP due to its superposition with the RW in the first BZ and in part with other phonon branches in its continuation.

Electron-phonon coupling

As shown in recent papers [26, 32, 47], the temperature dependence of the Debye-Waller (DW) exponent plotted in Fig. 4.23(b) permits to extract for a conducting surface the mass-enhancement parameter λ expressing the electron-phonon coupling strength. It is related to the DW exponent by the equations:

$$\lambda = \frac{\pi}{2n_s}\alpha\,, \quad \alpha \equiv \frac{\phi}{A_c\, k_{iz}^2}\frac{\partial \ln I(T_S)}{k_B\, \partial T_S}\,, \tag{4.28}$$

where $\phi = 4.9$ eV is the work function [129], $A_c = 14.92$ Å^2 the unit cell area, $I(T_S)$ the He-beam specular intensity, T_S the surface temperature, $k_{iz} = 3.18$ Å^{-1} the normal component of the incident wavevector, and n_s the number of conducting layers which contribute to the phonon-induced modulation of the surface charge density[5]. The latter is estimated to be $n_s = 2\lambda_{TF}/c_0$, where λ_{TF} is the Thomas-Fermi screening

[5]The (bulk) carrier concentration as extracted from Hall measurements of the current sample is in the region $(1.75 - 1.8) \cdot 10^{18}$ cm^{-3} , i.e. a particularly small conductivity in the bulk suggesting that the carrier concentration at the

length characterising the surface band-bending region (here $\approx 6\,\mathrm{nm}$) [227], $c_0 = 9.6\,\text{Å}$ the QL thickness, and the factor 2 indicates the 2DEG multiplicity as observed with ARPES in the current Bi_2Se_3 sample [227]. With these values and the experimental DW derivative with respect to T_S from Fig. 4.23(b), we obtain $\lambda = 0.51$.

We note that there appear to be weak oscillations in the temperature dependent data of Fig. 4.23(b). While deviations from a linear behaviour could occur due anharmonic effects at higher temperatures, or due to phonon-phonon coupling events, it appears from the experimental uncertainties that a linear regression provides still an accurate approximation in the present case. It should also be mentioned that, unlike in the case of low-index metal surfaces, characterised by a soft-wall repulsive potential and negligible corrugation, here the large electronic corrugation [24] implies a hard-wall potential. In this case one needs to correct k_{iz}^2 so as to account for the acceleration impressed by the attractive part of the potential on the He atom when approaching the surface turning point (Beeby correction [34]). Therefore k_{iz}^2 is replaced by $k_{iz}^{'2} = k_{iz}^2 + 2mD/\hbar^2$, where m is the He mass and $D = 6.54\,\mathrm{meV}$ the He-surface potential well depth [24]. With the Beeby correction it is found $\lambda = 0.23$.

The value compares quite well with values in the literature derived from other experiments, e.g., $\lambda = 0.25$ [213], and $\lambda = 0.17$ [215] from ARPES measurements and $\lambda = 0.26$ [253] from Landau level spectroscopy. A theoretical study by Giraud *et al.* [218] with phonons calculated in the isotropic continuum limit gives $\lambda = 0.42$, whereas for other ARPES measurements, where only Dirac states appear to be involved, values of λ as low as 0.076 to 0.088 have been found [214].

From the comparison it appears that the presence of a 2DEG due to quantum-well minibands (at least two in the present analysis) plays an important role in raising the e-ph coupling strength, which is quite small when exclusively due to the Dirac topological states, to values in the range of $0.2 - 0.4$. It seems to be a general phenomenon for TIs belonging to the class of bismuth chalcogenides as reported by Benedek *et al.* [26]. The same conclusion follows from the theoretical analysis by Heid *et al.* [226], who showed that raising the Fermi level from the Dirac point to above the conduction band minimum gives a corresponding increase of λ from values well below 0.1 to values in the range above 0.2, with a substantial contribution from interband coupling and in very good agreement with the present analysis. The role of n-type doping contributing to the formation of the surface quantum-well 2DEG is quite clear in the analysis of the e-ph coupling strength in Cu-doped Bi_2Se_3 , where an analysis based on the McMillan formula [254], indicates a value for λ as large as 0.62 [214].

Conclusions

In summary, we have determined the surface phonon dispersion curves of Bi_2Se_3 along both high symmetry directions, where the largest inelastic scattering intensity is provided by the Rayleigh wave. Thus our measurements show in contrast to previous studies that the Rayleigh mode exists and is a localised surface mode in one of the high-symmetry directions ($\overline{\Gamma\mathrm{M}}$), while in the other high-symmetry direction it is actually a pseudo-surface wave ($\overline{\Gamma\mathrm{K}}$). Comparison with density functional perturbation theory calculations shows excellent agreement with the experimental data. In addition to the phonon-related losses, we observe two additional dispersion curves in the gap well below the Rayleigh mode. These two low-energy branches may correspond to collective low-energy excitations of surface electrons.

The appearance of these collective electronic excitations in an unprecedentedly low energy region is probably associated with a small surface charge density and an appreciable electron-phonon coupling ($\lambda = 0.23$). However, much more detailed experiments and theoretical analysis will be needed in order

surface may even be larger, compared to the first generation samples [227] which had a much larger bulk charge carrier concentration.

to fully understand these excitations; e.g., what is the influence of the carrier concentration upon doping and what is the role of both the Dirac and the quantum-well states, with the latter providing a much larger electron-phonon interaction than the former. The analysis advocates for a more systematic study by means of elastic and inelastic HAS spectroscopy of the surface structure, the low-energy collective excitations, and the electron-phonon interaction of interesting 2D materials, where the superior space and energy resolution of HAS is hardly attainable with other current surface probes.

Acknowledgment

We are grateful to Prof. Evgueni V. Chulkov (DIPC) and Prof. Krzysztof Kempa (Boston College) for useful discussions. The authors are grateful for financial support by the FWF (Austrian Science Fund) within the project P29641-N36 and A.T acknowledges financial support within the project J3479-N20. We would like to thank the Aarhus University Research Foundation, VILLUM FOUNDATION via the Centre of Excellence for Dirac Materials (Grant No. 11744) and the SPP1666 of the DFG (Grant No. HO 5150/1-2) for financial support. M. Bremholm acknowledges financial support from the Center of Materials Crystallography (CMC) and the Danish National Research Foundation (DNRF93).

Appendices

Appendix A: Additional calculations and the effect of SOC

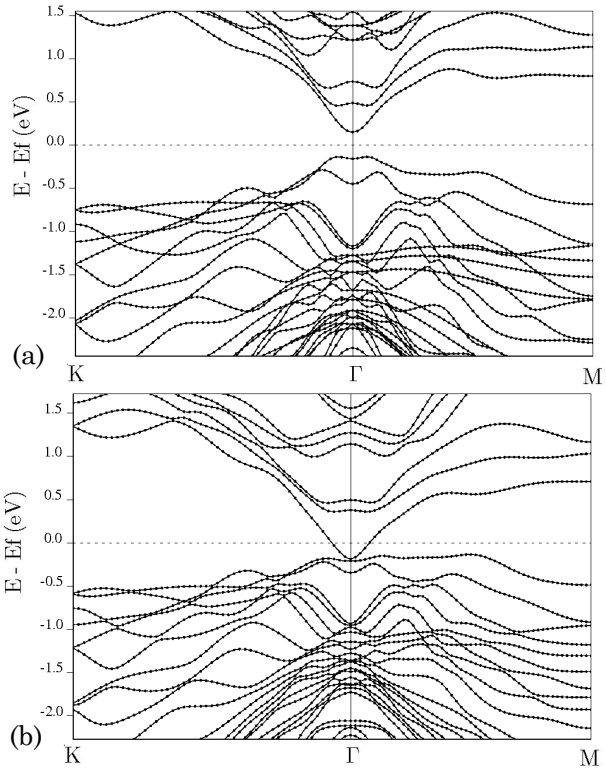

Figure 4.28: Surface electronic band structure of Bi_2Se_3(111) omitting spin-orbit coupling (a). The topological surface states appear when SOC is included as shown in (b).

Without SOC, Bi_2Se_3 exhibits a band gap, not only in the bulk but also at the surface with a band gap

of 0.35 eV as evident from density functional theory (DFT) calculations (Fig. 4.28(a)). By including SOC as shown in Fig. 4.28(b), the electronic band dispersion becomes gapless, with spin-polarised and Dirac cone shaped surface bands around the $\overline{\Gamma}$-point in the typical manner of 3D topological insulators.

The topologically protected Dirac cone forms a small Fermi circle around the $\overline{\Gamma}$-point which cannot be properly described with a coarse mesh and a large smearing resulting in the impossibility to capture subtle effects, such as the proposed KA [225] with a standard calculation. In order to verify the effect of such states on surface phonons we repeated the phonon calculations at the Q-point corresponding to the nesting vector ($2k_F$) by including SOC. We compared the result with that obtained by omitting the SOC.

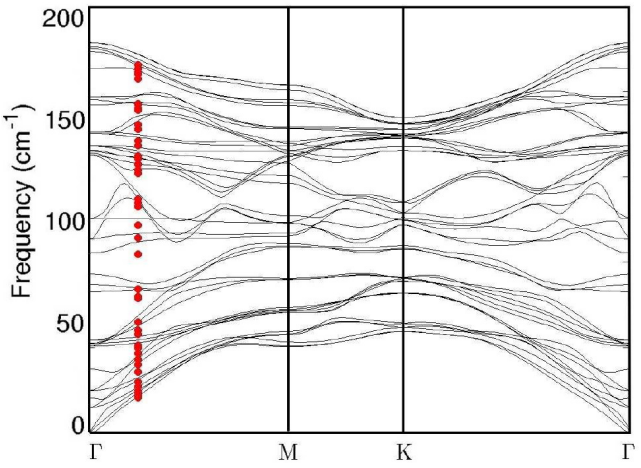

Figure 4.29: Surface phonon dispersion of Bi_2Se_3 omitting (black continuous line) and including spin-orbit coupling (red dots) at a Q-vector corresponding to the nesting vector $2k_F$. The inclusion of SOC gives rise to a softening of the phonon modes but no evidence for a KA is found.

To perform these calculations we had to improve the sampling of the Brillouin zone close to the Fermi surface which is particularly important to resolve a possibly existing anomaly. Given the peculiar shape of the Fermi surface in the $Bi_2Se_3(111)$ slabs consisting of a ring around the $\overline{\Gamma}$-point, we used a graded k-point mesh (equivalent to a $50 \times 50 \times 1$ uniform mesh) near the $\overline{\Gamma}$-point point and a coarser one (equivalent to a $8 \times 8 \times 1$ mesh) near the zone boundary. The results are reported in Fig. 4.29. A one to one comparison between phonon modes calculated with and without SOC shows that there is no evidence of a KA induced by the presence of the surface metallic states, involving any of the surface phonon modes. The spin-orbit coupling results merely in a overall softening of the phonon modes of at most 6 %.

In addition to the shear vertical and shear horizontal phonon densities shown in the main part of the article, Fig. 4.30 shows the shear horizontal polarisations projected onto the first, second and third layer (SH1, SH2, SH3). If the scattering plane, defined by the incoming and scattered He beam, coincides with a mirror plane of the surface, the detection of purely SH modes is in principle forbidden due to symmetry reasons [108] and we show the calculations of the SH modes here for completeness. However, phonon modes often exhibit a mixing of polarisation components and even a purely SH mode may give rise to charge density oscillations above the first atomic layer which are eventually observed in inelastic He atom scattering.

Appendix B: Additional diffraction scans

A comparison of two angular scans with 113 K and room temperature in the $\overline{\Gamma M}$ azimuth can be seen in Fig. 4.31. It shows that at higher temperatures the satellite peaks at constant momentum transfer are

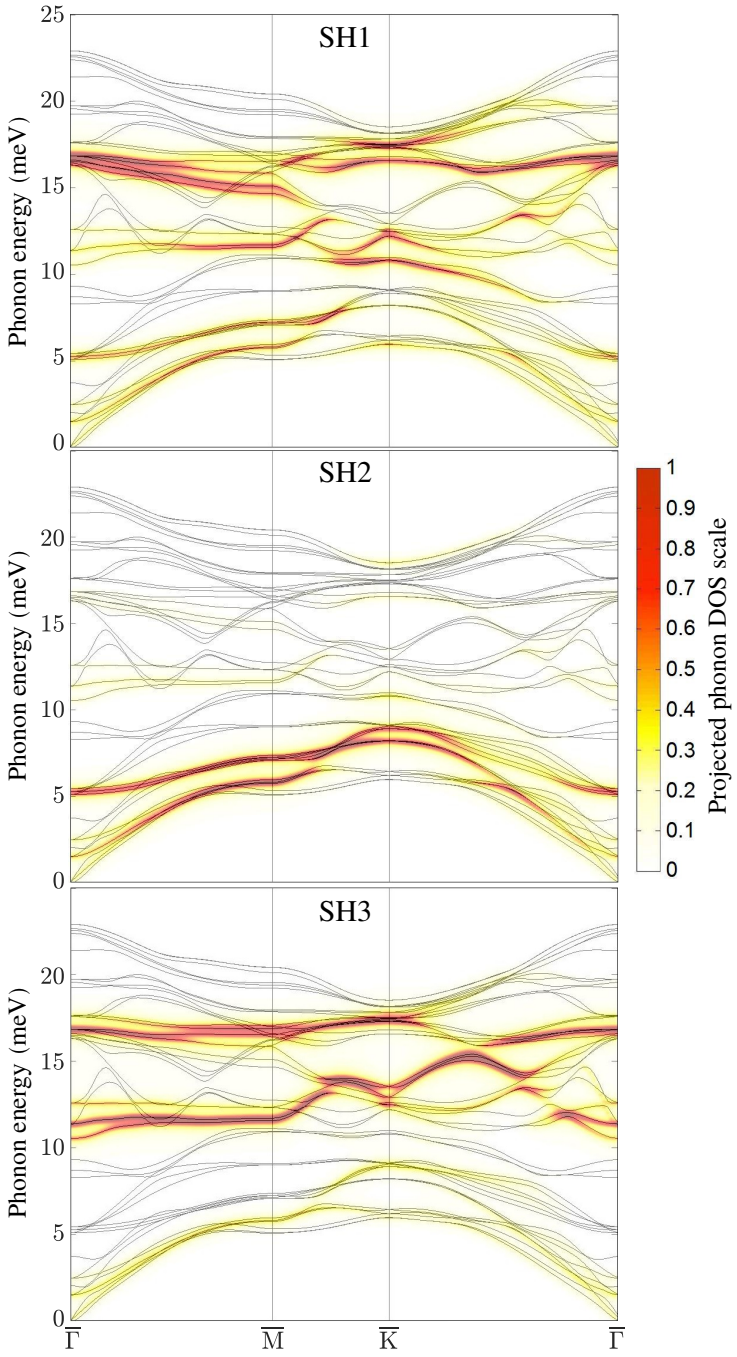

Figure 4.30: Shear horizontal (SH) polarisation of the calculated phonon dispersion of Bi_2Se_3 for the topmost three atomic layers (SH1-SH3) from DFPT without SOC. The colour code bar on the right-hand side gives the intensity of the mode projected onto the corresponding layer.

still present even though they are much smaller and sometimes appear as mere shoulders close to the diffraction peaks. In addition to the diffraction scans along $\overline{\Gamma M}$ which are already shown in the main part of the article, Fig. 4.31 shows a diffraction scan along the $\overline{\Gamma K}$ azimuth.

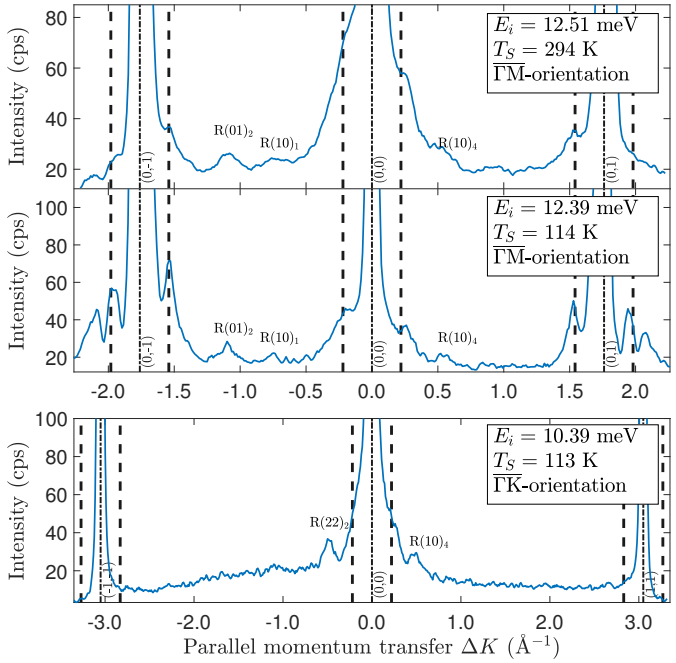

Figure 4.31: HAS diffraction scans for $Bi_2Se_3(111)$ measured at room temperature and 113 K along the high symmetry direction $\overline{\Gamma M}$ and at low temperature along $\overline{\Gamma K}$. The smaller features between the specular and the two diffraction peaks are due to bound-state resonances and kinematical focusing [24].

Note that along $\overline{\Gamma K}$ there is no evidence for additional peaks close to the diffraction peaks, despite two small features close to the specular reflection which can be assigned to resonances [24]. The fact that these peaks appear only along $\overline{\Gamma M}$ is indicative of the hexagonal shape of the quantum well states giving rise to a multitude of connecting vectors with similar momentum transfer between the flat sides of the hexagon and thus along the $\overline{\Gamma M}$ azimuth.

Appendix C: From TOF measurements to the phonon dispersion and additional TOF data

The phonon energies were determined by performing TOF measurements over a wide range of incident angles between the first-order diffraction peaks and at various beam energies. The phonon dispersion was then obtained by calculating the parallel momentum transfer $\Delta K = |\Delta \mathbf{K}|$ for each extracted phonon energy ΔE from the conservation laws of energy and parallel momentum providing the so-called scan curve for planar scattering [4, 243]:

$$\frac{\Delta E}{E_i} + 1 = \frac{\sin^2 \vartheta_i}{\sin^2 \vartheta_f} \left(1 + \frac{\Delta \mathbf{K}}{\mathbf{K}_i}\right)^2 \tag{4.29}$$

where E_i is the energy of the incident beam, $\mathbf{K}_i$ is the parallel component of the incident wavevector, and ϑ_i and ϑ_f are the incident and final angle, respectively.

Fig. 4.32 and Fig. 4.33 show some further examples of measured TOF spectra along the $\overline{\Gamma M}$ azimuth

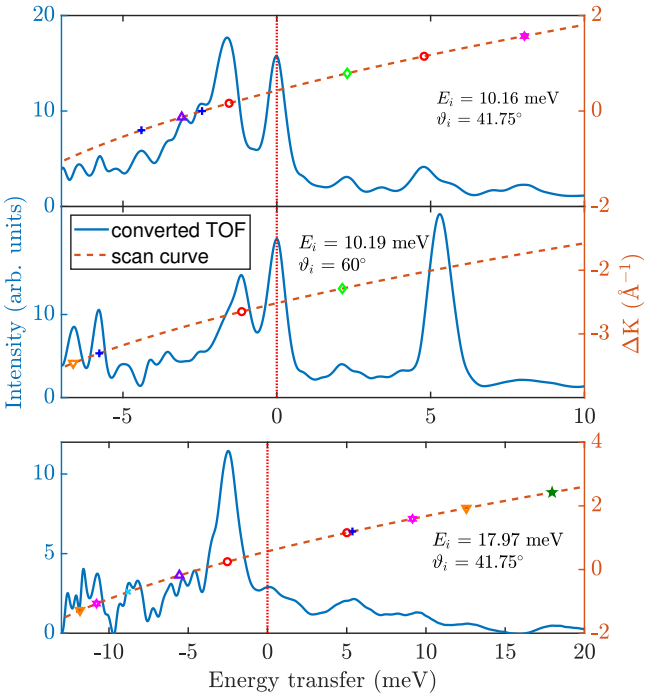

Figure 4.32: Comparison of different TOF spectra in the $\overline{\Gamma M}$ direction with various incident Energies E_i and angles ϑ_i. For the two upper graphs the nozzle temperature was set to 50 K and for the bottom one to 80 K while the sample was held at room temperature. The vertical red dotted line corresponds to elastically scattered atoms. The dashed line describes the scan curve which connects energy transfer with momentum transfer (y-axis on the right-hand side). The symbols denote peaks in the TOF spectrum which have been assigned to phonon events (same symbols as the main part of the article).

and the sample at room temperature. Each TOF spectrum consists of various peaks which are located on the creation (negative x-axis, $\Delta E < 0$) as well as the annihilation (positive x-axis, $\Delta E > 0$) side. The peak at zero energy transfer corresponds to elastically scattered helium atoms due to the diffuse elastic peak which is caused by scattering from surface imperfections such as steps [6, 34]. The scan curve associates each phonon event with a specific momentum transfer ΔK based on (Eq. (4.29)), since the incoming helium atom looses or gains momentum via inelastic scattering from a phonon.

Fig. 4.32 shows an additional set of TOF-spectra along the $\overline{\Gamma M}$ direction. Most measurements covering the low energy region with the acoustic phonon modes where performed with a ≈ 10 meV beam (top and centre panel in Fig. 4.32), while for the optical phonon modes higher incident beam energies (bottom panel in Fig. 4.32) where used, in order to cover the optical energy region on the creation side. Note that the particularly strong peak at around 5.5 eV in the centre panel is not assigned to a phonon event. This seemingly inelastic feature originates from elastic scattering and is caused by the outer tails of the velocity distribution in the incident beam. These so-called deceptons or spurions occur within the vicinity of the diffraction peaks and give rise to a large intensity in the inelastic spectra due to their elastic nature [255].

As mentioned in the main part of the article, there is no evidence for a strong KA in our measurements as reported by Zhu *et al.* [217, 225], who observed a strong V-shaped indentation at $\Delta K \approx 0.25$ Å^{-1} for an optical phonon branch originating at 7.4 meV at the $\overline{\Gamma}$-point. The scan curve on the phonon annihilation side (blue curve) in Fig. 4.33(a) covers exactly the 6–8 meV close to the $\overline{\Gamma}$-point. Neither the DFPT calculations (grey lines in Fig. 4.33(a)) support such a KA nor does the experimental data which in turn even shows a minimum of the scattered inelastic intensity in the 6–8 meV region of the $\Delta E > 0$

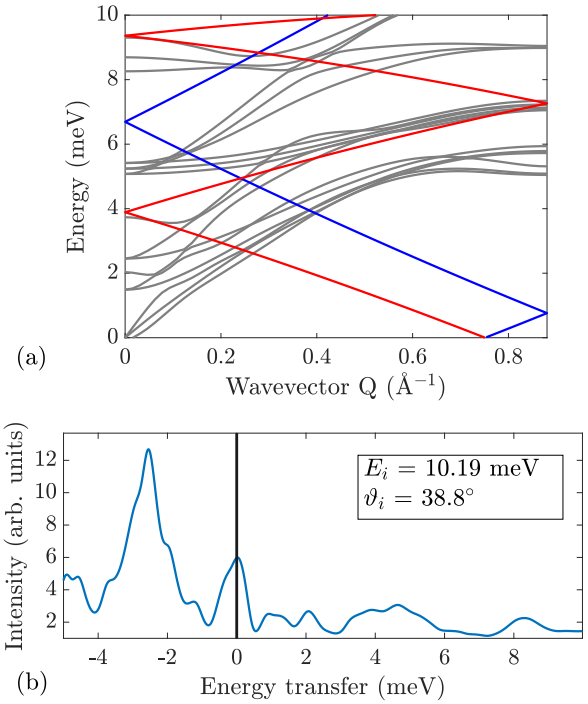

Figure 4.33: In (b) the TOF spectrum with the x-axis converted to energy transfer is shown. (a) depicts the corresponding scan curve (Eq. (4.29)), backfolded into the first Brillouin zone and superimposed onto the results of the DFPT calculation (grey lines).

side (Fig. 4.33(b)).

4.5 Inelastic Helium Atom Scattering from $Sb_2Te_3(111)$: Phonon Dispersion, Focusing Effects and Surfing

This section consists of the following published publication:

Inelastic Helium Atom Scattering from $Sb_2Te_3(111)$: Phonon Dispersion, Focusing Effects and Surfing

A. Ruckhofer*, S. Halbritter, H. E. Lund, A. J. Holt, M. Bianchi, M. Bremholm, G. Benedek, P. Hofmann, W. E. Ernst, and A. Tamtögl

Physical Chemistry Chemical Physics **23**, 7806-7813, 2021
http://dx.doi.org/10.1039/D0CP04738D

* corresponding author

contributions	
funding	W.E. Ernst, P. Hofmann
experimental design	A. Tamtögl, A. Ruckhofer, M. Bianchi, H. E. Lund
sample synthesis	M. Bremholm
data acquisition HAS	A. Ruckhofer, S. Halbritter
data acquisition ARPES	H. E. Lund, A. J. Holt, M. Bianchi
data analysis	A. Ruckhofer, A. Tamtögl, H. E. Lund, P. Hofmann
interpretation	A. Ruckhofer, A. Tamtögl, G. Benedek, P. Hofmann
publication writing	A. Ruckhofer, A. Tamtögl, H. E. Lund, P. Hofmann
discussion and editing	A. Ruckhofer, A. Tamtögl, W.E. Ernst, P. Hofmann

Abstract

We present an experimental study of inelastic scattering processes on the (111) surface of the topological insulator Sb_2Te_3 using helium atom scattering. In contrast to other binary topological insulators such as Bi_2Se_3 and Bi_2Te_3, Sb_2Te_3 is much less studied and the as-grown Sb_2Te_3 sample turns out to be *p*-doped, with the Fermi-level located below the Dirac-point as confirmed by angle-resolved photoemission spectroscopy. We report the surface phonon dispersion along both high symmetry directions in the energy region below 11 meV, where the Rayleigh mode exhibits the strongest intensity. The experimental data is compared with a study based on density functional perturbation theory calculations, providing good agreement except for a set of additional peculiar inelastic events below the Rayleigh mode. In addition, an analysis of angular scans with respect to a number of additional inelastic events is presented, including resonance enhancement, kinematical focusing, focused inelastic resonance and surfing. In the latter case, phonon-assisted adsorption of the incident helium atom gives rise to a bound state where the helium atom rides the created Rayleigh wave.

Introduction

Antimony telluride (Sb_2Te_3) is a prominent *p*-type semiconductor and multifunctional material, well known for its outstanding thermoelectric properties at room temperature [54] and is used in power generation, heat pumping, cooling applications and data storage [256]. Approaches to further improve thermoelectric efficiency in low dimensional systems [257–259] and the contribution of topological surface states to thermoelectric properties have been investigated by Hinsche *et al.* [260] and show a possible involvement to enhanced phonon scattering. Sb_2Te_3 also plays a major role in phase change memory alloys [261] and recently sparked great interest in the field of topological insulators (TIs) [88, 184, 262].

TIs are described as a new type of quantum material, where the band gap present in the bulk, is closed by topologically protected surface states, forming a single Dirac-cone at the $\overline{\Gamma}$-point. These states arise from the combination of spin-orbit interaction and time-reversal symmetry [263–265]. Besides the well investigated binary compounds Bi_2Se_3 and Bi_2Te_3, Sb_2Te_3 has been confirmed to be a three-dimensional TI with a single Dirac cone on the surface [88, 266–268].

The Fermi-level of as-grown *p*-doped Sb_2Te_3 is located below the Dirac-point and Sb_2Te_3 can exhibit hole pockets in the $\overline{\Gamma M}$ direction, depending on the position of the Fermi-level [268]. However, it has been shown that the surface Fermi level can be shifted above the Dirac point, without changing the band structure, by *n*-doping with Cs [269]. While the surface electronic states of $Sb_2Te_3(111)$ have been investigated, by angle-resolved photoemission spectroscopy (ARPES) [268, 270–273] and theoretical band structure calculations [274, 275], no experimental study exists for the surface phonon dispersion curves. On the one hand, for van der Waals layered structures, often the dynamics of surface layers does not differ that much from the bulk and preliminary information can be extracted from experimental [276–278] and theoretical [279] bulk data. On the other hand, the presence of topological surface electronic states at the Fermi level promises peculiar effects on the surface [25, 111, 119].

So far information about the surface phonon dispersion curves of $Sb_2Te_3(111)$ was limited to *ab initio* calculations using density functional perturbation theory (DFPT) [119]. In this work we determine the surface phonon dispersion and discuss several additional inelastic events in atom-surface scattering such as kinematical focusing, resonance enhancement and surfing. Using the time-of-flight (TOF) technique [34] we determine the surface phonon dispersion in the energy region below 11 meV based on helium atom scattering (HAS) and compare the results with existing *ab initio* calculations. HAS with incident energies in the low meV range has been widely used to probe low-energy surface excitations with the best

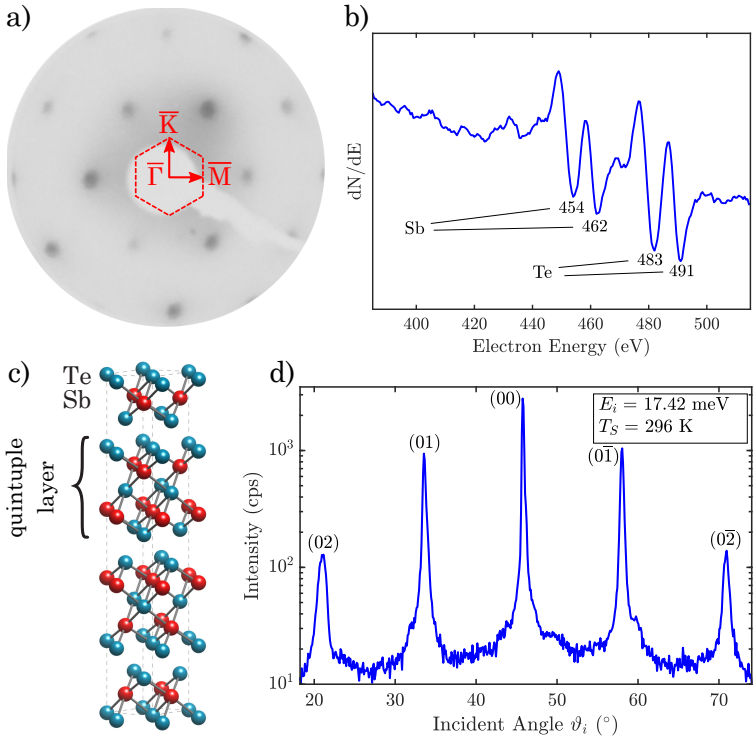

Figure 4.34: a) represents the observed low energy electron diffraction pattern with the first Brillouin zone and the high symmetry directions $\overline{\Gamma M}$ and $\overline{\Gamma K}$. In b) the Auger spectrum of the investigated sample is depicted, indicating the characteristic peaks for the MN-transition of Te and Sb, while c) shows the crystal structure of three quintuple layers of Sb_2Te_3 in the conventional hexagonal unit cell notation. A a plot of the angular helium scattering distribution along the $\overline{\Gamma M}$ azimuth in d) shows diffraction peaks up to second order.

available resolution, while being an inert completely non destructive technique [16, 34].

Experimental details and sample characterisation

The reported measurements were performed on a HAS apparatus which generates a nearly monochromatic beam ($\Delta E/E \approx 2\%$) of ^{4}He that is scattered off the sample surface in a fixed 91.5° source-sample-detector geometry. The beam is produced in a supersonic expansion of He through a 10 µm nozzle followed by extracting the core of the supersonic expansion via a 310 µm skimmer. For a detailed description of the apparatus refer to Ref. [3].

The analysis of the inelastically scattered He atoms allows to determine the surface phonon branches in the acoustic and optical regions. The impinging He atoms with energies in the low meV range are exclusively scattered by the surface charge density [4, 44]. Inelastic scattering from surface phonons occurs via the phonon-induced charge density oscillations, which can be used for the determination of the electron-phonon (e-ph) interaction constant [26, 48].

Antimony telluride has a rhombohedral crystal structure consisting of five atomic layers, arranged along the z-direction (perpendicular to the surface), known as quintuple layers (QLs) as seen in Fig. 4.34c) [114]. Each QL consists of two equivalent tellurium atoms, two equivalent antimony atoms and a third tellurium atom. The bonding is strong between the atomic layers within a QL but much weaker, predominantly of the van der Waals type, between two QLs. When cleaved along the (111) plane the upper-most atomic layer consists of tellurium, followed by an antimony layer below and so forth.

The investigated crystal was formed by slowly cooling the melt in a quartz tube similar to the procedure described in Refs. [240, 280] and the phase purity of the synthesised sample was measured by X-ray diffraction. The unit cell parameters were extracted based on a Rietveld refinement. Afterwards the crystal rod was cleaved along the (111) plane and for the measurements a small sample was attached onto a sample plate with electrically and thermally conductive epoxy. The surface electronic structure of the samples was characterised by ARPES at the SGM-3 beamline of ASTRID2 [281]. The total energy and angular resolution were ≈30 meV and 0.1°, respectively. The sample temperature was ≈30 K and the photon energy was chosen to be 22 eV.

Previously to the HAS measurements, in order to obtain a clean surface, the sample was cleaved *in-situ* under high vacuum conditions in a separate load lock chamber [113], before storing the sample in the sample mount of the main chamber, to ensure minimal surface contamination. The sample can be heated using a button heater on the backside of the sample mount or cooled down to 115 K via a thermal connection to a liquid nitrogen reservoir. Low energy electron diffraction was used for a first alignment of the sample along the high symmetry orientation (Fig. 4.34a)). Additionally, before running scattering experiments, the composition of the sample was analysed by Auger electron spectroscopy. The obtained spectrum can be seen in Fig. 4.34b), which shows significant intensities at the expected energies for single-elemental antimony and tellurium, when compared to spectra from literature [282].

The angular HAS distribution along the $\overline{\Gamma M}$ azimuth in Fig. 4.34d) shows diffraction peaks up to second order. The scattered intensity is plotted on a logarithmic scale with an incident energy of $E_i = 17.4$ meV and the sample held at room temperature. The high signal-to-noise ratio and the small full width at half maximum of the specular peak are an indication of the good crystal quality after cleaving. The high intensity of the diffraction peaks suggests a large surface electronic corrugation ($Sb_2Te_3(111)$ exhibits a surface electronic corrugation of 6.6 % of the lattice constant [283]) which is a necessary ingredient for various phenomena, e.g. involving bound state resonances.

Energy dispersive spectra for inelastic scattering were performed using TOF measurements with a pseudo-random chopper disc. After deconvolution with the pseudo-random chopper sequence, the TOF signal is further transformed to an energy transfer scale which allows to determine inelastic (phonon) scattering events [3]. The scattering spectra were mainly taken with the crystal at room temperature, while a few spectra were taken with the sample cooled down to 115 K and the incident He beam energy was varied between 10 and 18 meV.

Results and discussion

Details of the phonon dispersion are closely linked to the electronic structure and screening of a system and this is particularly relevant for the surface phonon dispersion of topological insulators where the surface electronic properties are drastically different from those of the bulk. It is therefore important to characterise the crystals in terms of their bulk doping in order to identify the Fermi surface elements that can contribute to screening. For Sb_2Te_3 the as-grown crystals are typically strongly *p*-doped, up to a degree where the valence band maximum at $\overline{\Gamma}$ and a hole pocket along the $\overline{\Gamma M}$ direction can contribute to the surface Fermi surface [119, 271, 272]. The latter is confirmed in ARPES measurements of the current sample as described in the following.

Surface electronic structure

The photoemission intensity at the Fermi energy is given in Fig. 4.35a), showing a flower-like pattern. The closed contour around $\overline{\Gamma}$ and the petals of the flower have both the character of hole pockets, as can

be seen from the detailed dispersion in Fig. 4.35b).

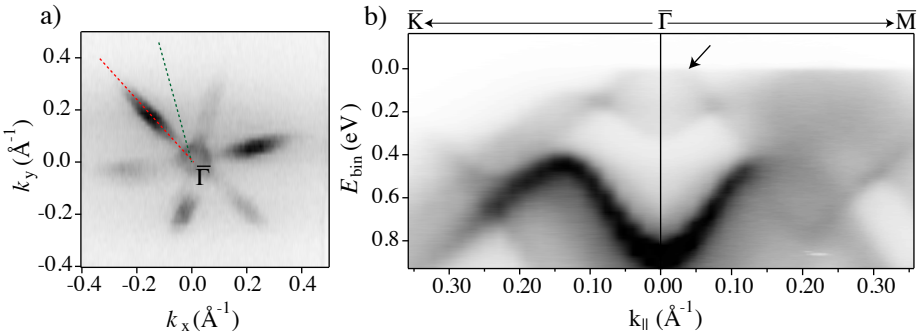

Figure 4.35: a) Photoemission intensity at the Fermi level with dark corresponding to high intensity. Red and green dashed lines indicate the $\overline{\Gamma M}$ and $\overline{\Gamma K}$ directions in the surface Brillouin zone, respectively. b) Photoemission intensity along $\overline{K\Gamma M}$ as a function of binding energy E_{bin}, illustrating the character of the features that give rise to the Fermi surface. The arrow marks the location of the topological surface state.

Indeed, it is seen that the state near $\overline{\Gamma}$ results from both the valence band maximum, leading to the blurred intensity near the Fermi level at $k_{\|} \approx 0$, and the lower part of the topological surface state dispersion that gives rise to a somewhat sharper linear feature, marked by an arrow in the figure. The band forming the hole pocket (flower petal) along $\overline{\Gamma M}$ is seen as a diffuse intensity in an energy interval between ≈0.3 eV and the Fermi energy. Note that the observation of broad bands from bulk states is common in ARPES and related to the $k_{\perp}$ smearing that results from the short inelastic mean free path of the photoelectrons. The conclusion from the ARPES characterisation is that the sample is indeed strongly *p*-doped, giving rise to two different types of (bulk) hole pockets.

Surface phonon dispersion

The surface phonon events were determined from a multitude of TOF spectra at various incident energies E_i and incident angles ϑ_i to fully cover the Brillouin zone along both high symmetry directions. (see "Appendix: Additional TOF spectra" for various TOF spectra) The peaks in the energy domain of the TOF spectra were transformed to the wavevector domain using the so called scancurve (SC). The SC links all accessible energy transfers to the corresponding parallel momentum transfer during an inelastic event and is given by

$$k_i \sin\vartheta_i + Q = \sin\vartheta_f \sqrt{2m(E_i + E_{ph})/\hbar} \tag{4.30}$$

with k_i being the incident wavevector, $\sin\vartheta_{i,f}$ the incident and final scattering angle, Q the wavevector, m the He atom mass and E_{ph} the phonon energy. For a more detailed description of the determination of the phonon energies see Refs. [25, 284].

As shown by D. Campi *et al.* [119], the inclusion of spin-orbit coupling (SOC) in *ab initio* calculations of the surface phonon dispersion has negligible effects. Hence, the reported surface phonon dispersion curves based on DFPT calculations (without SOC) for a slab consisting of three QLs are reproduced in Fig. 4.36 as solid grey lines. The experimentally obtained surface phonon energies are plotted as symbols on top of the theoretical calculations in Fig. 4.36.

We are able to resolve surface phonon events with energies up to 11 meV along both high symmetry directions. Each phonon event has been marked with a mode related colour and tag, according to its vicinity to the calculated modes. Due to many avoided crossings an accurate assignment of the optical modes becomes more difficult. In general the experimental surface phonon dispersion is in good agreement

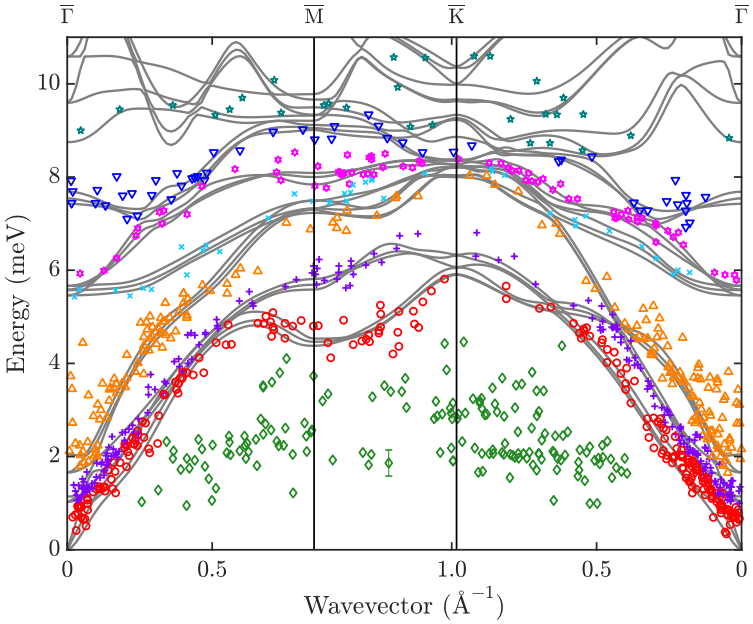

Figure 4.36: Experimental surface phonon dispersion of Sb_2Te_3(111) from helium atom scattering (symbols) in comparison with DFPT calculations for three quintuple layers in the lower part of the phonon spectrum (solid grey lines) [119]. The assignment of the data points (colour and tag) to different modes is based on the proximity to the theoretical modes. One exemplary error bar is shown at an energy of ≈2 meV

with the DFPT calculations except for the low energy modes (1–4 meV) marked as green diamonds which will be discussed below (section "Low energy modes").

According to the DFPT calculations, there are altogether 45 phonon branches (of which only the lower 24 are displayed as solid grey lines in Fig. 4.36), organised into 15 bands associated with the 15 degrees of freedom of Sb_2Te_3. Besides the 3 acoustic modes, there are two low-energy bands (< 2 meV at $\overline{\Gamma}$) where in each QL the central Te layer is at rest and the two external bilayers move rigidly and symmetrically normal ($A_g(1)$) or parallel ($E_g(1)$) to the slab [279].

The corresponding experimentally obtained acoustic branches are shown as red circles, purple crosses and orange triangles in Fig. 4.36, with the red circles being the Rayleigh wave (RW), starting with zero energy at the $\overline{\Gamma}$ point. In general, a high concentration of experimental data points is found in the acoustic region, including the Rayleigh mode. Inelastic events from the RW give the highest intensity in the respective TOF spectra, confirming the high intensity of the RW as also found for other binary TIs such as Bi_2Se_3 and Bi_2Te_3, respectively [25, 111]. Note that in contrast to the recent report of two RWs in Bi_2Te_3 [285] there exists only one RW, either as a surface-localised wave or as an in-band resonance (pseudo-surface wave), as a result of continuum theory [16, 25, 111].

Phonon group velocity

As mentioned above, the energetically lowest mode in the surface phonon dispersion is the RW. Its band starts at zero energy at the $\overline{\Gamma}$-point of the surface Brillouin zone with a linear dispersion in the long wavelength ($Q \to 0$) limit.

The group velocity of the RW can be determined from the slope of its dispersion curve at small wavevectors. Therefore, the measured data points are fitted with a linear relation in the low energy range assuming an intercept with the $\overline{\Gamma}$-point at $Q = 0$. Due to the fact, that for Sb_2Te_3 the RW and the

second acoustic mode proceed parallel and rather close to each other, the assignment of measured points is not always unambiguous, which leads to a rather high uncertainty for the determined slopes along $\overline{\Gamma M}$ and $\overline{\Gamma K}$ in Tab. 4.5.

Table 4.5: Slopes of the RW along the $\overline{\Gamma M}$ and $\overline{\Gamma K}$ direction based on a linear fit and the corresponding group velocities v_{RW} of the RW.

	slope (meV Å)	v_{RW} ($\mathrm{m\,s^{-1}}$)
$\overline{\Gamma M}$	10.9 ± 1.0	1650 ± 160
$\overline{\Gamma K}$	10.0 ± 0.5	1590 ± 80

By means of the elastic constants of Sb_2Te_3 calculated *ab initio* by Lu *et al.* [286], and a crystal density of $6.488\,\mathrm{g\,cm^{-3}}$, [287] the bulk transverse speed of sound along $\overline{\Gamma K}$ can be calculated [288] and is found to be $1620\,\mathrm{m\,s^{-1}}$. As seen in Tab. 4.5, the group velocity of the RW along this direction is only slightly less than the bulk transverse acoustic speed of sound with a difference that is, however, much smaller than the experimental uncertainty.

Low energy modes

When looking at Fig. 4.36 it becomes evident that several peaks at energies between 1–4 meV are not reproduced in the DFPT calculations. These events cannot be assigned to any surface phonon mode and need further discussion. One could possibly ascribe two separate branches with a dispersion to the plotted data points, though with some difficulty given the number of data points and their spread.

Similar low-energy excitations observed with HAS in the gap below the RW branch have been reported previously in two other topological materials, Sb(111) [49] and $Bi_2Se_3(111)$ [25]. In both cases they could be assigned to low-energy surface electron collective excitations, namely phasons and amplitons, associated with a charge density wave (CDW) induced by e-ph interaction. In Sb(111) a quasi-commensurate CDW originates from the Kelly-Falicov multivalley e-ph coupling connecting $\overline{M}$-point electron pockets [49], while in $Bi_2Se_3(111)$ a long-period CDW has been associated with e-ph coupling connecting surface quantum-well states [25]. In both cases distinct CDW features are observed at low temperature in the HAS diffraction spectra, though under bound-state resonance enhancement conditions in $Bi_2Se_3(111)$.

Although the similarities of present low-energy data with those observed in Sb(111) and $Bi_2Se_3(111)$ are quite evident, low-lying frustrated translational modes of adsorbates can be another possible source of these data points [289]. This possibility is however rather remote in view of the good quality of the surface during experiments, as witnessed by the comparatively low intensity of the diffuse elastic peak in the TOF spectra (see, e.g. Fig. 4.37a)).

Hence we conclude that the two branches are likely to be caused by phasons/amplitons in analogy to the observations made for Sb(111) and $Bi_2Se_3(111)$, although a more thorough investigation is needed in order to unambiguously assign and understand these excitations.

Resonance enhancement

The intensity of a specific phonon event might be increased if a bound state resonance is involved - therefore termed resonance enhancement. A He atom might go into a final state which is a bound state of energy $-|\epsilon_n|+\hbar^2K_f^2/2m^*$, with K_f being the final parallel vector and m^* the effective mass of the atom in the bound state [289]. Based on the conservation of energy and parallel momentum, the corresponding

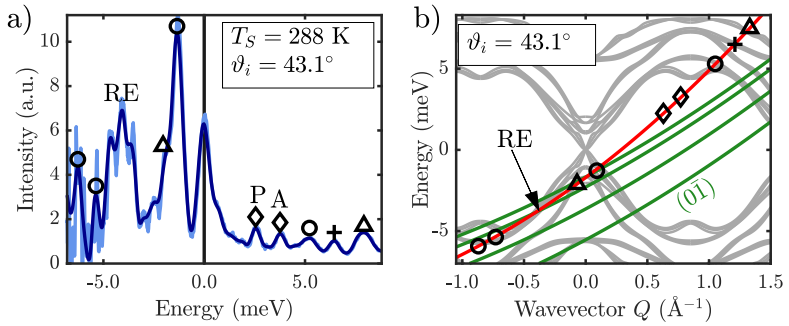

Figure 4.37: a) shows a TOF-spectrum at $\vartheta_i = 43.1°$ with the sample at room temperature, exhibiting phonon processes and low energy excitations as well as a resonance-enhanced phonon process. The light blue line depicts the raw data after conversion to an energy transfer scale while the dark blue line shows the signal after binning based on constant energy bins (see "Appendix: Additional TOF spectra"). In b) the resonance conditions (Eq. (4.31)) for the $(0\bar{1})$ **G**-vector together with the scancurve are drawn on top of the DFPT calculations (grey lines). The symbols correspond to the phonon events of the TOF spectrum to the left.

equation for inelastic selective adsorption is [289]

$$\hbar\omega(Q) = E_i + |\epsilon_n| - \frac{\hbar^2}{2m}\left[(k_i \sin\vartheta_i - G_{||} - Q)^2 + G_{\perp}^2\right] , \tag{4.31}$$

with $G_{||}$ and $G_{\perp}$ being the parallel and perpendicular components of the **G**-vector, respectively.

If the resonance condition Eq. (4.31) intersects with the SC Eq. (4.30) at a specific phonon branch, the intensity of this particular phonon will be enhanced in the TOF spectrum. Based on the bound states ϵ_n for Sb_2Te_3 ($\epsilon_0 = 4.27$ meV, $\epsilon_1 = 2.37$ meV, $\epsilon_2 = 0.9$ meV, $\epsilon_3 = 0.4$ meV) [283], the condition is fulfilled in Fig. 4.37b), where the bound state ϵ_2 of the resonance curve with an interacting **G**-vector $(0\bar{1})$ intersects the SC at an energy of -4 meV. The intensity of this created phonon is greatly enhanced in the TOF spectrum (Fig. 4.37a)), when compared to measurements which do not satisfy the condition. Recent work showed that these resonance enhancing effects can in turn be used to observe low-energy surface electron collective excitations [25].

Kinematical focusing, focused inelastic resonance and surfing

In addition to phonon resonance enhancement a variety of other resonance and focusing phenomena can arise upon scattering from a corrugated surface [289], as listed below. These processes can be described by looking at the equations for the SC and the resonance conditions as well as the lowest modes of the surface phonon dispersion. The upper left graph of Fig. 4.38 shows an angular scan where the incident angle ϑ_i is varied along the $\overline{\Gamma M}$ azimuth with the sample at a temperature of 113 K. Upon enlarging the y-scale compared to Fig. 4.34d), additional peaks and dips appear in the diffuse inelastic background. Below the measured curve the bound state resonances for the four known bound states [283] are depicted. The different colours correspond to the different interacting reciprocal lattice vectors.

The three scattering phenomena kinematical focusing (i), surfing (ii) and resonance enhancement (iii) are plotted in the lower panels of Fig. 4.38 as energy $\hbar\omega(Q)$ versus wavevector Q. Here we use the convention that the forward creation process is displayed in the third quadrant ($Q < 0$, $\hbar\omega(Q) < 0$) as frequently used in HAS analysis [2, 25]. Therefore positive energies in Fig. 4.38 correspond to annihilation and backward propagation. The purely inelastic process occurs when the SC intersects with a branch in the phonon dispersion and can be measured with the TOF technique described above.

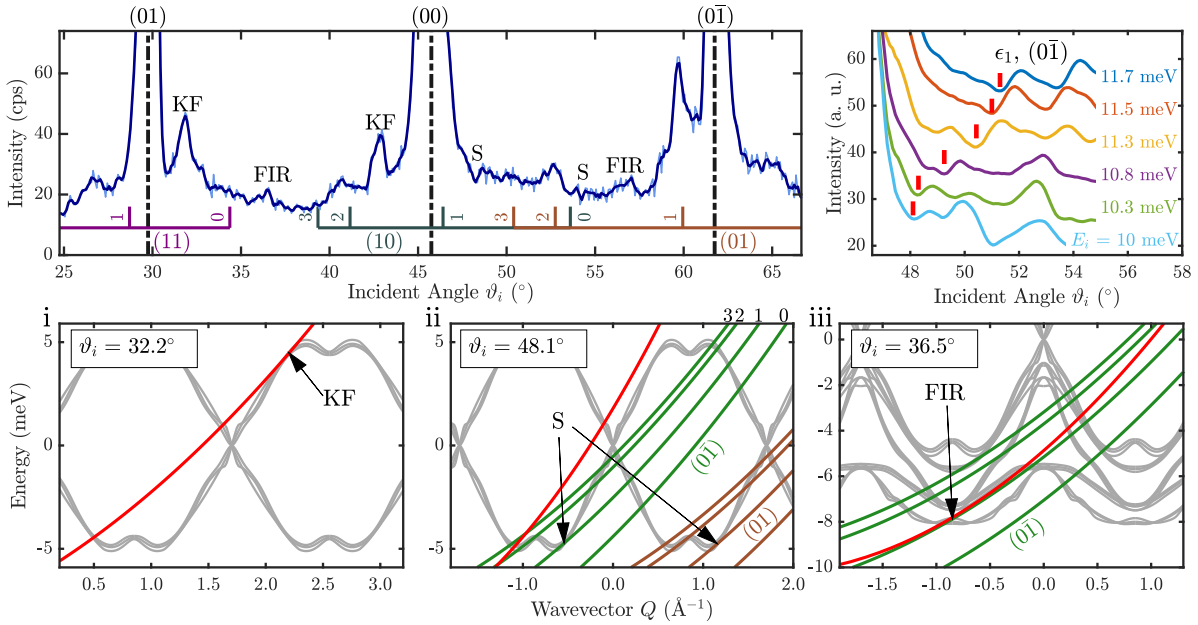

Figure 4.38: Diagrams illustrating various HAS focusing effects as a function of parallel momentum (wavevector) Q, for an incident energy $E_i = 10.3\,\text{meV}$. Top left panel: Angular scan along the $\overline{\Gamma M}$ azimuth at a surface temperature $T_s = 113\,\text{K}$ (light blue line: raw data, dark blue line: smoothed data). The lines below the measured curve indicate selective adsorption resonance processes with the colours corresponding to different interacting **G**-vectors. Top right: Tracking of the surfing feature (highlighted by the red bar) with increasing incident beam energy E_i. The lower panels show (from left to right) the effects kinematical focusing (KF), surfing (S) and focused inelastic resonance (FIR). The red curves depict the scancurve while the green curves show the resonance conditions (Eq. (4.31)) with the corresponding **G**-vector.

i An effect known as kinematical focusing [290] (KF) might show up at a specific incident angle ϑ_i and incident energy E_i when the SC lies tangent to a phonon branch. KF gives rise to a saw-tooth peak in the angular scattering distribution due to the increased inelastic background in the elastic signal. The characteristic peak shape can clearly be identified in the angular scan (upper left panel of Fig. 4.38) at $\vartheta_i = 32°$ and $\vartheta_i = 43°$. For the first angle the corresponding SC is plotted in red in Fig. 4.38i together with the two lowest modes of the calculated phonon dispersion. The point of tangency is marked with KF and can be observed in the angular distribution as well as in the corresponding TOF spectrum.

ii We now turn to the effect of surfing, which occurs when a resonance curve lies tangent to a surface phonon branch. In this case, the impinging He atom is selectively adsorbed into a bound state ϵ_n with the aid of a surface phonon. In comparison to the "ordinary" elastic selective adsorption this process can occur even without the exchange of a reciprocal lattice vector. The tangency condition yields a concentration of beams inelastically scattered into the given bound state and therefore a dip in the final beam around a special incident angle.
Using the bound state energy values for Sb_2Te_3 [283] a set of resonance curves are plotted as green lines in Fig. 4.38ii. The tangency of one of these curves with a phonon branch gives rise to a dip in the angular distribution. If this special condition is fulfilled the atom and the phonon wave exhibit the same velocity on the surface and travel together, hence the effect is called surfing. According to Ref. [289] the atom stays on the surface for a longer time during surfing compared to the lifetime of the He atom in a bound state [283]. However, based on the signal-to-noise ratio of our data it

is difficult to extract an actual linewidth and thus the corresponding lifetime. Hence we cannot conclude on any values for the lifetime.
In Fig. 4.38ii the surfing effect is shown for an incident angle of $\vartheta_i = 57.1°$, where the resonance curves of the bound state ϵ_1 for the **G**-vectors $(0\overline{1})$ and (01) are tangent to the acoustic phonon branch. In the angular spectrum the surfing conditions at various angles are indicated with an S, yielding a dip in the scattered intensity. To further support the finding of the surfing feature the dip can be monitored in dependence of the incident energy E_i. In the top right panel of Fig. 4.38 the surfing dip is shown for incident energies between $E_i = 10.7$ and $11.7\,\mathrm{meV}$. The angular spectra were smoothed using a Savitzky-Golay filter and the red bars mark sequences of features assigned to the $(0\overline{1})$ surfing condition including the ϵ_1 bound state.

iii Finally we discuss the effect of focussed inelastic resonance (FIR), which occurs when the SC Eq. (4.30) is tangent to a resonance curve Eq. (4.31) within an energy region where surface phonons are expected [16, 291]. When combining these two equations the expected FIR position is given by

$$\tan^2 \vartheta_f^{FIR} = \left[\frac{2m}{\hbar^2}\,|\epsilon_n| - \mathbf{G}^2\right] \frac{1}{G_{||}^2} \quad . \tag{4.32}$$

Hence the incident angle ϑ_i for a FIR follows from the fixed source-detector geometry (ϑ_i+ϑ_f=ϑ_{SD}). A very characteristic property of a FIR is the independence of Eq. (4.32) with respect to the incident energy.
In the angular scan of Fig. 4.38 two FIR features are present at $\vartheta_i = 36.5°$ and $\vartheta_i = 56.4°$ yielding an increased scattered intensity. A comparison with angular scans at similar incident energies shows that the FIR peaks are still present at the same incident angle as expected, according to Eq. (4.32). In the lower right most plot of Fig. 4.38 ($\vartheta_i = 36.5$) the resonance curve becomes tangent to the SC for an optical phonon branch at around 8 meV.

Following this systematic approach we are able to interpret all significant peaks of the angular scan in Fig. 4.38 using the effects described above. All peaks which are not labelled are attributed to selective adsorption resonances indicated by the vertical coloured lines below the measured data.

Conclusions

In summary, we have investigated various inelastic interactions of helium with Sb_2Te_3 which are experimentally detected in TOF spectra as well as in angular scans. A multitude of TOF spectra was used to determine the surface phonon dispersion for the $\overline{\Gamma M}$ and $\overline{\Gamma KM}$ directions. A comparison with theoretical calculations based on density functional perturbation theory shows good agreement with the experimental data. Similar to earlier works, the strongest phonon intensities originate from the Rayleigh mode. From the slope of the Rayleigh mode the phonon group velocity is determined to be $v_R \approx 1600\,\mathrm{m\,s^{-1}}$. In addition to phonon creation and annihilation processes, we observe further peculiar inelastic events below the Rayleigh mode. In view of similar observations made on the topological materials Sb(111) and Bi_2Se_3(111), they are tentatively assigned to the dispersion curves of phasons and amplitons associated with a charge density wave.

Furthermore, a systematic analysis of angular diffraction scans shows that several additional inelastic scattering events are observable for He atom scattering from Sb_2Te_3. These include resonance enhancement, kinematical focusing, focused inelastic resonances and surfing.

Acknowledgment

We would like to thank D. Campi for many helpful discussions and the *ab initio* surface phonon dispersion curves from Ref. [119]. The authors are grateful for financial support by the FWF (Austrian Science Fund) within the project P29641-N36, as well as by NAWI Graz. We would like to thank the Aarhus University Research Foundation, VILLUM FOUNDATION via the Centre of Excellence for Dirac Materials (Grant No. 11744) and the SPP1666 of the DFG (Grant No. HO 5150/1-2) for financial support. M. Bremholm acknowledges financial support from the Center of Materials Crystallography (CMC) and the Danish National Research Foundation (DNRF93).

Appendix: Additional TOF spectra

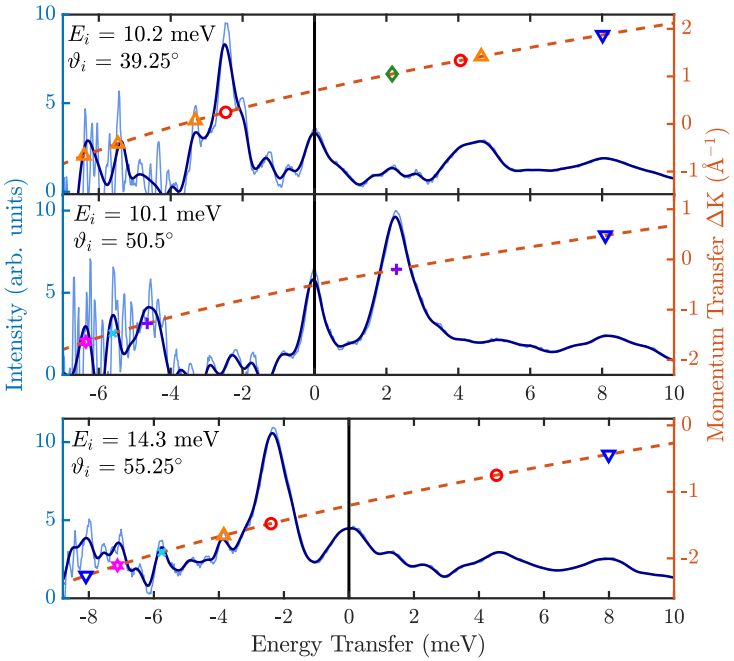

Figure 4.39: Compilation of several TOF spectra measured along the $\overline{\Gamma M}$ azimuth at various incident energies E_i and angles ϑ_i. For the two upper graphs the temperature of the He nozzle was set to 50 K and for the bottom one to 65 K. All shown scans were taken with the sample at room temperature. The light blue line shows the signal after conversion to the energy transfer scale while the dark blue line is the result of averaging based on constant energy bins (see text). The vertical black line illustrates diffuse elastic scattering while the dashed orange line is the scan curve Eq. (4.30) (y-axis on the right-handside), relating energy transfer to momentum transfer. The symbols denote peaks in the TOF spectrum which have been assigned to phonon events.

For the determination of the surface phonon dispersion (Fig. 4.36) a multitude of TOF spectra were measured with different incident energies E_i and incident angles ϑ_i. In Fig. 4.39 three exemplary TOF spectra are shown in the $\overline{\Gamma M}$ direction, after conversion to an energy transfer scale. Negative energy transfer corresponds to phonon creation, while positive energy transfer corresponds to phonon annihilation.

Because of the non-linearity introduced by the conversion from the flight time to the energy transfer scale, the data has to be multiplied with the corresponding Jacobian in order to preserve the intensity. Due to the process, experimental noise increases on the creation side ($\Delta E = E_f - E_i < 0$) as seen in the light blue line in Fig. 4.39. The latter makes it difficult to distinguish peaks in the (far) creation side and

therefore, the (non-linear) energy scale is usually divided in equally spaced energy bins over which the signal is averaged [5]. The dark blue line shows the signal after binning, resulting in a smoother line.

The peaks in Fig. 4.39 identified as phonon events are indicated with different symbols, which attribute the peaks to the specific phonon branches (same symbols as in Fig. 4.36). The symbols are drawn on the SC Eq. (4.30) plotted as a dashed orange line, relating the energy transfer of a phonon event to the momentum transfer ΔK (right ordinate in Fig. 4.39).

4.6 Strong-Coupling Charge Density Wave in a One-Dimensional Topological Metal

This section consists of the following published publication:

Strong-Coupling Charge Density Wave in a One-Dimensional Topological Metal

P. Hofmann*, M. M. Ugeda, A. Tamtögl, A. Ruckhofer, W. E. Ernst, G. Benedek, A. J. Martínez-Galera, A. Stróżecka, J. M. Gómez-Rodríguez, E. Rienks, M. Fuglsang Jensen, J. I. Pascual, and J. W. Wells

The Journal of Physical Review B **99**, 035438, 2019
https://doi.org/10.1103/PhysRevB.99.035438

* corresponding author

contributions

funding	W.E. Ernst, P. Hofmann
data acquisition (HAS)	A. Ruckhofer, A. Tamtögl
data analysis (HAS)	A. Ruckhofer, A. Tamtögl
data acquisition & analysis (LEED, STM, ARPES)	M. M. Ugeda, A. J. Martínez-Galera, A. Stróżecka, J. M. Gómez-Rodríguez, E. Rienks, M. Fuglsang Jensen, J. I. Pascual, and J. W. Wells
interpretation	A. Tamtögl, P. Hofmann, G. Benedek
publication writing	P. Hofmann, A. Tamtögl, G. Benedek
discussion and editing	all authors

Abstract

Scanning tunnelling microscopy, low energy electron diffraction and helium atom scattering show a transition to a dimerization-like reconstruction in the one-dimensional atomic chains on Bi(114) at low temperatures. One-dimensional metals are generally unstable against such a Peierls-like distortion, but neither the shape nor the spin texture of the Bi(114) Fermi contour favour the transition: While the Fermi contour is one-dimensional and thus perfectly nested, the very short nesting vector $2k_F$ is inconsistent with the periodicity of the distortion. Moreover, the nesting occurs between two Fermi contour branches of opposite spin, which is also expected to prevent the formation of a Peierls phase. Indeed, angle-resolved photoemission spectroscopy does not reveal any change in the electronic structure near the Fermi energy around the phase transition. On the other hand, distinct changes at higher binding energies are found to accompany the structural phase transition. This suggests that the transition of a strong-coupling type, and that it is driven by phonon entropy rather than electronic entropy. This picture is supported by the observed short correlation length of the pairing distortion, the second order-like character of the phase transition and pronounced differences between the surface phonon spectra of the high and low temperature phase.

Introduction

The experimental realization of systems with reduced dimensions has often been the key to the discovery of fundamentally new physics. Of particular importance is the situation in one dimension, with its drastically enhanced significance of electronic correlations and electron-phonon coupling [292, 293]. An attractive path to studying systems of reduced dimensionality is to create them on the surfaces of semiconducting or semimetallic substrates, as this opens the possibility to employ powerful spectroscopic techniques, such as scanning tunnelling microscopy (STM), angle-resolved photoemission (ARPES) and surface-sensitive transport measurements [294, 295]. Many systems have been realized and studied in this way, such as metallic chains or graphene nano-ribbons on semiconductors, see e.g. Refs. [296–302].

A particularly intriguing situation arises when low dimensionality is combined with an unconventional spin texture of the electronic states, as this imposes a number of restrictions on the allowed electronic instabilities [299, 303]. This combination is realized on the (114) [68, 304] and (441) [305] vicinal surfaces of Bi where strongly Rashba-split surface states span the gap of a semimetallic substrate. Moreover, due to the similarity of Bi to the topological insulator $Bi_{1-x}Sb_x$ [306, 307], all Bi surfaces have metallic surface states with a spin texture similar to that of topological insulators [58, 183] and several hallmark features of these states, such as the lack of backscattering [308], were first observed on Bi surfaces. It was also pointed out that a Fermi contour with a chiral spin texture should not lead to charge density wave formation, even in the presence of perfect nesting [303].

The fundamental difference between a conventional one-dimensional metal at half-filling and the electronic surface state on Bi(114) is illustrated in Fig. 4.40. A conventional electronic state in a lattice with spacing a and half-filling is unstable with respect to the formation of a one-dimensional charged density wave (CDW), also called a Peierls-distortion. Fig. 4.40(a) illustrates this situation of ideal nesting with a nesting vector length of $2k_F = \pi/a$, as indicated by the arrow in Fig. 4.40(a). As this corresponds to a real space periodicity of $2a$, a Peierls-type distortion involving a periodicity doubling via pairing of the atoms in a chain leads to a new Brillouin zone boundary at the Fermi level crossings of the unreconstructed phase, a gap opening, and hence to an electronic energy gain in the occupied states. The situation is quite different for the surface state on Bi(114) shown in Fig. 4.40(b). Here the state is no longer spin-degenerate and the spin texture (indicated by red and blue) and dispersion closely resemble

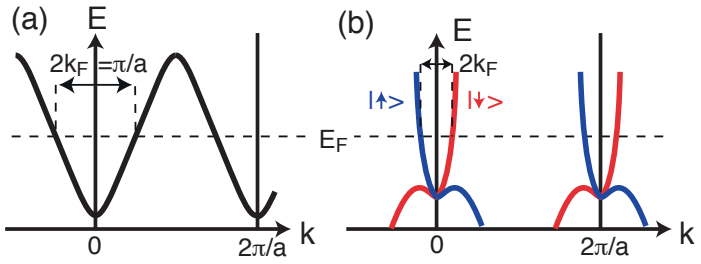

Figure 4.40: (a) Conventional one-dimensional electronic state at half-filling. The black dispersion is spin-degenerate. This system is sensitive to a Peierls-type instability due to the perfect nesting and the fact that the nesting vector's length corresponds to a real space periodicity of $2a$. (b) Situation on Bi(114). The spin degeneracy of the bands is lifted and while perfect nesting is still present, it takes place for a very short nesting vector and between states of opposite spin (indicated by the color of the bands and the arrows), thus protecting against a Peierls-type instability.

that of a one-dimensional edge state of a two-dimensional topological insulator, the so-called quantum spin Hall effect [309–312]. It is for this reason that Bi(114) has been called a 'one-dimensional topological metal' [68]. While perfect nesting is retained, as for any one-dimensional structure, $2k_F \ll \pi/a$ and a pairing-type reconstruction would not be expected to open a gap at the Fermi level crossing. More importantly, the spin texture prevents the singularity in the electronic susceptibility required to drive the instability [303], an effect closely related to the forbidden backscattering for such a one-dimensional state [308]. A Peierls-distortion would thus not be expected for the case of Bi(114).

Surprisingly, as we report here, such a pairing distortion is nevertheless observed at low temperature on the quasi one-dimensional Bi(114) surface. Temperature-dependent measurements of the electronic structure by ARPES do not show any signs of a Fermi surface change, as expected from the arguments above, but do show some clear spectral changes at higher binding energy. STM, low energy electron diffraction (LEED), and helium atom scattering (HAS), on the other hand, provide evidence that this transition is a strong-coupling CDW [313], driven by phonon entropy. Strong coupling CDWs that are not based on Fermi surface nesting are common for two-dimensional CDW systems [272, 313–318], consistent with strong sensitivity of the electronic susceptibility towards small deviations from ideal nesting conditions [319]. In one dimension, there is always perfect nesting but in the present case the nested Fermi surface is irrelevant for the phase transition.

Experimental Details

The Bi(114) surface was cleaned by sputtering with noble gas ions and annealing between 300 and 400 K. STM measurements were performed both at a fixed temperature (5 K) and at variable temperatures between 40 and 300 K in two different setups. LEED and ARPES data were collected on the SGM-3 end station of ASTRID [281] between 50 and 300 K. The energy resolution varied between 25 meV for the measurements at low photon energies and 65 meV for the large-scale Fermi surface maps collected with high photon energies. The angular resolution was better than 0.2°. For the HAS measurements, a nearly monochromatic beam of He ($\Delta E/E \approx 2\%$) was scattered off the sample surface in a fixed 91.5° source-sample-detector geometry. Energy dispersive measurements for inelastic scattering were performed using time-of-flight (TOF) technique with a pseudo-random chopper disc [3]. The momentum transfer parallel to the surface was calculated from the kinematic scattering conditions [4].

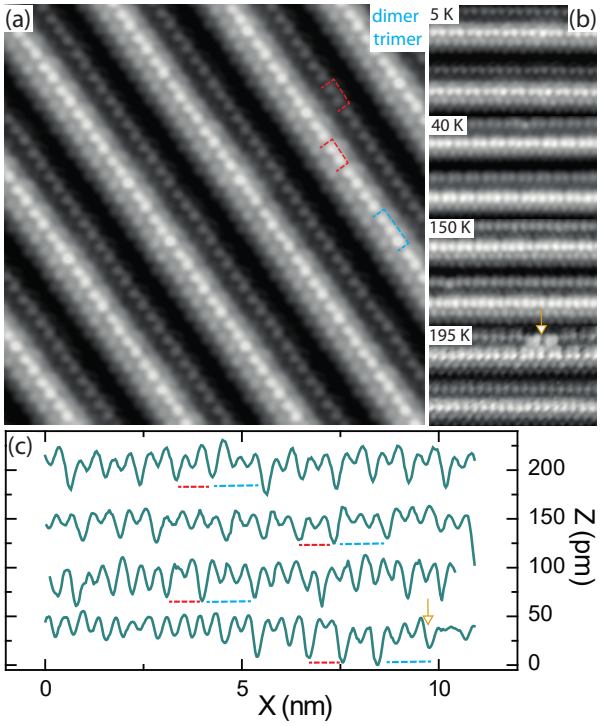

Figure 4.41: Dimerization distortion of the quasi one-dimensional lattice structure of Bi(114). (a) STM image at 5 K showing dimer formation in some of the protruding atomic rows (red dashed frames), with frequently appearing defects such as trimers (blue dashed frame). (b) STM images at higher temperatures and (c) profiles along the protruding atomic rows, measured at the indicated temperatures. At 195 K the dimerization is lifted and only observed in the immediately vicinity of defects. Tunnelling parameters: (a) $U = 0.2\,\mathrm{V}$ and $I = 0.1\,\mathrm{nA}$ (b) $U = 0.2, 1.0, -0.1, 0.25\,\mathrm{V}$ and $I = 0.1, 4.0, 2.0, 4.0\,\mathrm{nA}$. All STM data were processed with the WSxM software [320].

Results and Discussion

The atomic structure of Bi(114) consists of parallel atomic rows with an interatomic spacing of 4.54 Å along the rows [68]. A unit cell comprises several of these rows at different heights and the periodicity of the unreconstructed surface perpendicular to the rows is 14.20 Å. For the clean surface, a reconstruction-induced doubling of this periodicity has been reported [68], such that the actual periodicity perpendicular to the rows is twice this value. Fig. 4.41(a) shows a close-up STM image of the surface at 5 K. Due to the strong corrugation, the periodicity of 28.40 Å perpendicular to the atomic rows is immediately visible. On close inspection, it becomes clear that the periodicity along the rows is also doubled, i.e. the atoms in the rows are not equally spaced but most of them appear dimerized. A few of these dimers are emphasized in the figure by red frames. This reconstruction does not only affect the atoms in the top row but also those in deeper lying rows. The average interatomic distance in the dimers is (4.15 ± 0.10) Å, thus corresponding to ~ 0.2 Å atomic displacement from the equilibrium position. This is a substantial fraction of the equilibrium spacing, larger than typically found in Peierls systems [321]. While dimerization is dominant on a short length scale, long range ordering is poor. Indeed, defects such as trimers are found every few dimers in the row (also indicated by a blue frame in the figure). Moreover, the dimerization appears to be a strongly local phenomenon within each row, as no correlations between dimer positions in neighbouring atomic rows are evident.

We explored the temperature dependence of the dimerization along the atomic rows. Fig. 4.41(b) and Fig. 4.41(c) compare STM images and height profiles measured at increasing temperatures. While at

40 K the dimerization is still fully intact, at 150 K it starts vanishing, and is nearly absent at 195 K, with the exception of the immediate vicinity of structural defects (indicated by an arrow) that appear to serve as a seed for the dimerization. Thus, the dimerization is a low temperature phase, with an apparent transition temperature somewhere between 150 and 195 K.

The reconstruction is also observable in diffraction experiments, even though the coherence length is very short, as seen from the STM data. Fig. 4.42 shows LEED data taken at 250 and 55 K, i.e. well above and below the transition temperature range determined by STM. The LEED patterns consist of well-separated rows of closely placed sharp spots. The distance between the spots along the rows corresponds to the reciprocal lattice distance perpendicular to the chains ($2\pi/28.4\,\text{Å}^{-1}$), while the distance between the rows corresponds to the interatomic distance in the (unreconstructed) chains ($2\pi/4.54\,\text{Å}^{-1}$). In the low-temperature image, weak streaks of intensity are observed half-way between the rows (indicated by an arrow in Fig. 4.42) and thus consistent with a dimerized structure. The width of streaks along k_x reflects the short coherence of the CDW within the atomic rows and the (much larger) width along k_y is due to the lack of coherence between these rows. These findings are consistent with the STM results.

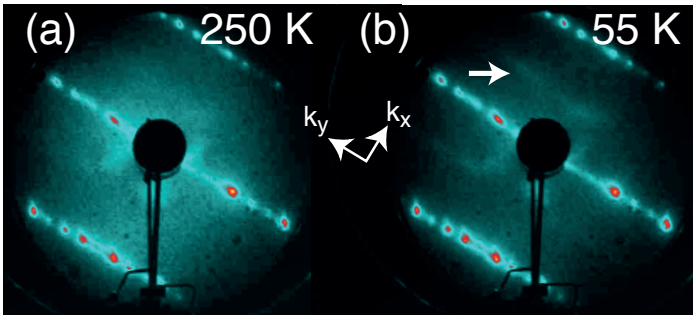

Figure 4.42: (a) and (b) LEED patterns collected above and below the temperature of the phase transition, respectively. The arrow in (b) shows the additional streaks induced by the periodicity doubling along the atomic chains. The electron kinetic energy is 27.2 eV.

A more detailed picture of the phase transition is provided by HAS. Fig. 4.43(a) displays the scattered He intensity versus momentum transfer k_x for various sample temperatures T using an incident beam energy E_i of 14.5 meV. At low temperature a small enhancement of the scattered intensity appears, halfway between the diffraction peaks which is consistent with a superstructure based on a doubled periodicity along the rows, as observed by the LEED and STM measurements. Scans with different beam energies show that this cannot be due to any resonance effect and is indeed caused by a reconstruction [6].

Fig. 4.43(b) shows the temperature dependence of the square root of the integrated intensity for the CDW superlattice peak half-way between the $(\overline{2},0)$ and $(\overline{1},0)$ Bragg peaks (see Fig. 4.43(a)). In order to access the intensity change relevant to the critical fluctuations of the CDW [322, 323] as opposed to the intensity changes due to the Debye-Waller factor [37], the integrated intensity $I(T)$ shown in the figure has been normalized to that of the specular beam (see "Appendix B: Debye-Waller correction of the order parameter" for more details on the procedure). This correction is particularly necessary in view of the low surface Debye temperature of Bi ($\Theta_D = 85\,\text{K} < T_c$ [80, 324], where T_c is the CDW transition temperature). The square root of the resulting $I(T)$ can then be viewed as the order parameter of the CDW [325, 326]. $I(T)$ shows a sharp onset below approximately 250 K, followed by a continuous rise at lower temperatures.

The temperature dependence of the order parameter $\sqrt{I(T)}$ can be used to determine T_c and the critical exponent β belonging to the phase transition [322, 323, 327–329]. This is achieved by fitting the

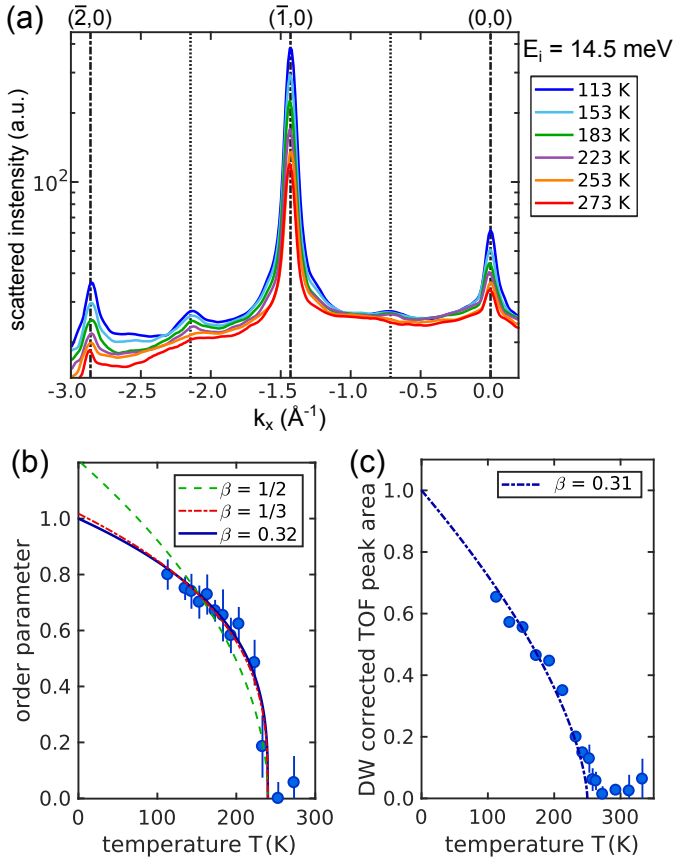

Figure 4.43: (a) Scattered He intensities (logarithmic scale) versus parallel momentum transfer k_x (crystal azimuth aligned along $\overline{\Gamma}-\overline{\mathrm{X}}$) for various sample temperatures T. A small vertical offset between the individual scans was added for better visibility. The vertical dotted lines illustrate the position of the CDW superlattice peaks due to the doubled periodicity. (b) Normalised square root of the CDW superlattice peak's integrated intensity (peak at $k_x = -2.15\,\text{Å}^{-1}$), which is proportional to the CDW order parameter. The lines represent fits to (Eq. (4.33)) for different choices of the order parameter β. (c) Peak area of the CDW superlattice peak when integrated over energy in the energy-resolved TOF measurements.

power law

$$\sqrt{\frac{I(T)}{I(0)}} = \left(1 - \frac{T}{T_c}\right)^{\beta}, \tag{4.33}$$

to the data in Fig. 4.43(b) ($I(0)$ is the extrapolated intensity at 0 K), resulting in $T_c = (245 \pm 8)\,\text{K}$ and $\beta = (0.32 \pm 0.03)$. The fit is represented by the blue solid line in Fig. 4.43(b).

Our finding of $\beta = (0.32 \pm 0.03)$ is very close to the universal exponent of 1/3 as predicted in the presence of fluctuations [329], in agreement with the findings of other CDWs in layered chalcogenides and quasi 1D systems [14, 15, 323, 330, 331]. On the other hand, using mean field theory ($\beta = 1/2$) where fluctuations are neglected, results in the green dashed curve which does not represent a satisfactory fit to the data. When fitting the data under the constraint that $\beta = 1/3$, we obtain the red dashed curve in Fig. 4.43(b), and a transition temperature of $T_c = (245 \pm 8)\,\text{K}$.

At first glance, the transition temperature determined from HAS appears to be inconsistent with the STM data that does not show any short range order above 195 K. We must keep in mind, however, that strong fluctuations are to be expected and that STM, being a slow technique, only measures the *average* position of the atomic motion and might thus not be able to show the preserved local dimerization at high

temperatures. This actually explains why close to defects, dimerization can still be observed frozen in the 195 K images. Indeed, LEED patterns taken at 200 and even 250 K do still show very weak signatures of the superstructure (see Fig. 4.42(a) and "Appendix A: Additional measurements").

Energy-resolved scans were performed at the position of the CDW superlattice peak which confirm that the enhanced elastic intensity is indeed due to a static change in the structure and cannot be caused by any inelastic effects such as kinematical focussing [6]. Fig. 4.43(c) shows the TOF peak intensity versus surface temperature which was obtained by fitting the energy-resolved scans with a single Gaussian, and applying a correction for the Debye-Waller attenuation (for the original TOF data see "Appendix B: Debye-Waller correction of the order parameter"). The temperature range where the peak intensity shows a strong rise is consistent with T_c as determined from Fig. 4.43(b) and fitting a critical exponent gives rise to $\beta = (0.31 \pm 0.04)$ in accordance with the result from analyzing the data in Fig. 4.43(b).

After characterizing the phase transition using structural techniques, we now move to the spectroscopic characterization of the electronic and vibrational states by ARPES and HAS. Fig. 4.44(a) shows the $k_\parallel$-dependent photoemission intensity at the Fermi level at 60 K. It is dominated by intense lines in the direction perpendicular to the atomic rows. As has been shown by spin-resolved photoemission, these intense lines are actually caused by the two unresolved spin-polarized Fermi surface elements due to the spin-split surface state in Fig. 4.40(b) [68]. This unresolved Fermi contour is indicated as a sketch, extending the observed Fermi contour in the figure. Apart from the intense linear features, the photoemission intensity shows some weak structures that can be assigned to bulk states. A projection of the (small) bulk Fermi surface of Bi onto the (114) surface is given in Ref. [68].

Since the Fermi surface of Fig. 4.44(a) is measured in the dimerized phase, one might expect replicas of the Fermi surface lines in between the two intense lines, similar to the additional weak streaks in between the lines of densely spaced spots in the LEED image of Fig. 4.42(b). Such replicas are not observed, neither at the Fermi surface in Fig. 4.44(a) nor for the higher binding energy of 170 meV in Fig. 4.44(b). Note that the lack of replica bands in a CDW is also found for many two-dimensional CDW systems where the spectral weight in the CDW phase tracks that of the normal phase [315]. Hence the CDW period observed in direct space may not correspond to nesting, i.e., to the $2k_F$ measured with high-resolution ARPES in reciprocal space.

Fig. 4.44(c) and (d) show the electronic structure of the one-dimensional states above and below the dimerization transition temperature, respectively, as a function of binding energy in the k_x-direction perpendicular to the one-dimensional Fermi surface, along a cut indicated by the black dashed line in Fig. 4.44(a). No spectroscopic signature of the transition is observed near the Fermi energy. Indeed, when taking momentum distribution curves (MDCs) through a temperature-dependent series of similar data sets, no significant changes can be observed (see Fig. 4.44(e)), except for a minor sharpening of the MDC peak at low temperatures, as expected due to electron-phonon coupling [42, 332].

However, there is a significant change in the electronic structure rather far away from the Fermi energy, at around 150 meV, where a single intense feature at 110 meV in the high temperature phase of Fig. 4.44(c) splits into two peaks, one essentially staying at the same binding energy and one moved to a higher energy of 175 meV. This spectral change is especially well seen in energy distribution curves through the center of a series of temperature-dependent data shown in Fig. 4.44(f). These changes in the electronic structure at high binding energy do not lead to observable replicas in the constant energy surfaces either, as seen in Fig. 4.44(b) which shows the photoemission intensity at a binding energy of 170 meV.

The observation of spectral changes only at high binding energy rules out that the transition is due to a nesting-driven weak CDW, such as the Peierls distortion in Fig. 4.40(b), as this would require a gap opening at the Fermi energy. On the other hand, an electronic structure change in which states are shifted to a substantially higher binding energy can certainly explain the stabilization of the reconstructed

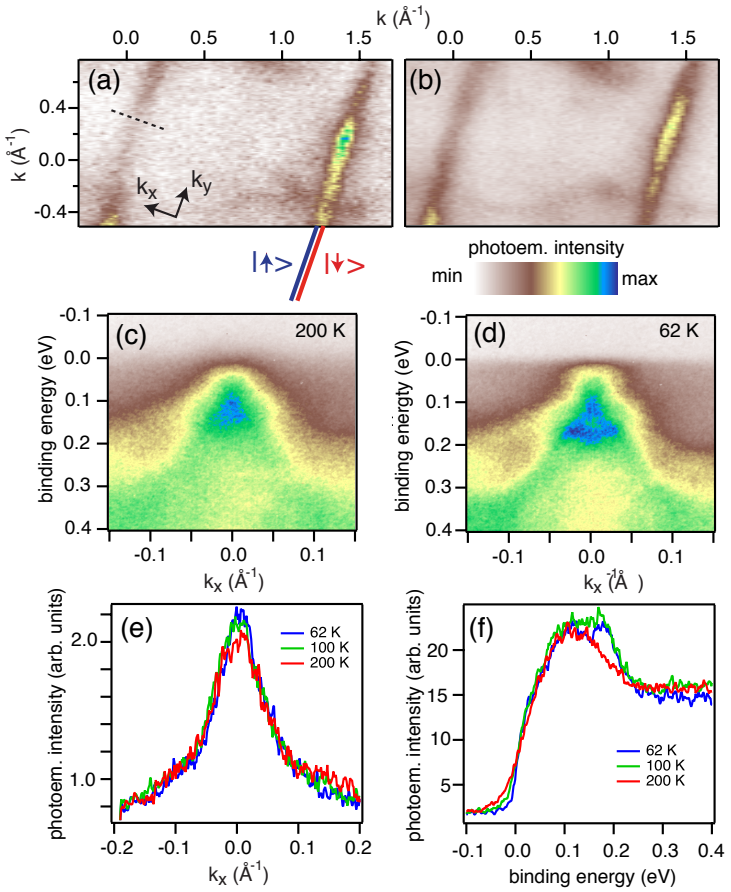

Figure 4.44: (a),(b) Photoemission intensity in the low-temperature phase at $T = 60\,\mathrm{K}$ in a 20 meV window around the Fermi energy and a binding energy of 170 meV, respectively. The sketched continuation of the Fermi surface illustrates that the observed line-like intensity is comprised of two unresolved spin-polarized Fermi level crossings [68], see also Fig. 4.40(b). The photon energy is $h\nu = 70\,\mathrm{eV}$. The dashed line shows the direction of the data in (c)-(e). (c), (d) Photoemission intensity close to and below the CDW transition (at $T = 200$ and 62 K), respectively, along the dashed black line in (a). (e) Momentum distribution curves at the Fermi energy along the dashed line in (a) as a function of temperature. (f) Energy distribution curves along the crossing point of the dashed line in (a) and the Fermi surface at $k_x = 0$, i.e. through the center of the images in (c) and (d). $h\nu = 17\,\mathrm{eV}$ in (c)-(f).

phase. This gives a qualitative explanation for the stability of the pairing distortion at low temperatures, but it does not explain why the pairing should be lifted at higher temperature. In a conventional Peierls scenario, the transition from the CDW state to the normal state is driven by electronic entropy when the thermal energy becomes comparable to the gap energy. This cannot be the case here. We also note that the CDW is unlikely to be caused by bulk states because of the extremely small density of bulk states at E_F and because of the absence of a CDW in bulk Bi.

A plausible alternative scenario is that the transition is a strong coupling CDW, driven by phonon entropy [272, 313, 325, 333] and this is supported by several experimental facts, such as the short coherence length and considerable atomic displacements observed here as well as by a significant electron-phonon coupling λ. A strong-coupling CDW would not be uncommon for a one-dimensional surface structure. A similar mechanism has also been suggested for the CDW of In nanowires on Si(111) [334] which, however, also shows a pronounced gap opening at the Fermi energy [296, 335]. Most importantly, the strong coupling picture would explain why a temperature-dependent distortion can appear in a system with this

particular spin texture, for which it would otherwise not be expected.

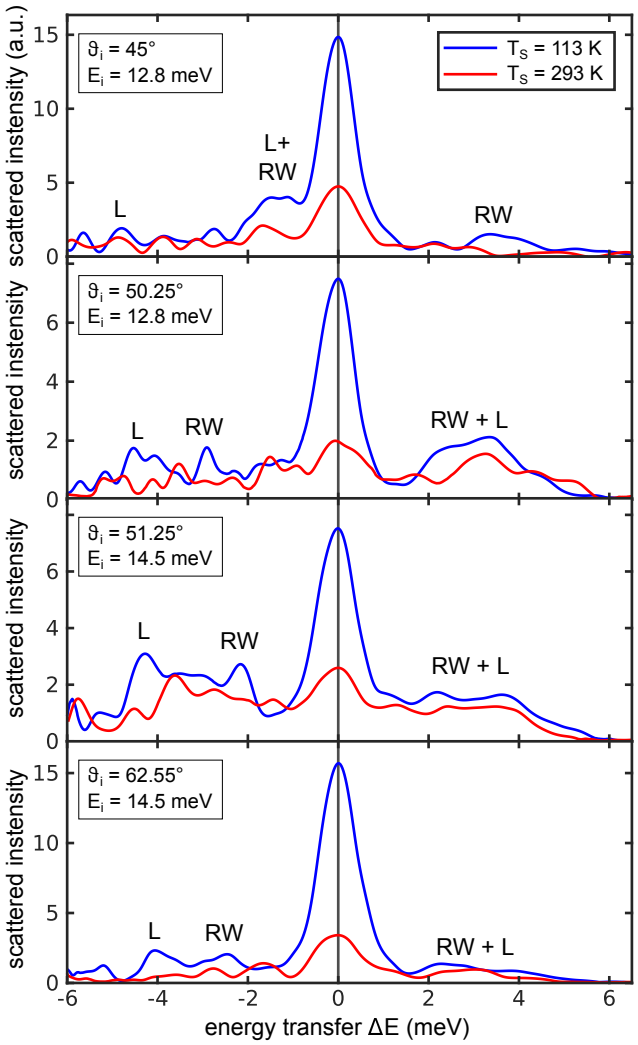

Figure 4.45: Comparison of several TOF spectra for the cooled sample and the sample at room temperature, transformed to energy transfer spectra $\Delta E = E_f - E_i$. Energy loss ($\Delta E < 0$) corresponds to the creation of a phonon with phonon energy $\Delta E = \hbar\omega$ and energy gain ($\Delta E > 0$) corresponds to the annihilation of a phonon. RW and L stand for the Rayleigh wave and longitudinal phonon modes, respectively.

A phonon entropy driven phase transition typically gives rise to a change of the phonon density of states (PDOS), as recently observed for the metal insulator transition in VO_2 [333]. HAS can, in principle, be used to map the full surface phonon dispersion and is especially valuable because its high resolution gives access to low energy phonons. In the case of Bi(114), the cross section for inelastic phonon scattering turned out to be extremely small, such that only spectra at a few values of the momentum transfer could be measured. TOF spectra were recorded along the $\overline{\Gamma} - \overline{X}$ azimuth with the sample at room temperature and $T = 113\,\mathrm{K}$. The TOF spectra were then transformed to energy transfer spectra which allows inelastic (phonon) scattering events to be determined. The energy transfer $\Delta E = E_f - E_i$ was determined by the initial energy E_i and final energy E_f of the helium atom and energy loss ($\Delta E < 0$) and gain peaks ($\Delta E > 0$) correspond to the creation and annihilation of a phonon, respectively [4].

Fig. 4.45 gives a selection of inelastic spectra measured at different incident energies and angles. The most prominent inelastic features are labelled as Rayleigh wave (RW) and longitudinal (L), based on the

experimentally and theoretically determined surface phonon dispersion of Bi(111) along $\overline{\Gamma}-\overline{\mathrm{M}}$ [4]. While the data does not give the full surface phonon dispersion, two important conclusions can be drawn: First, we observe a significant change of the phonon spectrum between the two phases. Although the Jacobian scaling upon transforming from TOF to energy transfer increases the height of the experimental noise on the phonon creation side of the spectrum ($\Delta E < 0$), this can be clearly seen on the loss side by comparing the most pronounced peaks at the two temperatures. Second, the low temperature phase generally shows more intense features on the gain side (phonon annihilation) of the elastic peak, consistent with a higher phonon occupation in the low temperature phase. Since the Bose factor for the low energy acoustic modes is not substantially different between both temperatures it indicates that the PDOS changes below T_c. Hence the observation of an enhanced intensity of the low energy acoustic surface phonon modes below T_c is in line with a strong phonon contribution to the transition entropy.

Conclusion

In conclusion, we have reported the observation of a dimerization transition below (245 ± 8) K on Bi(114). Such a transition is highly unexpected, even in the presence of a perfectly nested one-dimensional Fermi contour, because it appears to be forbidden by the spin texture of the states and the non-matching nesting vector $2k_F$. Indeed, the transition does not involve the states near the Fermi energy but spectral changes at higher binding energy are observed. This, as well as the short coherence length and significant changes in the phonon spectrum, support the interpretation of the low-temperature state as a strong-coupling CDW, illustrating that such transitions are still possible in topological systems.

More detailed insight into the driving force of the phase transition could, in principle, be gained by first principles calculations of the electronic structure, vibrational properties and electron-phonon coupling in the system, similar to the work that has been carried out for In on Si(111) [334]. In the present case such calculations are extremely challenging due to the large unit cell, the need to include the spin-orbit interaction for an adequate description of the electronic states, and the need for a thick slab in the calculation in order to decouple the deeply penetrating surface states. However, in the present case they could give unprecedented insight into role of the spin-split surface states (if any) in a surface CDW of a topological material.

Acknowledgement

We gratefully acknowledge stimulating discussions with Kai Rossnagel, Matthias Hengsberger and Jürg Osterwalder. This work was supported by the Danish Council for Independent Research, Natural Sciences under the Sapere Aude program (Grant No. DFF-4002-00029) and by VILLUM FONDEN via the center of Excellence for Dirac Materials (Grant No. 11744). JW acknowledges support from the Institute for Storage Ring Facilities, Aarhus University, during the beamtime for this project, and from the Research Council of Norway through its Centres of Excellence funding scheme, project number 262633, "QuSpin", as well as via the Fripro program, project number 250985 "FunTopoMat". A.J.M.-G. acknowledges funding from the Spanish MINECO through the Juan de la Cierva program. J.M.G.-R acknowledges financial support from the Spanish MINECO under project number MAT2016-77852-C2-2-R. A.T. and W.E.E. acknowledge financial support provided by the FWF (Austrian Science Fund) within the project P29641-N36.

Appendices

Appendix A: Additional measurements

This appendix provides LEED and ARPES data sets taken at more temperatures than given in the main paper, as well as a data set of HAS TOF spectra taken at the position of the CDW superlattice peak. Fig. 4.46 shows a series of LEED images for a kinetic energy of 27.7 eV for different temperatures, up to 200 K where the streaks of the reconstruction are still faintly visible. The figure also shows a cut through the images integrated along k_y, showing how the superstructure spots decay in intensity.

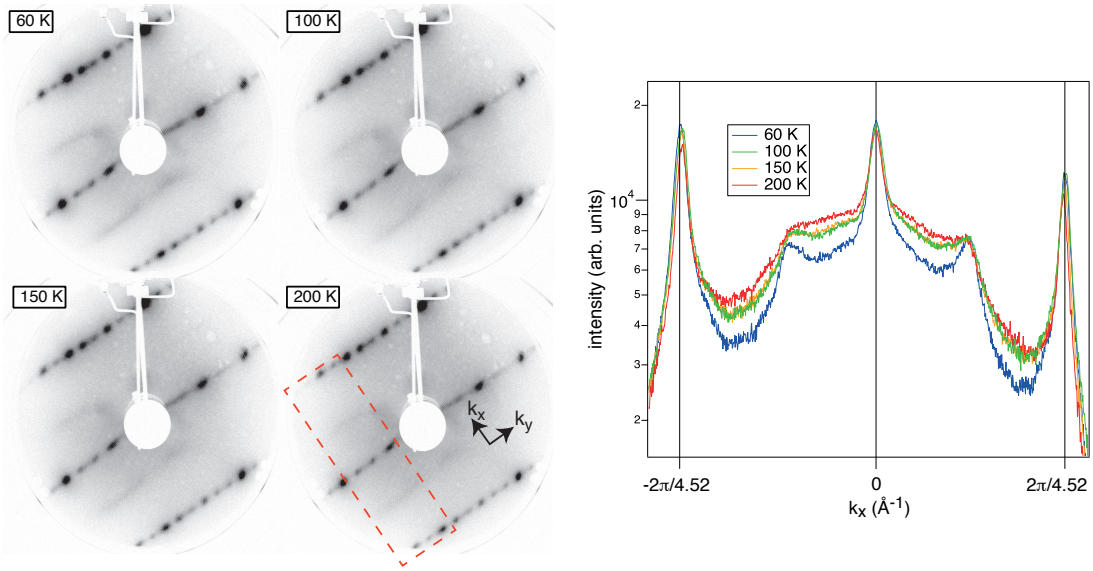

Figure 4.46: Left: LEED data sets for several temperatures. Right: LEED intensity integrated along k_y in the red dashed box shown for the 200 K LEED image.

Fig. 4.47(a)-(e) show data corresponding to Fig. 4.44(c) and (d) in the main paper and Fig. 4.47(f) shows the intensity through $k_x = 0\,\text{Å}^{-1}$ for these images.

Fig. 4.48(a) shows a series of energy scans (TOF measurements) at different surface temperatures for HAS at the position of the CDW superlattice peak Fig. 4.48(b) shows the normalised peak area versus surface temperature which was obtained by fitting the energy-resolved scans in Fig. 4.48(a) with a single Gaussian. The temperature range where the peak intensity shows a strong rise is consistent with T_c as determined from the intensity of the superlattice peak.

Fig. 4.48(c) shows a Debye-Waller plot, comparing the temperature dependence of the specular reflection upon scattering from Bi(114) and Bi(111) (data from Ref. [80]). The plot shows the temperature dependence of the logarithmic peak intensity $\ln[I(T)]$ times $1/k_{iz}^2$. k_{iz} is the momentum of the incident He beam perpendicular to the surface and accounts for the fact that different incident energies where used in both experiments.

Appendix B: Debye-Waller correction of the order parameter

The Debye-Waller (DW) factor e^{-2W} relates the diffraction intensities $I(T)$ of a sample at temperature T to the intensity $I(0)$ of a sample at $T = 0$ and can be written down for both the specular I_{spec} and the

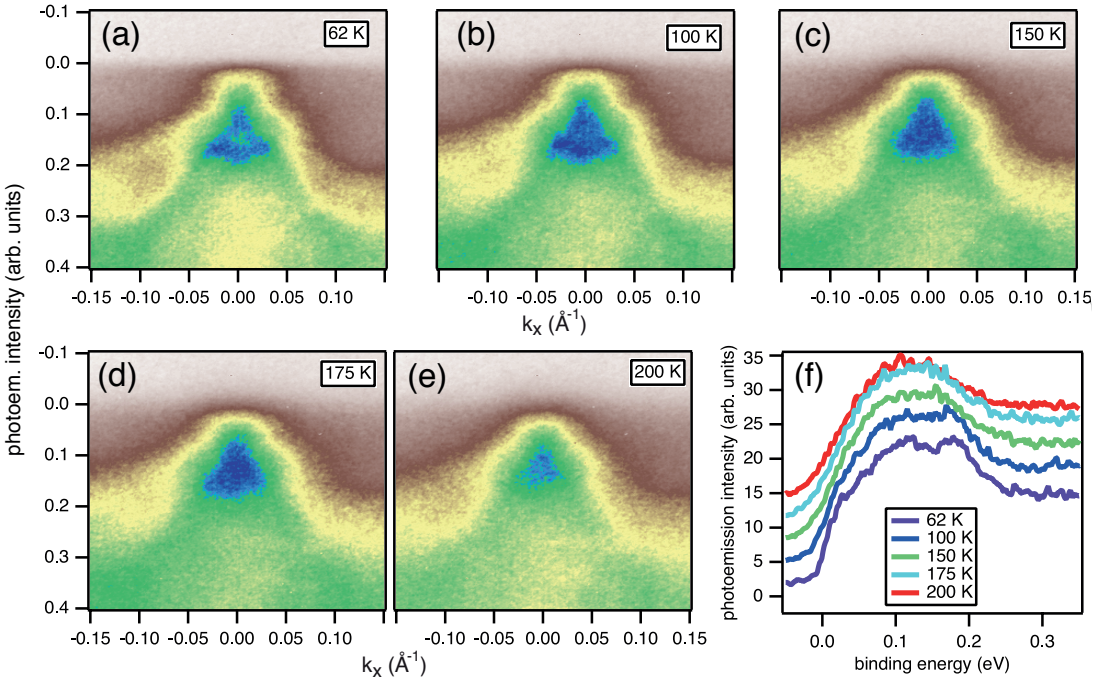

Figure 4.47: Photoemission along the dashed line of Fig. 4.44(a) in the main paper, i.e. data sets corresponding to Fig. 4.44(c) and (d) of the main paper but for more temperatures. (f) Photoemission intensity through $k_x = 0\,\text{Å}^{-1}$ for these images. The curves are vertically displaced to improve clarity.

CDW peak intensities I_{CDW}:

$$\begin{aligned} I_{spec}(T) &= I_{spec}(0)\ \mathrm{e}^{-2W_\perp\left(k_{iz}^{spec},T\right)} \\ I_{CDW}(T) &= I_{CDW}(0)\ \mathrm{e}^{-2W_\perp\left(k_{iz}^{CDW},T\right)}\ \mathrm{e}^{-2W_\parallel\left(k_\parallel^{CDW},T\right)}\,, \end{aligned} \tag{4.34}$$

where $\perp$ and $\parallel$ denote the components perpendicular and parallel to the surface and k_{iz} and $k_\parallel$ are the corresponding perpendicular and parallel momenta. Note that the DW factor of the CDW has also a parallel component since it appears off-specular. Assuming that the surface perpendicular component of the incident momentum is approximately the same in both cases ($k_{iz}^{spec} \cong k_{iz}^{CDW}$) yields:

$$I_{CDW}(T) = I_{CDW}(0)\frac{I_{spec}(T)}{I_{spec}(0)}\ \mathrm{e}^{-2W_\parallel\left(k_\parallel^{CDW},T\right)}\,. \tag{4.35}$$

Eq. (4.35) can be used to divide the DW factor out of the order parameter (Eq. (4.34) in the main part of the manuscript) giving rise to the following for the square of the order parameter Π :

$$\Pi^2 = \frac{I_{CDW}(T)}{I_{CDW}(0)}\frac{I_{spec}(0)}{I_{spec}(T)} = \mathrm{e}^{-2W_\parallel\left(k_\parallel^{CDW},T\right)} = \mathrm{e}^{-\left\langle\left(2\,k_F\cdot u_\parallel\right)^2\right\rangle_T}\,, \tag{4.36}$$

which relates the order parameter Π with the mean square displacement parallel to the surface $\langle u_\parallel^2\rangle_T$. Hence together with:

$$\ln\Pi^2 = 2\beta\,\ln\left(1-\tfrac{T}{T_c}\right) = -2W_\parallel\left(k_\parallel^{CDW},T\right)\,, \tag{4.37}$$

the mean square displacement parallel to the surface is related to the transition temperature of the CDW wave via:

$$\left\langle\left(2\,k_F\cdot u_\parallel\right)^2\right\rangle_T = -\ln\left(1-\tfrac{T}{T_c}\right)\,. \tag{4.38}$$

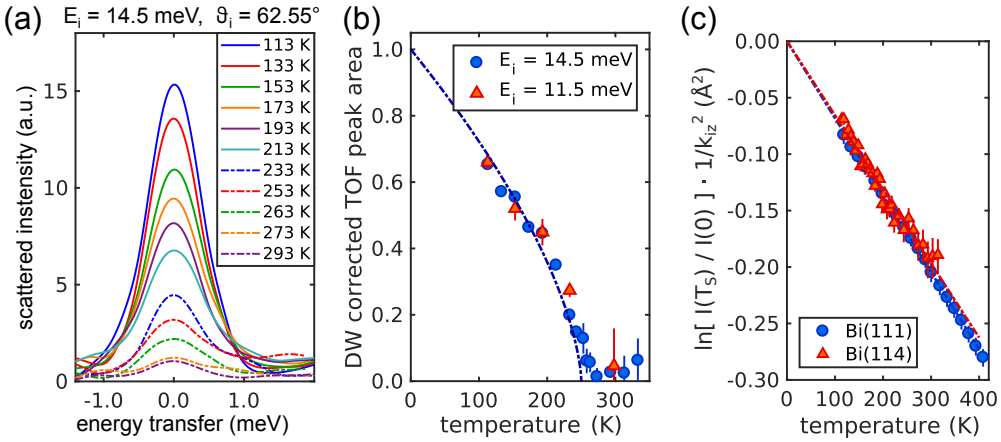

Figure 4.48: (a) Time-of-flight (TOF) scans at the position of the CDW superlattice peak half-way between the $(\overline{2}, 0)$ and $(\overline{1}, 0)$ diffraction peaks, converted to energy scale. (b) TOF peak area obtained by fitting the energy-resolved scans with a single Gaussian which is further corrected by dividing the DW factor out. A couple of additional data points measured at the position of the CDW superlattice peak at lower beam energy (11.5 meV, red triangles) show the same temperature behaviour. (c) Comparison between the decay of the logarithmic specular peak intensity $\ln[I(T)]$ times $1/k_{iz}^2$ with temperature T for the Bi(114) and the Bi(111) surface.

Eq. (4.38) describes the fact that the CDW transition is driven by the fluctuations in the electron gas associated (coupled via e-ph interaction) to the parallel phonon fluctuations around the atom equilibrium positions, which eventually ends into a divergence at T_c, resulting in atoms that are displaced by a finite amount to a new equilibrium position.

4.7 Origin of the Electron-Phonon Interaction of Topological Semimetal Surfaces Measured with Helium Atom Scattering

This section consists of the following published publication:

Origin of the Electron-Phonon Interaction of Topological Semimetal Surfaces Measured with Helium Atom Scattering

G. Benedek, S. Miret-Artés*, J. R. Manson, A. Ruckhofer, W. E. Ernst, and A. Tamtögl

The Journal of Physical Chemistry Letters **11**, 1927–1933, 2020
https://doi.org/10.1021/acs.jpclett.9b03829

* corresponding author

contributions

funding	W.E. Ernst, A. Tamtögl
experimental design	A. Ruckhofer, A. Tamtögl
data acquisition	A. Ruckhofer, A. Tamtögl
theoretical analysis	G. Benedek, S. Miret-Artés, J. R. Manson
data analysis HAS	A. Ruckhofer, A. Tamtögl
interpretation	A. Tamtögl, G. Benedek
publication writing	A. Tamtögl, S. Miret-Artés, G. Benedek, J. R. Manson
discussion and editing	all authors

Abstract

He atom scattering has been demonstrated to be a sensitive probe of the electron-phonon interaction parameter λ at metal and metal-overlayer surfaces. Here it is shown that the theory linking λ to the thermal attenuation of atom scattering spectra (the Debye-Waller factor), can be applied to topological semimetal surfaces, such as the quasi-one dimensional charge-density-wave system Bi(114) and the layered pnictogen chalcogenides.

Results and Discussion

Knowledge of the electron-phonon (e-ph) interaction at conducting surfaces and the specific role of dimensionality are of great relevance both from a fundamental point of view as well as for various applications, such as two-dimensional (2D) [336] and quasi-1D superconductivity [337] in nanotechnology. Similarly, the e-ph interaction plays a relevant role in other transport properties, e.g., thermoelectricity, in low-dimensional systems such as layered Bi and Sb chalcogenides [221], and in quasi-crystalline materials which are often viewed as periodic solids in higher dimensions [338].

In a series of recent experimental and theoretical works, it was shown that the e-ph coupling constants for individual phonons $\lambda_{\mathbf{Q},\nu}$, as well as their average λ (also known as the mass-enhancement parameter or factor) [41, 254, 339], can be measured directly with He-atom scattering (HAS) [32, 45, 46, 229]. In particular, the study of multilayer metallic structures [32, 229] has shown that HAS can detect subsurface phonons as deep as those that contribute to the e-ph interaction. For example, HAS can detect phonons spanning as many as 10 atomic layers in Pb films [45, 229] (known as the *quantum sonar effect*), thus providing the individual $\lambda_{\mathbf{Q},\nu}$ values for phonons which provide the dominant contributions to λ. The values of λ are obtained directly from the temperature dependence of the HAS Debye-Waller (DW) exponent, and the interaction range can be assessed from the number of layers, n_{sat}, above which the measured λ becomes thickness-independent. In that analysis, the conducting surface region of a 3D material could be viewed as a stack of (interacting) 2D electron gases (2DEGs), allowing for the simpler formalism characterizing the 2DEG [32]. Due to the appreciable depth explored by the e-ph interaction, the values of λ obtained from HAS (hereafter called λ_{HAS}) generally are close to the most reliable values found in the literature [32, 46], thus allowing one to assess the validity of the new method.

In this work we investigate the specific role of dimensionality in the e-ph mass-enhancement factor λ_{HAS} as derived from HAS. The method is shown to be particularly suitable for different classes of conducting 2D materials, such as layered chalcogenides, topological insulators, and systems characterized by a quasi-1D free electron gas, including Bi(114). The present analysis shows that the charge density wave (CDW) transition in Bi(114), recently observed with HAS [28], is sustained by multi-valley e-ph interaction with a pronounced 1D character. In the case of topological materials, the present analysis of previous HAS data on Bi_2Te_3(111) [47] and Bi_2Se_3(111) [25] as well as new experimental data on Bi_2Te_2Se(111) indicates the overwhelming contribution to λ_{HAS} from the surface quantum well states as compared to that of the Dirac states.

The DW factor describes the attenuation due to the thermal atomic motion of the elastically scattered intensity $I(T)$ observed at temperature T, with respect to the elastic intensity of the corresponding rigid surface I_0. It is a multiplicative factor usually written as an exponential function, $\exp\{-2W(\mathbf{k}_f, \mathbf{k}_i, T)\}$, of the final ($\mathbf{k}_f$) and incident ($\mathbf{k}_i$) wavevectors of the scattered atom, i.e.

$$I(T) \;=\; I_0 e^{-2W(T)} \;, \tag{4.39}$$

where it is implicit that all quantities in Eq. (4.39) depend on the scattering wavevectors $(\mathbf{k}_f, \mathbf{k}_i)$. For a two-body collision model, where the incident atom directly interacts with the surface target, the DW exponent is simply expressed by $2W(\mathbf{k}_f, \mathbf{k}_i, T) = \left\langle (\Delta\mathbf{k} \cdot \mathbf{u})^2 \right\rangle_T$, where $\Delta\mathbf{k} = (\mathbf{k}_f - \mathbf{k}_i)$ is the scattering vector, $\mathbf{u}$ is the phonon displacement experienced by the projectile atom upon collision, and $\langle \cdots \rangle_T$ indicates a thermal average. However, atoms incident on a conducting surface with energies generally well below 100 meV are scattered exclusively by the surface free-electron density, a few Å away from the first atomic layer, so that the exchange of energy with the phonon gas only occurs via the phonon-induced modulation of the surface free-electron gas, i.e., via the e-ph interaction. Therefore, it is logical that $2W(\mathbf{k}_f, \mathbf{k}_i, T)$, which originates from the integrated action of all phonons weighted by their respective Bose factors, turns out to be directly proportional, under reasonable approximations, to the mass-enhancement factor λ.

The expression of λ_{HAS} derived in Ref. [46, 340] for a 3D free-electron gas is readily extended to any dimension d:

$$\lambda_{HAS}^{(d)} \;=\; -\frac{\phi\gamma_d}{(k_F r_0)^d}\,\frac{k_F^2}{k_{iz}^2}\,\frac{\partial \ln\{I\,(T)\}}{k_B\;\partial T}\;, \tag{4.40}$$

where r_0 is a lattice distance ($r_0^2 \equiv A_c$ for the surface unit cell area in 2D, $r_0^3 \equiv V_c$ the unit cell volume in 3D), ϕ the workfunction, k_F the Fermi wavevector, k_{iz} is the perpendicular component of the incident wave vector, k_B is the Boltzmann constant, $I(T)$ is the diffraction peak intensity, and $\gamma_d \;\equiv\; 2^{d-1}\,\pi^{d/2}\,\Gamma\left(\frac{d}{2}\right)$ [341], with Γ the Gamma-function. As mentioned above and discussed in Ref. [32] , the 3DEG of a thick slab can be viewed as a stack of n_{sat} 2DEGs, where n_{sat} is the number above the one at which HAS reflectivity becomes independent of thickness. This yields the definition $n_{sat} \;=\; c^* k_{F\perp}/\pi$, where $k_{F\perp}$ is the Fermi wavevector normal to the surface and c^* is the e-ph interaction range normal to the surface, i.e., the maximum depth beneath the surface from where phonon displacements can modulate the surface charge density. Note that $\pi/k_{F\perp}$ is the wavelength of a Fermi-level charge density $\cos^2 k_{F\perp} z$, i.e., the nominal thickness of a single 2DEG.

In this way the 2D expression of the e-ph coupling constant for a three-dimensional crystal is obtained [32], which is reproduced here for the special case of measurements at the specular condition:

$$\lambda_{HAS}^{(2D)} \;=\; \frac{\pi}{2n_{sat}}\alpha, \qquad \alpha \;\equiv\; -\frac{\phi}{A_c k_{iz}^2}\frac{\partial \ln\{I(T)\}}{k_B \partial T}\;. \tag{4.41}$$

When applying Eq. (4.41), it is important to distinguish between metallic surfaces, which present to the He atoms a soft repulsive potential plus a weak long-range attractive well, and layered semimetal surfaces, where the free electron gas is protected by an anion surface layer that results in a hard-wall potential plus a comparatively deep attractive van der Waals potential. In the latter case, k_{iz}^2 needs to be corrected due to the acceleration that the He atom undergoes when entering the attractive well, before being repelled by the hard wall (Beeby correction [342]). This is made with the substitution $k_{iz}^2 \longrightarrow k_{iz}^2 + 2mD/\hbar^2$, where m is the He atom mass and D is the attractive potential depth (generally derived from He-surface bound-state resonances). In many experiments, the incident energy E_i is generally much larger than D, so the Beeby correction may be neglected, but not, for example, in ^{3}He spin-echo experiments, where E_i is low and comparable to D [18].

Low-dimensional free electron gases are often characterized by a CDW instability below a critical temperature T_c, generally induced by e-ph interaction via the Fröhlich-Peierls [292, 343] or the Kelly-Falicov multivalley mechanisms; [344–346] the former typically applying to metal surfaces with a CDW wavevector corresponding to some nesting wavevector at the Fermi contours, the latter more appropriate to semimetal surfaces with pocket states at the Fermi level [49]. The phonon-induced transitions between narrow pockets (nests) realize what is meant as perfect nesting. Since He atoms scattered from a conduct-

ing surface probe the surface charge density directly, the occurrence of a CDW below T_c yields additional T-dependent diffraction peaks in the elastic scattering angular distribution at parallel wavevector transfers $\Delta K = |\Delta\mathbf{K}|$ equal or close to the nesting vectors Q_c (i.e., $Q_c = 2k_F$ for the 1D Peierls mechanism). It should be noted that the high sensitivity of HAS permits the detection of weak surface CDWs that are difficult to detect with other methods. An interesting question is whether the temperature dependence of the CDW diffraction peaks carries additional information on the e-ph interaction which sustains the CDW transition.

When considering the temperature dependence of a diffraction peak intensity for a wavevector transfer $\Delta\mathbf{K}$ equal to either a $\mathbf{G}$-vector of the unreconstructed surface lattice ($\Delta\mathbf{K} = \mathbf{G}$), or to a CDW wavevector Q_c, the DW exponent also involves the longitudinal mean-square phonon displacement. For an isotropic mean-square displacement, Eq. (4.40) also can be applied to diffraction peaks by replacing $4k_{iz}^2$ with $\Delta k_z^2 + \Delta\mathbf{K}^2$, calculated at the actual scattering geometry at which the diffraction peak is observed. In most HAS experiments the condition $\Delta\mathbf{K}^2 << \Delta k_z^2$ holds, so little difference is expected between the T-dependence of the diffraction and specular peaks, provided λ_{HAS} is independent, as it should be, of the scattering channel chosen in the experiment.

There is, however, a caveat for the use of a CDW diffraction intensity $I_{CDW}(T)$. In Eq. (4.39) it has been assumed implicitly that $W(T)$ includes all the temperature dependence of $I(T)$ and that this originates exclusively from thermal vibrations. This is clearly not true for the diffraction from a surface CDW which forms below T_c from a Fermi surface instability and has the temperature-dependent population of electron states near the Fermi level according to Fermi statistics. In this case I_0 has an implicit dependence on T, which generally is negligible with respect to that of $W(T)$, except near T_c: here its square root $\sqrt{I_0}$ works as an order parameter, [347, 348] and vanishes for increasing $T \to T_c$ as $(1 - T/T_c)^\beta$, where β is the order-parameter critical exponent (typically $\beta = 1/3$ [28, 349–351], while $T_c \approx 280\,\mathrm{K}$ in the present case [28]).

As a good 1DEG example, it is shown that a CDW diffraction peak also may be used to extract λ_{HAS} away from the critical region. The ideal (114) truncation of bismuth (Fig. 4.49) is characterized by parallel atomic rows along the $x \equiv [1\bar{1}0]$ direction, separated by 7.1 Å in the normal direction $y \equiv [22\bar{1}]$, with a unit cell including two rows ($b = 14.2\,\text{Å}$) and one atom per row (atom spacing along the rows $a = 4.54\,\text{Å}$). At room temperature, the Bi(114) surface is reconstructed in a (1×2) fashion with 3 missing rows out of 4, so as to have one row per unit cell ($b = 28.4\,\text{Å}$) and one atom per row (Fig. 4.49a) and b)). The electronic structure, calculated by Wells *et al.* [68] for the (1×1) phase (Fig. 4.49c), left), shows cones centered at the $\overline{\mathrm{X}}$ and $\overline{\mathrm{Y}}$ points (Fig. 4.49c) and d)) at the Fermi level. Those at $\overline{\mathrm{Y}}$ are folded into $\overline{\Gamma}$ in the (1×2) reconstructed phase. Both electronic structures allow for a multivalley CDW via e-ph interaction, the former with a 2D character, the latter with a pure 1D character due to the cone alignment along $\overline{\Gamma\mathrm{X}}$ with a $G/2$ spacing. HAS angular distributions along $\overline{\Gamma\mathrm{X}}$ [28] (Fig. 4.50a)) show the growth of additional peaks at $\pm G/2$ and $\pm 3/2$ below $T \approx 280\,\mathrm{K}$, indicating the formation of a surface commensurate CDW [28]. The associated (2×2) reconstruction consists of a dimerisation along the rows. The portion of the Bi(114)-(2×2) STM image reproduced in Fig. 4.49b) from Hofmann *et al.* [28, 183] suggests a phase correlation between rows, giving an oblique (2×2) unit cell and a corresponding elongated hexagonal Brillouin zone (BZ) (Fig. 4.49d)).

The HAS DW exponents for the specular $\mathbf{G} = (0, 0)$, diffraction $\mathbf{G} = (\bar{1}, 0)$, and CDW $(\bar{3}/2, 0)$ peaks measured as a function of temperature below T_c are plotted in Fig. 4.50b). The specular and diffraction DW exponents have almost the same slopes, the small difference being compensated by the ratio $(\Delta k_{iz}^2)_{(0,0)}/[\Delta k_z^2 + \Delta\mathbf{K}^2]_{(\bar{1},0)}$, resulting in the same values of λ_{HAS}^{1D} within less than 1%. The input data in Eq. (4.40) for $d = 1$ are $\phi = 4.23\,\mathrm{eV}$ [352], $2k_F = G/2 = 0.7\,\text{Å}^{-1}$, $r_0(2 \times 2) = 9.08\,\text{Å}$, incident energy $E_i = 14.5\,\mathrm{meV}$, and fixed scattering angle of 91.5°, so $(\Delta k_{iz}^2)_{(0,0)} = 54.3\,\text{Å}^{-2}$. The $(\bar{1}, 0)$ diffraction

occurs at the incident angle of 51.2°, which gives $(\Delta k_{iz}^2)_{(\bar{1},0)} = 53.8\,\text{Å}^{-2}$, and the resulting e-ph coupling constant is $\lambda_{HAS}^{1D} = 0.45 \pm 0.03$, being the same value for both specular and diffractive channels.

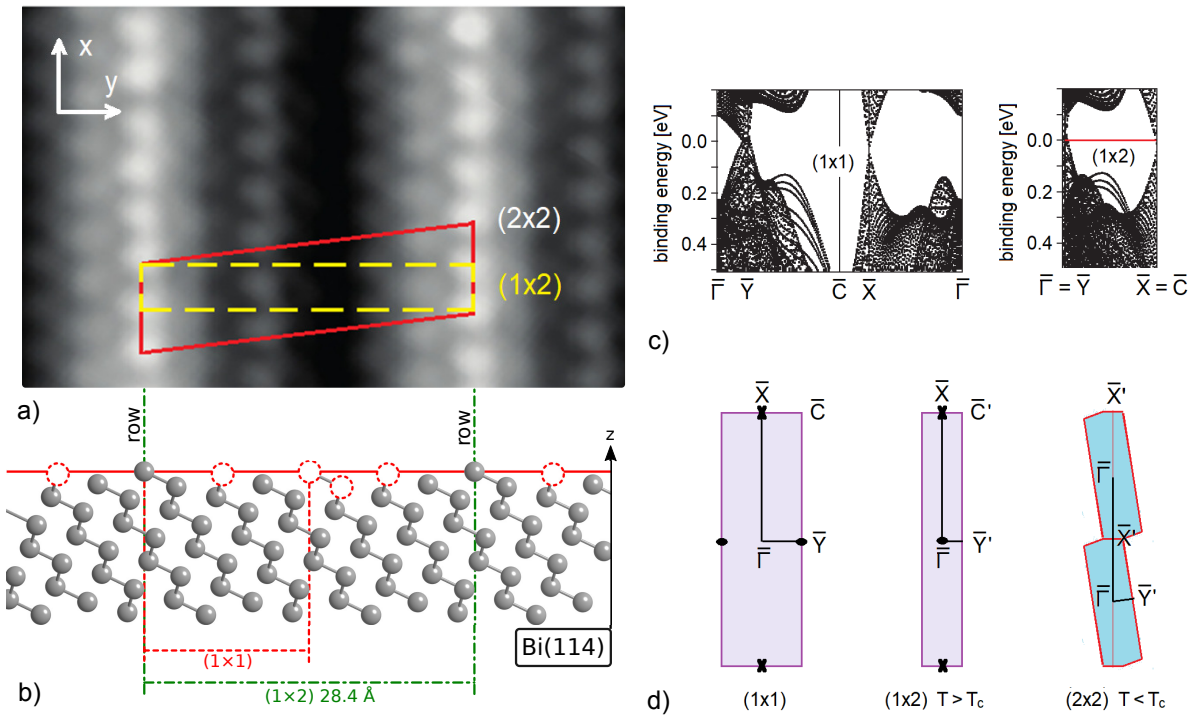

Figure 4.49: a) The Bi(114) surface is characterized by parallel atomic rows due to a (1×2) surface reconstruction as visualised in STM images [68][6]. b) A side view of the ideal (114) truncation of bismuth (including the red dashed circles) and the actual (1×2) surface reconstruction (circles removed), giving rise to the parallel atomic rows with an inter-row distance of 28.4 Å and an interatomic distance of 4.54 Å. The corresponding (1×2) electronic structure c) is schematically represented as a folding of the calculated electronic structure [68][6] for the truncated Bi(114) (1×1) surface, with the corresponding surface BZ shown in d). In particular, the cones of electronic states occurring at the Fermi level at the $\overline{\text{X}}$ and $\overline{\text{Y}}$ symmetry points turn out to be aligned in the $\overline{\Gamma\text{X}}$ direction after the (1×2) folding (panel d)). It allows for a multivalley 1D CDW instability along the rows leading to a (2×2) dimerization below $\approx 280\,\text{K}$ and a corresponding CDW observed with HAS [28]. The (2×2) surface portion reproduced in a) [68] shows a π-dephasing of two adjacent rows so as to give a rhombohedric cell, with the corresponding BZ shown in d).

The CDW $(\bar{3}/2, 0)$ peak intensity, Fig. 4.50b), shows the expected critical behavior with $\beta \cong 1/3$, so that a value of λ_{HAS}^{1D} can only be estimated from the slope at the lowest temperatures. This is smaller than that for the specular peak by $\sim 5\,\%$ and is compensated for approximately the same amount by the correcting factor $(\Delta k_{iz}^2)_{(0,0)}/[\Delta k_z^2 + \Delta\mathbf{K}^2]_{(\bar{3}/2,0)} = 1.047$, the incident angle for the CDW peak at $(\bar{3}/2, 0)$ being 62.75°. Thus it is reasonable to conclude that consistent values of λ_{HAS}^{1D} can be extracted from the T-dependence of the CDW peaks.

It is interesting to compare the value $\lambda_{HAS}^{1D} = 0.45$ for Bi(114) to that previously derived for Bi(111), either treated as a 3D system where $\lambda_{HAS}^{3D} = 0.57$ [46], in agreement with the value of $\lambda = 0.60$ in Hofmann's review [183], or as a 2D system with $n_s = 2$ (a single bilayer) where it is found that $\lambda_{HAS}^{2D} = 0.40$, in fair agreement with a recent ab initio calculation by Ortigoza *et al.* for Bi(111) [242] which yielded $\lambda = 0.45$, just as found here for Bi(114). As seen in Fig. 4.50c), the DW exponent has about the same slope for Bi(111) and Bi(114), when it is divided by k_{iz}^2, in order to account for the different incident energy used in HAS experiments. The fact that $\lambda_{HAS}^{(1D)}$ [Bi(114)] $< \lambda_{HAS}^{(3D)}$[Bi(111)] reflects the

[6] reproduced with permission, copyright 2009 by the American Physical Society

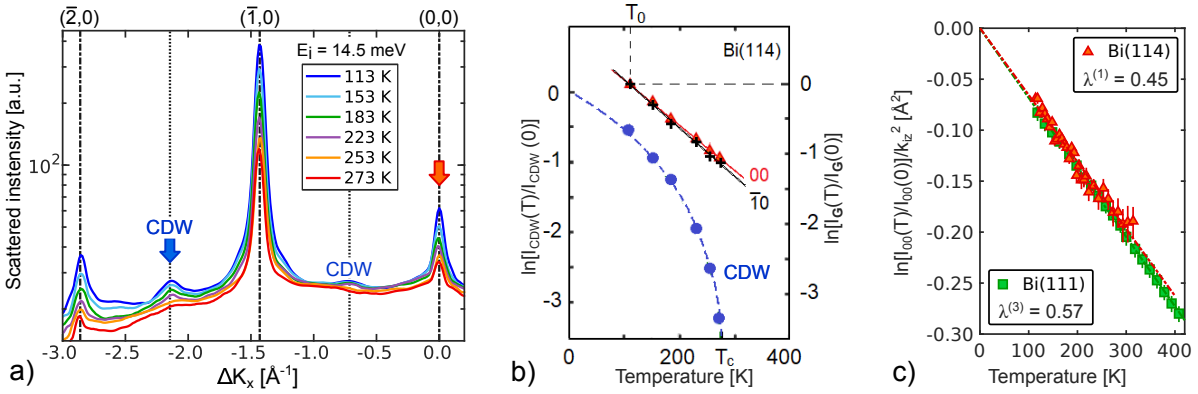

Figure 4.50: Helium atom scattering data from Bi(114): a) HAS angular distributions for several different temperatures, ranging from 113 to 273 K as marked, showing both diffraction peaks of the (2×1) reconstruction and the appearance of the CDW feature according to a (2×2) superstructure. b) The temperature dependence of the $\frac{3}{2}(\bar{1}, 0)$ CDW peak (left ordinate scale) and of the $(0, 0)$ (specular) and $(\bar{1}, 0)$ (diffraction) peak DW exponents referred to the lowest temperature measured, $T = 113$ K. c) The DW exponents of the Bi(114) and Bi(111) specular peaks, when divided by the respective squared perpendicular wavevector transfers, show similar slopes but lead to different e-ph coupling strengths.

dimensionality effect of γ_d, in the prefactor of Eq. (4.40). Incidentally, we note that treating Bi(114) as a 2D system would yield a five times smaller, probably unphysical, value for λ_{HAS} due to the large surface unit cell area.

Layered chalcogenides, such as 2D topological materials, with strong intralayer and weak interlayer forces form a wide class of quasi-2D materials with a conducting surface. Some transition-metal dichalcogenides (TMDC) have been investigated with HAS since the late eighties in connection with CDW transitions, related Kohn anomalies in the bulk, and surface phonon dispersion curves [13, 14, 353–355]. More recently, HAS studies have been extended to the surface of other TMDCs such as 2H-MoS_2(0001) [116] and 1T-$PtTe_2$ [356], as well as to pnictogen chalcogenides with surface topological electronic bands at the Fermi level, such as Bi_2Te_3 [47, 111, 357], Bi_2Se_3 [25, 225], etc. The 2D expression for the e-ph coupling constant $\lambda_{HAS}^{(2D)}$ in Eq. (4.41) is the one to be used for these systems. When dealing with the e-ph coupling constant λ_{HAS} expressed as an average over the whole phonon spectrum and over all electronic transitions across the Fermi level, natural questions are: a) which phonons contribute most, and b) which electronic states at the Fermi level are more important.

The theoretical analysis by Heid *et al.* [226] of the mode-selected e-ph coupling constants $\lambda_{\mathbf{Q}\nu}$ shows that in pnictogen chalcogenides, optical phonons give the major contribution to e-ph interaction, and therefore to the DW exponent. Both Bi_2Se_3(111) [25] and Bi_2Te_3(111) [111] exhibit two highly dispersed optical branches with deep minima at $\overline{\Gamma}$ for 3$^{\text{rd}}$-layer longitudinal polarization and at $\approx\overline{\Gamma\text{M}}/2$ for (mostly) 3$^{\text{rd}}$-layer shear-vertical (SV3) polarisation. Their optical character and largest amplitude at the central chalcogen layer of the quintuple layer endow these modes with a dipolar character and therefore a large e-ph interaction, consistent with the Heid *et al.* theoretical analysis [226]. Spin-echo ^{3}He scattering data from Bi_2Te_3(111) [111] suggest a Kohn anomaly also in the longitudinal acoustic branch corresponding to a nesting across the Dirac cone above the surface conduction-band minimum. As discussed in [226], the interband e-ph coupling occurring when the Fermi level is above the surface conduction-band minimum is enhanced largely by the involvement of surface quantum-well states. This conclusion is confirmed by the following analysis of $\lambda_{HAS}^{(2D)}$ in Bi chalcogenides as a function of the Fermi level position.

The temperature dependence of HAS specular reflectivity from the three Bi chalcogenide surfaces

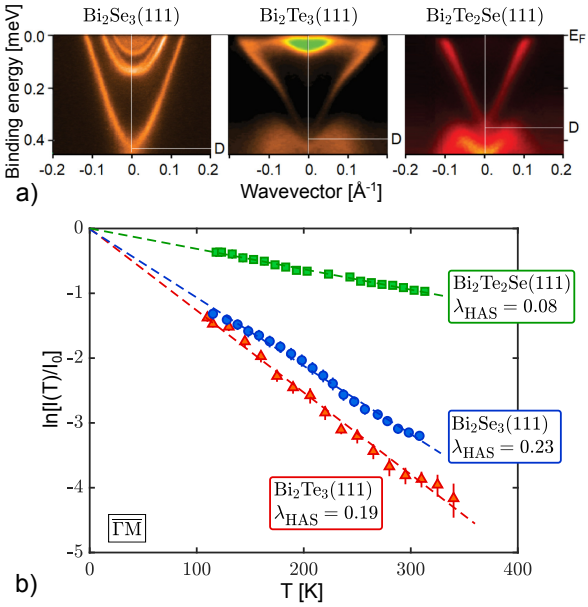

Figure 4.51: Three different Bi chalcogenides Bi_2Se_3, Bi_2Te_3 and Bi_2Te_2Se: a) ARPES data for the (111) surface of three Bi chalcogenides with decreasing binding energy of the Dirac point (D) and of the surface conduction-band minimum (from 0.15 eV in Bi_2Se_3 [112][a] to 0.08 eV in Bi_2Te_3 [240][b], and ≈ 0 in Bi_2Te_2Se [358][c]). b) The DW exponent slopes from HAS specular intensity measured as functions of temperature with the scattering plane in the $\overline{\Gamma M}$ direction for the same samples. The corresponding e-ph coupling constants λ_{HAS} decrease from $Bi_2Se_3(111)$ to $Bi_2Te_2Se(111)$, suggesting a dominant role in the e-ph interaction of the conduction band quantum-well electronic states over the Dirac electrons.

[a] reproduced with permission, copyright 2012 by the Institute of Physics
[b] reproduced with permission, copyright 2014 by the American Physical Society
[c] reproduced with permission, copyright 2014 by the American Chemical Society

$Bi_2Se_3(111)$, $Bi_2Te_3(111)$, and $Bi_2Te_{3-x}Se_x(111)$ (phase II with $x \approx 1$ [280][7], hereafter approximated by $Bi_2Te_2Se(111)$) has been measured for three samples whose surface electronic states near the Fermi level, in particular the topological Dirac states and the quantum-well states above the surface conduction-band minimum, are known from angle-resolved photoemission spectroscopy (ARPES) data [112, 227, 240, 358]. As seen in Fig. 4.51 (top panel), the binding energy of the Dirac point (D) with respect to the Fermi energy E_F decreases in the sequence $Bi_2Se_3(111)$, $Bi_2Te_3(111)$, $Bi_2Te_2Se(111)$, as does the surface conduction-band minimum (from 0.15 eV, to 0.08 eV and ≈ 0, respectively). Correspondingly, the DW exponent slope derived from the HAS specular intensity as a function of temperature also decreases. Similar behavior is expected for the e-ph coupling constant $\lambda_{HAS}^{(2D)}$, which is shown in Tab. 4.6. The latter is derived from Eq. (4.41) by setting $n_{sat} = 2\lambda_{TF}/c_0$, where c_0 is the quintuple layer (QL) thickness and λ_{TF} is the Thomas-Fermi screening length, accounting for the surface band-bending extension in degenerate semiconductors and semimetals [359]. The factor 2 in the above expression of n_{sat} accounts for the fact that each QL contains two metal (Bi) layers. Note that the Fermi-level density of states includes the factor 2 for spin multiplicity, and this is appropriate for the quantum-well states above the surface conduction-band minimum that mostly contribute to $\lambda_{HAS}^{(2D)}$. On the other hand, no factor of 2 in n_{sat} is necessary when only the Dirac states are involved, due to their multiplicity of 1. The uncertainties (±) given for λ_{HAS} in the following are based on the confidence bounds of the DW slope. Other sources

[7] According to the surface lattice constant $a = 4.31$ Å as determined by HAS and Fig. 1(b) of [280] $x \approx 1$ for the present sample.

in terms of the uncertainty are A_c, ϕ and λ_{TF} with the largest contribution likely to be due to λ_{TF}. Taken together it is safe to assume a relative uncertainty of about 10 % for λ_{HAS} as shown in Tab. 4.6.

Table 4.6: Input data for the calculation from the HAS DW exponent, and results for the e-ph coupling constant $\lambda_{HAS}^{(2D)}$ (with a relative uncertainty of about 10 %) and comparison with values from other sources.

Surface	k_{iz}^2 [Å^{-2}]	ϕ [eV]	λ_{TF} [Å]	A_c [Å^2]	c_0 [Å]	D [meV]	$\lambda_{HAS}^{(2D)}$	λ (other Refs.)
Bi_2Se_3(111)	10.1 [24]	4.9 [129]	≈ 60 [227]	14.92	9.60	6.54 [24]	0.23	0.17 [215] 0.25 [213] 0.26 [253]
Bi_2Te_3(111)	9.9 [47]	4.9 [129]	≈ 100 [360]	16.46	10.16	6.22 [115]	0.19	0.19 [215]
Bi_2Te_2Se(111)	10.71[(a)]	4.9 [129]	≈ 100 [361]	16.09	10.0	6.4[(b)]	0.08	0.12 [215]

(a) This work

(b) Average over Bi_2Se_3(111) and Bi_2Te_3(111)

With the input data collected in Tab. 4.6 and the DW exponent slopes displayed in Fig. 4.51 (bottom panel), it is found that $\lambda_{HAS}^{(2D)} = 0.23 \pm 0.01$ for Bi_2Se_3(111), 0.19 ± 0.01 for Bi_2Te_3(111), and 0.080 ± 0.004 for Bi_2Te_2Se(111), in good agreement with selected results from other sources (Tab. 4.6, last column). This clearly indicates the dominant role of surface quantum well (QW) states over the modest contribution of Dirac electrons. The enhancement effect of QW states and related interband transitions has been investigated thoroughly by Chen *et al.* [215] with high resolution ARPES for the family $Bi_2Te_{3-x}Se_x$(111) ($0 \leq x \leq 3$), including n-type Bi_2Te_3(111), and theoretically for Bi_2Se_3(111) and Bi_2Te_3(111) by Heid *et al.* [226]. As shown by Pan *et al.* [214], in accurate ARPES studies on bulk Bi_2Se_3(111) samples, where only Dirac topological states are involved because the Fermi level is less than 0.3 eV above the Dirac point, the e-ph coupling constant turns out to be quite small, ranging from 0.076 ± 0.007 to 0.088 ± 0.009, similar to that found with HAS in Bi_2Te_2Se(111) under similar conditions.

Since the surface QW states extend into the bulk on the order of λ_{TF}, i.e., much longer than the penetration of surface Dirac states, it is interesting to compare the above results for $\lambda_{HAS}^{(2D)}$ with the corresponding values of $\lambda_{HAS}^{(3D)}$ when these materials are treated as 3D materials. The ratio $\lambda_{HAS}^{(3D)}/\lambda_{HAS}^{(2D)} = \pi/(k_F\lambda_{TF})$, with $k_F \simeq 0.1$ Å^{-1} (Fig. 4.51 (top)) and λ_{TF} representing the 3DEG thickness, turns out to be $\simeq 1$.

Unlike Bi(114), where the quasi-1D character of the electron gas is quite evident, in layered pnictogen chalcogenides the considerable penetration of the QW states gives $\lambda_{HAS}^{(2D)} \simeq \lambda_{HAS}^{(3D)}$. This is consistent with the fact that the QW states are the surface states which provide the major contribution to the e-ph interaction. Information about which phonons contribute most to λ can also be obtained from inelastic HAS intensities, as explained in the introduction. The Kohn anomalies reported in the lower part of the phonon spectrum [111, 225, 357] are indicative of a strong e-ph coupling for specific wavevectors and frequencies, though it has been predicted that the major contribution in these materials comes from polar optical modes [226]. Indeed this is in agreement with recent HAS measurements of the phonon dispersion curves in Bi_2Se_3(111) [25], which indicate the longitudinal optical branch L3 (with the largest displacement on the 3$^{\text{rd}}$ (Se) atomic plane) as the one having the largest mode-selective e-ph coupling.

Conclusion

In conclusion, it has been shown that the temperature dependence of HAS specular reflectivity allows for the determination of the electron-phonon coupling constant of topological semimetal surfaces. In the case of the quasi-1D Bi(114) surface, the DW factor from the CDW diffraction peak yields an e-ph coupling constant $\lambda_{HAS}^{(1D)}$ consistent with that derived from the reflectivity. Therefore the e-ph interaction acts as the driving mechanism for the observed multi-valley CDW transition. In the absence of spin-orbit coupling, the phonon angular momentum cannot convert into an electron spin-flip, so no good nesting would be allowed across the Dirac cone, and only the strong spin-orbit coupling occurring in topological materials allows for a comparatively weak e-ph *intra*-cone interaction. The multi-valley mechanism at the zone boundary overcomes the nesting problem, because with more Dirac cones separated by less than a **G** vector, there is always a good *inter*-cone (i.e., multi-valley) nesting, even for opposite chiralities. Such a favorable circumstance, allowing for a substantial $\lambda_{HAS}^{(1D)}$ in Bi(114) and a CDW transition, does not occur in pnictogen chalcogenides, due to the single Dirac cone location at the center of the BZ. Most of their appreciable e-ph interaction is provided by the QW states, as long as they are located at the Fermi level. The present extension of HAS λ-analysis from metal surfaces [45, 46] and thin metal films [32] to topological semimetal surfaces qualifies He atom scattering as a universal tool for the measurement of electron-phonon coupling in conducting low-dimensional systems.

Experimental Methods

The experimental data of this work was obtained at the HAS apparatus in Graz [3] and the ^{3}He spin-echo scattering apparatus in Cambridge [18]. In both cases the scattered intensity of a nearly monochromatic He beam in the range of 8–15 meV is monitored as a function of incident angle ϑ_i and at various surface temperatures. The DW measurement of Bi_2Te_3 can be found in [47] while the DW data of Bi_2Se_3 is reported in Ref. [25]. Most of the Bi(114) data has been published in the work of Hofmann *et al.* [28], whereas the Bi_2Te_2Se experimental data is presented here for the first time.

Acknowledgement

One of us (G.B.) would like to thank Profs. M. Bernasconi (Milano-Bicocca) and E. V. Chulkov and P. M. Echenique (DIPC, San Sebastian) for many helpful discussions. This work is partially supported by a grant with Ref. FIS2017-83473-C2-1-P from the Ministerio de Ciencia Universidades e Innovación (Spain). A.R., W.E.E. and A.T. acknowledge financial support provided by the FWF (Austrian Science Fund) within the projects J3479-N20 and P29641-N36. G. B. gratefully acknowledges the Italian Ministry of University and Research (MIUR) for financial support through grant "Dipartimenti di Eccellenza - 2017 Materials for Energy". We would like to thank Martin Bremholm, Ellen M. J. Hedegaard, and Bo B. Iversen for the synthesis of the samples, Marco Bianchi for his advice and help in terms of the sample preparation, and Philip Hofmann as well as the aforementioned people for many helpful discussions and additional characterizations of the samples.

4.8 *In Situ* Analysis of Intermediate Structures in 2D Materials Growth: h-BN on Ru(0001).

This section consists of the following publication:

In Situ Analysis of Intermediate Structures in 2D Materials Growth: h-BN on Ru(0001).

A. Ruckhofer*, M. Sacchi, A. Payne, A.P. Jardine, W. E. Ernst, N. Avidor, and A. Tamtögl

submitted to Small, 2021

* corresponding author

contributions

funding	W.E. Ernst, A. Tamtögl, A.P. Jardine
experimental design	A. Ruckhofer, A. Tamtögl, N. Avidor
data acquisition HAS	A. Ruckhofer, N. Avidor
DFT calculations	M. Sacchi, A. Payne
data analysis	A. Ruckhofer, A. Tamtögl, N. Avidor
interpretation	A. Ruckhofer, A. Tamtögl, N. Avidor, M. Sacchi
publication writing	A. Ruckhofer, A. Tamtögl, N. Avidor
discussion and editing	all authors

Abstract

Intermediate structures during the growth of hexagonal boron nitride (h-BN) are revealed through helium diffraction and first-principles calculations. We find that prior to the formation of h-BN from borazine molecules, a metastable (3×3) structure is formed, and that excess deposition on the resulting 2D h-BN leads to the emergence of a (3×4) structure. We attribute these findings to partial dehydrogenation and polymerisation of the borazine molecules upon adsorption. These steps are largely unexplored during the synthesis of 2D materials and the reported novel h-BN growth scheme means that different routes are likely to exist for other 2D materials as well. Our findings have implications for the wider class of chemical vapour deposition processes with potential applications based on exploiting these intermediate structures for the synthesis of covalent self-assembled 2D networks.

Introduction

Two-dimensional (2D) materials such as graphene and h-BN offer technological promise [362, 363] but their properties are highly dependent on the perfection of the 2D layers. For this reason, intense efforts have been devoted to study and improve the growth of defect-free 2D materials [364, 365]. A promising method of synthesising large-area 2D layers is chemical vapour deposition (CVD) and the CVD synthesis of atomically thin h-BN on metal substrates is described in several review articles [69, 366]. The process, which is illustrated in Fig. 4.52, involves a gas-phase precursor deposited on a solid substrate at elevated temperatures. By diffusion and dehydrogenation or fragmentation of the precursor, the adsorbates are attached to growing clusters and eventually form the 2D layer. A complete dehydrogenation of the precursor requires overcoming multiple energy barriers. As a result, it might be expected that at intermediate temperatures, dehydrogenation would not be complete, which in-turn can result in metastable or intermediate structures. For the synthesis of bulk h-BN it is known that the process involves several steps of borazine-polymerisation [367–370]. There are several routes, but even in the bulk the process has not been studied in great detail. Here, we follow a series of structural changes to identify intermediate structures in 2D growth.

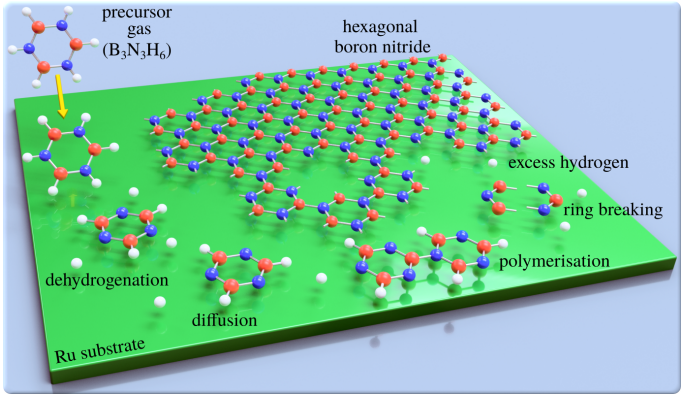

Figure 4.52: Schematic illustrating the epitaxial growth of h-BN by chemical vapour deposition: A gaseous precursor (e.g. borazine, $B_3N_3H_6$) is brought into contact with a (hot) catalyst surface (Ru), triggering the chemical reactions such as breaking of the borazine rings and dehydrogenation, followed by the assembly of the epitaxial overlayer.

While it is crucial to understand the growth process, mechanistic and kinetic studies are rare and mostly focus on the growth of nanocarbons [371–373]. Dehydrogenation and intermediate structures

during CVD of 2D materials have been proposed [374–379], but to the best of our knowledge have not been studied experimentally. In particular, kinetics and the thermochemistry of intermediate products, may lead to metastable structures. However, phase-diagrams due to partially dehydrogenated precursors have not been reported. Most studies report completed overlayer structures while the complexity and individual steps, as illustrated in Fig. 4.52, are often ignored. In particular, previous h-BN studies using real space methods [380–383] concentrate on local order in completed h-BN structures, while reciprocal space studies [384–386] provide information about long-range order [387].

In this paper we present a systematic analysis, at various temperatures beyond the ones reported for best growth conditions (1050–1100 K [380, 382, 385]) and at various dosing rates. By following h-BN growth *in situ* using helium atom scattering (HAS) we demonstrate the existence of metastable structures during the formation of h-BN from borazine ($B_3N_3H_6$). In particular, we find that there is one precursor structure with a well-defined (3×3) periodicity, meaning a well-defined route for the polymerisation reaction which leads to h-BN. We further find a (3×4) structure which could be attributed to a partially polymerised second-layer on top of the formed h-BN.

Our experimental results are complemented by van der Waals (vdW) corrected density functional theory (DFT) calculations which confirm the nature of the system, helping us to determine which self-assembled structures are compatible with the experimental results.

Results

The adsorption of the precursor gas (borazine) on the Ru substrate has been investigated in several other studies using Auger electron spectroscopy, X-ray photoelectron spectroscopy, electron energy loss spectroscopy and low energy electron diffraction [388–390]. There is general consensus in the literature, that borazine only adsorbs molecularly at low (<140 K) temperatures [389–391] with dehydrogenation setting in at temperatures of 150-250 K, depending on the substrate [389, 390, 392]. Starting from about 600 K, again depending on the metallic substrate, the B-N ring is reported to break down into its atomic constituents [391, 392]. According to Paffet *et al.* 1000 K is necessary for h-BN formation on Ru(0001) [388, 389] while hydrogen desorption occurs over a wide temperature range [390] and may even intercalate in the h-BN layer [393, 394].

Helium diffraction allows *in situ* measurements even at growth temperature, and is known for its unique sensitivity to adsorbates, including hydrogen atoms [185, 283, 395–401]. Furthermore, unlike other established techniques [402], HAS is completely inert and does not modify the process under investigation [16]. While the specular reflection gives an estimate of adsorbate coverage on the clean surface, the angular distribution provides insight in the time evolution of periodic structures being formed on the surface [108, 387]. In the present work, CVD growth was performed at a set crystal temperature while monitoring the surface using repeated one-dimensional angular diffraction scans, where we observe the emergence and disappearance of additional superstructures followed by the formation of h-BN.

For ease of comparison, the diffraction scans for the different structures are plotted as a function of the parallel momentum transfer, ΔK, (see Experimental Section) relative to the G_{01} peak of the Ru(0001) substrate, $|\Delta K/G_{01}|$. By converting the abscissa in this way, the position of the observed diffraction peaks directly reflects their periodicity with respect to the substrate lattice spacing.

A precursor structure to h-BN growth First, we describe how borazine exposure at low temperature ($T < 880$ K) reveals a precursor structure on Ru(0001), which by further annealing at $T = 880$ K can be converted to h-BN.

The purple line in Fig. 4.53(a) shows a diffraction scan of the clean Ru(0001) substrate. Exposing Ru to 7 Langmuir (L) of borazine at a surface temperature of 600 K, results in decreased diffraction intensities and helium reflectivity. Moreover, the lack of any additional diffraction peaks is typical of a disordered structure [401]. The behaviour is consistent with earlier studies showing that the B-N ring starts to break down into its constituents only above about 600 K [388, 391, 392].

Upon increasing the temperature to 750 K while maintaining borazine overpressure, additional peaks start to appear between the specular and first order Ru diffraction peaks. Fig. 4.53(b) (blue curve) shows the characteristic diffraction pattern that emerges. Equidistant peaks at $|\Delta K/G_{01}| = 0.33$ and 0.66 indicate a (3×3) periodic structure on the surface, which we label BN_I. If dosing is performed at even higher temperatures ($T \geq 880$ K), in addition to the observed BN_I structure, a shoulder appears to the right-hand side of the first order Ru diffraction peak, indicating the formation of a h-BN structure on the surface (vertical red dotted line in Fig. 4.53). The peak, which occurs at $|\Delta K/G_{01}| = 1.08$, is a result of the commensurate Moiré pattern on Ru [385] (see also h-BN periodicity, below).

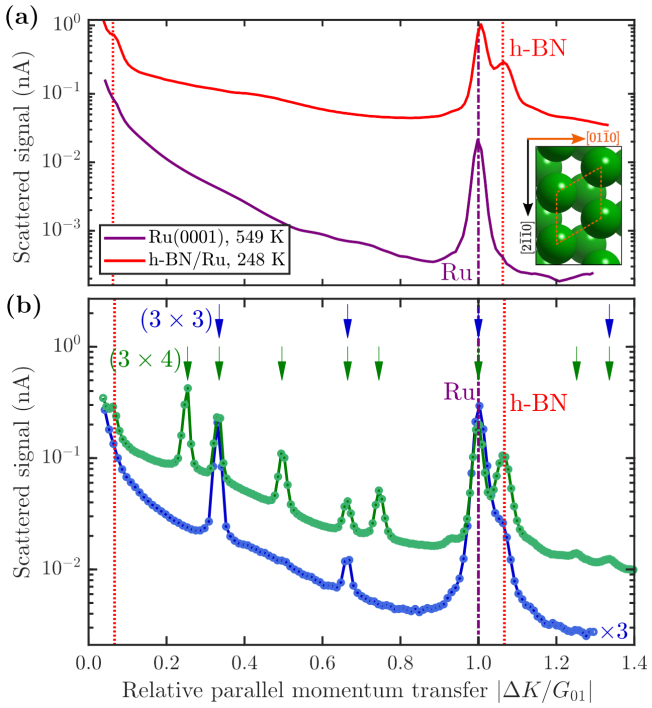

Figure 4.53: (a) Comparison of the angular diffraction scans for clean Ru(0001) in purple and the completed h-BN overlayer on Ru in red. The $\langle 01\bar{1}0 \rangle$ scanning direction ($\overline{\Gamma M}$) is shown in the inset. The purple dash-dotted line indicates the position of the first order Ru diffraction peak and the red dotted lines the h-BN Moiré peaks. (b) Diffraction scans during borazine exposure reveal additional superstructures, depending on the growth temperature and total exposure. The position (shown by the arrows at the top) and spacing of the additional peaks reveal a (3×3) / (3×4) superstructure plotted in blue / green. Low exposure at lower temperatures reveals a (3×3) structure (blue curve, grown at 950 K), while at higher exposures and higher temperatures an intermediate (3×4) pattern emerges (green curve, grown at 1020 K). To improve the signal to noise ratio, the sample was subsequently cooled down for the duration of both scans and the blue curve was scaled by a factor of 3 to facilitate comparison.

Fig. 4.54 illustrates *in situ* monitoring of the integrated peak intensities, which demonstrates that the BN_I structure precedes the growth of h-BN. The exposure dependent intensities are obtained from repeated angular diffraction scans. Immediately after dosing begins, the (3×3) peaks start to rise rapidly (blue line), while only after a short delay the h-BN diffraction peak increases (red line), although less

quickly than the BN_I structure. The h-BN peak intensity reaches its maximum at the same point where the BN_I structure disappears. We conclude that the BN_I structure is converted into h-BN and acts as a precursor structure to the complete h-BN overlayer. Since the intensity of the BN_I structure drops to almost zero at ≈9 L, it indicates that virtually all (3×3) domains are converted to h-BN.

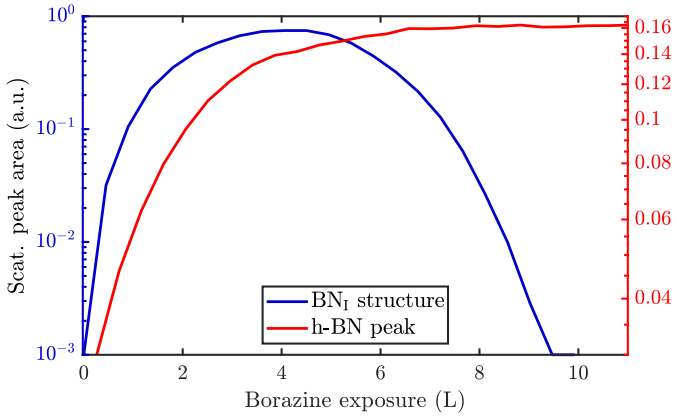

Figure 4.54: *In situ* monitoring of the integrated peak intensities reveals that the BN_I structure acts as precursor to the h-BN overlayer. The characteristic diffraction peaks for the BN_I structure and the h-BN peak are plotted versus borazine exposure at a substrate temperature of 880 K. The BN_I structure increases prior to the h-BN intensity and has already disappeared when the h-BN intensity exhibits its maximum.

We suggest that the BN_I structure is formed from partially dehydrogenated borazine molecules, since the temperature region where the BN_I structure evolves is in excellent agreement with the desorption temperature of hydrogen reported by Paffett *et al.* [388]. Further, as mentioned earlier, bulk h-BN is known to form by a sequence of dehydrogenation processes, in which borazine polymerises to polyborazylene, which is then cross-linked in one or more steps [368, 369]. Our results suggest that a similar process happens at the ruthenium surface. However, we show that in the 2D case, there is one clear intermediate step, i.e. the BN_I structure, before the formation of h-BN. Several possible real space structures, which are in line with the observed periodicity are now discussed.

DFT structural modelling We understand the BN_I structure to consist of partially dehydrogenated, polymerised borazine analogous to the synthesis of bulk h-BN. Thus it is apparent that the 2D growth occurs in a step-by-step process and that not all hydrogen atoms are expected to be removed at the same time, due to the different bonding strengths to N and B atoms as well as the bond formation between the N and the Ru atoms. Based on this attribution, we have made a vdW-corrected DFT investigation into the energetics of the BN_I structure, from adsorption of the precursor gas to the complete h-BN overlayer. We start by considering a single borazine molecule in a (3×3) supercell (see Computational methods), and move on to partially dehydrogenated borazine polymers. From the adsorption energies of isolated borazine molecules we observe that the bonding becomes much stronger with dehydrogenation, but the calculations cannot provide a definitive answer in terms of the dehydrogenation sequence (dehydrogenation of the B atoms is slightly more favourable than of the N atoms by ≈15 meV). However, as shown later for two borazine molecules per supercell, the N atoms can dehydrogenate more easily than the B atoms and the candidate structures for our observations can be clearly distinguished in terms of the adsorption energies.

In Tab. 4.7 we compare the binding energies from vdW-corrected DFT for an intact ($B_3N_3H_6$) and a partially dehydrogenated ($B_3N_3H_3$) borazine molecule with one molecule per (3×3) supercell, confirming a much stronger bonding of $B_3N_3H_3$. We consider various initial adsorption sites (Fig. 4.55(a)) with respect

Table 4.7: DFT calculations for the adsorption structures of the borazine precursor on Ru(0001), based on one molecule per (3×3) supercell. The results are shown for an intact ($B_3N_3H_6$) and partially dehydrogenated ($B_3N_3H_3$) adsorbate, considering various initial adsorption sites and a rotation of 60° (see Fig. 4.55(a)). The adsorption energies E_{ads} are given for the final optimised adsorption sites and ΔE is the difference with respect to the minimum energy configuration of the system with the same dehydrogenation state.

$\mathbf{B_3N_3H_6}$			$\mathbf{B_3N_3H_3}$		
Site	E_{ads} (eV)	ΔE (eV)	Site	E_{ads} (eV)	ΔE (eV)
fcc	-4.08	0.00	fcc	-8.95	0.00
top	-1.21	2.86	top	-6.60	2.35
b→fcc	-4.08	0.00	b→fcc	-8.95	0.00
hcp	-1.31	2.77	hcp	-5.88	3.07

to the C_3 rotational axis through the centre of the molecule and a rotation of 60°. Adsorption occurs in a flat face-to-face configuration, while bonding of the same adsorbates with a rotation of 0° is slightly weaker with the results shown in the Supplementary Information (see Appendix A: Supplementary DFT calculations).

In Tab. 4.7 the energy differences ΔE are given with respect to the minimum energy of the same dehydrogenation state in addition to the respective adsorption energies E_{ads}. For both stoichiometric configurations the most favourable position is the fcc site and if the borazine molecule is initially placed on a bridge site it undergoes a transition to this position. The fcc configuration for partially dehydrogenated borazine yields an adsorption energy of E_{ads}=−8.95 eV and is shown in Fig. 4.55(a) with the (3×3) supercell highlighted by the black dashed rhombus. The results for the intact borazine molecule ($B_3N_3H_6$) are very similar with respect to the adsorption site, however, we obtain significantly weaker bonding strengths compared to the dehydrogenated molecule.

Based on bulk h-BN studies we conclude that it is more likely that polymerised networks are formed [368, 369]. Starting from the minimum energy configuration of a single borazine molecule on the fcc site we continue by adding a second borazine molecule in the supercell. By considering various initial rotations of the additional molecule the energetically most favourable configurations were then identified. In contrast to the case of an isolated borazine molecule, the dehydrogenation sequence becomes clearly discernible in terms of the adsorption energies, with two borazine molecules. The N atoms in the ring adsorb on top of the Ru atoms and the borazine molecules lose all hydrogen atoms associated with the N atoms upon bond formation, in line with experimental results of the completed h-BN overlayer where inter-layer bonding is facilitated via the N atoms [69, 380]. Such a scenario is, however, different to bulk h-BN growth where ruthenium is not present and thus interaction with the substrate may give rise to an even faster loss of hydrogen compared to bulk studies.

The calculations for two intact borazine molecules per supercell ($2B_3N_3H_6$, not shown) yield weak binding, since the H atoms start to overlap resulting in a tilt of the complete molecules with respect to the surface. Moreover, due to desorption of hydrogen atoms from the borazine at low temperatures it is unlikely that intact borazine will remain and so intact molecules will not be considered further [388].

Therefore, we concentrate on partially and fully dehydrogenated borazine molecules. Fig. 4.55(b,c) shows the final optimised structure for $2B_3N_3H_3$ per supercell, illustrating that individual borazine molecules form bonds to each other. The bound B-N rings build up a nanostructured network with nanopores, i.e. where in between the B-N rings vacancies/pores of the Ru substrate are left behind. The high binding energy of the structure in Fig. 4.55(b) with −6.28 eV compared to −6.74 eV for the complete

h-BN/Ru, may therefore explain the stability of the BN_I structure at temperatures ≈750 K as observed in the experiments.

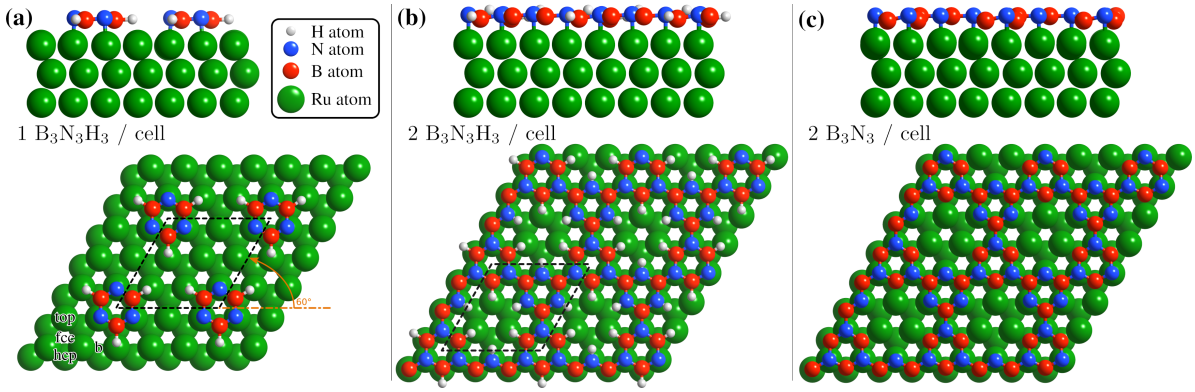

Figure 4.55: Side and top view of the energetically most favourable configurations on the Ru(0001) surface, from one to two borazine molecules per supercell. (a) For one partially dehydrogenated borazine molecule ($B_3N_3H_3$) adsorption occurs on the fcc site, forming a (3×3) structure. (b) shows the structure for two partially dehydrogenated $B_3N_3H_3$ molecules per supercell, where bound B-N rings form a nanostructured network and hydrogen atoms remain adsorbed on the Ru lattice inside the nanopores. In (c) the optimised structure for two fully dehydrogenated borazine molecules is shown, leading to the same nanopore structure with a (3×3) periodicity.

The structure in Fig. 4.55(b) acts as an intermediate prior to complete dehydrogenation which is expected at elevated temperatures. The calculations show that first the hydrogen atoms detach from the nitrogen and bind to the Ru substrate on the hcp sites, inside the nanopores. The excess hydrogen adatoms inside the nanopores are likely to desorb relatively quickly at the temperature of the experiment [403]. Therefore, Fig. 4.55(c) shows the optimised structure, starting with two fully dehydrogenated borazine molecules per supercell, leading again to the formation of nanopores. Such an open structure could easily act as a precursor to the complete h-BN overlayer, since each pore only has to be "filled" with an additional dehydrogenated borazine molecule. Finally, the addition of further borazine molecules in the calculations, i.e. three per supercell, essentially leads to the formation of h-BN which gives also rise to the strongest binding energy in the calculations. The route from the precursor BN_I structure to the final h-BN overlayer, with several intermediate steps, is illustrated in Fig. 4.60.

In addition to providing us with real-space structures of the observed BN_I precursor, there are several points which we note from the vdW DFT calculations: Dehydrogenation of borazine always gives rise to a stronger bonding to the substrate and the results show that the thermodynamically most stable configuration for three adsorbed borazine molecules is h-BN (Fig. 4.59(b)). We also see from the side views in Fig. 4.55 that there occurs always some buckling (0.21–0.35 Å) and the adlayer is never perfectly flat. The results show that by carefully controlling the substrate temperature and thus the amount of excess hydrogen in future experiments, several BN nano-structures could be synthesized as shown for two cases in Fig. 4.55(b,c). Moreover, careful changes of the starting conditions in the DFT calculations may even yield a "local" minimum energy configuration as in Fig. 4.59(c). Thus the system may be an ideal playground for the growth of different nano-structures and further metastable networks beside the ones reported in this work.

Additional structures accompanying the h-BN growth So far, we have described the formation of a BN_I structure at $T \geq 750$ K, which is converted to h-BN at $T \geq 880$ K. However, upon complete conversion of the BN_I structure to h-BN, exposing the surface to excess borazine results in the emergence

of an additional structure with a (3×4) periodicity, which we label BN_{II}. The green line in Fig. 4.53(b) illustrates the corresponding diffraction pattern with the h-BN Moiré diffraction peak being still present next to the first order Ru peak. As shown in a two-dimensional diffraction scan in Fig. 4.62, the (3×4) peaks are not a subset of the h-BN Moiré pattern. In addition, a smaller peak to the left of the first order Ru peak becomes visible which can be attributed to a substrate reconstruction peak [385] due to the h-BN growth.

To monitor the growth of the BN_{II} structure we use a smaller borazine overpressure while holding the sample temperature at 915 K. Fig. 4.56(a) shows the evolution of the BN_{II} and the BN_{I} structure as blue and green curves, respectively. Here, the red line is again the integrated peak intensity of the h-BN diffraction peak. Immediately after exposing the surface to borazine, the BN_{I} structure increases together with the h-BN peak. Further exposure leads to a decay of the BN_{I} structure, while the h-BN feature still rises, indicating the growth of h-BN islands. At 7 L the h-BN diffraction peak saturates, while at the same time the BN_{I} structure disappears. At this stage the h-BN overlayer is complete and after further dosing of borazine, the BN_{II} structure starts to emerge. As discussed later this may be interpreted as a second layer being formed on top of h-BN.

The measurement was repeated at an even lower dosing pressure, while holding the sample at the lower temperature of 880 K. In Fig. 4.56(b) the same behaviour is reproduced, yielding a h-BN layer with two additional structures, except that the emergence is delayed to longer/higher exposures, thus indicating a kinetically driven conversion.

With continuing borazine exposure to 20 L in Fig. 4.56(b), the BN_{II} structure reaches its maximum with no further changes in the scattered intensity. Together with the rise of the BN_{II} structure the h-BN peak intensity slowly starts to decay, likely due to diffuse scattering from additional adsorbates at the surface or from domain walls of the BN_{II} structure. Increasing the surface temperature to 1000 K gives rise to a decay of the BN_{II} structure while the h-BN peak intensity starts to recover to its original value. Further temperature increase accelerates this process giving rise to a faster transition/conversion until the intermediate peaks disappear, leaving behind only the h-BN layer. Such a behaviour illustrates that ultimately h-BN is the most stable structure. Even though the borazine overpressure was still present, no additional peaks formed and the h-BN overlayer is the only remaining structure at the surface.
From Fig. 4.56(b) it becomes evident, that in contrast to the BN_{I} structure, the BN_{II} structure is much more stable at higher temperatures since the (3×4) diffraction peaks are observed up to 1000 K. Further increase of the temperature to $\approx$ 1200 K gives rise to the surface migration of bulk-dissolved carbon, leading to the formation of graphene (see Appendix B: Supplementary diffraction scans) and thus eventually destroys the h-BN overlayer. The latter may open up the possibility to study the growth of h-BN/graphene heterostructures [404–407] but is beyond the scope of the current study.

From our experiments it is likely that the BN_{II} structure is a second chemisorbed layer on top of already grown h-BN. Earlier works on an Ir(111) substrate showed the evolution of additional compact reconstructed regions with (6×2) superstructure, which were attributed to reconstructed boron areas [408]. On the other hand, CVD growth on polycrystalline Cu provided evidence for boron dissolution into the bulk together with multilayer h-BN formation via intercalation [409]. However, both systems and studies are significantly different from our approach. E.g., the different behaviour in the first study could be due to changes of both the lattice constant and the h-BN-substrate bonding between Ru and Ir.

The BN_{II} structure, as a second chemisorbed layer, consists of partly or completely dehydrogenated borazine molecules with a desorption temperature slightly above our performed measurements, since we see an adsorption/desorption equilibrium at temperatures $<\approx$ 1000 K with an ultimate desorption at temperatures above this value. The existence of such a structure might be a precursor to multilayer synthesis if the original h-BN layer is of poor quality providing a high density of growth nuclei and thus

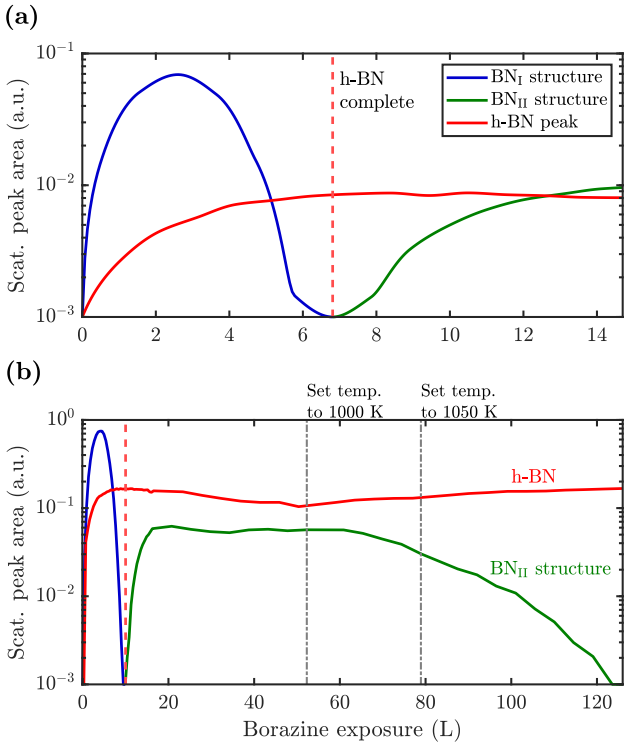

Figure 4.56: Peak areas of the characteristic diffraction peaks representing the different structures versus borazine exposure. After the BN_I structure has disappeared the h-BN peak saturates giving rise to a conversion and further exposure leads to the rise of the BN_{II} structure. Due to a higher substrate temperature of 915 K in (a), the BN_I structure disappears already after an exposure of ≈7 L compared to 10 L at 880 K in (b), thus indicating a kinetically driven conversion. Dosing in (b) is then further continued with subsequent changes of the surface temperature as stated above the diagram. After long enough exposure the BN_{II} structure disappears leaving a strong h-BN intensity behind.

explaining the reports of multilayer growth [409–412].

In a set of additional DFT calculations summarised in Tab. 4.9, we considered also the possibility of borazine adsorption on top of h-BN/Ru as well as the formation of bi-layer h-BN [409–412]. However, we can rule out the latter according to our deposition measurements, since we do not detect oscillations of the BN_{II} structure or observations of any other periodicity, that would be indicative of multilayer h-BN growth. In line with the multi-stage process of h-BN bulk formation it is more likely that the BN_{II} structure consists of adsorbed molecules or polymerised borazine structures - with a weaker bonding compared to the first h-BN layer and therefore more likely to desorb. Further unlikely scenarios are discussed in Appendix C: Supplementary discussion.

h-BN growth diagram on Ru(0001) The combination of measurements and DFT calculations allows us to conclude that the whole system passes through various structural phases:

$$\mathrm{Ru} + \mathrm{BZ} \rightarrow \mathrm{BN_I} + \text{h-BN} \rightarrow \text{h-BN} \rightarrow \mathrm{BN_{II}} + \text{h-BN} \rightarrow \text{h-BN}\,,$$

with the outcome depending strongly on substrate temperature, borazine exposure and the point where one stops. In particular, the surface temperature strongly influences the kinetics and thus the duration and appearance of the additional superstructures. Combining the experimental results we derive a growth diagram as shown in Fig. 4.57, which describes the phenomenology of various structures arising during the CVD growth of h-BN on Ru(0001).

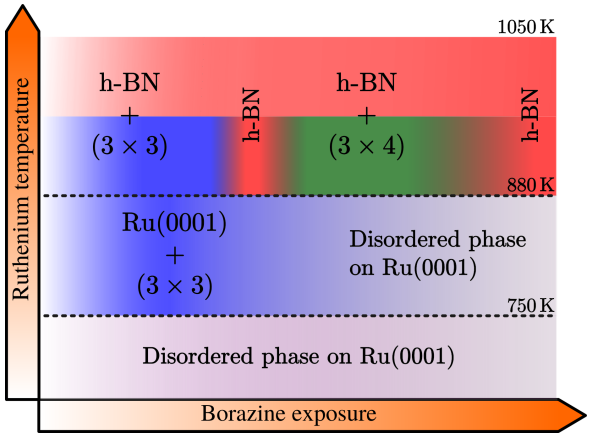

Figure 4.57: Schematic growth diagram of the different BN structures observed on a Ru surface within various temperature ranges and with increasing borazine exposure. At temperatures below 750 K no periodic structure is formed, while above, a (3×3) pattern is observed, disappearing again at higher exposures. Above 880 K the (3×3) structure precedes the growth of h-BN, with the temperature being necessary for the formation of h-BN. With increasing borazine exposure, the latter is followed by a structure with (3×4) periodicity with respect to the Ru lattice, leading again to h-BN after long enough exposure. (See text for a precise explanation of the structures.)

Below 750 K no periodic overlayer structure on the Ru(0001) surface is found. Between 750 and 880 K the BN_I structure forms on the surface which upon further borazine exposure vanishes and leaves a disordered phase behind. The minimum temperature to form a h-BN overlayer on the surface was determined to be 880 K. Above this temperature we observe additional structures, starting with a (3×3) structure (BN_I) followed by a (3×4) periodic diffraction pattern (BN_{II}). These structures always appear in addition to the h-BN layer and ultimately vanish, leaving a complete h-BN overlayer behind (see Fig. 4.53(a) for a diffraction scan of a complete h-BN overlayer without any additional structures).

h-BN periodicity and reconstruction Finally, we illustrate that the h-BN periodicity and superstructure are strongly dependent on the experimental parameters, in particular the growth temperature. It is well known that h-BN forms a Moiré pattern on the Ru(0001) surface [380, 382] due to the small lattice mismatch between $a_{\mathrm{h-BN}} = 2.505\,\text{Å}$ and $a_{\mathrm{Ru(0001)}} = 2.706\,\text{Å}$ [413, 414]. At room temperature, such a mismatch results in a superstructure where 13 unit cells of h-BN coincide with 12 unit cells of Ru: (13×13) on (12×12). On the other hand, previous studies on a similar substrate showed that the h-BN overlayer and the substrate lock in at the temperature during the growth with the strong interlayer bonding causing the superstructure ratio to remain constant after cooling back down [415].

We show that the same holds for different growth temperatures of h-BN on Ru(0001). Detailed diffraction scans around the h-BN (01)-peak in Fig. 4.58 illustrate that for a h-BN synthesis at 1020 K (blue curve), the h-BN peak at $|\Delta K/G_{01}| = 1.067$ fits a superstructure ratio of 16/15 perfectly, as shown by the green vertical dash-dotted line. Upon growing the h-BN overlayer at a lower temperature of 900 K (cyan curve) the h-BN peak appears at a ratio of 13/12. The small peaks to the left of the first order Ru peak in Fig. 4.58 originate from the surface reconstruction with a 14/15 and 11/12 ratio, respectively. These reconstruction peaks can only arise if the system exhibits a true commensurate superstructure [415, 416]. Our HAS measurements show a strong temperature dependence and thus a strong "lock-in" effect, with additional details and calculations for the superstructure ratio in Appendix D: Supplementary details about the h-BN superstructure. Compared to X-ray diffraction where a commensurate 14-on-13 superstructure was reported [385], we see that only h-BN growth at lower temperature (900 K with a borazine

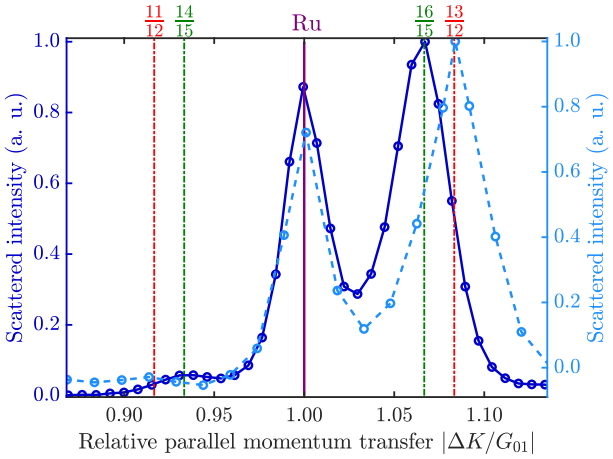

Figure 4.58: Diffraction scans of the h-BN periodicity illustrate that the exact superstructure of the overlayer depends on the growth temperature, with the blue scan for h-BN grown at 1020 K and the dashed cyan curve for h-BN grown at 900 K. The h-BN peaks at the right-hand side of the Ru peak at $|\Delta K/G_{01}| = 1$ show, that h-BN adopts a larger superstructure with increasing growth temperature. Due to the decreasing lattice mismatch the overlayer adopts a 16/15 ratio versus a 13/12 ratio at 900 K. The "lock-in" effect (see text) is confirmed by the small (substrate) reconstruction peaks on the left-hand side. For better identification of the peaks a linear background was subtracted from the untreated data and the sample was subsequently cooled down to room temperature for the duration of the scan.

exposure of 15 L) followed by a slow subsequent cooling provides a 13 over 12 superstructure, similar to previous studies [380]. After all, compared to the h-BN/Rh(111) system [417], the bonding strength of the N-atoms to the Ru substrate is predicted to increase and thus one expects a stronger "lock-in" effect on Ru as observed above. Moreover, due to HAS being strictly surface sensitive, our results can be interpreted as scattering that stems solely from the h-BN nanomesh while other methods may contain contributions from the substrate structure. E.g, a coincidental overlay of the flat h-BN monolayer on a completely flat Ru substrate would not give rise to a diffraction pattern as shown in Fig. 4.53(a) and Fig. 4.58. Together with the above reported additional structures, it confirms the complexity of the whole system and its dependence on minute changes of the growth parameters.

Conclusion

In summary, we investigated the growth of h-BN on a Ru(0001) substrate using helium atom scattering. Employing various growth conditions, characteristic periodic structures are measured during borazine exposure in addition to the h-BN diffraction peak as outlined in the diagram of Fig. 4.57. Between 750 and 880 K a structure with (3×3) periodicity, that precedes the growth of h-BN, is observed with the minimum temperature necessary to form a h-BN overlayer being 880 K. Above this temperature, in addition to the emerging h-BN layer, we observe additional structures with a (3×3) superstructure followed by a (3×4) diffraction pattern, eventually disappearing and leaving a complete h-BN overlayer behind.

It is clearly evident from our observations that a precursor structure precedes the growth of h-BN at lower temperatures and an additional structure co-exists with h-BN at higher temperatures. Both are strongly dependent on the growth conditions, but always transform into a fully h-BN covered substrate at sufficiently high temperatures, thus confirming that the latter is the thermodynamically most stable structure.

We believe that these intermediate metastable structures may be present in many more systems where 2D materials are grown based on precursor-based CVD, at least at lower temperatures and for higher amounts of excess hydrogen compared to the "ideal" growth conditions. In the case studied here, they ultimately always transform into the complete 2D layer - and thus usually higher temperatures are reported as the "ideal" growth conditions for h-BN in the literature.

These intermediate structures seem to have been largely overlooked so far. Possibly, because they are difficult to detect owing to experimental complications since the structural advent of 2D materials is often not investigated during the growth itself, or is only accessible *ex situ*. More importantly, with increasing growth temperature the transformation to h-BN may occur so fast that they are easily missed [383].

The strong dependence regarding the emergence of these structures on temperature and exposure suggests that further uncovered "routes" and polymerisation steps are viable and the system may present an ideal playground to end up with different nano-structures. It further suggests that a careful tuning of the growth conditions via temperature and excess hydrogen from the precursor may provide new broadly applicable strategies for controlling the growth of specific nanostructures. Additional possibilities involve changing the substrate or the precursor gas, and hence tuning the thermochemistry of the surface-adsorbate complex which may further alter the subsequent reaction pathway. E.g. by changing the substrate, the metal-N bond strength may be tuned since one expects the bonding strength to increase as one moves from right to left in the transition metal series. We hope that the wide ranging implications for a controlled growth of 2D materials and nanostructures will stimulate a broad range of new research, understanding and application.

Methods

Experimental section All experimental data was obtained with the Cambridge spin-echo apparatus which uses a nearly monochromatic atomic beam of ^{3}He. The helium atoms scatter off the sample in a total scattering angle of 44.4° and an incident energy of 8 meV. The parallel momentum transfer ΔK is given by $\Delta K = |\Delta\mathbf{K}| = |\mathbf{K}_f - \mathbf{K}_i| = |\mathbf{k}_i|\,(\sin\vartheta_f - \sin\vartheta_i)$, with $\mathbf{k}_i$ being the incident wavevector and ϑ_i and ϑ_f the incident and final angles with respect to the surface normal, respectively. Compared to techniques such as scanning tunnelling microscopy, HAS averages over larger surface areas, typically $\approx 3\,\mathrm{mm}^2$. A more detailed description of the apparatus can be found elsewhere [17, 18, 78]. The Ru(0001) surface was cleaned by Ar-sputtering and annealing to 1300 K with subsequent O_2 treatment to not less than 20 L at 700 K. The adsorbed O_2 was removed by repeated flashing cycles to 1200 K. The cleanliness of the sample was determined by helium reflectivity measurements and diffraction scans to show no features of adsorbed species . After reaching reflectivities of $\approx 23\%$ the sample was ready for the various dosing conditions. h-BN overlayers were removed by oxygen treatment at a sample temperature of 900 K, followed by the cleaning explained above. Borazine was provided by Katchem and supplied to the sample by backfilling the chamber through a leak-valve with typical overpressures between 1×10^{-9} and 5×10^{-8} mbar.

Computational methods For the DFT calculations we employed CASTEP [418], a plane wave periodic boundary condition code. The plane wave basis set was truncated at an electron energy cut-off of 400 eV and we employ Vanderbilt ultrasoft pseudopotentials [419]. The Brillouin zone was sampled with a $(4\times4\times1)$ Monkhorst-Pack k-point mesh [212]. The Perdew Burke Ernzerhof exchange correlation functional [211] was applied in combination with the Tkatchenko and Scheffler dispersion correction method [170]. The Ru(0001) surface was modelled by a 5-layer slab in a (3×3) supercell, and an additional 15 Å vacuum layer for separating the periodically repeated supercells in the z-direction. Positions of the

atoms in the adsorbate and in the top three layers of the Ru substrate were left fully unconstrained. For the structural optimisations, the force tolerance was set to 0.05 eV/Å.

The adsorption energies E_{ads} are defined to be:

$$E_{\mathrm{ads}} = E_{\mathrm{tot}}(x + n\,y) - E_{\mathrm{tot}}(x) - nE_{\mathrm{tot}}(y)$$

where $E_{\mathrm{tot}}(x + n\,y)$ is the total energy of the system, $E_{\mathrm{tot}}(x)$ is the energy of the substrate, $E_{\mathrm{tot}}(y)$ is the energy of the adsorbate and n is the number of adsorbed molecules. The more negative E_{ads}, the more thermodynamically favourable it is for the species to adsorb.

In order to compare the intermediate structures with a different number of atoms we calculate the binding energy E_{bin} relative to Ru(0001) + 3 borazine molecules (3 borazine molecules are needed to form h-BN on a (3×3) cell) by appropriately adding or subtracting the energy of H_2 and borazine in the gas phase, to preserve stoichiometry:

$$E_{\mathrm{bin}} = E_{\mathrm{tot}} + \frac{n_{\mathrm{H}}}{2} E_{\mathrm{tot}}(\mathrm{H_2}) + n_{\mathrm{BZ}} E_{\mathrm{tot}}(\mathrm{BZ}) - E_{\mathrm{tot}}(\mathrm{Ru}) - E_{\mathrm{tot}}(3\mathrm{BZ})$$

where E_{tot} is the total energy of the system, $E_{\mathrm{tot}}(\mathrm{H_2})$ and $E_{\mathrm{tot}}(\mathrm{BZ})$ are the energies of H_2 and borazine which remain in the gas phase, respectively and $E_{\mathrm{tot}}(\mathrm{Ru})$ and $E_{\mathrm{tot}}(3\mathrm{BZ})$ are the total energies of pristine Ru(0001) and 3 borazine molecules in the gas phase. The more negative E_{bin}, the stronger the binding and it becomes thermodynamically more favourable for the species to form.

Acknowledgement

The authors are grateful for financial support by the FWF (Austrian Science Fund) within the project P29641-N36. We would also like to thank W. Allison for helpful discussion regarding the interpretation of the data and Chris Pickard for additional structure calculations based on a neural network approach and Moritz Will for his advice in terms of the precursor (borazine) purchase and treatment. A. R. acknowledges funding by the Doctoral School and a scholarship of TU Graz. The authors acknowledge use of facilities at and support by the Cambridge Atom Scattering Centre (https://atomscattering.phy.cam.ac.uk) and the EPSRC award EP/T00634X/1 with the help of J. Ellis. M.S. is grateful for support from the Royal Society (URF/R/191029) and funding through the EPSRC (EP/S029834/1).

Appendices

Appendix A: Supplementary DFT calculations

The energetically most favourable adsorption site for a single intact borazine molecule per (3×3) supercell according to DFT calculations is shown in Fig. 4.59(a). The adsorption sites (top, hcp, fcc, b) are given relative to the centre of the borazine molecule.

In addition to the calculations for one borazine molecule given in the main text we show the results for the intact and partly dehydrogenated molecule with an initial rotation of 0° in Tab. 4.8. When comparing the results we now see that in this case the hcp site is energetically most favourable with an adsorption energy of E_{ads}=−8.85 eV. If the borazine molecule is initially placed on a bridge site it undergoes a transition to the hcp position. Still, the results for the 60° rotation are energetically more favourable by ≈ 0.1 eV.

Fig. 4.59(c,d) shows that the outcome for calculations considering three partially dehydrogenated borazine molecules on Ru(0001), results in a structure similar to h-BN, except for the fact that the H

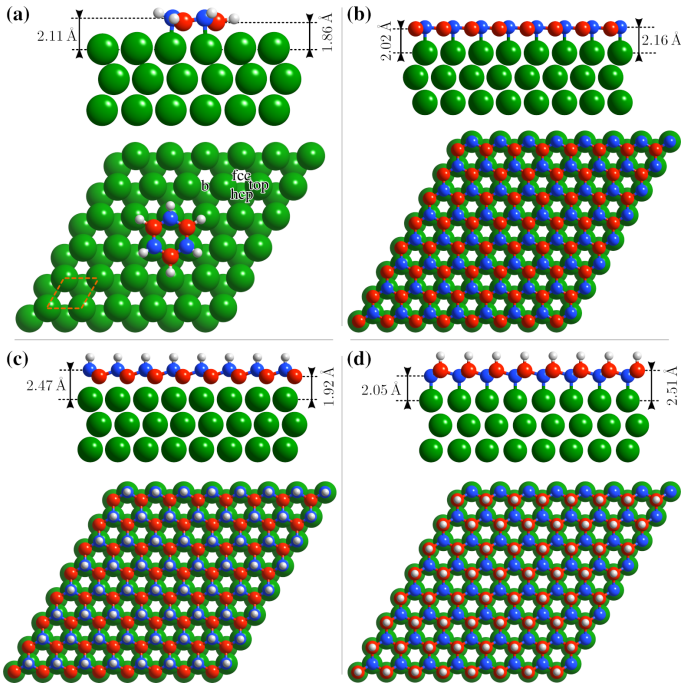

Figure 4.59: (a) depicts the outcome of vdW-corrected DFT calculations for one borazine molecule ($B_3N_3H_6$) on Ru(0001), with the most favourable adsorption site being the fcc position. All possible adsorption sites are given with their according labels. (b) shows the top and side-view of h-BN on Ru(0001) with the corresponding interatomic distances. In (c) and (d) the optimised geometry for three partially dehydrogenated borazine molecules is illustrated, which essentially forms a hydrogenated version of h-BN/Ru(0001). Here (c) represents a "local" minimum as also seen from Tab. 4.9. The hydrogen atoms stick out of the surface, yielding a high corrugation and hence the buckling will be different once the structure is dehydrogenated, such as for a complete h-BN layer with its corrugation reflecting the Moiré pattern.

atoms remain attached to the boron/nitrogen atoms. For comparison, Fig. 4.59(b) depicts the optimised structure for h-BN/Ru(0001).

Tab. 4.9 illustrates that hydrogenation of the h-BN overlayer becomes thermodynamically unfavourable due to the correction with respect to molecular hydrogen in the gas phase and the high binding energy of the latter. The result is in line with hydrogenation experiments of metal supported h-BN, where atomic hydrogen exposure is required in order to facilitate the hydrogenation [393]. Interestingly, in contrast to h-BN/Ni(111) [393], H adsorption on top of the N-site is slightly more favourable than on top of the boron site for h-BN/Ru(0001) as can be seen from the adsorption energy per hydrogen atom.

From the side view in Fig. 4.59(c,d) it becomes evident that the closest atom to the Ru substrate and the bond length change, depending whether nitrogen or boron remain hydrogenated. In Fig. 4.59(d) the hydrogen atoms appear to "pull" the boron away from the surface by 0.5 Å and the sp^2 hybridised bonds to nitrogen gain more sp^3 character. Therefore the boron atom moves away from the surface to optimise these bonds, forming a tetrahedral (bond angle 106°). Likewise the nitrogen binds to the Ru orbitals, thus moving closer to the surface. If hydrogen desorbs from this structure pure h-BN is formed, as seen in Fig. 4.59(b). The boron-nitrogen bonds become stronger and therefore boron moves 0.5 Å towards the Ru, to be in the same plane as the nitrogen. In addition the nitrogen orbitals are populated from the boron and the nitrogen-Ru interaction is weakened, resulting in a movement of the nitrogen atoms 0.11 Å away from the Ru surface. For pure h-BN on Ru, the boron atoms are positioned only slightly lower than the nitrogen atoms (0.14 Å). This may reflect the gain in stability from Ru-B bonding when boron

Table 4.8: DFT calculations for the adsorption structures of the borazine precursor on Ru(0001), based on a (3×3) supercell with one molecule per cell. The results are shown for an intact ($B_3N_3H_6$) and partially dehydrogenated ($B_3N_3H_3$) adsorbate, considering various initial adsorption sites and a rotation of 0°. The adsorption energies E_{ads} are given for the final optimised adsorption site and ΔE is the difference with respect to the minimum energy configuration of the system with the same dehydrogenation state.

$B_3N_3H_6$			$B_3N_3H_3$		
Site	E_{ads} (eV)	ΔE (eV)	Site	E_{ads} (eV)	ΔE (eV)
fcc	-1.28	2.80	fcc	-5.96	2.99
top	-1.21	2.87	top	-6.60	2.35
b→hcp	-3.99	0.08	b→hcp	-8.85	0.11
hcp	-3.99	0.08	hcp	-8.85	0.11

is moved slightly into the hole site, compared to maintaining perfect sp^2 hybridised bonds.

As mentioned in the main text, we considered also borazine adsorption on top of h-BN/Ru as well as the formation of bi-layer h-BN. The physisorption energies are shown in the lower part of Tab. 4.9, illustrating that both are thermodynamically favourable with a stronger physisorption energy for a second h-BN layer on top of h-BN/Ru. On the other hand, the corresponding binding energy for a single complete h-BN layer is -6.74 eV upon formation from 3 borazine molecules per supercell on Ru(0001). In the following we consider a possible route to the complete h-BN layer starting from the precursor structure as described in the main paper.

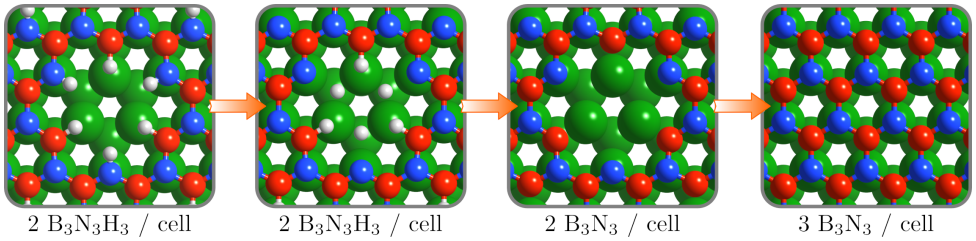

Figure 4.60: Schematic of the possible route from the partially dehydrogenated precursor structure to h-BN via several intermediate structures based on vdW-corrected DFT calculations. As noted in the text, the precursor structure is already quite close to the binding energy for the complete h-BN layer. In contrast to the DFT calculations, where entropy contributions were not considered, additional dehdrogenation and bond breaking may occur due to the high experimental temperatures.

Fig. 4.60 shows the route through various steps based on DFT calculations. The first (precursor) structure is strongly bound with a binding energy E_{bind} (see Computational methods) of -6.28 eV in relation to the bare Ru surface and the molecules in the gas phase. The next step towards h-BN formation, involves dehydrogenation. The calculations show that if the three hydrogen atoms are detached only from the boron atoms they eventually reattach to the same boron sites. Therefore, initially the hydrogen atoms are detached from the nitrogen atoms which adsorb on the Ru substrate within the nanopores, yielding a binding energy of -3.27 eV. At sufficient surface temperature eventually all hydrogen atoms will desorb from the surface yielding the third structure with a less favourable energy of 1.26 eV. If now the nanopore is filled with one additional borazine atom, h-BN is formed yielding the lowest binding energy (-6.74 eV). Therefore we conclude that the first structure is nearly as stable as h-BN and that on the route to h-BN several energy barriers have to be overcome. It should be mentioned however, that the calculations were performed at 0 K and that no entropy contributions were considered.

Table 4.9: DFT calculations for different configurations/structures with their respective energies.

Configuration	Adsorption energy per H atom (eV)	Adsorption site
hydrogenated h-BN/Ru	0.84	H on top of B
hydrogenated h-BN/Ru	0.81	H on top of N

Configuration	Physisorption energy (eV)	Stacking
h-BN on h-BN/Ru	-2.09	AB
Borazine on h-BN/Ru	-0.73	AB

Appendix B: Supplementary diffraction scans

h-BN, sometimes also called "white graphene", typically forms a Moiré pattern on the surfaces of reactive transition metals such as Rh(111) or Ru(0001), as mentioned in the main text. The two-dimensional h-BN layer on such surfaces exhibits periodic nanometric structures, often called "nanomesh", with areas which are elevated from the surface, and areas closer to the surface. In Fig. 4.61 the characteristic diffraction pattern of the clean Ru sample (green) is compared to two overlayers on the same substrate. The scans of the single layer graphene and h-BN covered Ru show additional peaks close to the specular and first order Ru diffraction peaks. The blue curve depicts the scattering result for a graphene monolayer on Ru which has been studied extensively in earlier works [420, 421]. The graphene layer was grown by heating the Ru crystal to 1250 K for several minutes. Leaving the crystal at such high temperatures brings the carbon out of the bulk which then forms the honeycomb single layer graphene sheet. Graphene forms a (12-on-11) superstructure in which a (12×12) supercell of graphene coincides with a (11×11) supercell of ruthenium, giving rise to additional diffraction peaks at $|\Delta K/G_{01}| = 1/11 \equiv 0.09$ and $|\Delta K/G_{01}| = 12/11 \equiv 1.09$.

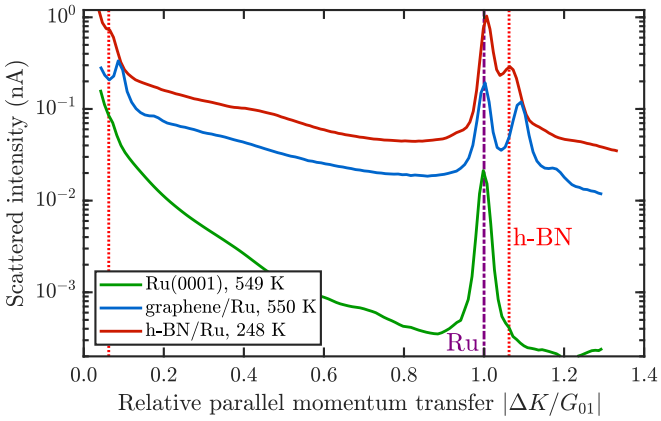

Figure 4.61: Angular diffraction patterns using helium scattering. Comparison of the diffraction scans of the clean Ru(0001) surface (green), graphene on Ru (blue) and h-BN on Ru. The purple dash-dotted line indicates the first order diffraction position and the red dotted lines the h-BN reconstruction peaks.

The diffraction pattern for h-BN on a Ru substrate is depicted in red in Fig. 4.61. Earlier works indicate that h-BN forms a (13-on-12) superstructure which can be identified by position of the diffraction peaks [422]. Indeed the feature originating from the h-BN nanomesh to the right of the Ru diffraction peak shifts to smaller values of $|\Delta K/G_{01}|$ with respect to graphene, giving rise to a bigger supercell.

In Fig. 4.61 the scans for pure Ru and graphene were performed at a sample temperature of $T = 550\,\mathrm{K}$ while the scan of h-BN was taken at 248 K. Due to thermal expansion it gives rise to a deviation of the position of the first order substrate (Ru) peak for the h-BN scan compared to the other two measurements as indicated by the purple line. In all scans the specular peak (at $|\Delta K/G_{01}| = 0$) was cut off due the high intensity and the first order diffraction peak of the Ru surface corresponds to $|\Delta K/G_{01}| = 1$.

In addition Fig. 4.61 clearly shows that the background intensity between the Ru diffraction peaks is much lower, indicating less inelastic scattering and fewer diffuse scattering when probing the clean Ru crystal. In both diffraction scans of h-BN and graphene the background increases by two orders of magnitude due to the increase of diffuse scattering. In addition, adlayers change the corrugation at the surface which is observed by the He atoms. X-ray studies showed that the peak-to-peak corrugation height of graphene is (0.82 ± 0.15), whereas for the uppermost Ru-atomic layer it is (0.19 ± 0.02) [422].

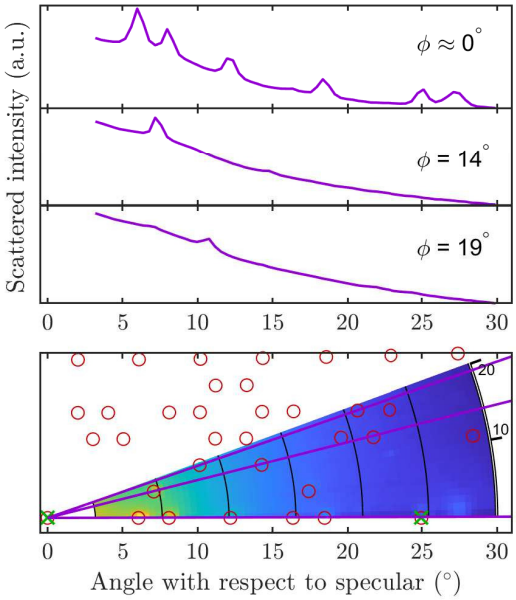

Figure 4.62: 2-dimensional scan of the (3×4) structure of the adsorbed borazine molecules on the Ru surface. The polar plot consists of 22 individual logarithmic diffraction scans at various azimuthal orientations φ and a surface temperature of 300 K. The red circles indicate the calculated scattering positions for a (3×4) superstructure while the green crosses mark the Ru diffraction positions. Three exemplary scans at the top are drawn to elucidate the diffractions peak positions in dependence of φ.

Performing a two-dimensional (2D) scan confirms that the diffraction peaks in the 1D angular diffraction scan of Figure 4.53(b) in the main text are correctly assigned to a (3×4) periodicity and cannot be explained as a subset of another periodicity or as domains with different rotations. Therefore we performed diffraction scans at various azimuthal orientations, since the BN_{II} structure has very distinct diffraction peaks in the high symmetry direction as well as along other azimuthal orientations. By rotation of the azimuthal angle of the sample a 2D-plot in reciprocal space can be created (see Fig. 4.62). The green cross marks the Ru diffraction peak while the red circles indicate the calculated positions of the (3×4) structure peaks. In the top panel three exemplary diffraction scans at specific azimuthal angles φ are depicted. Small angles close to the specular peak are not shown due to their high intensity in all scans. The identification of the peaks verifies the assumption that the (3×4) structure is present in addition to the h-BN layer on the surface and cannot be explained e.g. as being part of another superstructure or rotated domains of a (3×3) structure.

Appendix C: Supplementary discussion

In the following we discuss further scenarios of the BN_{II} structure. As mentioned in the main text, the surface temperature strongly influences the kinetics and thus the duration and appearance of the additional superstructures. At temperatures above 1000 K the (3×4) structure (BN_{II}) slowly vanishes (see Figure 4.56 in the main text) which leads to the assumption that either strongly bound atoms/molecules desorb into the gas phase or convert into another structure. As mentioned earlier the dehydrogenation of borazine already starts at lower temperatures [389] leading to the assumption that the adsorbed species on Ru(0001) are at least partly dehydrogenated.

In the following we provide several scenarios for the origin of the (3×4) structure and discuss their plausibilities. The results could be interpreted as if borazine converts upon adsorption to both h-BN and a (3×3) structure (BN_I). However, given the results which are reported in the main paper, it is clear that borazine only adsorbs in a (3×3) superstructure, and at 880 K a (relatively fast) conversion to h-BN occurs. The h-BN and BN_I structure grow together until the BN_I reservoir is depleted, and no more h-BN is created. At this point we can conclude that the (3×4) (BN_{II}) is not a precursor to h-BN and is also not converted from the BN_I structure. Since the (3×3) peaks degrade completely, the rise of the BN_{II} structure does not compete with the conversion of the BN_I structure to h-BN.

When looking at Figure 4.56 in the main paper one might also think that after the BN_I structure vanishes and the h-BN peak saturates, that the h-BN monolayer is complete and the additional borazine exposure gives rise to a second layer being formed. This layer could consist of partly dehydrogenated borazine forming a periodic structure on top of the existing h-BN layer. According to literature, the CVD process for h-BN growth is usually considered to be self-terminating after a single layer, while some works also showed that multilayers are formed [409], however, typically these require different growth approaches [411, 423–425]. As described in the main paper, from our experimental observations we can rule out the behaviour of multilayer h-BN growth and ascribed the BN_{II} structure to a second chemisorbed layer on top of h-BN.

Another possible scenario would be the growth of a superstructure in-between the already grown h-BN islands. As mentioned in the main manuscript an earlier work investigated the CVD growth of h-BN on Ir(111) and identified a (6×2) superstructure in-between the h-BN islands [408]. A similar behaviour could lead to the formation of a (3×4) structure in-between the h-BN islands on Ru. This intermediate structure eventually upon further borazine exposure converts into h-BN which connects the previously formed h-BN islands. However the areas which formed under this condition are less stable since they convert back to a (3×4) structure upon heating of the sample (see phenomenological cycle equation in the main paper). Upon further annealing of the surface the structures in-between the stable h-BN islands eventually desorb from the surface leaving behind some h-BN islands.

Appendix D: Supplementary details about the h-BN superstructure

Looking at the thermal expansion coefficients of bulk h-BN and the Ru(0001) surface gives a rough estimation for the temperature at which the 13/12 superstructure is favourable. The thermal expansion of bulk h-BN [426] and the Ru surface [427] are given by:

$$a_{\mathrm{h-BN}} = 2.505 - 7.42 \times 10^{-6} \cdot (T - 297) + 4.79 \times 10^{-9} \cdot (T - 297)^2 \quad (4.42)\text{a}$$

$$a_{\mathrm{Ru}} = 2.706 + 9.22 \times 10^{-6} \cdot (T - 293) \quad (4.42)\text{b}$$

Here the lattice constant for Ru $a_{\mathrm{Ru}} = 2.706$ Å was taken for a surface temperature of 293 K, with 297 K for $a_{\mathrm{h-BN}}$, hence the subtraction of these values.

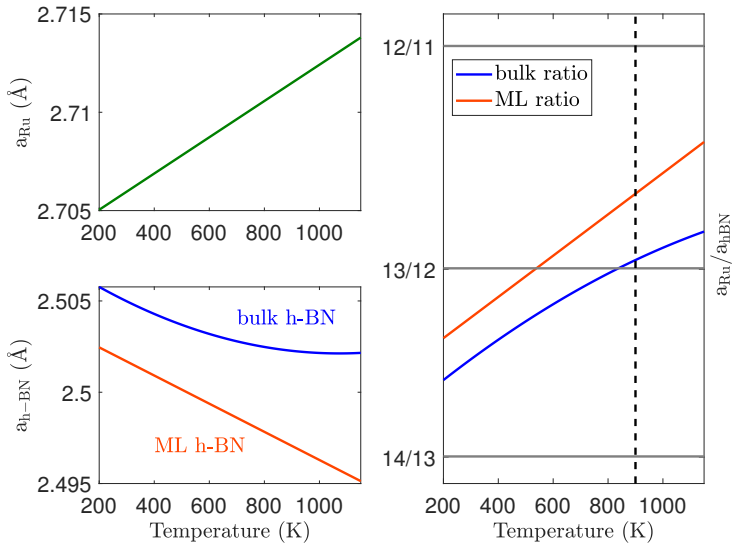

Figure 4.63: Thermal expansion for the Ru surface (upper left panel) and bulk h-BN as well as monolayer (ML) h-BN (lower left panel). The ratio of the Ru surface lattice constant and the h-BN lattice constant versus temperature (right panel) provides an estimate of the expected superstructure. The grey horizontal lines depict the respective superstructure ratios while the dashed vertical line indicates a growth temperature of 900 K.

The Ru thermal expansion is depicted in the upper left panel of Figure 4.63, while the slope of bulk h-BN is shown as a blue line in the lower left panel. In addition, the thermal expansion for a single monolayer (ML) of h-BN as calculated by Thomas *et al.* [428] is drawn in orange. Taking the ratio of the values for h-BN and Ru then yields the expected superstructure at a given surface temperature, as shown in the right panel of Figure 4.63. The expected fraction of 13/12 nicely fits the value of 900 K when using the bulk value of the thermal expansion.

Chapter 5

Summary and conclusion

Within this presented work the experimental technique of helium atom scattering from surfaces was used to gain information on the structure, interaction and dynamics of various surfaces. The thesis consists of selected publications investigating the topological insulators $Bi_2Se_3(111)$ and $Sb_2Te_3(111)$, the vicinal semimetal Bi(114) and the two-dimensional material hexagonal boron nitride.

The atom-surface interaction potential for the He–$Bi_2Se_3(111)$ system is determined by analysing selective adsorption resonances in the angular distributions of scattered helium atoms. First, the laterally averaged atom-surface interaction potential is obtained which is then further improved and refined based on close-coupled calculations in order to determine an accurate three-dimensional interaction potential. The scattering intensities are best represented by a corrugated Morse potential with a well depth $D = (6.54 \pm 0.05)\,\mathrm{meV}$ and a stiffness $\kappa = (0.58 \pm 0.02)\,\mathrm{Å}^{-1}$. The surface electronic corrugation varies slightly depending on the incident beam energy with an average of $(5.8 \pm 0.2)\%$ of the lattice constant. In addition the lifetimes of the helium atoms in the various bound states are determined.

This systematic approach to get information about the fundamentals of weak adsorption systems in the van der Waals regime is generalized in the subsequent publication. Helium scattering data are used to determine the interaction potential for the He–$Sb_2Te_3(111)$ system, followed by a comparative overview and perspective of recent results for topological semimetal and insulator surfaces. Moreover, the possibilities of calculating helium-surface interaction potentials from *ab initio* calculations are discussed. In addition, the effects of elastic and inelastic scattering on the linewidth and lifetime of the trapped He atom is presented with an outlook on future developments and applications.

In the following article, Bi_2Se_3 was investigated with respect to its surface dynamical properties. Using time-of-flight measurements, the surface phonon dispersion curves of Bi_2Se_3 along both high symmetry directions are obtained. A comparison with density functional perturbation theory calculations shows excellent agreement with the experimental data except for two additional dispersion curves below the Rayleigh mode, which are attributed to collective low-energy excitations of surface electrons. From the attenuation of the specular intensity the electron-phonon (e-ph) coupling is found to be $\lambda = 0.23$.

In the same experimental manner the vibronic states of $Sb_2Te_3(111)$ were determined in the next work. From the slope of the Rayleigh mode the phonon group velocity is estimated to be $v_R \approx 1600\,\mathrm{m\,s^{-1}}$. Furthermore, additional inelastic scattering events such as resonance enhancement, kinematical focusing, focused inelastic resonances and surfing are observable in helium atom scattering from Sb_2Te_3.

In the following publication the dimerization transition of Bi(114) below $(245 \pm 8)\,\mathrm{K}$ is reported, which

is driven by vibrational properties and e-ph coupling in this system. The phase transition is accurately monitored by looking at the helium diffraction peaks as well as in time-of-flight spectra at the charge density wave half-order peaks.

Additionally, an approach for the determination of the e-ph coupling strength for topological semimetal surfaces from the thermal attenuation of the helium diffraction peaks is described. Using this novel method, the e-ph interaction parameter λ for the topological insulators Bi_2Se_3, Sb_2Te_3, Bi_2Te_2Se as well as for the charge-density-wave system Bi(114) are compared. For these materials most of the appreciable e-ph interaction is provided by quantum well states, as long as these are located at the Fermi level. This new application of HAS for λ-analysis from topological semimetal surfaces qualifies He atom scattering as a universal tool for the measurement of e-ph coupling in conducting low-dimensional systems.

Lastly, the *in situ* investigation during the chemical vapour deposition of hexagonal boron nitride on Ru(0001) revealed a precursor phase in the formation of the 2D-layer. The observation of various nanostructures allows for the determination of a temperature dependent growth diagram. These findings have implications for the wider class of chemical vapour deposition processes with potential applications based on exploiting these intermediate structures for the synthesis of covalent self-assembled 2D networks.

In summary, all presented publications demonstrate that helium atom scattering provides a sensitive technique to determine the atom-surface interaction, surface phonon dispersion, energy dissipation processes in terms of the e-ph interaction parameter and *in situ* growth investigations. The obtained experimental studies of TIs and a semimetal promise to evolve a more general picture about the surface dynamics and the atom-surface interaction of these peculiar surfaces and offer new perspectives in future applications.

Bibliography

1. Bledsoe, J. R. & Fisher, S. S. "Scattering of helium nozzle beams from LiF(001) and NaCl(001) crystal surfaces: I. Elastic and inelastic transitions". *Surf. Sci.* **46,** 129–156 (1974).
2. Brusdeylins, G., Doak, R. B. & Toennies, J. P. "High-resolution helium time of flight studies of Rayleigh surface-phonon dispersion curves of LiF, NaF, and KCl". *Phys. Rev. B* **27,** 3662–3685 (1983).
3. Tamtögl, A., Mayrhofer-Reinhartshuber, M., Balak, N., Ernst, W. E. & Rieder, K. H. "Elastic and inelastic scattering of He atoms from Bi(111)". *J. Phys.: Cond. Matt.* **22,** 304019 (2010).
4. Tamtögl, A., Kraus, P., Mayrhofer-Reinhartshuber, M., Campi, D., Bernasconi, M., Benedek, G. & Ernst, W. E. "Surface and subsurface phonons of Bi(111) measured with helium atom scattering". *Phys. Rev. B* **87,** 035410 (2013).
5. Kraus, P., Tamtögl, A., Mayrhofer-Reinhartshuber, M., Benedek, G. & Ernst, W. E. "Resonance-enhanced inelastic He-atom scattering from subsurface optical phonons of Bi(111)". *Phys. Rev. B* **87,** 245433 (2013).
6. Mayrhofer-Reinhartshuber, M., Kraus, P., Tamtögl, A., Miret-Artés, S. & Ernst, W. E. "Helium-surface interaction potential of Sb(111) from scattering experiments and close-coupling calculations". *Phys. Rev. B* **88,** 205425 (2013).
7. Mayrhofer-Reinhartshuber, M., Tamtögl, A., Kraus, P. & Ernst, W. E. "Helium atom scattering investigation of the Sb(111) surface". *J. Phys.: Cond. Matt.* **25,** 395002 (2013).
8. Lapujoulade, J., Perreau, J. & Kara, A. "The thermal attenuation of elastic scattering of helium from copper single crystal surfaces". *Surf. Sci.* **129,** 59 (1983).
9. Kaden, C., Ruggerone, P., Toennies, J. P., Zhang, G. & Benedek, G. "Electronic pseudocharge model for the Cu(111) longitudinal-surface-phonon anomaly observed by helium-atom scattering". *Phys. Rev. B* **46,** 13509–13525 (1992).
10. Hinch, B. J., Koziol, C., Toennies, J. P. & Zhang, G. "Evidence for quantum size effects observed by helium atom scattering during the growth of Pb on Cu(111)". *Europhys. Lett.* **10,** 341–346 (1989).
11. Braun, J. & Toennies, J. P. "A helium atom scattering study of ultrathin lead films grown on Cu(111)". *Surf. Sci.* **368,** 226–231 (1996).
12. Brusdeylins, G., Heimlich, C. & Toennies, J. P. "Helium scattering from the layered compound single crystal surface of 1T-TaS_2 in the temperature region of charge density wave reconstruction". *Surf. Sci.* **211-212,** 98–105 (1989).
13. Benedek, G., Brusdeylins, G., Hofmann, F., Ruggerone, P., Toennies, J. P., Vollmer, R. & Skofronick, J. G. "Strong coupling of Rayleigh phonons to charge density waves in 1T-TaS_2". *Surf. Sci.* **304,** 185–190 (1994).

14. Brusdeylins, G., Heimlich, C., Skofronick, J. G., Toennies, J. P., Vollmer, R. & Benedek, G. "Determination of the critical exponent for a charge density wave transition in 2H-$TaSe_2$ by helium atom scattering". *Europhys. Lett.* **9,** 563–568 (1989).
15. Brusdeylins, G., Heimlich, C., Skofronick, J. G., Toennies, J. P., Vollmer, R., Benedek, G. & Miglio, L. "He-atom scattering study of the temperature-dependent charge-density-wave surface structure and lattice dynamics of 2H-$TaSe_2$(001)". *Phys. Rev. B* **41,** 5707–5716 (1990).
16. Benedek, G. & Toennies, J. P. *Atomic Scale Dynamics at Surfaces* (Springer Berlin Heidelberg, 2018).
17. Alexandrowicz, G. & Jardine, A. P. "Helium spin-echo spectroscopy: studying surface dynamics with ultra-high-energy resolution". *Journal of Physics: Condensed Matter* **19,** 305001 (2007).
18. Jardine, A. P., Hedgeland, H., Alexandrowicz, G., Allison, W. & Ellis, J. "Helium-3 spin-echo: Principles and application to dynamics at surfaces". *Prog. Surf. Sci.* **84,** 323 (2009).
19. Jardine, A. P., Alexandrowicz, G., Hedgeland, H., Allison, W. & Ellis, J. "Studying the microscopic nature of diffusion with helium-3 spin-echo". *Phys. Chem. Chem. Phys.* **11,** 3355–3374 (2009).
20. Rotter, P., Lechner, B. A. J., Morherr, A., Chisnall, D. M., Ward, D. J., Jardine, A., Ellis, J., Allison, W., Eckhardt, B. & Witte, G. "Coupling between diffusion and orientation of pentacene molecules on an organic surface". *Nature Materials* **15,** 397–400 (2016).
21. Ward, D. J., Raghavan, A., Tamtögl, A., Jardine, A. P., Bahn, E., Ellis, J., Miret-Artès, S. & Allison, W. "Inter-adsorbate forces and coherent scattering in helium spin-echo experiments". *Phys. Chem. Chem. Phys.* **23,** 7799–7805 (2021).
22. Jardine, A. P., Dworski, S., Fouquet, P., Alexandrowicz, G., Riley, D. J., Lee, G. Y. H., Ellis, J. & Allison, W. "Ultrahigh-resolution spin-echo measurement of surface potential energy landscapes". *Science* **304,** 1790 (2004).
23. Fouquet, P., Hedgeland, H., Jardine, A., Alexandrowicz, G., Allison, W. & Ellis, J. "Measurements of molecule diffusion on surfaces using neutron and helium spin echo". *Physica B: Condensed Matter* **385-386,** 269–271 (2006).
24. Ruckhofer, A., Tamtögl, A., Pusterhofer, M., Bremholm, M. & Ernst, W. E. "Helium-surface interaction and electronic corrugation of Bi_2Se_3(111)". *J. Phys. Chem. C* **123,** 17829–17841 (2019).
25. Ruckhofer, A., Campi, D., Bremholm, M., Hofmann, P., Benedek, G., Bernasconi, M., Ernst, W. E. & Tamtögl, A. "Terahertz surface modes and electron-phonon coupling on Bi_2Se_3(111)". *Phys. Rev. Research* **2,** 023186 (2020).
26. Benedek, G., Miret-Artés, S., Manson, J. R., Ruckhofer, A., Ernst, W. E. & Tamtögl, A. "Origin of the electron–phonon interaction of topological semimetal surfaces measured with helium atom scattering". *J. Phys. Chem. Lett.* **11,** 1927–1933 (2020).
27. Ruckhofer, A., Halbritter, S., Lund, H. E., Holt, A. J. U., Bianchi, M., Bremholm, M., Benedek, G., Hofmann, P., Ernst, W. E. & Tamtögl, A. "Inelastic helium atom scattering from Sb_2Te_3(111): phonon dispersion, focusing effects and surfing". *Phys. Chem. Chem. Phys.* **23,** 7806–7813 (2021).
28. Hofmann, P., Ugeda, M. M., Tamtögl, A., Ruckhofer, A., Ernst, W. E., Benedek, G., Martínez-Galera, A. J., Gómez-Rodríguez, J. M., Rienks, E., Jensen, M. F., Pascual, J. I. & Wells, J. W. "Strong-coupling charge density wave in a one-dimensional topological metal". *Phys. Rev. B* **99,** 035438 (2019).
29. Tamtögl, A. *Surface Dynamics and Structure of Bi(111) from Helium Atom Scattering*. PhD thesis (Graz University of Technology, 2012), 035438.
30. Frantzeskakis, E., Ramankutty, S. V., de Jong, N., Huang, Y. K., Pan, Y., Tytarenko, A., Radovic, M., Plumb, N. C., Shi, M., Varykhalov, A., de Visser, A., van Heumen, E. & Golden, M. S.

"Trigger of the ubiquitous surface band bending in 3D topological insulators". *Phys. Rev. X* **7,** 041041 (2017).

31. Kraus, P., Mayrhofer-Reinhartshuber, M., Gösweiner, C., Apolloner, F., Miret-Artés, S. & Ernst, W. E. "A comparative study of the He-Sb(111) interaction potential from close-coupling calculations and helium atom scattering experiments". *Surf. Sci.* **630,** 208–215 (2014).
32. Benedek, G., Miret-Artés, S., Toennies, J. P. & Manson, J. R. "Electron-phonon coupling constant of metallic overlayers from specular He atom scattering". *J. Phys. Chem. Lett.* **9,** 76–83 (2018).
33. Sanz, A. S. & Miret-Artés, S. "Selective adsorption resonances: Quantum and stochastic approaches". *Phys. Rep.* **451,** 37–154 (2007).
34. Farías, D. & Rieder, K.-H. "Atomic beam diffraction from solid surfaces". *Rep. Prog. Phys.* **61,** 1575 (1998).
35. Miret-Artés, S. "Resonant inelastic scattering of atoms from surfaces". *Surf. Sci.* **339,** 205–220 (1995).
36. Quartapelle, L. & Rebay, S. "Numerical solution of two-point boundary value problems". *J. Comput. Phys.* **86,** 314–354 (1990).
37. Kraus, P., Tamtögl, A., Mayrhofer-Reinhartshuber, M., Apolloner, F., Gösweiner, C., Miret-Artés, S. & Ernst, W. E. "Surface structure of Bi(111) from helium atom scattering measurements. Inelastic close-coupling formalism". *J. Phys. Chem. C* **119,** 17235–17242 (2015).
38. Kole, P. R., Jardine, A. P., Hedgeland, H. & Alexandrowicz, G. "Measuring surface phonons with a ^{3}He spin echo spectrometer: A two-dimensional approach". *J. Phys.: Cond. Matt.* **22,** 304018 (2010).
39. Chis, V., Hellsing, B., Benedek, G., Bernasconi, M., Chulkov, E. V. & Toennies, J. P. "Large surface charge density oscillations induced by subsurface phonon resonances". *Phys. Rev. Lett.* **101,** 206102 (2008).
40. Pauly, H. *Atom, Molecule, and Cluster Beams I,* 035438 (American Physical Society, 2000).
41. Grimvall, G. "The electron-phonon interaction in normal metals". *Phys. Scripta* **14,** 63–78 (1976).
42. Hofmann, P., Sklyadneva, I. Y., Rienks, E. D. L. & Chulkov, E. V. "Electron–phonon coupling at surfaces and interfaces". *New J. Phys.* **11,** 125005 (2009).
43. Howard, C. & El-Batanouny, M. "Connecting electron and phonon spectroscopy data to consistently determine quasiparticle-phonon coupling on the surface of topological insulators". *Phys. Rev. B* **89,** 075425 (2014).
44. Tamtögl, A., Mayrhofer-Reinhartshuber, M., Kraus, P. & Ernst, W. E. "Surface Debye temperature and vibrational dynamics of antimony(111) from helium atom scattering measurements". *Surf. Sci.* **617,** 225–228 (2013).
45. Benedek, G., Bernasconi, M., Bohnen, K.-P., Campi, D., Chulkov, E. V., Echenique, P. M., Heid, R., Sklyadneva, I. Y. & Toennies, J. P. "Unveiling mode-selected electron-phonon interactions in metal films by helium atom scattering". *Phys. Chem. Chem. Phys.* **16,** 7159 (2014).
46. Manson, J. R., Benedek, G. & Miret-Artés, S. "Electron-phonon coupling strength at metal surfaces directly determined from the helium atom scattering Debye-Waller factor". *J. Phys. Chem. Lett.* **7,** 1016–1021 (2016).
47. Tamtögl, A., Kraus, P., Avidor, N., Bremholm, M., Hedegaard, E. M. J., Iversen, B. B., Bianchi, M., Hofmann, P., Ellis, J., Allison, W., Benedek, G. & Ernst, W. E. "Electron-phonon coupling and surface Debye temperature of Bi_2Te_3(111) from helium atom scattering". *Phys. Rev. B* **95,** 195401 (2017).

48. Benedek, G., Manson, J. R. & Miret-Artés, S. "The electron-phonon interaction of low-dimensional and multi-dimensional materials from He atom scattering". *Adv. Mater.* **32,** 2002072 (2020).
49. Tamtögl, A., Kraus, P., Mayrhofer-Reinhartshuber, M., Benedek, G., Bernasconi, M., Dragoni, D., Campi, D. & Ernst, W. E. "Statics and dynamics of multivalley charge density waves in Sb(111)". *npj Quantum Materials* **4,** 28 (2019).
50. Kittel, C. *Introduction to Solid State Physics,* 035438 (Wiley, 2004).
51. Moore, J. "Topological insulators: The next generation". *Nat. Phys.* **5,** 378–380 (2009).
52. Hasan, M. Z. & Kane, C. L. "Colloquium: Topological insulators". *Rev. Mod. Phys.* **82,** 3045–3067 (2010).
53. Mishra, S. K., Satpathy, S. & Jepsen, O. "Electronic structure and thermoelectric properties of bismuth telluride and bismuth selenide". *J. Phys.: Cond. Matt.* **9,** 461–470 (1997).
54. Snyder, G. J. & Toberer, E. S. "Complex thermoelectric materials". *Nat. Mater.* **7,** 105–114 (2008).
55. Kadel, K., Kumari, L., Li, W. Z., Huang, J. Y. & Provencio, P. P. "Synthesis and thermoelectric properties of Bi_2Se_3 nanostructures". *Nanoscale Res Lett* **99,** 035438 (2010).
56. Rittweger, F., Hinsche, N. F., Zahn, P. & Mertig, I. "Signature of the topological surface state in the thermoelectric properties of Bi_2Te_3". *Phys. Rev. B* **89,** 035439 (2014).
57. Venkatasubramanian, R., Siivola, E., Colpitts, T. & O'Quinn, B. "Thin-film thermoelectric devices with high room-temperature figures of merit". *Nature* **413,** 597–602 (2001).
58. Qi, X.-L. & Zhang, S.-C. "Topological insulators and superconductors". *Rev. Mod. Phys.* **83,** 1057–1110 (2011).
59. Hsieh, D., Xia, Y., Qian, D., Wray, L., Dil, J. H., Meier, F., Osterwalder, J., Patthey, L., Checkelsky, J. G., Ong, N. P., Fedorov, A. V., Lin, H., Bansil, A., Grauer, D., Hor, Y. S., Cava, R. J. & Hasan, M. Z. "A tunable topological insulator in the spin helical Dirac transport regime". *Nature* **460,** 1101–1105 (2009).
60. Caputo, M., Panighel, M., Lisi, S., Khalil, L., Santo, G. D., Papalazarou, E., Hruban, A., Konczykowski, M., Krusin-Elbaum, L., Aliev, Z. S., Babanly, M. B., Otrokov, M. M., Politano, A., Chulkov, E. V., Arnau, A., Marinova, V., Das, P. K., Fujii, J., Vobornik, I., Perfetti, L., Mugarza, A., Goldoni, A. & Marsi, M. "Manipulating the topological interface by molecular adsorbates: Adsorption of Co-Phthalocyanine on Bi_2Se_3". *Nano Lett.* **16,** 3409–3414 (2016).
61. Schoop, L. M., Pielnhofer, F. & Lotsch, B. V. "Chemical principles of topological semimetals". *Chem. Mater.* **30,** 3155–3176 (2018).
62. Peng, H., Dang, W., Cao, J., Chen, Y., Wu, D., Zheng, W., Li, H., Shen, Z.-X. & Liu, Z. "Topological insulator nanostructures for near-infrared transparent flexible electrodes". *Nat. Chem.* **4,** 281–286 (2012).
63. Witte, G., Braun, J., Nowack, D., Bartels, L., Neu, B. & Meyer, G. "Oxygen-induced reconstructions on Cu(211)". *Phys. Rev. B* **58,** 13224–13232 (1998).
64. Kaufman, D. S., Aten, R. M., Conrad, E. H., Allen, L. R. & Engel, T. "A helium diffraction study of the structure of the Ni(115) surface". *J. Chem. Phys.* **86,** 3682–3692 (1987).
65. Miret-Artes, S., Toennies, J. P. & Witte, G. "Surface-scattering study of the interaction potential of He atoms with the step edges of the Cu(211) and Cu(511) vicinal surfaces". *Phys. Rev. B* **54,** 5881–5892 (1996).
66. Witte, G. & Toennies, J. P. "Lattice dynamics of the Ni(977) surface". *Phys. Rev. B* **55,** 1395–1397 (1997).
67. Lapujoulade, J., Perreau, J. & Kara, A. "The thermal attenuation of elastic scattering of helium from copper single crystal surfaces". *Surface Science* **129,** 59–78 (1983).

68. Wells, J. W., Dil, J. H., Meier, F., Lobo-Checa, J., Petrov, V. N., Osterwalder, J., Ugeda, M. M., Fernandez-Torrente, I., Pascual, J. I., Rienks, E. D. L., Jensen, M. F. & Hofmann, P. "Nondegenerate metallic states on Bi(114): A one-dimensional topological metal". *Phys. Rev. Lett.* **102,** 096802 (2009).
69. Auwärter, W. "Hexagonal boron nitride monolayers on metal supports: Versatile templates for atoms, molecules and nanostructures". *Surf. Sci. Rep.* **74,** 1–95 (2019).
70. Novoselov, K. S., Geim, A. K., Morozov, S. V., Jiang, D., Zhang, Y., Dubonos, S. V., Grigorieva, I. V. & Firsov, A. A. "Electric field effect in atomically thin carbon films". *Science* **306,** 666–669 (2004).
71. Li, G., Zhang, Y.-Y., Guo, H., Huang, L., Lu, H., Lin, X., Wang, Y.-L., Du, S. & Gao, H.-J. "Epitaxial growth and physical properties of 2D materials beyond graphene: from monatomic materials to binary compounds". *Chem. Soc. Rev.* **47,** 6073–6100 (2018).
72. Söhnchen, S., Lukas, S. & Witte, G. "Epitaxial growth of pentacene films on Cu(110)". *J. Chem. Phys.* **121,** 525–534 (2004).
73. Li, H., Li, Y., Aljarb, A., Shi, Y. & Li, L.-J. "Epitaxial growth of two-dimensional layered transition-metal dichalcogenides: Growth mechanism, controllability, and scalability". *Chem. Rev.* **118,** 6134–6150 (2018).
74. Tan, C., Chen, J., Wu, X.-J. & Zhang, H. "Epitaxial growth of hybrid nanostructures". *Nature Reviews Materials* **3,** 17089 (2018).
75. Lindsay, L. & Broido, D. A. "Enhanced thermal conductivity and isotope effect in single-layer hexagonal boron nitride". *Phys. Rev. B* **84,** 155421 (2011).
76. Sun, S., Bao, J., Mu, W., Fu, Y., Zhang, Y., Ye, L. & Liu, J. *Cooling hot spots by hexagonal boron nitride heat spreaders.* in *2015 IEEE 65th Electronic Components and Technology Conference (ECTC)* **99** (American Physical Society, 2015), 1658–1663.
77. Tamtögl, A. *Energy dissipation on Dirac and semimetal surfaces: Understanding surface dynamics on the nano-scale.* Habilitation (Graz University of Technology, 2021), 035438.
78. Holst, B., Alexandrowicz, G., Avidor, N., Benedek, G., Bracco, G., Ernst, W. E., Farías, D., Jardine, A. P., Lefmann, K., Manson, J. R., Marquardt, R., Artés, S. M., Sibener, S. J., Wells, J. W., Tamtögl, A. & Allison, W. "Material properties particularly suited to be measured with helium scattering: selected examples from 2D materials, van der Waals heterostructures, glassy materials, catalytic substrates, topological insulators and superconducting radio frequency materials". *Phys. Chem. Chem. Phys.* **23,** 7653–7672 (2021).
79. Mayrhofer-Reinhartshuber, M. *Helium Atom Scattering from Surfaces including the Pseudo Random Chopper Technique.* MA thesis (Graz University of Technology, 2010), 035438.
80. Mayrhofer-Reinhartshuber, M., Tamtögl, A., Kraus, P., Rieder, K. H. & Ernst, W. E. "Vibrational dynamics and surface structure of Bi(111) from helium atom scattering measurements". *J. Phys.: Cond. Matt.* **24,** 104008 (2012).
81. Ruckhofer, A. *Surface Dynamics of the Topological Insulator Bi_2Se_3 from Helium Atom Scattering.* MA thesis (Graz University of Technology, 2017), 035438.
82. Bradlyn, B., Elcoro, L., Cano, J., Vergniory, M. G., Wang, Z., Felser, C., Aroyo, M. I. & Bernevig, B. A. "Topological quantum chemistry". *Nature* **547,** 298–305 (2017).
83. Bansil, A., Lin, H. & Das, T. "Colloquium: Topological band theory". *Rev. Mod. Phys.* **88,** 021004 (2016).
84. Hasan, M. Z., Xu, S.-Y. & Bian, G. "Topological insulators, topological superconductors and Weyl fermion semimetals: Discoveries, perspectives and outlooks". *Phys. Scr.* **T164,** 014001 (2015).

85. Ando, Y. "Topological insulator materials". *J. Phys. Soc. Jpn.* **82,** 102001 (2013).
86. Moore, J. E. "The birth of topological insulators". *Nature* **464,** 194–198 (2010).
87. Chen, Y. L., Analytis, J. G., Chu, J.-H., Liu, Z. K., Mo, S.-K., Qi, X. L., Zhang, H. J., Lu, D. H., Dai, X., Fang, Z., Zhang, S. C., Fisher, I. R., Hussain, Z. & Shen, Z.-X. "Experimental realization of a three-dimensional topological insulator, Bi_2Te_3". *Science* **325,** 178–181 (2009).
88. Zhang, H., Liu, C.-X., Qi, X.-L., Dai, X., Fang, Z. & Zhang, S.-C. "Topological insulators in Bi_2Se_3, Bi_2Te_3 and Sb_2Te_3 with a single Dirac cone on the surface". *Nat. Phys.* **5,** 438 (2009).
89. Xia, Y., Qian, D., Hsieh, D., Wray, L., Pal, A., Lin, H., Bansil, A., Grauer, D., Hor, Y. S., Cava, R. J. & Hasan, M. Z. "Observation of a large-gap topological-insulator class with a single Dirac cone on the surface". *Nat. Phys.* **5,** 398 (2009).
90. Wray, L. A., Xu, S.-Y., Xia, Y., Hsieh, D., Fedorov, A. V., Hor, Y. S., Cava, R. J., Bansil, A., Lin, H. & Hasan, M. Z. "A topological insulator surface under strong Coulomb, magnetic and disorder perturbations". *Nat. Phys.* **7,** 32–37 (2011).
91. Wang, E., Tang, P., Wan, G., Fedorov, A. V., Miotkowski, I., Chen, Y. P., Duan, W. & Zhou, S. "Robust gapless surface state and Rashba-splitting bands upon surface deposition of magnetic Cr on Bi_2Se_3". *Nano Lett.* **15,** 2031–2036 (2015).
92. Kong, D., Dang, W., Cha, J. J., Li, H., Meister, S., Peng, H., Liu, Z. & Cui, Y. "Few-layer nanoplates of Bi_2Se_3 and Bi_2Te_3 with highly tunable chemical potential". *Nano Lett.* **10,** 2245–2250 (2010).
93. Otrokov, M. M., Chulkov, E. V. & Arnau, A. "Breaking time-reversal symmetry at the topological insulator surface by metal-organic coordination networks". *Phys. Rev. B* **92,** 165309 (2015).
94. Pia, A. D., Lisi, S., Luca, O. D., Warr, D. A., Lawrence, J., Otrokov, M. M., Aliev, Z. S., Chulkov, E. V., Agostino, R. G., Arnau, A., Papagno, M. & Costantini, G. "TCNQ physisorption on the topological insulator Bi_2Se_3". *ChemPhysChem* **19,** 2405–2410 (2018).
95. Förster, T., Krüger, P. & Rohlfing, M. "*Ab initio* studies of adatom- and vacancy-induced band bending in Bi_2Se_3". *Phys. Rev. B* **91,** 035313 (2015).
96. Riley, D. J., Jardine, A. P., Dworski, S., Alexandrowicz, G., Fouquet, P., Ellis, J. & Allison, W. "A refined He-LiF(001) potential from selective adsorption resonances measured with high-resolution helium spin-echo spectroscopy". *J. Chem. Phys* **126,** 104702 (2007).
97. Hoinkes, H. "The physical interaction potential of gas atoms with single-crystal surfaces, determined from gas-surface diffraction experiments". *Rev. Mod. Phys.* **52,** 933–970 (1980).
98. Eichenauer, D. & Toennies, J. P. "Pairwise additive potential models for the interaction of He atoms with the (001) surfaces of LiF, NaF, NaCl and LiCl". *Surf. Sci.* **197,** 267–276 (1988).
99. Benedek, G., Brusdeylins, G., Senz, V., Skofronick, J. G., Toennies, J. P., Traeger, F. & Vollmer, R. "Helium atom scattering study of the surface structure and dynamics of *in situ* cleaved MgO(001) single crystals". *Phys. Rev. B* **64,** 125421 (2001).
100. Debiossac, M., Zugarramurdi, A., Lunca-Popa, P., Momeni, A., Khemliche, H., Borisov, A. G. & Roncin, P. "Transient quantum trapping of fast atoms at surfaces". *Phys. Rev. Lett.* **112,** 023203 (2014).
101. Tuddenham, F. E., Hedgeland, H., Knowling, J., Jardine, A. P., MacLaren, D. A., Alexandrowicz, G., Ellis, J. & Allison, W. "Linewidths in bound state resonances for helium scattering from Si(111)-(1×1)H". *J. Phys.: Cond. Matt.* **21,** 264004 (2009).
102. Brivio, G. P. & Trioni, M. I. "The adiabatic molecule–metal surface interaction: Theoretical approaches". *Rev. Mod. Phys.* **71,** 231–265 (1999).
103. Martínez-Casado, R., Usvyat, D., Maschio, L., Mallia, G., Casassa, S., Ellis, J., Schütz, M. & Harrison, N. M. "Approaching an exact treatment of electronic correlations at solid surfaces: The

binding energy of the lowest bound state of helium adsorbed on MgO(100)". *Phys. Rev. B* **89,** 205138 (2014).

104. De Lara-Castells, M. P., Fernández-Perea, R., Madzharova, F. & Voloshina, E. "Post-Hartree-Fock studies of the He/Mg(0001) interaction: Anti-corrugation, screening, and pairwise additivity". *J. Chem. Phys* **144,** 244707 (2016).
105. Wu, X., Vargas, M. C., Nayak, S., Lotrich, V. & Scoles, G. "Towards extending the applicability of density functional theory to weakly bound systems". *J. Chem. Phys.* **115,** 8748–8757 (2001).
106. Jean, N., Trioni, M. I., Brivio, G. P. & Bortolani, V. "Corrugating and anticorrugating static interactions in helium-atom scattering from metal surfaces". *Phys. Rev. Lett.* **92,** 013201 (2004).
107. Martinez-Casado, R., Usvyat, D., Mallia, G., Maschio, L., Casassa, S., Ellis, J., Schütz, M. & Harrison, N. M. "Diffraction of helium on MgO(100) surface calculated from first-principles". *Phys. Chem. Chem. Phys.* **16,** 21106–21113 (2014).
108. Tamtögl, A., Bahn, E., Zhu, J., Fouquet, P., Ellis, J. & Allison, W. "Graphene on Ni(111): Electronic corrugation and dynamics from helium atom scattering". *J. Phys. Chem. C* **119,** 25983–25990 (2015).
109. Del Cueto, M., Muzas, A. S., Füchsel, G., Gatti, F., Martín, F. & Díaz, C. "Role of van der Waals forces in the diffraction of noble gases from metal surfaces". *Phys. Rev. B* **93,** 060301 (2016).
110. Del Cueto, M., Maurer, R., Taleb, A. A., Farías, D., Martin, F. & Diaz, C. "Performance of van der Waals DFT approaches for helium diffraction on metal surfaces". *J. Phys.: Cond. Matt.* **31,** 135901 (2019).
111. Tamtögl, A., Campi, D., Bremholm, M., Hedegaard, E. M. J., Iversen, B. B., Bianchi, M., Hofmann, P., Marzari, N., Benedek, G., Ellis, J. & Allison, W. "Nanoscale surface dynamics of Bi_2Te_3(111): Observation of a prominent surface acoustic wave and the role of van der Waals interactions". *Nanoscale* **10,** 14627–14636 (2018).
112. Bianchi, M., Hatch, R. C., Guan, D., Planke, T., Mi, J., Iversen, B. B. & Hofmann, P. "The electronic structure of clean and adsorbate-covered Bi_2Se_3: An angle-resolved photoemission study". *Semicond. Sci. Technol.* **27,** 124001 (2012).
113. Tamtögl, A., Carter, E. A., Ward, D. J., Avidor, N., Kole, P. R., Jardine, A. P., Ellis, J. & Allison, W. "Note: A simple sample transfer alignment for ultra-high vacuum systems". *Rev. Sci. Instrum.* **87,** 066108 (2016).
114. Chen, X., Zhou, H. D., Kiswandhi, A., Miotkowski, I., Chen, Y. P., Sharma, P. A., Lima Sharma, A. L., Hekmaty, M. A., Smirnov, D. & Jiang, Z. "Thermal expansion coefficients of Bi_2Se_3 and Sb_2Te_3 crystals from 10 K to 270 K". *Appl. Phys. Lett.* **99,** 261912 (2011).
115. Tamtögl, A., Pusterhofer, M., Bremholm, M., Hedegaard, E. M. J., Iversen, B. B., Hofmann, P., Ellis, J., Allison, W., Miret-Artés, S. & Ernst, W. E. "A helium-surface interaction potential of Bi_2Te_3(111) from ultrahigh-resolution spin-echo measurements". *Surf. Sci.* **678,** 25–31 (2018).
116. Anemone, G., Taleb, A. A., Benedek, G., Castellanos-Gomez, A. & Farías, D. "Electron-phonon coupling constant of 2H-MoS_2(0001) from helium-atom scattering". *J. Phys. Chem. C* **123,** 3682–3686 (2019).
117. Armand, G. & Manson, J. R. "Scattering of neutral atoms by a periodic potential: The Morse corrugated potential". *J. Phys. France* **44,** 473–487 (1983).
118. Hutchison, J. S. "Effect of inelastic scattering on the resonance line shapes in He-graphite". *Phys. Rev. B* **22,** 5671–5678 (1980).
119. Campi, D., Bernasconi, M. & Benedek, G. "*Ab initio* calculation of surface phonons at the Sb_2Te_3(111) surface". *Surf. Sci.* **678,** 46–51 (2018).

120. Martínez-Casado, R., Meyer, B., Miret-Artés, S., Traeger, F. & Wöll, C. "Diffraction patterns of He atoms from the MgO(100) surface calculated by the close-coupling method". *J. Phys.: Cond. Matt.* **19,** 305006 (2007).
121. Guantes, R., Borondo, F., Margalef-Roig, J., Miret-Artés, S. & Manson, J. R. "Threshold resonances in classical chaotic atom-surface scattering". *Surf. Sci.* **375,** L379–L384 (1997).
122. Zhao, B. S., Zhang, W. & Schöllkopf, W. "Universal diffraction of atoms and molecules from a quantum reflection grating". *Sci. Adv.* **2,** e1500901 (2016).
123. Miret-Artés, S. "Elementary resonance processes in atom-surface scattering". *Surf. Sci.* **366,** L735–L741 (1996).
124. Šiber, A. & Gumhalter, B. "Phonon-mediated bound state resonances in inelastic atom-surface scattering". *J. Phys.: Cond. Matt.* **20,** 224002 (2008).
125. Pendry, J. B. "Reliability factors for LEED calculations". *J. Phys. C: Solid State Physics* **13,** 937–944 (1980).
126. Lee, G. Y. H. *Resonant Scattering of Helium Atoms from Corrugated Surfaces.* PhD thesis (University of Cambridge, 2004), 035438.
127. Anderson, T. L. & Krause, H. B. "Refinement of the Sb_2Te_3 and Sb_2Te_2Se structures and their relationship to nonstoichiometric $Sb_2Te_{3-y}Se_y$ compounds". *Acta Cryst. B* **30,** 1307–1310 (1974).
128. West, D., Sun, Y. Y., Wang, H., Bang, J. & Zhang, S. B. "Native defects in second-generation topological insulators: Effect of spin-orbit interaction on Bi_2Se_3". *Phys. Rev. B* **86,** 121201 (2012).
129. Suh, J., Fu, D., Liu, X., Furdyna, J. K., Yu, K. M., Walukiewicz, W. & Wu, J. "Fermi-level stabilization in the topological insulators Bi_2Se_3 and Bi_2Te_3: Origin of the surface electron gas". *Phys. Rev. B* **89,** 115307 (2014).
130. Brusdeylins, G., Doak, R. B. & Toennies, J. P. "Observation of selective desorption of one-phonon inelastically scattered He atoms from a LiF crystal surface". *J. Chem. Phys* **75,** 1784–1793 (1981).
131. Hernández, M. I., Campos-Martínez, J., Miret-Artés, S. & Coalson, R. D. "Lifetimes of selective-adsorption resonances in atom-surface elastic scattering". *Phys. Rev. B* **49,** 8300–8309 (1994).
132. Pan, F. M., Pflitsch, C., David, R., Verheij, L. K. & Franchy, R. "Reconstruction of the CoGa(100) surface studied by thermal-energy helium-atom scattering, LEED, and AES". *Phys. Rev. B* **63,** 125414 (2001).
133. Jeon, J. H., Jang, W. J., Yoon, J. K. & Kahng, S.-J. "Metal-supported high crystalline Bi_2Se_3 quintuple layers". *Nanotechnology* **22,** 465602 (2011).
134. Benedek, G. & Toennies, J. P. in *Atomic Scale Dynamics at Surfaces: Theory and Experimental Studies with Helium Atom Scattering* 441–486 (Springer Berlin Heidelberg, Berlin, Heidelberg, 2018).
135. Zhang, G., Qin, H., Teng, J., Guo, J., Guo, Q., Dai, X., Fang, Z. & Wu, K. "Quintuple-layer epitaxy of thin films of topological insulator Bi_2Se_3". *Appl. Phys. Lett.* **95,** 053114 (2009).
136. Borisova, S., Kampmeier, J., Luysberg, M., Mussler, G. & Grützmacher, D. "Domain formation due to surface steps in topological insulator Bi_2Te_3 thin films grown on Si(111) by molecular beam epitaxy". *Appl. Phys. Lett.* **103,** 081902 (2013).
137. Hewitt, A. S., Wang, J., Boltersdorf, J., Maggard, P. A. & Dougherty, D. B. "Coexisting Bi and Se surface terminations of cleaved Bi_2Se_3 single crystals". *J. Vac. Sci. Technol.* **32,** 04E103 (2014).
138. Hermanowicz, M., Koczorowski, W., Bazarnik, M., Kopciuszyński, M., Zdyb, R., Materna, A., Hruban, A., Czajka, R. & Radny, M. W. "Stable bismuth sub-monolayer termination of Bi_2Se_3". *Appl. Surf. Sci.* **476,** 701–705 (2019).

139. Frisch, R. & Stern, O. "Anomalien bei der spiegelnden Reflexion und Beugung von Molekularstrahlen an Kristallspaltflächen. I". *Z. Phy.* **84,** 430–442 (1933).
140. Lennard-Jones, J. E. & Devonshire, A. F. "The interaction of atoms and molecules with solid surfaces III - The condensation and evaporation of atoms and molecules". *Proc. R. Soc. London A - Math Phys. Sci.* **156,** 6–28 (1936).
141. Kroes, G.-J. & Díaz, C. "Quantum and classical dynamics of reactive scattering of H_2 from metal surfaces". *Chem. Soc. Rev.* **45,** 3658–3700 (2016).
142. Park, G. B., Krüger, B. C., Borodin, D., Kitsopoulos, T. N. & Wodtke, A. M. "Fundamental mechanisms for molecular energy conversion and chemical reactions at surfaces". *Rep. Prog. Phys.* **82,** 096401 (2019).
143. Alkoby, Y., Chadwick, H., Godsi, O., Labiad, H., Bergin, M., Cantin, J. T., Litvin, I., Maniv, T. & Alexandrowicz, G. "Setting benchmarks for modelling gas-surface interactions using coherent control of rotational orientation states". *Nat. Commun* **11,** 3110 (2020).
144. Bruch, L. W., Diehl, R. D. & Venables, J. A. "Progress in the measurement and modeling of physisorbed layers". *Rev. Mod. Phys.* **79,** 1381–1454 (2007).
145. Bünermann, O., Jiang, H., Dorenkamp, Y., Kandratsenka, A., Janke, S. M., Auerbach, D. J. & Wodtke, A. M. "Electron-hole pair excitation determines the mechanism of hydrogen atom adsorption". *Science* **350,** 1346–1349 (2015).
146. Jiang, H., Kammler, M., Ding, F., Dorenkamp, Y., Manby, F. R., Wodtke, A. M., Miller, T. F., Kandratsenka, A. & Bünermann, O. "Imaging covalent bond formation by H atom scattering from graphene". *Science* **364,** 379–382 (2019).
147. Wagner, C., Fournier, N., Ruiz, V. G., Li, C., Müllen, K., Rohlfing, M., Tkatchenko, A., Temirov, R. & Tautz, F. S. "Non-additivity of molecule-surface van der Waals potentials from force measurements". *Nat. Commun* **5,** 5568 (2014).
148. Woods, L. M., Dalvit, D. A. R., Tkatchenko, A., Rodriguez-Lopez, P., Rodriguez, A. W. & Podgornik, R. "Materials perspective on Casimir and van der Waals interactions". *Rev. Mod. Phys.* **88,** 045003 (2016).
149. Rojas-Lorenzo, G., Rubayo-Soneira, J., Miret-Artés, S. & Pollak, E. "Quantum threshold reflection of He-atom beams from rough surfaces". *Phys. Rev. A* **101,** 022506 (2020).
150. Debiossac, M., Roncin, P. & Borisov, A. G. "Refraction of fast Ne atoms in the attractive well of a LiF(001) surface". *J. Phys. Chem. Lett.* **11,** 4564–4569 (2020).
151. Guantes, R., Sanz, A. S., Margalef-Roig, J. & Miret-Artés, S. "Atom-surface diffraction: A trajectory description". *Surf. Sci. Rep.* **53,** 199–330 (2004).
152. Sanz, A. S. & Miret-Artés, S. "Quantum trajectories in elastic atom-surface scattering: Threshold and selective adsorption resonances". *J. Chem. Phys* **122,** 014702 (2005).
153. Moix, J. M., Pollak, E. & Allison, W. "Quantum and classical study of surface characterization by three-dimensional helium atom scattering". *J. Chem. Phys* **134,** 024319 (2011).
154. Alderwick, A. R., Jardine, A. P., Allison, W. & Ellis, J. "An evaluation of the kinematic approximation in helium atom scattering using wavepacket calculations". *Surf. Sci.* **678,** 65–71 (2018).
155. Debiossac, M., Zugarramurdi, A., Mu, Z., Lunca-Popa, P., Mayne, A. J. & Roncin, P. "Helium diffraction on SiC grown graphene: Qualitative and quantitative descriptions with the hard-corrugated-wall model". *Phys. Rev. B* **94,** 205403 (2016).
156. Pernal, K., Podeszwa, R., Patkowski, K. & Szalewicz, K. "Dispersionless density functional theory". *Phys. Rev. Lett.* **103,** 263201 (2009).

157. Liao, M., Grenier, R., To, Q.-D., de Lara-Castells, M. P. & Léonard, C. "Helium and argon interactions with gold surfaces: *Ab initio*-assisted determination of the He-Au pairwise potential and its application to accommodation coefficient determination". *J. Phys. Chem. C* **122,** 14606–14614 (2018).
158. Nguyen, N. L., Colonna, N. & de Gironcoli, S. "*Ab initio* self-consistent total-energy calculations within the EXX/RPA formalism". *Phys. Rev. B* **90,** 045138 (2014).
159. Vahdat, M. T., Campi, D., Colonna, N., Villalobos, L. F., Marzari, N. & Agrawal, K. V. "Efficient Kr/Xe separation from triangular g-C_3N_4 nanopores, a simulation study". *J. Mater. Chem. A* **8,** 17747–17755 (2020).
160. Nardelli, M. B. "A density-functional study of van der Waals forces: He interaction with a semiconductor surface". *Solid State Commun.* **97,** 215–219 (1996).
161. Schüller, A., Winter, H., Gravielle, M. S., Pruneda, J. M. & Miraglia, J. E. "He-LiF surface interaction potential from fast atom diffraction". *Phys. Rev. A* **80,** 062903 (2009).
162. Minniti, M., Díaz, C., Cuñado, J. L. F., Politano, A., Maccariello, D., Martín, F., Farías, D. & Miranda, R. "Helium, neon and argon diffraction from Ru(0001)". *J. Phys.: Cond. Matt.* **24,** 354002 (2012).
163. De Lara-Castells, M. P., Stoll, H. & Mitrushchenkov, A. O. "Assessing the performance of dispersionless and dispersion-accounting methods: Helium interaction with cluster models of the TiO_2(110) surface". *J. Phys. Chem. A* **118,** 6367–6384 (2014).
164. Tamijani, A. A., Salam, A. & de Lara-Castells, M. P. "Adsorption of noble-gas atoms on the TiO_2(110) surface: An *ab initio*-assisted study with van der Waals-corrected DFT". *J. Phys. Chem. C* **120,** 18126–18139 (2016).
165. Zhang, G., Xiang, X., Yang, F., Liu, L., Tang, T., Shi, Y. & Wang, X. "First principles investigation of helium physisorption on an α-Al_2O_3(0001) surface". *Phys. Chem. Chem. Phys.* **18,** 15711–15718 (2016).
166. Adhikari, S., Tang, H., Neupane, B., Ruzsinszky, A. & Csonka, G. I. "Molecule-surface interaction from van der Waals-corrected semilocal density functionals: The example of thiophene on transition-metal surfaces". *Phys. Rev. Materials* **4,** 025005 (2020).
167. Grimme, S. "Accurate description of van der Waals complexes by density functional theory including empirical corrections". *J. Comput. Chem.* **25,** 1463–1473 (2004).
168. Grimme, S. "Semiempirical GGA-type density functional constructed with a long-range dispersion correction". *J. Comput. Chem.* **27,** 1787–1799 (2006).
169. Grimme, S., Antony, J., Ehrlich, S. & Krieg, H. "A consistent and accurate *ab initio* parametrization of density functional dispersion correction (DFT-D) for the 94 elements H-Pu". *J. Chem. Phys* **132,** 154104 (2010).
170. Tkatchenko, A. & Scheffler, M. "Accurate molecular van der Waals interactions from ground-state electron density and free-atom reference data". *Phys. Rev. Lett.* **102,** 073005 (2009).
171. Díaz, C., Wang, Y. & Martín, F. in *Encyclopedia of Interfacial Chemistry* (ed Wandelt, K.) 1–9 (Elsevier, Oxford, 2018).
172. Dion, M., Rydberg, H., Schröder, E., Langreth, D. C. & Lundqvist, B. I. "Van der Waals density functional for general geometries". *Phys. Rev. Lett.* **92,** 246401 (24 2004).
173. Berland, K., Cooper, V. R., Lee, K., Schrtöder, E., Thonhauser, T., Hyldgaard, P. & Lundqvist, B. I. "Van der Waals forces in density functional theory: A review of the vdW-DF method". *Rep. Prog. Phys.* **78,** 066501 (2015).

174. Sabatini, R., Gorni, T. & de Gironcoli, S. "Nonlocal van der Waals density functional made simple and efficient". *Phys. Rev. B* **87,** 041108 (2013).
175. Kolb, B., Luo, X., Zhou, X., Jiang, B. & Guo, H. "High-dimensional atomistic neural network potentials for molecule-surface interactions: HCl scattering from Au(111)". *J. Phys. Chem. Lett.* **8,** 666–672 (2017).
176. Chen, D.-L., Al-Saidi, W. A. & Johnson, J. K. "The role of van der Waals interactions in the adsorption of noble gases on metal surfaces". *J. Phys.: Cond. Matt.* **24,** 424211 (2012).
177. Prates-Ramalho, J. P., Gomes, J. R. B. & Illas, F. "Accounting for van der Waals interactions between adsorbates and surfaces in density functional theory based calculations: Selected examples". *RSC Adv.* **3,** 13085–13100 (2013).
178. Patil, S. H., Tang, K. T. & Toennies, J. P. "Damping functions for the pairwise sum model of the atom-surface potential". *J. Chem. Phys.* **116,** 8118–8123 (2002).
179. Wolfe-Brannon, K. & Weare, J. H. "Perturbative calculations of selective adsorption intensity features". *Phys. Rev. B* **24,** 5753–5762 (1981).
180. Muzas, A. S., Gatti, F., Martín, F. & Díaz, C. "Diffraction of H from LiF(001): From slow normal incidence to fast grazing incidence". *Nucl. Instrum. Methods Phys. Res., Sect. B* **382,** 49–53 (2016).
181. Del Cueto, M., Muzas, A. S., Martín, F. & Díaz, C. "Accurate simulations of atomic diffractive scattering from KCl(001) under fast grazing incidence conditions". *Nucl. Instrum. Methods Phys. Res., Sect. B* **476,** 1–9 (2020).
182. Del Cueto, M., Muzas, A. S., Frankcombe, T. J., Martín, F. & Díaz, C. "Prominent out-of-plane diffraction in helium scattering from a methyl-terminated Si(111) surface". *Phys. Chem. Chem. Phys.* **21,** 15879–15887 (2019).
183. Hofmann, P. "The surfaces of bismuth: Structural and electronic properties". *Prog. Surf. Sci.* **81,** 191–245 (2006).
184. Zhang, J., Chang, C.-Z., Zhang, Z., Wen, J., Feng, X., Li, K., Liu, M., He, K., Wang, L., Chen, X., Xue, Q.-K., Ma, X. & Wang, Y. "Band structure engineering in $(Bi_{1-x}Sb_x)_2Te_3$ ternary topological insulators". *Nat. Commun* **2,** 574 (2011).
185. Tamtögl, A., Sacchi, M., Avidor, N., Calvo-Almazán, I., Townsend, P. S. M., Bremholm, M., Hofmann, P., Ellis, J. & Allison, W. "Nanoscopic diffusion of water on a topological insulator". *Nat. Commun* **11,** 035438 (2020).
186. Rodriguez-Lopez, P., Kort-Kamp, W. J. M., Dalvit, D. A. R. & Woods, L. M. "Casimir force phase transitions in the graphene family". *Nat. Commun* **8,** 14699 (2017).
187. Carlos, W. E. & Cole, M. W. "Band structure and thermodynamic properties of He atoms near a graphite surface". *Phys. Rev. B* **21,** 3713–3720 (1980).
188. Manson, J. R. & Armand, G. "Band structure of an atom adsorbed on a surface; application to the He/Cu (113) system". *Surf. Sci.* **126,** 681–688 (1983).
189. Andersson, T., Linde, P., Hassel, M. & Andersson, S. "Selective adsorption, bound states, and potential parameters for He, Ne, and Ar interacting with a Cu(110) surface". *J. Chem. Phys* **124,** 114703 (2006).
190. Riley, D. J., Jardine, A. P., Alexandrowicz, G., Hedgeland, H., Ellis, J. & Allison, W. "Analysis and refinement of the Cu(001)$c(2\times2)$CO-He potential using ^{3}He selective adsorption resonances". *J. Chem. Phys* **128,** 154712 (2008).
191. Stiles, M. D. & Wilkins, J. W. "Inelastic gas-surface scattering. II. Results". *Phys. Rev. B* **37,** 7306–7325 (1988).

192. Persson, M., Wilzén, L. & Andersson, S. "Mean free path of a trapped physisorbed hydrogen molecule". *Phys. Rev. B* **42,** 5331–5334 (1990).
193. Hernández, M., Miret-Artés, S., Villarreal, P. & Delgado-Barrio, G. "Study of the selective adsorption phenomenon in the ^{4}He/Cu(11α) (with $\alpha = 0, 3, 5, 7$) elastic scattering: The critical kinematic effect". *Surf. Sci.* **274,** 21–34 (1992).
194. Armand, G., Lapujoulade, J. & Manson, J. R. "Temperature dependence of resonance signatures in atom-surface scattering". *Phys. Rev. B* **39,** 10514–10518 (1989).
195. He, L., Kou, X. & Wang, K. L. "Review of 3D topological insulator thin-film growth by molecular beam epitaxy and potential applications". *Phys. Status Solidi RRL* **7,** 50–63 (2013).
196. Ngabonziza, P., Heimbuch, R., de Jong, N., Klaassen, R. A., Stehno, M. P., Snelder, M., Solmaz, A., Ramankutty, S. V., Frantzeskakis, E., van Heumen, E., Koster, G., Golden, M. S., Zandvliet, H. J. W. & Brinkman, A. "In situ spectroscopy of intrinsic Bi_2Te_3 topological insulator thin films and impact of extrinsic defects". *Phys. Rev. B* **92,** 035405 (2015).
197. Borisova, S., Krumrain, J., Luysberg, M., Mussler, G. & Grützmacher, D. "Mode of growth of ultrathin topological insulator Bi_2Te_3 films on Si(111) substrates". *Crystal Growth & Design* **12,** 6098–6103 (2012).
198. Jiang, Y., Wang, Y., Chen, M., Li, Z., Song, C., He, K., Wang, L., Chen, X., Ma, X. & Xue, Q.-K. "Landau quantization and the thickness limit of topological insulator thin films of Sb_2Te_3". *Phys. Rev. Lett.* **108,** 016401 (2012).
199. Kim, S., Ye, M., Kuroda, K., Yamada, Y., Krasovskii, E. E., Chulkov, E. V., Miyamoto, K., Nakatake, M., Okuda, T., Ueda, Y., Shimada, K., Namatame, H., Taniguchi, M. & Kimura, A. "Surface scattering via bulk continuum states in the 3D topological insulator Bi_2Se_3". *Phys. Rev. Lett.* **107,** 056803 (2011).
200. Das, S., Amit, Sirohi, A., Yadav, L., Gayen, S., Singh, Y. & Sheet, G. "Conventional superconductivity in the type-II Dirac semimetal $PdTe_2$". *Phys. Rev. B* **97,** 014523 (2018).
201. Zheng, H., Choi, Y., Baniasadi, F., Hu, D., Jiao, L., Park, K. & Tao, C. "Visualization of point defects in ultrathin layered 1T-$PtSe_2$". *2D Mater.* **6,** 041005 (2019).
202. Wesner, D., Derry, G., Vidali, G., Thwaites, T. & Frankl, D. R. "Inelastic effects in the scattering of ^{4}He by a graphite surface". *Surf. Sci.* **95,** 367–379 (1980).
203. Cantini, P., Terreni, S. & Salvo, C. "Inelastic effect on the resonance lineshapes in He-graphite scattering". *Surf. Sci.* **109,** L491–L496 (1981).
204. Celli, V., Marvin, A. M. & Benedek, G. "Effect of inelastic transitions on the line shape of surface resonances". *Surf. Sci.* **148,** 54–57 (1984).
205. Kawai, S., Foster, A. S., Björkman, T., Nowakowska, S., Björk, J., Canova, F. F., Gade, L. H., Jung, T. A. & Meyer, E. "Van der Waals interactions and the limits of isolated atom models at interfaces". *Nat. Commun* **7,** 11559 (2016).
206. Wolfe, K. L. & Weare, J. H. "Theoretical correlation of intensity features of selective adsorption with fourier components of the atom-surface potential". *Phys. Rev. Lett.* **41,** 1663–1666 (1978).
207. Persson, M. "Effects of the phonon structure on the elastic scattering probabilities of light particles from surfaces". *Phys. Rev. B* **36,** 7870–7882 (1987).
208. Medina, Z. & Jackson, B. "Quantum studies of light particle trapping, sticking, and desorption on metal and graphite surfaces". *J. Chem. Phys* **128,** 114704 (2008).
209. Bruch, L. W., Hansen, F. Y. & Dammann, B. "Unified quantum theory of elastic and inelastic atomic scattering from a physisorbed monolayer solid." *Phys. Rev. B* **95,** 214303 (2017).

210. Giannozzi, P., Baroni, S., Bonini, N., Calandra, M., Car, R., Cavazzoni, C., Ceresoli, D., Chiarotti, G. L., Cococcioni, M., Dabo, I., Dal Corso, A., de Gironcoli, S., Fabris, S., Fratesi, G., Gebauer, R., Gerstmann, U., Gougoussis, C., Kokalj, A., Lazzeri, M., Martin-Samos, L., Marzari, N., Mauri, F., Mazzarello, R., Paolini, S., Pasquarello, A., Paulatto, L., Sbraccia, C., Scandolo, S., Sclauzero, G., Seitsonen, A. P., Smogunov, A., Umari, P. & Wentzcovitch, R. M. "Quantum espresso: A modular and open-source software project for quantum simulations of materials". *J. Phys.: Cond. Matt.* **21,** 395502 (2009).
211. Perdew, J. P., Burke, K. & Ernzerhof, M. "Generalized gradient approximation made simple". *Phys. Rev. Lett.* **77,** 3865–3868 (1996).
212. Monkhorst, H. J. & Pack, J. D. "Special points for Brillouin-zone integrations". en. *Phys. Rev. B* **13,** 5188–5192 (1976).
213. Hatch, R. C., Bianchi, M., Guan, D., Bao, S., Mi, J., Iversen, B. B., Nilsson, L., Hornekær, L. & Hofmann, P. "Stability of the Bi_2Se_3(111) topological state: Electron-phonon and electron-defect scattering". *Phys. Rev. B* **83,** 035438 (2011).
214. Pan, Z.-H., Fedorov, A. V., Gardner, D., Lee, Y. S., Chu, S. & Valla, T. "Measurement of an exceptionally weak electron-phonon coupling on the surface of the topological insulator Bi_2Se_3 using angle-resolved photoemission spectroscopy". *Phys. Rev. Lett.* **108,** 187001 (2012).
215. Chen, C., Xie, Z., Feng, Y., Yi, H., Liang, A., He, S., Mou, D., He, J., Peng, Y., Liu, X., Liu, Y., Zhao, L., Liu, G., Dong, X., Zhang, J., Yu, L., Wang, X., Peng, Q., Wang, Z., Zhang, S., Yang, F., Chen, C., Xu, Z. & Zhou, X. J. "Tunable Dirac fermion dynamics in topological insulators". *Sci. Rep.* **3,** 2411 (2013).
216. Kondo, T., Nakashima, Y., Ota, Y., Ishida, Y., Malaeb, W., Okazaki, K., Shin, S., Kriener, M., Sasaki, S., Segawa, K. & Ando, Y. "Anomalous dressing of Dirac fermions in the topological surface state of Bi_2Se_3, Bi_2Te_3, and Cu-doped Bi_2Se_3". *Phys. Rev. Lett.* **110,** 217601 (2013).
217. Zhu, X., Santos, L., Howard, C., Sankar, R., Chou, F. C., Chamon, C. & El-Batanouny, M. "Electron-phonon coupling on the surface of the topological insulator Bi_2Se_3 determined from surface-phonon dispersion measurements". *Phys. Rev. Lett.* **108,** 185501 (2012).
218. Giraud, S. & Egger, R. "Electron-phonon scattering in topological insulators". *Phys. Rev. B* **83,** 245322 (2012).
219. Pietro, P. D., Ortolani, M., Limaj, O., Gaspare, A. D., Giliberti, V., Giorgianni, F., Brahlek, M., Bansal, N., Koirala, N., Oh, S., Calvani, P. & Lupi, S. "Observation of Dirac plasmons in a topological insulator". *Nat. Nanotechnology* **8,** 556–560 (2013).
220. Goldsmid, H. J. in *Thermoelectric Refrigeration* Springer US, 210–223 (The International Cryogenics Monograph Series, 1964).
221. Liang, J., Cheng, L., Zhang, J., Liu, H. & Zhang, Z. "Maximizing the thermoelectric performance of topological insulator Bi_2Te_3 films in the few-quintuple layer regime". *Nanoscale* **8,** 8855–8862 (2016).
222. Tang, H., Wang, X., Xiong, Y., Zhao, Y., Zhang, Y., Zhang, Y., Yang, J. & Xu, D. "Thermoelectric characterization of individual bismuth selenide topological insulator nanoribbons". *Nanoscale* **7,** 6683–6690 (2015).
223. Minnich, A. J., Dresselhaus, M. S., Ren, Z. F. & Chen, G. "Bulk nanostructured thermoelectric materials: Current research and future prospects". *Energy & Environmental Science* **2,** 466 (2009).
224. Hsiung, T.-C., Mou, C.-Y., Lee, T.-K. & Chen, Y.-Y. "Surface-dominated transport and enhanced thermoelectric figure of merit in topological insulator $Bi_{1.5}Bb_{0.5}Te_{1.7}Se_{1.3}$". *Nanoscale* **7,** 518–523 (2015).

225. Zhu, X., Santos, L., Sankar, R., Chikara, S., Howard, C., Chou, F. C., Chamon, C. & El-Batanouny, M. "Interaction of phonons and Dirac fermions on the surface of Bi_2Se_3: A strong Kohn anomaly". *Phys. Rev. Lett.* **107,** 035438 (2011).
226. Heid, R., Sklyadneva, I. Y. & Chulkov, E. V. "Electron-phonon coupling in topological surface states: The role of polar optical modes". *Sci. Rep.* **7,** 035438 (2017).
227. Bianchi, M., Guan, D., Bao, S., Mi, J., Iversen, B. B., King, P. D. C. & Hofmann, P. "Coexistence of the topological state and a two-dimensional electron gas on the surface of Bi_2Se_3". *Nat. Commun* **1,** 035438 (2010).
228. King, P. D. C., Hatch, R. C., Bianchi, M., Ovsyannikov, R., Lupulescu, C., Landolt, G., Slomski, B., Dil, J. H., Guan, D., Mi, J. L., Rienks, E. D. L., Fink, J., Lindblad, A., Svensson, S., Bao, S., Balakrishnan, G., Iversen, B. B., Osterwalder, J., Eberhardt, W., Baumberger, F. & Hofmann, P. "Large tunable Rashba spin splitting of a two-dimensional electron gas in Bi_2Se_3". *Phys. Rev. Lett.* **107,** 035438 (2011).
229. Sklyadneva, I. Y., Benedek, G., Chulkov, E. V., Echenique, P. M., Heid, R., Bohnen, K.-P. & Toennies, J. P. "Mode-selected electron-phonon coupling in superconducting Pb nanofilms determined from He atom scattering". *Phys. Rev. Lett.* **107,** 035438 (2011).
230. Silkin, V. M., García-Lekue, A., Pitarke, J. M., Chulkov, E. V., Zaremba, E. & Echenique, P. M. "Novel low-energy collective excitation at metal surfaces". *Europhysics Letters (EPL)* **66,** 260–264 (2004).
231. Evans, D., Celli, V., Benedek, G., Toennies, J. P. & Doak, R. B. "Resonance-enhanced atom scattering from surface phonons". *Phys. Rev. Lett.* **50,** 1854–1857 (1983).
232. Jia, X., Zhang, S., Sankar, R., Chou, F.-C., Wang, W., Kempa, K., Plummer, E., Zhang, J., Zhu, X. & Guo, J. "Anomalous acoustic plasmon mode from topologically protected states". *Phys. Rev. Lett.* **119,** 035438 (2017).
233. Stern, F. "Polarizability of a two-dimensional electron gas". *Phys. Rev. Lett.* **18,** 546–548 (1967).
234. Ando, T., Fowler, A. B. & Stern, F. "Electronic properties of two-dimensional systems". *RMP* **54,** 437–672 (1982).
235. Shvonski, A., Kong, J. & Kempa, K. "Plasmon-polaron of the topological metallic surface states". *Phys. Rev. B* **99,** 035438 (2019).
236. Yu, H. & Hermanson, J. C. "Subband structure and plasmon-phonon coupled excitations in the accumulation layer of ZnO". *Phys. Rev. B* **41,** 5991–6000 (1990).
237. Pitarke, J. M., Silkin, V. M., Chulkov, E. V. & Echenique, P. M. "Theory of surface plasmons and surface-plasmon polaritons". *Rep. Prog. Phys.* **70,** 1–87 (2006).
238. Wang, Y., Plummer, E. W. & Kempa, K. "Foundations of plasmonics". *Adv. Phys.* **60,** 799–898 (2011).
239. Diaconescu, B., Pohl, K., Vattuone, L., Savio, L., Hofmann, P., Silkin, V. M., Pitarke, J. M., Chulkov, E. V., Echenique, P. M., Farías, D. & Rocca, M. "Low-energy acoustic plasmons at metal surfaces". *Nature* **448,** 57–59 (2007).
240. Michiardi, M., Aguilera, I., Bianchi, M., de Carvalho, V. E., Ladeira, L. O., Teixeira, N. G., Soares, E. A., Friedrich, C., Blügel, S. & Hofmann, P. "Bulk band structure of Bi_2Te_3". *Phys. Rev. B* **90,** 075105 (2014).
241. Baroni, S., de Gironcoli, S., Corso, A. D. & Giannozzi, P. "Phonons and related crystal properties from density-functional perturbation theory". *Rev. Mod. Phys.* **73,** 515–562 (2001).

242. Ortigoza, M. A., Sklyadneva, I. Y., Heid, R., Chulkov, E. V., Rahman, T. S., Bohnen, K.-P. & Echenique, P. M. "*Ab initio* lattice dynamics and electron-phonon coupling of Bi(111)". *Phys. Rev. B* **90,** 035438 (2014).
243. Safron, S. A. "High-resolution helium atom scattering as a probe of surface vibrations". *Adv. Chem. Phys.* **95,** 129 (1996).
244. Boulares, I., Shi, G., Kioupakis, E., Lošťák, P., Uher, C. & Merlin, R. "Surface phonons in the topological insulators Bi_2Se_3 and Bi_2Te_3". *Solid State Commun.* **271,** 1–5 (2018).
245. Sobota, J. A., Yang, S.-L., Leuenberger, D., Kemper, A. F., Analytis, J. G., Fisher, I. R., Kirchmann, P. S., Devereaux, T. P. & Shen, Z.-X. "Distinguishing bulk and surface electron-phonon coupling in the topological insulator Bi_2Se_3 using time-resolved photoemission spectroscopy". *Phys. Rev. Lett.* **113,** 157401 (2014).
246. Gao, X., Zhou, M., Cheng, Y. & Ji, G. "First-principles study of structural, elastic, electronic and thermodynamic properties of topological insulator Bi_2Se_3 under pressure". *Philos. Mag.* **96,** 208–222 (2016).
247. Farnell, G. W. in *Physical Acoustics* 109–166 (Elsevier, 1970).
248. Oliner, A. A. *Acoustic Surface Waves,* 035438 (Springer Berlin Heidelberg, 1978).
249. Glinka, Y. D., Babakiray, S., Johnson, T. A., Holcomb, M. B. & Lederman, D. "Acoustic phonon dynamics in thin-films of the topological insulator Bi_2Se_3". *J. Appl. Phys.* **117,** 165703 (2015).
250. Maradudin, A. A. & Stegeman, G. I. *Surface Phonons* (eds Kress, W. & de Wette, F. W.) 035438 (Springer Berlin Heidelberg, 1991).
251. Bracco, G., Tatarek, R., Terreni, S. & Tommasini, F. "Surface optical phonons in LiF(001) observed by inelastic helium scattering". *Phys. Rev. B* **34,** 9045–9046 (1986).
252. Graham, A. P. "The low energy dynamics of adsorbates on metal surfaces investigated with helium atom scattering". *Surf Sci Rep* **49,** 115–168 (2003).
253. Zeljkovic, I., Scipioni, K. L., Walkup, D., Okada, Y., Zhou, W., Sankar, R., Chang, G., Wang, Y. J., Lin, H., Bansil, A., Chou, F., Wang, Z. & Madhavan, V. "Nanoscale determination of the mass enhancement factor in the lightly doped bulk insulator lead selenide". *Nat. Commun* **6,** 035438 (2015).
254. McMillan, W. L. "Transition temperature of strong-coupled superconductors". *Phys. Rev.* **167,** 331–344 (1968).
255. Allison, W., Willis, R. F. & Cardillo, M. "Origin of the anomalouslow-frequency losses observed in the inelastic scattering of He atoms from LiF(001)". *Phys. Rev. B* **23,** 6824–6827 (1981).
256. Wuttig, M. & Yamada, N. "Phase-change materials for rewriteable data storage". *Nat. Mater.* **6,** 824–832 (2007).
257. Hicks, L. D. & Dresselhaus, M. S. "Use of quantum-well superlattices to obtain a high figure of merit from nonconventional thermoelectric materials". *MRS Proc.* **326,** 413 (1993).
258. Zastrow, S., Gooth, J., Boehnert, T., Heiderich, S., Toellner, W., Heimann, S., Schulz, S. & Nielsch, K. "Thermoelectric transport and Hall measurements of low defect Sb_2Te_3 thin films grown by atomic layer deposition". *Semicond Sci. Technol.* **28,** 035010 (2013).
259. Zhang, Z., Zhang, H., Wu, Y., Zeng, Z. & Hu, Z. "Optimization of the thermopower of antimony telluride thin film by introducing tellurium nanoparticles". *Appl. Phys. A* **118,** 1043–1051 (2015).
260. Hinsche, N. F., Zastrow, S., Gooth, J., Pudewill, L., Zierold, R., Rittweger, F., Rauch, T., Henk, J., Nielsch, K. & Mertig, I. "Impact of the topological surface state on the thermoelectric transport in Sb_2Te_3 thin films". *ACS Nano* **9,** 4406–4411 (2015).

261. Fujimori, S., Yagi, S., Yamazaki, H. & Funakoshi, N. "Crystallization process of Sb-Te alloy films for optical storage". *J. Appl. Phys.* **64,** 1000–1004 (1988).
262. Sessi, P., Storz, O., Bathon, T., Wilfert, S., Kokh, K. A., Tereshchenko, O. E., Bihlmayer, G. & Bode, M. "Scattering properties of the three-dimensional topological insulator Sb_2Te_3: Coexistence of topologically trivial and nontrivial surface states with opposite spin-momentum helicity". *Phys. Rev. B* **93,** 035110 (2016).
263. Pankratov, O. A., Pakhomov, S. V. & Volkov, B. A. "Supersymmetry in heterojunctions: Band-inverting contact on the basis of $Pb_{1-x}Sn_xTe$ and $Hg_{1-x}Cd_xTe$". *Solid State Commun.* **61,** 93–96 (1987).
264. Wu, C., Bernevig, B. A. & Zhang, S.-C. "Helical liquid and the edge of quantum spin Hall systems". *Phys. Rev. Lett.* **96,** 106401 (2006).
265. Fu, L., Kane, C. L. & Mele, E. J. "Topological insulators in three dimensions". *Phys. Rev. Lett.* **98,** 106803 (2007).
266. Qi, X.-L. & Zhang, S.-C. "The quantum spin Hall effect and topological insulators". *Phys. Today* **63,** 33–38 (2010).
267. Pauly, C., Bihlmayer, G., Liebmann, M., Grob, M., Georgi, A., Subramaniam, D., Scholz, M. R., Sánchez-Barriga, J., Varykhalov, A., Blügel, S., Rader, O. & Morgenstern, M. "Probing two topological surface bands of Sb_2Te_3 by spin-polarized photoemission spectroscopy". *Phys. Rev. B* **86,** 235106 (2012).
268. Plucinski, L., Herdt, A., Fahrendorf, S., Bihlmayer, G., Mussler, G., Döring, S., Kampmeier, J., Matthes, F., Bürgler, D. E., Grützmacher, D., Blügel, S. & Schneider, C. M. "Electronic structure, surface morphology and topologically protected surface states of Sb_2Te_3 thin films grown on Si(111)". *J. Appl. Phys.* **113,** 053706 (2013).
269. Wang, G., Zhu, X., Wen, J., Chen, X., He, K., Wang, L., Ma, X., Liu, Y., Dai, X., Fang, Z., Jia, J. & Xue, Q. "Atomically smooth ultrathin films of topological insulator Sb_2Te_3". *Nano Res.* **3,** 874–880 (2010).
270. Seibel, C., Maaß, H., Ohtaka, M., Fiedler, S., Jünger, C., Min, C.-H., Bentmann, H., Sakamoto, K. & Reinert, F. "Single Dirac cone on the Cs-covered topological insulator surface $Sb_2Te_3(0001)$". *Phys. Rev. B* **86,** 161105 (2012).
271. Reimann, J., Güdde, J., Kuroda, K., Chulkov, E. V. & Höfer, U. "Spectroscopy and dynamics of unoccupied electronic states of the topological insulators Sb_2Te_3 and Sb_2Te_2S". *Phys. Rev. B* **90,** 081106 (2014).
272. Zhu, X., Cao, Y., Zhang, J., Plummer, E. W. & Guo, J. "Classification of charge density waves based on their nature". *Proc. Natl. Acad. Sci.* **112,** 2367–2371 (2015).
273. Arango, Y. C., Huang, L., Chen, C., Avila, J., Asensio, M. C., Grützmacher, D., Lüth, H., Lu, J. G. & Schäpers, T. "Quantum transport and nano angle-resolved photoemission spectroscopy on the topological surface states of single Sb_2Te_3 nanowires". *Sci. Rep.* **6,** 29493 (2016).
274. Yavorsky, B. Y., Hinsche, N. F., Mertig, I. & Zahn, P. "Electronic structure and transport anisotropy of Bi_2Te_3 and Sb_2Te_3". *Phys. Rev. B* **84,** 165208 (2011).
275. Nechaev, I. A., Aguilera, I., De Renzi, V., di Bona, A., Lodi Rizzini, A., Mio, A. M., Nicotra, G., Politano, A., Scalese, S., Aliev, Z. S., Babanly, M. B., Friedrich, C., Blügel, S. & Chulkov, E. V. "Quasiparticle spectrum and plasmonic excitations in the topological insulator Sb_2Te_3". *Phys. Rev. B* **91,** 245123 (2015).

276. Richter, W. & Becker, C. R. "A Raman and far-Infrared investigation of phonons in the rhombohedral V_2-VI_3 compounds Bi_2Te_3, Bi_2Se_3, Sb_2Te_3 and $Bi_2(Te_{1-x}Se_x)_3$ $(0 < x < 1)$, $(Bi_{1-y}Sb_y)_2Te_3$ $(0 < y < 1)$". *Phys. Status Solidi B* **84,** 619–628 (1977).
277. Kim, Y., Chen, X., Wang, Z., Shi, J., Miotkowski, I., Chen, Y. P., Sharma, P. A., Lima Sharma, A. L., Hekmaty, M. A., Jiang, Z. & Smirnov, D. "Temperature dependence of Raman-active optical phonons in Bi_2Se_3 and Sb_2Te_3". *Appl. Phys. Lett.* **100,** 071907 (2012).
278. Bragaglia, V., Ramsteiner, M., Schick, D., Boschker, J. E., Mitzner, R., Calarco, R. & Holldack, K. "Phonon anharmonicities and ultrafast dynamics in epitaxial Sb_2Te_3". *Sci. Rep.* **10,** 12962 (2020).
279. Sosso, G. C., Caravati, S. & Bernasconi, M. "Vibrational properties of crystalline Sb_2Te_3 from first principles". *J. Phys.: Cond. Matt.* **21,** 095410 (2009).
280. Mi, J.-L., Bremholm, M., Bianchi, M., Borup, K., Johnsen, S., Søndergaard, M., Guan, D., Hatch, R. C., Hofmann, P. & Iversen, B. B. "Phase separation and bulk p-n transition in single crystals of Bi_2Te_2Se topological insulator". *Adv. Mater.* **25,** 889–893 (2013).
281. Hoffmann, S. V., Søndergaard, C., Schultz, C., Li, Z. & Hofmann, P. "An undulator-based spherical grating monochromator beamline for angle-resolved photoemission spectroscopy". *Nucl. Instr. Meth. Phys. Res. A* **523,** 441 (2004).
282. Davis, L. E. *Handbook of Auger Electron Spectroscopy: A Reference Book of Standard Data for Identification and Interpretation of Auger Electron Spectroscopy Data,* 035438 (Physical Electronics, 1996).
283. Tamtögl, A., Ruckhofer, A., Campi, D., Allison, W. & Ernst, W. E. "Atom-surface van der Waals potentials of topological insulators and semimetals from scattering measurements". *Phys. Chem. Chem. Phys.* **23,** 7637–7652 (2021).
284. Toennies, J. P. in *Surface Phonons* (eds Kress, W. & de Wette, F. W.) 111–166 (Springer Berlin Heidelberg, Berlin, Heidelberg, 1991).
285. Trzaskowska, A. & Mroz, B. "Surface phonons in topological insulator Bi_2Te_3 investigated by Brillouin light scattering". *Sci. Rep.* **10,** 11812 (2020).
286. Lu, Q., Zhang, H.-Y., Cheng, Y., Chen, X.-R. & Ji, G.-F. "Phase transition, elastic and electronic properties of topological insulator Sb_2Te_3 under pressure: First principle study". *Chin. Phys. B* **25,** 026401 (2016).
287. Bessas, D., Sergueev, I., Wille, H.-C., Perßon, J., Ebling, D. & Hermann, R. P. "Lattice dynamics in Bi_2Te_3 and Sb_2Te_3: Te and Sb density of phonon states". *Phys. Rev. B* **86,** 224301 (2012).
288. Akgöz, Y. C., Saunders, G. A. & Sümengen, Z. "Elastic wave propagation in $Bi_{1.60}Sb_{0.40}Te_3$ and Bi_2Te_3". *J Mater Sci* **7,** 279–288 (1972).
289. Benedek, G., Bernasconi, M., Chis, V., Chulkov, E., Echenique, P. M., Hellsing, B. & Toennies, J. P. "Theory of surface phonons at metal surfaces: Recent advances". *J. Phys.: Cond. Matt.* **22,** 084020 (2010).
290. Benedek, G., Brusdeylins, G., Toennies, J. P. & Doak, R. B. "Experimental evidence for kinematical focusing in the inelastic scattering of helium from the NaF(001) surface". *Phys. Rev. B* **27,** 2488–2493 (1983).
291. Benedek, G., Gerlach, R., Glebov, A., Lange, G., Miret-Artés, S., Skofronick, J. G. & Toennies, J. P. "Focused inelastic resonances in the scattering of He atoms from NaCl(001)". *Phys. Rev. B* **53,** 11211–11217 (1996).
292. Peierls, R. E. & Roberts, L. D. "Quantum theory of solids". *Phys. Today* **9,** 29–29 (1956).
293. Luttinger, J. M. & Ward, J. C. "Ground-state energy of a many-fermion system. II". *Phys. Rev.* **118,** 1417–1427 (1960).

294. Hofmann, P. & Wells, J. W. "Surface-sensitive conductance measurements". *J. Phys.: Cond. Matt.* **21,** 013003 (2009).
295. Wells, J. W., Handrup, K., Kallehauge, J. F., Gammelgaard, L., Boggild, P., Balslev, M. B., Hansen, J. E., Petersen, P. R. E. & Hofmann, P. "The conductivity of Bi(111) investigated with nanoscale four point probes". *J. Appl. Phys.* **104,** 053717 (2008).
296. Yeom, H. W., Takeda, S., Rotenberg, E., Matsuda, I., Horikoshi, K., Schaefer, J., Lee, C. M., Kevan, S. D., Ohta, T., Nagao, T. & Hasegawa, S. "Instability and charge density wave of metallic quantum chains on a silicon surface". *Phys. Rev. Lett.* **82,** 035438 (1999).
297. Crain, J. N., Kirakosian, A., Altmann, K. N., Bromberger, C., Erwin, S. C., McChesney, J. L., Lin, J.-L. & Himpsel, F. J. "Fractional band filling in an atomic chain structure". *Phys. Rev. Lett.* **90,** 176805 (2003).
298. Tegenkamp, C., Ohta, T., McChesney, J. L., Dil, H., Rotenberg, E., Pfnur, H. & Horn, K. "Coupled Pb chains on Si(557): Origin of one-dimensional conductance". *Phys. Rev. Lett.* **100,** 076802 (2008).
299. Tegenkamp, C., Lükermann, D., Pfnür, H., Slomski, B., Landolt, G. & Dil, J. H. "Fermi nesting between atomic wires with strong spin-orbit coupling". *Phys. Rev. Lett.* **109,** 266401 (2012).
300. Park, J., Jung, S. W., Jung, M.-C., Yamane, H., Kosugi, N. & Yeom, H. W. "Self-assembled nanowires with giant rashba split bands". *Phys. Rev. Lett.* **110,** 036801 (2013).
301. Baringhaus, J., Ruan, M., Edler, F., Tejeda, A., Sicot, M., Taleb-IbrahimiAmina, Li, A.-P., Jiang, Z., Conrad, E. H., Berger, C., Tegenkamp, C. & de Heer, W. A. "Exceptional ballistic transport in epitaxial graphene nanoribbons". *Nature* **506,** 349–354 (2014).
302. Cheon, S., Kim, T.-H., Lee, S.-H. & Yeom, H. W. "Chiral solitons in a coupled double Peierls chain". *Science* **350,** 182–185 (2015).
303. Kim, T. K., Wells, J., Kirkegaard, C., Li, Z., Hoffmann, S. V., Gayone, J. E., Fernandez-Torrente, I., Haberle, P., Pascual, J. I., Moore, K. T., Schwartz, A. J., He, H., Spence, J. C. H., Downing, K. H., Lazar, S., Tichelaar, F. D., Borisenko, S. V., Knupfer, M. & Hofmann, P. "Evidence against a charge density wave on Bi(111)". *Phys. Rev. B* **72,** 085440 (2005).
304. Leuenberger, D., Yanagisawa, H., Roth, S., Dil, J. H., Wells, J. W., Hofmann, P., Osterwalder, J. & Hengsberger, M. "Excitation of coherent phonons in the one-dimensional Bi(114) surface". *Phys. Rev. Lett.* **110,** 136806 (2013).
305. Bianchi, M., Song, F., Cooil, S., Monsen, F., Wahlström, E., Miwa, J. A., Rienks, E. D. L., Evans, D. A., Strozecka, A., Pascual, J. I., Leandersson, M., Balasubramanian, T., Hofmann, P. & Wells, J. W. "One-dimensional spin texture of Bi(441): Quantum spin Hall properties without a topological insulator". *Phys. Rev. B* **91,** 165307 (2015).
306. Teo, J. C. Y., Fu, L. & Kane, C. L. "Surface states and topological invariants in three-dimensional topological insulators: Application to Bi_{1-x} Sb_x". *Phys. Rev. B* **78,** 045426 (2008).
307. Hsieh, D., Qian, D., Wray, L., Xia, Y., Hor, Y. S., Cava, R. J. & Hasan, M. Z. "A topological Dirac insulator in a quantum spin Hall phase". *Nature* **452,** 970–974 (2008).
308. Pascual, J. I., Bihlmayer, G., Koroteev, Y. M., Rust, H. P., Ceballos, G., Hansmann, M., Horn, K., Chulkov, E. V., Blugel, S., Echenique, P. M. & Hofmann, P. "Role of spin in quasiparticle interference". *Phys. Rev. Lett.* **93,** 196802 (2004).
309. Kane, C. L. & Mele, E. J. "Quantum spin Hall effect in graphene". *Phys. Rev. Lett.* **95,** 226801 (2005).
310. Murakami, S. "Quantum spin Hall effect and enhanced magnetic response by spin-orbit coupling". *Phys. Rev. Lett.* **97,** 236805 (2006).
311. Bernevig, B. A. & Zhang, S.-C. "Quantum spin Hall effect". *Phys. Rev. Lett.* **96,** 106802 (2006).

312. König, M., Wiedmann, S., Brüne, C., Roth, A., Buhmann, H., Molenkamp, L. W., Qi, X.-L. & Zhang, S.-C. "Quantum spin Hall insulator state in HgTe quantum wells". *Science* **318,** 766 (2007).
313. McMillan, W. L. "Microscopic model of charge-density waves in 2H-$TaSe_2$". *Phys. Rev. B* **16,** 643–650 (1977).
314. Johannes, M., Mazin, I. & Howells, C. "Fermi-surface nesting and the origin of the charge-density wave in $NbSe_2$". *Phys. Rev. B* **73,** 205102 (2006).
315. Rossnagel, K. "On the origin of charge-density waves in select layered transition-metal dichalcogenides". *Journal of Physics: Condensed Matter* **23,** 213001 (2011).
316. Calandra, M., Mazin, I. I. & Mauri, F. "Effect of dimensionality on the charge-density wave in few-layer 2H-$NbSe_2$". *Phys. Rev. B* **80,** 241108 (2009).
317. Chatterjee, U., Zhao, J., Iavarone, M., Di Capua, R., Castellan, J. P., Karapetrov, G., Malliakas, C. D., Kanatzidis, M. G., Claus, H., Ruff, J. P. C., Weber, F., van Wezel, J., Campuzano, J. C., Osborn, R., Randeria, M., Trivedi, N., Norman, M. R. & Rosenkranz, S. "Emergence of coherence in the charge-density wave state of 2H-$NbSe_2$". *Nature Communications* **6,** 6313 (2015).
318. Chen, C.-W., Choe, J. & Morosan, E. "Charge density waves in strongly correlated electron systems". *Rep. Prog. Phys.* **79,** 084505 (2016).
319. Johannes, M. D. & Mazin, I. I. "Fermi surface nesting and the origin of charge density waves in metals". *Phys. Rev. B* **77,** 165135 (2008).
320. Horcas, I., Fernández, R., Gómez-Rodríguez, J. M., Colchero, J., Gómez-Herrero, J. & Baro, A. M. "WSXM: A software for scanning probe microscopy and a tool for nanotechnology". *Rev. Sci. Instrum.* **78,** 013705 (2007).
321. Pouget, J.-P. "The Peierls instability and charge density wave in one-dimensional electronic conductors". *C. R. Phys.* **17,** 332–356 (2016).
322. Girault, S., Moudden, A. H. & Pouget, J. P. "Critical x-ray scattering at the Peierls transition of the blue bronze". *Phys. Rev. B* **39,** 4430–4434 (1989).
323. Requardt, H., Kalning, M., Burandt, B., Press, W. & Currat, R. "Critical x-ray scattering at the Peierls transition in the quasi-one-dimensional system $(TaSe_4)_2I$". *J. Phys.: Cond. Matt.* **8,** 2327 (1996).
324. Mönig, H., Sun, J., Koroteev, M., Bihlmayer, G., Wells, J., Chulkov, E. V., Pohl, K. & Hofmann, P. "The structure of the (111) surface of bismuth: LEED analysis and first principles calculations". *Phys. Rev. B* **72,** 085410 (2005).
325. Grüner, G. *Density Waves in Solids,* 035438 (Perseus Publishing, Cambridge, Massachusetts, 1994).
326. Grüner, G. "The dynamics of charge-density waves". *Rev. Mod. Phys.* **60,** 1129–1181 (1988).
327. Nishimori, H. & Ortiz, G. *Elements of Phase Transitions and Critical Phenomena,* 035438 (OUP Oxford, 2010).
328. Pathria, R. K. & Beale, P. D. *Statistical Mechanics,* 035438 (Elsevier, 2011).
329. Ma, T. & Wang, S. *Phase Transition Dynamics,* 035438 (Springer, 2014).
330. Lorenzo, J. E., Currat, R., Monceau, P., Hennion, B., Berger, H. & Levy, F. "A neutron scattering study of the quasi-one-dimensional conductor $(TaSe_4)_2I$". *J. Phys.: Cond. Matt.* **10,** 5039 (1998).
331. Hoesch, M., Bosak, A., Chernyshov, D., Berger, H. & Krisch, M. "Giant Kohn anomaly and the phase transition in charge density wave $ZrTe_3$". *Phys. Rev. Lett.* **102,** 086402 (2009).
332. Gayone, J. E., Hoffmann, S. V., Li, Z. & Hofmann, P. "Strong energy dependence of the electron-phonon coupling on Bi(100)". *Phys. Rev. Lett.* **91,** 127601 (2003).

333. Budai, J. D., Hong, J., Manley, M. E., Specht, E. D., Li, C. W., Tischler, J. Z., Abernathy, D. L., Said, A. H., Leu, B. M., Boatner, L. A., McQueeney, R. J. & Delaire, O. "Metallization of vanadium dioxide driven by large phonon entropy". *Nature* **515,** 535–539 (2014).
334. Wippermann, S. & Schmidt, W. G. "Entropy explains metal-insulator transition of the Si(111)-In nanowire array". *Phys. Rev. Lett.* **105,** 126102 (2010).
335. Frigge, T., Hafke, B., Witte, T., Krenzer, B., Streubühr, C., Samad Syed, A., Mikšić Trontl, V., Avigo, I., Zhou, P., Ligges, M., von der Linde, D., Bovensiepen, U., Horn-von Hoegen, M., Wippermann, S., Lücke, A., Sanna, S., Gerstmann, U. & Schmidt, W. G. "Optically excited structural transition in atomic wires on surfaces at the quantum limit". *Nature* **544,** 207–211 (2017).
336. Saito, Y., Nojima, T. & Iwasa, Y. "Highly crystalline 2D superconductors". *Nat. Rev. Mater.* **2,** 16094 (2016).
337. Zhang, W. & Melo, C. *Quasi-One-Dimensional Organic Superconductors* Advanced Physics Series (ed Zhang, W.) 035438 (World Scientific, 2018).
338. Dolinsek, J., Smontara, A., Barisic, O. S. & Gille, P. "Phonon-enhanced thermoelectric power of Y-Al-Ni-Co decagonal approximant". *Zeitschrift für Kristallographie - Crystalline Materials* **224,** 035438 (2009).
339. Allen, P. B. "Neutron spectroscopy of superconductors". *Phys. Rev. B* **6,** 2577–2579 (1972).
340. Manson, J. R., Benedek, G. & Miret-Artés, S. "Correction to "Electron-phonon coupling strength at metal surfaces directly determined from the helium atom scattering Debye-Waller factor"". *J. Phys. Chem. Lett.* **7,** 1691–1691 (2016).
341. Coxeter, H. S. M. *Introduction to Geometry,* 035438 (John Wiley and Sons: New York, 1969).
342. Beeby, J. L. "Scattering of helium atoms from surfaces". *J. Phys. C: Solid State Phys.* **4,** L359–L362 (1971).
343. Fröhlich, H. "On the theory of superconductivity: The one-dimensional case". *Proceedings of the Royal Society of London. Series A. Mathematical and Physical Sciences* **223,** 296–305 (1954).
344. Kelly, M. J. & Falicov, L. M. "Electronic ground-state of inversion layers in many-valley semiconductors". *Phys. Rev. B* **15,** 1974–1982 (1977).
345. Kelly, M. J. & Falicov, L. M. "Optical-properties of charge-density-wave ground-states for inversion layers in many-valley semiconductors". *Phys. Rev. B* **15,** 1983–1987 (1977).
346. Kelly, M. J. & Falicov, L. M. "Electronic structure of inversion layers in many-valley semiconductors". *Phys. Rev. Lett.* **37,** 1021–1024 (1976).
347. Liu, R., Ma, T., Wang, S. & Yang, J. "Thermodynamical potentials of classical and quantum systems". *Discrete & Continuous Dynamical Systems - B* **24,** 1411–1448 (2019).
348. Ma, T. & Wang, S. "Cahn-Hilliard equations and phase transition dynamics for binary systems". *Discrete & Continuous Dynamical Systems - B* **11,** 741–784 (2009).
349. Ge, Y. & Liu, A. Y. "Phonon-mediated superconductivity in electron-doped single-layer MoS_2: A first-principles prediction". *Phys. Rev. B* **87,** 241408 (2013).
350. Liu, A. Y. "Electron-phonon coupling in compressed 1T-TaS_2: Stability and superconductivity from first principles". *Phys. Rev. B* **79,** 220515 (2009).
351. Benedek, G., Hofmann, F., Ruggerone, P., Onida, G. & Miglio, L. "Surface phonons in layered crystals: Theoretical aspects". *Surf Sci Rep* **20,** 1–43 (1994).
352. Michaelson, H. B. "The work function of the elements and its periodicity". *J. Appl. Phys.* **48,** 4729–4733 (1977).
353. Benedek, G., Miglio, L., Brusdeylins, G., Heimlich, C., Skofronick, J. G. & Toennies, J. P. "Surface phonon dynamics in 2H-$TaSe_2$(001)". *Europhys. Lett.* **5,** 253–258 (1988).

354. Benedek, G., Brusdeylins, G., Heimlich, C., Miglio, L., Skofronick, J. G., Toennies, J. P. & Vollmer, R. "Shifted surface phonon anomaly in 2H-$TaSe_2$(001)". *Phys. Rev. Lett.* **60,** 1037–1040 (1988).
355. Hulpke, E. *Helium Atom Scattering from Surfaces* (ed Hulpke, E.) 035438 (Springer-Verlag, 1992).
356. Anemone, G., Garnica, M., Zappia, M., Aguilar, P. C., Al Taleb, A., Kuo, C.-N., Lue, C. S., Politano, A., Benedek, G., de Parga, A. L. V., Miranda, R. & Farías, D. "Experimental determination of surface thermal expansion and electron-phonon coupling constant of 1T-$PtTe_2$". *2D Mater.* **7,** 025007 (2020).
357. Howard, C., El-Batanouny, M., Sankar, R. & Chou, F. C. "Anomalous behavior in the phonon dispersion of the (001) surface of Bi_2Te_3 determined from helium atom-surface scattering measurements". *Phys. Rev. B* **88,** 035402 (2013).
358. Barreto, L., Kühnemund, L., Edler, F., Tegenkamp, C., Mi, J., Bremholm, M., Iversen, B. B., Frydendahl, C., Bianchi, M. & Hofmann, P. "Surface-dominated transport on a bulk topological insulator". *Nano Lett.* **14,** 3755–3760 (2014).
359. Shklovskii, B. I. & Efros, A. L. "Electronic properties of doped semiconductors". *Moscow Izdatel Nauka* **99,** 035438 (1979).
360. Pettes, M. T., Maassen, J., Jo, I., Lundstrom, M. S. & Shi, L. "Effects of surface band bending and scattering on thermoelectric transport in suspended bismuth telluride nanoplates". *Nano Lett.* **13,** 5316–5322 (2013).
361. Gehring, P., Gao, B. F., Burghard, M. & Kern, K. "Growth of high-mobility Bi_2Te_2Se nanoplatelets on hBN sheets by van der Waals epitaxy". *Nano Lett.* **12,** 5137–5142 (2012).
362. Anichini, C., Czepa, W., Pakulski, D., Aliprandi, A., Ciesielski, A. & Samorì, P. "Chemical sensing with 2D materials". *Chem. Soc. Rev.* **47,** 4860–4908 (2018).
363. Jiang, H. X. & Lin, J. Y. "Hexagonal boron nitride for deep ultraviolet photonic devices". *Semicond. Sci. Technol.* **29,** 084003 (2014).
364. Zavabeti, A., Jannat, A., Zhong, L., Haidry, A. A., Yao, Z. & Ou, J. Z. "Two-dimensional materials in large-areas: Synthesis, properties and applications". *Nano-Micro Lett.* **12,** 66 (2020).
365. Zhang, K., Feng, Y., Wang, F., Yang, Z. & Wang, J. "Two dimensional hexagonal boron nitride (2D-hBN): Synthesis, properties and applications". *J. Mater. Chem. C* **5,** 11992–12022 (2017).
366. Jana, M. & Singh, R. N. "Progress in CVD synthesis of layered hexagonal boron nitride with tunable properties and their applications". *Int. Mater. Rev.* **63,** 162–203 (2018).
367. Fazen, P. J., Remsen, E. E., Beck, J. S., Carroll, P. J., McGhie, A. R. & Sneddon, L. G. "Synthesis, properties, and ceramic conversion reactions of polyborazylene. A high-yield polymeric precursor to boron nitride". *Chem. Mater.* **7,** 1942–1956 (1995).
368. Shi, Y., Hamsen, C., Jia, X., Kim, K. K., Reina, A., Hofmann, M., Hsu, A. L., Zhang, K., Li, H., Juang, Z.-Y., Dresselhaus, M. S., Li, L.-J. & Kong, J. "Synthesis of few-layer hexagonal boron nitride thin film by chemical vapor deposition". *Nano Lett.* **10,** 4134–4139 (2010).
369. Bernard, S. & Miele, P. "Nanostructured and architectured boron nitride from boron, nitrogen and hydrogen-containing molecular and polymeric precursors". *Mater. Today* **17,** 443–450 (2014).
370. Bernard, S., Salameh, C. & Miele, P. "Boron nitride ceramics from molecular precursors: synthesis, properties and applications". *Dalton Trans.* **45,** 861–873 (2016).
371. Talyzin, A. V., Luzan, S. M., Leifer, K., Akhtar, S., Fetzer, J., Cataldo, F., Tsybin, Y. O., Tai, C. W., Dzwilewski, A. & Moons, E. "Coronene fusion by heat treatment: Road to nanographenes". *J. Phys. Chem. C* **115,** 13207–13214 (2011).
372. Li, J., Croiset, E. & Ricardez-Sandoval, L. "Carbon clusters on the Ni(111) surface: A density functional theory study". *Phys. Chem. Chem. Phys.* **16,** 2954–2961 (2014).

373. Chen, H., Zhu, W. & Zhang, Z. "Contrasting behavior of carbon nucleation in the initial stages of graphene epitaxial growth on stepped metal surfaces". *Phys. Rev. Lett.* **104,** 186101 (2010).
374. Losurdo, M., Giangregorio, M. M., Capezzuto, P. & Bruno, G. "Graphene CVD growth on copper and nickel: Role of hydrogen in kinetics and structure". *Phys. Chem. Chem. Phys.* **13,** 20836–20843 (2011).
375. Zhang, X., Wang, L., Xin, J., Yakobson, B. I. & Ding, F. "Role of hydrogen in graphene chemical vapor deposition growth on a copper surface". *J. Am. Chem. Soc.* **136,** 3040–3047 (2014).
376. Lu, G., Wu, T., Yuan, Q., Wang, H., Wang, H., Ding, F., Xie, X. & Jiang, M. "Synthesis of large single-crystal hexagonal boron nitride grains on Cu-Ni alloy". *Nat. Commun.* **6,** 6160 (2015).
377. Choi, J.-H., Cui, P., Chen, W., Cho, J.-H. & Zhang, Z. "Atomistic mechanisms of van der Waals epitaxy and property optimization of layered materials". *WIREs Comput Mol Sci* **7,** e1300 (2017).
378. Qiu, Z., Li, P., Li, Z. & Yang, J. "Atomistic simulations of graphene growth: From kinetics to mechanism". *Acc. Chem. Res.* **51,** 728–735 (2018).
379. Habib, M. R., Liang, T., Yu, X., Pi, X., Liu, Y. & Xu, M. "A review of theoretical study of graphene chemical vapor deposition synthesis on metals: Nucleation, growth, and the role of hydrogen and oxygen". *Rep. on Prog. Phys.* **81,** 036501 (2018).
380. Goriachko, A., He, Knapp, M., Over, H., Corso, M., Brugger, T., Berner, S., Osterwalder, J. & Greber, T. "Self-assembly of a hexagonal boron nitride nanomesh on Ru(0001)". *Langmuir* **23,** 2928–2931 (2007).
381. Joshi, S., Ecija, D., Koitz, R., Iannuzzi, M., Seitsonen, A. P., Hutter, J., Sachdev, H., Vijayaraghavan, S., Bischoff, F., Seufert, K., Barth, J. V. & Auwärter, W. "Boron nitride on Cu(111): An electronically corrugated monolayer". *Nano Lett.* **12,** 5821–5828 (2012).
382. Lu, J., Yeo, P. S. E., Zheng, Y., Xu, H., Gan, C. K., Sullivan, M. B., Castro Neto, A. H. & Loh, K. P. "Step flow versus mosaic film growth in hexagonal boron nitride". *J. Am. Chem. Soc.* **135,** 2368–2373 (2013).
383. Steiner, D., Mittendorfer, F. & Bertel, E. "Quasiliquid layer promotes hexagonal boron nitride (h-BN) single-domain growth: h-BN on Pt(110)". *ACS Nano* **13,** 7083–7090 (2019).
384. Müller, F., Hüfner, S. & Sachdev, H. "Epitaxial growth of boron nitride on a Rh(111) multilayer system: Formation and fine tuning of a BN-nanomesh". *Surf. Sci.* **603,** 425–432 (2009).
385. Martoccia, D., Brugger, T., Björck, M., Schlepütz, C. M., Pauli, S. A., Greber, T., Patterson, B. D. & Willmott, P. R. "h-BN/Ru(0001) nanomesh: A 14-on-13 superstructure with 3.5 nm periodicity". *Surf. Sci.* **604,** L16–L19 (2010).
386. Orlando, F., Lacovig, P., Omiciuolo, L., Apostol, N. G., Larciprete, R., Baraldi, A. & Lizzit, S. "Epitaxial growth of a single-domain hexagonal boron nitride monolayer". *ACS Nano* **8,** 12063–12070 (2014).
387. Kelsall, J., Townsend, P. S. M., Ellis, J., Jardine, A. P. & Avidor, N. "Ultrafast diffusion at the onset of growth: O/Ru(0001)". *Phys. Rev. Lett.* **126,** 155901 (15 2021).
388. Paffett, M. T., Simonson, R. J., Papin, P. & Paine, R. T. "Borazine adsorption and decomposition at Pt(111) and Ru(001) surfaces". *Surf. Sci.* **232,** 286–296 (1990).
389. Orlando, F., Larciprete, R., Lacovig, P., Boscarato, I., Baraldi, A. & Lizzit, S. "Epitaxial growth of hexagonal boron nitride on Ir(111)". *J. Phys. Chem. C* **116,** 157–164 (2012).
390. Farkas, A. P., Török, P., Solymosi, F., Kiss, J. & Kónya, Z. "Investigation of the adsorption properties of borazine and characterisation of boron nitride on Rh(111) by electron spectroscopic methods". *Appl. Surf. Sci.* **354,** 367–372 (2015).

391. He, J.-W. & Goodman, D. W. "Interaction of borazine with a Re(0001) surface, studied by LEED, TDS, AES and ELS". *Surf. Sci.* **232,** 138–148 (1990).
392. Haug, L., Roth, J. P., Thaler, M., Steiner, D., Menzel, A., Tosoni, S., Pacchioni, G. & Bertel, E. "Precursor chemistry of h-BN: Adsorption, desorption, and decomposition of borazine on Pt(110)". en. *Phys. Chem. Chem. Phys.* **22,** 11704–11712 (2020).
393. Späth, F., Gebhardt, J., Düll, F., Bauer, U., Bachmann, P., Gleichweit, C., Görling, A., Steinrück, H.-P. & Papp, C. "Hydrogenation and hydrogen intercalation of hexagonal boron nitride on Ni(111): reactivity and electronic structure". *2D Mater.* **4,** 035026 (2017).
394. Kim, M., Moon, S. W., Kim, G., Yoon, S. I., Kim, K., Min, S. K. & Shin, H. S. "Effect of Pt crystal surface on hydrogenation of monolayer h-BN and its conversion to graphene". en. *Chem. Mater.* **32,** 4584–4590 (2020).
395. Lau, J. A., Calvo-Almazán, I., Townsend, P. S. M., Ward, D. J., Jardine, A. P., Allison, W., Ellis, J., Hinch, B. J. & Avidor, N. "Structural evolution of a cyclooctatetraene adlayer on Cu(111) during isothermal desorption". *J. Phys. Chem. C* **122,** 8941–8945 (2018).
396. Avidor, N., Hedgeland, H., Held, G., Jardine, A. P., Allison, W., Ellis, J., Kravchuk, T. & Alexandrowicz, G. "Highly proton-ordered water structures on oxygen precovered Ru {0001}". *J. Phys. Chem. A* **115,** 7205–7209 (2011).
397. Kraus, P., Gösweiner, C., Tamtögl, A., Apolloner, F. & Ernst, W. E. "Adhesion properties of hydrogen on Sb(111) probed by helium atom scattering". *EPL (Europhysics Letters)* **114,** 56001 (2016).
398. Bahn, E., Tamtögl, A., Ellis, J., Allison, W. & Fouquet, P. "Structure and dynamics investigations of a partially hydrogenated graphene/Ni(111) surface". *Carbon* **114,** 504–510 (2017).
399. Avidor, N. & Allison, W. "Helium diffraction as a probe of structure and proton order on model ice surfaces". *J. Phys. Chem. Lett* **7,** 4520–4523 (2016).
400. Lin, C., Corem, G., Godsi, O., Alexandrowicz, G., Darling, G. R. & Hodgson, A. "Ice nucleation on a corrugated surface". *J. Am. Chem. Soc.* **140,** 15804–15811 (2018).
401. Tamtögl, A., Bahn, E., Sacchi, M., Zhu, J., Ward, D. J., Jardine, A. P., Jenkins, S. J., Fouquet, P., Ellis, J. & Allison, W. "Motion of water monomers reveals a kinetic barrier to ice nucleation on graphene". *Nat. Commun.* **12,** 3120 (2021).
402. Lin, C.-Y., Cheng, C.-E., Wang, S., Shiu, H. W., Chang, L. Y., Chen, C.-H., Lin, T.-W., Chang, C.-S. & Chien, F. S.-S. "Synchrotron radiation soft x-ray induced reduction in graphene oxide characterized by time-resolved photoelectron spectroscopy". *J. Phys. Chem. C* **119,** 12910–12915 (2015).
403. Feulner, P. & Menzel, D. "The adsorption of hydrogen on ruthenium(001): Adsorption states, dipole moments and kinetics of adsorption and desorption". *Surf. Sci.* **154,** 465–488 (1985).
404. Sutter, P., Cortes, R., Lahiri, J. & Sutter, E. "Interface formation in monolayer graphene-boron nitride heterostructures". *Nano Lett.* **12,** 4869–4874 (2012).
405. Yin, J., Li, J., Hang, Y., Yu, J., Tai, G., Li, X., Zhang, Z. & Guo, W. "Boron nitride nanostructures: Fabrication, functionalization and applications". *Small* **12,** 2942–2968 (2016).
406. Zhang, C., Zhao, S., Jin, C., Koh, A. L., Zhou, Y., Xu, W., Li, Q., Xiong, Q., Peng, H. & Liu, Z. "Direct growth of large-area graphene and boron nitride heterostructures by a co-segregation method". *Nat. Commun.* **6,** 6519 (2015).
407. Kutana, A., Goriachko, A., Hu, Z., Sachdev, H., Over, H. & Yakobson, B. I. "Buckling patterns of graphene-boron nitride alloy on Ru(0001)". *Adv. Mater. Interfaces* **2,** 1500322 (2015).

408. Petrović, M., Hagemann, U., Horn-von Hoegen, M. & Meyer zu Heringdorf, F.-J. "Microanalysis of single-layer hexagonal boron nitride islands on Ir(111)". *Appl. Surf. Sci.* **420,** 504–510 (2017).
409. Kidambi, P. R., Blume, R., Kling, J., Wagner, J. B., Baehtz, C., Weatherup, R. S., Schloegl, R., Bayer, B. C. & Hofmann, S. "In situ observations during chemical vapor deposition of hexagonal boron nitride on polycrystalline copper". *Chem. Mater.* **26,** 6380–6392 (2014).
410. Song, L., Ci, L., Lu, H., Sorokin, P. B., Jin, C., Ni, J., Kvashnin, A. G., Kvashnin, D. G., Lou, J., Yakobson, B. I. & Ajayan, P. M. "Large scale growth and characterization of atomic hexagonal boron nitride layers". *Nano Lett.* **10,** 3209–3215 (2010).
411. Guo, N., Wei, J., Fan, L., Jia, Y., Liang, D., Zhu, H., Wang, K. & Wu, D. "Controllable growth of triangular hexagonal boron nitride domains on copper foils by an improved low-pressure chemical vapor deposition method". *Nanotechnology* **23,** 415605 (2012).
412. Gilbert, S. M., Pham, T., Dogan, M., Oh, S., Shevitski, B., Schumm, G., Liu, S., Ercius, P., Aloni, S., Cohen, M. L. & Zettl, A. "Alternative stacking sequences in hexagonal boron nitride". *2D Mater.* **6,** 021006 (2019).
413. Paszkowicz, W., Pelka, J. B., Knapp, M., Szyszko, T. & Podsiadlo, S. "Lattice parameters and anisotropic thermal expansion of hexagonal boron nitride in the $10 - 297.5$ K temperature range". *Appl. Phys. A* **75,** 431–435 (2002).
414. Arblaster, J. W. "Crystallographic properties of ruthenium". *Platinum Met. Rev.* **57,** 127–136 (2013).
415. Martoccia, D., Pauli, S. A., Brugger, T., Greber, T., Patterson, B. D. & Willmott, P. R. "h-BN on Rh(111): Persistence of a commensurate 13-on-12 superstructure up to high temperatures". *Surf. Sci.* **604,** L9–L11 (2010).
416. Leconte, N. & Jung, J. "Commensurate and incommensurate double moire interference in graphene encapsulated by hexagonal boron nitride". *2D Mater.* **7,** 031005 (2020).
417. Laskowski, R., Blaha, P. & Schwarz, K. "Bonding of hexagonal BN to transition metal surfaces: An *ab initio* density-functional theory study". *Phys. Rev. B* **78,** 045409 (2008).
418. Clark, S. J., Segall, M. D., Pickard, C. J., Hasnip, P. J., Probert, M. I. J., Refson, K. & Payne, M. C. "First principles methods using CASTEP". *Z. Kristallogr. Cryst. Mater.* **220,** 567–570 (2009).
419. Vanderbilt, D. "Soft self-consistent pseudopotentials in a generalized eigenvalue formalism". en. *Phys. Rev. B* **41,** 7892–7895 (1990).
420. Borca, B., Barja, S., Garnica, M., Minniti, M., Politano, A., Rodriguez-García, J. M., Hinarejos, J. J., Farías, D., Parga, A. L. V. d. & Miranda, R. "Electronic and geometric corrugation of periodically rippled, self-nanostructured graphene epitaxially grown on Ru(0001)". *New J. Phys.* **12,** 093018 (2010).
421. Maccariello, D., Campi, D., Al Taleb, A., Benedek, G., Farías, D., Bernasconi, M. & Miranda. "Low-energy excitations of graphene on Ru(0 0 0 1)". *Carbon* **93,** 1–10 (2015).
422. Martoccia, D., Björck, M., Schlepütz, C. M., Brugger, T., Pauli, S. A., Patterson, B. D., Greber, T. & Willmott, P. R. "Graphene on Ru(0001): A corrugated and chiral structure". *New Journal of Physics* **12,** 043028 (2010).
423. Tonkikh, A. A., Voloshina, E. N., Werner, P., Blumtritt, H., Senkovskiy, B., Güntherodt, G., Parkin, S. S. P. & Dedkov, Y. S. "Structural and electronic properties of epitaxial multilayer h-BN on Ni(111) for spintronics applications". *Sci. Rep.* **6,** 23547 (2016).
424. Jang, A.-R., Hong, S., Hyun, C., Yoon, S. I., Kim, G., Jeong, H. Y., Shin, T. J., Park, S. O., Wong, K., Kwak, S. K., Park, N., Yu, K., Choi, E., Mishchenko, A., Withers, F., Novoselov, K. S.,

Lim, H. & Shin, H. S. "Wafer-scale and wrinkle-free epitaxial growth of single-orientated multilayer hexagonal boron nitride on sapphire". *Nano Lett.* **16,** 3360–3366 (2016).

425. Sutter, P., Lahiri, J., Zahl, P., Wang, B. & Sutter, E. "Scalable synthesis of uniform few-layer hexagonal boron nitride dielectric films". *Nano Lett.* **13,** 276–281 (2013).
426. Pease, R. S. "An x-ray study of boron nitride". *Acta Crystallogr.* **5,** 356–361 (1952).
427. Ferrari, E., Galli, L., Miniussi, E., Morri, M., Panighel, M., Ricci, M., Lacovig, P., Lizzit, S. & Baraldi, A. "Layer-dependent debye temperature and thermal expansion of Ru(0001) by means of high-energy resolution core-level photoelectron spectroscopy". *Phys. Rev. B* **82,** 195420 (2010).
428. Thomas, S., Ajith, K. M., Chandra, S. & Valsakumar, M. C. "Temperature dependent structural properties and bending rigidity of pristine and defective hexagonal boron nitride". *J. Phys.: Condens. Matter* **27,** 315302 (2015).

Danksagung

Nach nun insgesamt fast fünf Jahren am Institut für Experimentalphysik an der TU Graz ist es an der Zeit, zurückzublicken und Resümee zu ziehen. Im Rahmen dieser Retrospektive möchte ich einigen WegbegleiterInnen meinen besonderen Dank aussprechen.

Das größte Dankeschön gilt meinen beiden Betreuern Univ.-Prof. Dipl.-Phys. Dr.rer.nat Wolfgang E. Ernst und Priv.-Doz. Dipl.-Ing. Dr.techn. Anton Tamtögl, die mich über all diese Jahre mit vollster Unterstützung begleitet haben. Prof. Ernst sorgte mit seiner kompetente Herangehensweise während Diskussionen und Besprechungen innerhalb der Forschungsgruppe immer wieder für neue Denkanstöße. Durch seine langjährige Erfahrung in der Wissenschaft brachte er oft völlig neue Sichtweisen ein und unterstützte damit den Werdegang meiner Arbeit.

Während meiner Zeit unter den "Heliumstreuern" hatte ich aber noch eine zweite wichtige Stütze mit Priv.-Doz. Tamtögl, oder Toni. Er war meine erste Anlaufstelle für Fragen jeglicher Art und zu jeder Zeit. Unsere gemeinsamen Diskussionen haben einen wesentlichen Beitrag zur Entstehung dieser Arbeit geleistet. Durch sein ruhiges und sachliches Auftreten fanden unsere Gespräche immer auf Augenhöhe statt. Wann auch immer etwas im Labor nicht funktionierte oder Fragen auftauchten, stand er mir behilflich zu Seite. Ich danke ihm für seine Kollegialität, seine konstruktive Kritik beim Verfassen von Papers, die Korrektur-Vorschläge für diese Dissertation und die entstandene Freundschaft.

Weiters möchte ich mich bei Michael Pusterhofer bedanken, der mir mit seinen großartigen Fähigkeiten im Programmieren und durch das mathematischen Lösen von Aufgaben bei so manchen Python-Problemen geholfen hat. Durch sein Engagement im Programmieren der HASlib stand er mir sogar nach seiner Zeit an der TU immer noch mit einem Rat zur Seite.

Ebenso danke ich Simon Halbritter für seine Arbeit im Labor, die den Grundstein für einige Publikationen gelegt hat.

Danke auch an Stephan Schmutzler für sein Engagement beim Python-Programmieren und die gemeinsame Zeit im Büro und Labor danken. Die unglaublich entspannte und lockere Atmosphäre in unserem Büro war an so manch stressigem Arbeitstag von großer Bedeutung.

Mein Dank gebührt ebenso meinen mittlerweile langjährigen Instituts-Gefährten Bernhard Thaler, Maximilian Lasserus, Roman Messner, Leonhard Treiber, Martin Schnedlitz, Ralf Meyer und Alexander Schiffmann, die alle beinahe zeitgleich mit mir ihre Diplomarbeit und Dissertation begonnen haben. Ihnen möchte ich für viele Ratschläge im Labor, für unzählige lustige Stunden und für spannende Unterhaltungen beim wöchentlichen Nudel- und Toast-Essen danken.

Weiters bedanke ich mich bei allen KollegInnen am gesamten Institut für Experimentalphysik für die respektvolle und umgängliche Art. Den Kollegen in der mechanischen und elektronischen Werkstatt möchte ich für ihre kompetente und professionelle Hilfe bei technischen Aufgabenstellungen und Problemen danken.

Dank gebührt auch Prof. Giorgio Benedek, der bei seinem einmonatigen Besuch für den nötigen theoretischen Input in unserer Arbeitsgruppe sorgte. Durch sein unerschöpfliches Wissen konnten wir unsere experimentellen Daten mit der nötigen Theorie versehen.

Neben diesem tollen wissenschaftlichen Umfeld möchte ich auch noch einige Personen aus meinem privaten Kreis hervorheben, die mich stets motivieren und mir den nötigen Rückhalt geben. Danke an meine MusikkollegInnen im Vokalensemble und am Konservatorium für den Ausgleich zum technischen Leben. Insbesondere möchte ich Johannes, Vogi und Birgitt nennen.

Ein großer Dank geht an meine tolle Familie, angefangen bei den Großeltern am Janneckweg, Ruckiopa, meinem Bruder Roman und zu guter Letzt meinen lieben Eltern. Danke Mama und danke Papa für eure immerwährende Unterstützung und euren starken Rückhalt, den ich unglaublich schätze und ohne den ich niemals so weit gekommen wäre.

Ich danke meiner größten Unterstützerin Anna für die Kraft, die sie mir gibt. Du hast mich immer motiviert und in meinem Tun unterstützt und mir damit den nötigen Rahmen geschaffen, um voranzukommen. Danke!

Graz, Juli 2021